NOTE TO USERS

This reproduction is the best copy available.

UMI®

University of Alberta

The Temporal Dynamics and Regulation of Posttranslational Histone Modifications

by

Kirk James McManus ©

A thesis submitted to the Faculty of Graduate Studies and Research in partial fulfillment
of the requirements for the degree of Doctor of Philosophy

in

Medical Sciences-Oncology

Edmonton, Alberta

Spring, 2005

Library and
Archives Canada

Published Heritage
Branch

395 Wellington Street
Ottawa ON K1A 0N4
Canada

Bibliothèque et
Archives Canada

Direction du
Patrimoine de l'édition

395, rue Wellington
Ottawa ON K1A 0N4
Canada

0-494-08272-0

Your file Votre référence
ISBN
Our file Notre reference
ISBN

NOTICE:
The author has granted a non-exclusive license allowing Library and Archives Canada to reproduce, publish, archive, preserve, conserve, communicate to the public by telecommunication or on the Internet, loan, distribute and sell theses worldwide, for commercial or non-commercial purposes, in microform, paper, electronic and/or any other formats.

The author retains copyright ownership and moral rights in this thesis. Neither the thesis nor substantial extracts from it may be printed or otherwise reproduced without the author's permission.

AVIS:
L'auteur a accordé une licence non exclusive permettant à la Bibliothèque et Archives Canada de reproduire, publier, archiver, sauvegarder, conserver, transmettre au public par télécommunication ou par l'Internet, prêter, distribuer et vendre des thèses partout dans le monde, à des fins commerciales ou autres, sur support microforme, papier, électronique et/ou autres formats.

L'auteur conserve la propriété du droit d'auteur et des droits moraux qui protège cette thèse. Ni la thèse ni des extraits substantiels de celle-ci ne doivent être imprimés ou autrement reproduits sans son autorisation.

In compliance with the Canadian Privacy Act some supporting forms may have been removed from this thesis.

While these forms may be included in the document page count, their removal does not represent any loss of content from the thesis.

Conformément à la loi canadienne sur la protection de la vie privée, quelques formulaires secondaires ont été enlevés de cette thèse.

Bien que ces formulaires aient inclus dans la pagination, il n'y aura aucun contenu manquant.

Canada

ABSTRACT

Over the past century, we have witnessed a tremendous growth in our understanding of the inheritance and regulation of genetic information. Novel biochemical, molecular and cytological approaches have been instrumental in furthering our understanding of DNA structure and function. What is now clear is that the underlying processes involving DNA are far more complicated that originally envisioned. In fact, it is often ignored that all cellular processes involving DNA are not performed on naked DNA but rather in the context of histones and higher-order chromatin structure. In turn, mechanisms regulating chromatin structure, such as posttranslational histone modifications, have far reaching implications for replication, transcription, DNA repair, apoptosis and mitosis and as a corollary, tumorigenesis.

A major focus of this thesis has been to develop novel *in situ* approaches to investigate the dynamics of posttranslational histone modifications and the substrate specificity preference profiles of enzymes regulating their dynamics. The results described in this thesis focus primarily on the characterization of histone methylation and phosphorylation dynamics and the substrate specificity preferences of two highly related histone acetyltransferases (HATs). We document previously uncharacterized cell cycle associated dynamics of several specific methylations occurring in histones H3 and H4 and establish that one specific modification is critical for genomic integrity. Next, we identify and characterize a previously unrecognized population of phosphorylated H2AX foci that are independent of DNA DSB repair. We identify mitosis-associated dynamics for these foci that are regulated by functional ATM expression. Finally, we demonstrate that CBP and P300 exhibit subtle differences in their HAT specificity preferences, which

may account for the recent functional differences ascribed to each. We propose that the complex regulation and dynamics of many posttranslational histone modifications are critical to many nuclear processes, particularly to the fidelity of mitosis.

ACKNOWLEDGEMENTS

First and foremost I would like to thank my supervisor, Dr. Michael Hendzel, for providing me numerous opportunities to further my research career and foster my interest in science. I would also like to thank my supervisory committee members, Drs. Roseline Godbout and Michael Schultz for providing valuable input and direction during my tenure as a PhD student at the Cross Cancer Institute.

I wish to acknowledge additional individuals for technical assistance during my PhD program including Dr. Xuejun Sun (Imaging Facility), Ms. Juanita Wizniak (Flow Cytometry Facility), Ms. Mary Packer (immunoblotting), Ms. Heather Jenkins (immunoblotting), Ms. Linda Harris (library), and Ms. Gina Kennedy (administrative assistance).

I would like to extend a large 'thank-you' to Mr. Darin McDonald who not only provided technical advice but was also invaluable during the writing of this thesis and numerous papers. I truly appreciate your friendship. I would also like to acknowledge all present and past laboratory members for helpful discussions and technical assistance and in particular Ms. Maryse Fillion, Mr. Greg Chan and Ms. Carmen Tomkinson (Gittens).

I would also like to thank the additional members of my Candidacy Examination Committee, Drs. Gordon Chan, Ellen Shibuya and Neil Adames and the additional members of my Thesis Examination Committee, Drs. Gordon Chan and J. B. Rattner (University of Calgary).

I would like to acknowledge the various funding agencies that have provided me funding in the form of studentships and travel awards during my tenure as a PhD student; the Natural Sciences and Engineering Research Council of Canada (NSERC), the Canadian Institutes of Health Research (CIHR), the Alberta Heritage Foundation for Medical Research (AHFMR), the Endowed PhD Studentship Incentive Award (Department of Oncology), the 75th Anniversary Graduate Studentship Award (University of Alberta), the Walter H. Johns Award (University of Alberta), Dr. Herbert Meltzer Memorial Award (Department of Oncology) and the PhD Travel Award (National Cancer Institute of Canada).

I wish to extend a heart-felt thank you to my family for their continued love and support: Mom and Dad, Wendy, Mike, Ryan and Matthew Stasiuk, Brian and Annmarie McManus, and Ken and Della Heaman.

Finally, I thank my wife, Jacki, for her unconditional love, support and understanding… particularly during the stresses of the last year. I truly appreciate everything you have done to help me out!

Table of Contents

CHAPTER 1 – Introduction ... 1
- 1.0 INTRODUCTION ... 1
- 1.1 THE HISTONES ... 2
- 1.2 THE NUCLEOSOME – A HISTORICAL PERSPECTIVE ... 7
- 1.3 NUCLEOSOME DIVERSITY AND HETEROGENEITY ... 8
- 1.4 HISTONE VARIANTS ... 10
  - 1.4.1 Histone H2A and H2A Variants ... 11
  - 1.4.2 Histone H2B and H2B Variants ... 12
  - 1.4.3 Histone H3 and H3 Variants ... 13
  - 1.4.4 Histone H4 and H4 Variants ... 15
- 1.5 HISTONE AMINO-TERMINAL DOMAINS – STRUCTURE AND FUNCTION ... 16
- 1.6 POSTTRANSLATIONAL MODIFICATIONS OF THE CORE HISTONE ... 20
  - 1.6.1 Histone Acetylation ... 24
  - 1.6.2 Histone Phosphorylation ... 31
  - 1.6.3 Histone Methylation ... 35
  - 1.6.4 Histone Ubiquitination ... 40
  - 1.6.5 Histone Biotinylation ... 43
  - 1.6.6 Histone Sumoylation ... 44
  - 1.6.7 Histone ADP-Ribosylation ... 46
- 1.7 HIGHER ORDER CHROMATIN STRUCTURE ... 47
- 1.8 HISTONE CODE HYPOTHESIS ... 56
  - 1.8.1 Binary Switches ... 61
- 1.9 RESEARCH OBJECTIVES ... 63
  - 1.9.1 Chapter 3 – Dynamic Changes in Histone Lysine Methylations: Identification of a Mitosis-specific Function for Dynamic Methylation in Chromosome Congression and Segregation ... 63
  - 1.9.2 Chapter 4 – ATM-dependent Mitotic Phosphorylation of H2AX in Normally Growing Mammalian Cells ... 63
  - 1.9.3 Chapter 5 – Quantitative Analysis of CBP- and P300-Induced Histone Acetylations In Situ Using a Native Chromatin Template ... 64
- 1.10 REFERENCES ... 66

CHAPTER 2 – Materials and Methods ... 89
- 2.1 REAGENTS ... 89
- 2.2 CELL LINES AND TISSUE CULTURE ... 89
- 2.3 IMMUNOFLUORESCENT LABELING ... 91
  - 2.3.1 Indirect Immunofluorescent Labeling ... 91
  - 2.3.2 In Situ Indirect Immunofluorescent Peptide Competition Assay ... 95
  - 2.3.3 Embryo Indirect Immunofluorescence ... 95
  - 2.3.4 In Situ Calf Intestinal Alkaline Phosphatase Assay ... 97
  - 2.3.5 5-Fluorouridine Labeling and Transcription ... 98

2.3.6 5-Bromo-2'-deoxyuridine Labeling and DNA Replication ... 98
2.4 CELL SYNCHRONIZATION AND MITOTIC ENRICHMENT 99
2.4.1 Double Thymidine Block ... 99
2.4.2 Nocodazole Treatment ... 99
2.4.3 ALLN Treatment ... 100
2.5 FLOW CYTOMETRY ... 100
2.5.1 Ethanol Fixation ... 101
2.5.2 Indirect Immunofluorescent Staining ... 102
2.5.3 Propidium Iodide Staining ... 102
2.5.4 Flow Cytometric Analysis ... 103
2.6 IMMUNOBLOT ANALYSIS ... 103
2.6.1 Nuclear Preparation ... 104
2.6.2 Acid-Extraction of Nuclear Proteins ... 104
2.6.3 Gel Preparation and Protein Resolution ... 105
2.6.4 Immunoblotting and Development ... 106
2.7 PLASMID CONSTRUCTS AND TRANSIENT EXPRESSION ... 108
2.7.1 Plasmid Constructs ... 108
2.7.2 Lipid-based Transient Transfection ... 109
2.8 CELLULAR IMAGING ... 109
2.8.1 Digital Imaging Microscopy ... 110
2.8.2 Confocal Microscopy ... 110
2.9 QUANTITATIVE IMAGING MICROSCOPY ... 111
2.9.1 Normalizing Signal Intensity Data to Account for Histone Variability ... 114
2.9.2 Identification of Specific Cell Cycle Stages ... 114
2.9.3 Determining Protein Expression Levels by DIM ... 115
2.9.4 Three-Dimensional Colocalization Analysis ... 116
2.10 IMAGE DECONVOLUTION ... 116
2.11 IMAGE PREPARATION – IMARIS AND METAMORPH ... 117
2.11.1 3D Projections, Isosurface Renderings and Qualitative and Quantitative Measurements ... 118
2.11.2 Line Scanning in MetaMorph ... 118
2.12 STATISTICAL APPROACHES AND ANALYSES ... 118
2.12.1 Flow Cytometry Dot Plots and Cell Cycle Analyses ... 119
2.12.2 Analysis of Variance (ANOVA) ... 119
2.12.3 Tukey-Kramer Post-tests ... 120
2.12.4 Student t-tests ... 120
2.12.5 Histogram Distributions ... 121
2.12.6 Scatter Plots and Linear Regression Analysis ... 121
2.12.7 Calculating Relative Protein Expression Levels ... 122
2.13 REFERENCES ... 123

CHAPTER 3 – Dynamic Changes in Histone Lysine Methylations: Identification of a Mitosis-specific Function for Dynamic Methylation in Chromosome Congression and Segregation 124
- 3.1 INTRODUCTION 125
- 3.2 RESULTS 129
  - 3.2.1 Histone Methylation in Asynchronous Cell Cultures 129
  - 3.2.2 Epitope Accessibility is Not Responsible for Qualitative Differences in Methylation Status 140
  - 3.2.3 Global Histone Methylation Dynamics Throughout the Cell Cycle 142
  - 3.2.4 Quantitative Imaging Microscopy Identifies Mitosis-Specific Methylation and Demethylation Cycles in Cycling Cells 147
  - 3.2.5 Replication-Independent Nucleosome Assembly Does Not Account for the Dramatic Decrease in tMeK9 Abundance in the Late Stages of Mitosis. 149
  - 3.2.6 Dynamic Methylation of Lysine Residues in Developing Mouse Embryos and Primary Tissue Cultures 150
  - 3.2.7 Cells Lacking tMeK9 Exhibit a Wide Range of Abnormal Mitotic Phenotypes 153
- 3.3 DISCUSSION 158
- 3.4 ACKNOWLEDGMENTS 166
- 3.5 REFERENCES 167

CHAPTER 4 – ATM-dependent Mitotic Phosphorylation of H2AX in Normally Growing Mammalian Cells 172
- 4.1 INTRODUCTION 173
- 4.2 RESULTS 177
  - 4.2.1 Distinctive γ-H2AX Focal Populations in Unirradiated Nuclei 177
  - 4.2.2 Anti-γ-H2AX Antibodies Specifically Recognize Phosphorylated H2AX 181
  - 4.2.2 Small and Large γ-H2AX Foci Partition in Both Heterochromatin and Euchromatin 187
  - 4.2.4 Small γ-H2AX Foci are Distinguishable from Large γ-H2AX DNA Repair Foci 188
  - 4.2.5 Dynamic Changes in the Abundance of γ-H2AX Accompany Cell Cycle Progression in Unirradiated Mammalian Cells. 190
  - 4.2.6 Mitosis-specific Increases in γ-H2AX do not Reflect Changes in Epitope Accessibility 194
  - 4.2.7 Functional ATM Expression Correlates with Mitosis-specific H2AX Phosphorylation 198
  - 4.2.8 Quantitative Imaging Microscopy Reveals that Functional ATM is Required for Mitotic H2AX Phosphorylation 201
  - 4.2.9 Functional ATM Expression is Required for Mitosis-Associated Increases in γ-H2AX 205
- 4.3 DISCUSSION 209

4.4 ACKNOWLEDGEMENTS 215
4.5 REFERENCES 216

CHAPTER 5 – Quantitative Analysis of CBP- and P300-Induced Histone Acetylations In Situ Using a Native Chromatin Template 222
5.1 INTRODUCTION 223
5.2 RESULTS 227
5.2.1 Development of an in vivo HAT Assay 227
5.2.2 GFP-CBP and HA-P300 Recapitulate Endogenous Expression Patterns 229
5.2.3 Transient HAT Expression Results in Minimal Increases in Total Protein Expression 232
5.2.4 Transient HAT Expression Does Not Alter HDAC or other HAT Expression 236
5.2.5 Transient and Minimal Increases in HAT Expression Correlate with Acetylation Increases 241
5.2.6 GFP-CBP and HA-P300 Alter the Steady-state Levels of Specific Acetylated Species of Histones 243
5.2.7 Transient HAT Expression Correlates with Increased Histone Acetylation 245
5.2.8 Transient HAT Expression Induces Acetylation at Specific Histone Residues 252
5.3 DISCUSSION 253
5.4 ACKNOWLEDGEMENTS 258
5.5 REFERENCES 259

CHAPTER 6 – Discussion 263
6.0 DISCUSSION 263
6.1 HISTONE CODE HYPOTHESIS – DOES A HISTONE CODE EXIST? 266
6.2 BINARY SWITCHES – DO THEY REGULATE PROTEIN (HP1) DYNAMICS? 270
6.3 FUTURE DIRECTIONS 272
6.3.1 Identification of All Posttranslational Histone Modifications 273
6.3.2 Characterization of the Temporal Dynamics of Posttranslational Histone Modifications 277
6.3.3 Evaluating and Identifying Potential Functions Regulated by Posttranslational Histone Modifications 278
6.3.4 Identification of Histone Modifying Enzyme Specificity Preferences In Vivo 279
6.3.5 Epigenetic Regulation as Novel Therapeutic Targets 280
6.4 REFERENCES 283

APPENDIX A – Solutions and Recipes 289

APPENDIX B – Supplemental Statistical Analyses from Chapter 3 300

List of Tables

Table	Title	
1.1	Properties of mammalian histones	5
1.2	Histone modifications and their general effects on gene transcription	23
1.3	Targets of CBP and P300 acetylation activities	30
2.1	Descriptions of the mammalian cell lines utlized	90
2.2	Antibodies, their dilutions and sources	93-94
2.3	Characteristics of the blocking peptides	96
3.1	Analysis of variance of unweighted means for methylated histone epitopes in 10T1/2 cells as measured by flow cytometry	145
3.2	Mitotic aberrations in Suv39h1/2 dn IMEFs	157
4.1	Volumetric distribution of γ-H2AX foci in unirradiated and irradiated IM fibroblasts	180
4.2	Relative percentage of cells in specific cell cycle stages	197
4.3	Quantitative analysis of normalized γ-H2AX signal intensity in mitotic and interphase cells	204
4.4	Quantitative analysis of mean normalized γ-H2AX signal intensity in interphase and mitotic AT5BI cells	208
5.1	Total BCP and P300 expression levels in cells transiently expressing GFP-CBP and HA-P300	235
5.2	Calculation of total HDAC and HAT expression levels in GFP-CBP expressing COS-7 cells	239
5.3	Calculation of total HDAC and HAT expression levels in HA-P300 expressing HeLa cells	240
5.4	Anti-acetylation antibody panel	242

List of Figures

Figure	Title	Page
1.1	Nucleosome and chromatin structure	3
1.2	Structural elements of the core histones	6
1.3	Single amino acid sequences of the core histone NTDs	17
1.4	Location of various posttranslational histone modifications	22
1.5	The histone acetylation and deacetylation reactions	25
1.6	The histone phosphoryation and dephosphorylation reactions	32
1.7	The histone methylation reactions	36
1.8	A putative model depicting the hierarchical series of folding events involved in the generation of higher-order chromatin structure	48
1.9	Side views of three putative 30nm fiber models	50
1.10	Putative models of higher-order chromatin structure	54
1.11	Histone code hypothesis and binary switches	57
2.1	Schematic description of the principle steps involved in QIM	112
3.1	Indirect immunofluorescent peptide competition assays	130
3.2	Indirect immunofluorescent peptide competition assays for anti-tMeK9	131
3.3	Spatial localization and progression of various methylated lysine residues	132
3.4	High-resolution images of various lysine methylation epitopes in mouse cells	134
3.5	Temporal and spatial progression patterns of tMeK9 through mitosis	135
3.5	Phosphatase-treatment does not diminish anti-tMeK9 immunoreactivity	137
3.7	Chromosome banding patterns of tMeK4 and tMeK9	139
3.8	Qualitative assessment of the abundance of various methylated lysine residues at different cell cycle stages	141
3.9	Cell cycle-dependent progression patterns of methylation epitopes as demonstrated by flow cytometry	143
3.10	Quantitative comparisons of normalized methylation signal intensities at specific cell cycle stages	147
3.11	tMeK9 dynamics during mouse embryonic neural tube development	152
3.12	Suv39h1/2 dn IMEFs are devoid of tMeK9 in pericentromeric heterochromatin	154
3.13	Typical abnormal mitotic phenotypes observed in the absence of tMeK9 (H3)	155
4.1	Focal distribution of γ-H2AX in S-phase cells	179
4.2	Localization of γ-H2AX foci using three different anti-γ-H2AX antibodies	183
4.3	The anti-γ-H2AX antibody speicifally recognizes a phospho-epitope *in situ*	185
4.4	*In situ* indirect immunofluorescent peptide competition assay	186
4.5	Spatial localization of the small γ-H2AX foci with DNA DSB	

repair proteins 189
4.6 Mitotic-specific increases in γ-H2AX signal intensities in unirradiated mammalian cells 191
4.7 Typical γ-H2AX signal intensity variability observed throughout the cell cycle 193
4.8 Qualitative increases in the abundance of γ-H2AX in mitotically-enriched cells 196
4.9 Localization of γ-H2AX in AT2BE and AT5BI fibroblasts 199
4.10 QIM reveals a mitotic-specific phosphorylation event that correlates with functional ATM expression 203
4.11 Normally growing AT5BI cells do not exhibit mitosis-associated increases in γ-H2AX 206
4.12 Spatial localization of phospho-ATM in IM fibroblasts 211
5.1 GFP-CBP and HA-P300 expression correlate with increased lysine 5 acetylation 228
5.2 Sub-nuclear distribution of transiently expressed GFP-CBP/HA-P300 and endogenous CBP/P300 in relation to acetylation and chromatin 230
5.3 Determination of total HAT expression in GFP-CBP and HA-P300 expressing cells 233
5.4 Determination of HDAC and HAT expression levels in GFP-CBP expressing cells 238
5.5 Distribution of normalized acetylation intensities 244
5.6 Relationship between GFP-CBP and acetylation 247
5.7 Relationship between HA-P300 and acetylation 248
5.8 Relationship between ASF-GFP and acetylation 249
5.9 Relationships between HAT expression and acetylation of specific lysine residues 251

LIST OF ABBREVIATIONS

%	percent
˚C	degrees celcius
3D	three-dimensional
Å	Ångstrom
aa	amino acid(s)
Acetyl-CoA	acetyl-coenzyme A
ADP	adenosine diphosphate
ALLN	*N*-acetyl-*L*-leucyl-*L*-leucyl-*L*-norleucinal
ANOVA	analysis of variance
AP-2	activator protein 2
ASF	alternative splicing factor
ATM	ataxia telangiectasia mutated
ATP	adenosine triphosphate
ATR	ATM and Rad3-related
bp	base pair(s)
BrdU	5-bromo-2'-deoxyuridine
cAMP	cyclic adenosine monophosphate
CBP	CREB binding protein
CD	circular dichroism
CENPA	centromeric protein A
CHD	chromodomain-helicase-DNA-binding protein
ChIP	chromatin immunoprecipitation
chromodomain	chromatin organization modifier
CIP	calf intestinal alkaline phosphatase
Clr4	cryptic loci regulator
cm	centimeter(s)
CO_2	carbon dioxide
CPTS	copper phthalocyanine 3,4',4'',4'''-tetrasulfonic acid tetrasodium salt
CRAS	coding region activating sequence
CREB	camp response element binding protein
C-SET	carboxy-SET
CTD	carboxy-terminal domain
C-terminal	carboxy-terminal
Cy3	Cyanin 3
D	aspartic acid
DAPI	4',6-diamidino-2-phenylindole
df	degrees of freedom
DHFR	dihydrofolate reductase
DIM	digital imaging microscopy
dMeK4	dimethylated K4 (H3)
dMeK9	dimethylated K9 (H3)
DNA	deoxyribonucleic acid
DNA-PK$_{CS}$	DNA-protein kinase (catalytic subunit)

Dot1	disrupter of telomere silencing 1
DSB	double-strand break
E	glutamic acid
ECL	enhanced chemi-luminescence
EDTA	ethylenediaminetetraacetic acid
EM	electron microscopy
FU	5-Fluorouridine
GFP	green fluorescent protein
GNAT	Gcn5-related *N*-acetyltransferase
GTP	guanosine triphosphate
H_0	null hypothesis
H_2SO_4	sulfuric acid
HA	hemagglutinin
HAT(s)	histone acetyltransferase(s)
HCl	hydrogen chloride
HDAC(s)	histone deacetylase(s)
HDM(s)	histone demethylase(s)
HFD	histone fold domain
HMG	high mobility group
HMT(s)	histone methyltransferase(s)
HP1	heterochromatin protein 1
hr	hour(s)
HRP	horse-radish peroxidase
HSF	heat shock factor
IIF	indirect immunofluorescence
IR	γ-irradiation
I-SET	intervening-SET domain
K	lysine
kDa	kilodalton(s)
M	molar
mA	milliamp(s)
MDM2	mouse double minute 2
min	minute(s)
mL	milliliters
mM	millimolar
mMeK20	monomethylated K20 (H4)
mMeK4	monomethylated K4 (H3)
mMeK9	monomethylated K9 (H3)
MOD	mammalian modifier
MSK	mitogen- and stress-response kinase
MYST	MOZ, YBF2/Sas3, Sas2 and TIP60
NA	numerical aperature
NaOH	sodium hydroxide
ng	nanogram(s)
nm	nanometer(s)
nM	nanomolar

Norm-Ac	normalized acetylation
N-SET	amino-SET domain
NTD	amino-terminal domain
OTF	optical transfer file
PAGE	polyacrylamide gel electrophoresis
PARP	poly-ADP-ribose polymerase
PBS	phosphate buffered saline
PCAF	P300/CBP associated factor
PhosS10	phosphorylated S10 (H3)
PhosS28	phosphorylated S28 (H3)
PI	propidium iodide
PI3-K	phosphatidyl-inositol-3-kinase
PML	promyelocytic leukemia
PMSF	phenylmethanesulfonyl fluoride
*p*PDA	*p*-paraphenylenediamine
Q	glutamine
QIM	quantitative imaging microscopy
r	radius
R	Arginine
RanGAP1	Ran-GTPase-activating protein 1
RDNA	replication-dependent nucleosome assembly
RINA	replication-independent nucleosome assembly
RNA	ribonucleic acid
RPM	revolutions per minute
S	serine
SAHA	suberolylanilide hydroxamic acid
SAM	S-adenosyl methionine
SD	standard deviation
SDS	sodium dodecyl sulfate
SEM	standard error of the mean
SET	Su(var)3-9, Enhancer of zeste and Trithorax
Su(var)3-9	suppressor of variegation 3-9
SUMO	small ubiquitin-related modifier
T	threonine
TBS	tris buffered saline
TBST	tris buffered saline with Tween-20
TEMED	N,N,N',N'-tetramethylethylene diamine
TIF	tagged image format
tMeK20	trimethylated K20 (H4)
tMeK4	trimethylated K4 (H3)
tMeK9	trimethylated K9 (H3)
TSA	trichostatin-A
TSI	total signal intensity
U	units
UAS	upstream activator sequence
UV	ultraviolet

V	volts
v/v	volume per volume
W	watts
w/v	weight per volume
α	alpha
β	beta
γ	gamma
γ-H2AX	gamma-H2AX (phosphorylated at serine 139)
μl	microlitres
μM	micromolar
π	pie (3.141592)
Φ	represents a hydrophobic amino acid residue

CHAPTER 1

Introduction

1.0 INTRODUCTION

Over the past century, our knowledge about the inheritance and regulation of genetic information has increased tremendously. Technical advances in biochemistry, molecular biology and genetics have all been essential in expanding the current understanding of DNA structure and function. Much of the detail about how DNA is manipulated *in vivo* in the orchestration of DNA replication, transcription and DNA repair is now available. However, what has become increasingly clear, is that the underlying mechanism(s) regulating these processes are far more complicated than originally perceived. For instance, it is often unappreciated that eukaryotic DNA is packed into chromatin through its interaction with histones and that chromatin itself represents the physiological substrate of all cellular processes involving DNA. In turn, mechanisms that regulate chromatin structure, such as posttranslational modifications, either directly or indirectly regulate replication, transcription, apoptosis and DNA repair thereby influencing numerous processes including embryogenesis, development, and tumorigenesis.

A recent resurgence surrounding the investigation of posttranslational histone modifications has begun, driven primarily by the development of new immunological reagents. Antibodies have been, and are currently being developed, that recognize individual or combinations of posttranslational modifications occurring at different residues on each of the histones. Unfortunately however, much of the current understanding of posttranslational histone modifications including their regulation, dynamics and functions has been based solely on *in vitro* experiments using simplified chromatin templates. These templates are incapable of reconstituting chromatin as it exists *in vivo*. In an attempt to define chromatin structure and functional relationships in a physiological environment, a major goal of this thesis was to develop novel *in situ* approaches that utilize these immunological reagents. The quantitative *in situ* methodology that I developed was employed to define the temporal dynamics of posttranslational modification (Chapters 3 and 4) and the substrate specificity preferences of enzymes (Chapter 5) using native substrates where higher-order chromatin structures dominate the chromatin organization.

1.1 THE HISTONES

The histones are the primary proteins that mediate DNA folding into chromatin fibers. As such, they form the fundamental structural unit, the nucleosome (Figure 1.1A). The nucleosome is comprised of an octomeric protein core around which DNA is wrapped. The individual nucleosomes are connected by short intervening sequences of approximately 20 to 40 base pairs (bp) termed linker DNA, forming the 10 nm fiber, or 'beads-on-a-string' conformation (Figure 1.1B). Chemical cross-linking and X-ray crystallographic data indicate that core histones are arranged as an H3-H4 tetramer ($[H3\text{-}H4]_2$) with two H2A-H2B dimers positioned on either side (Figure 1.1A). The 146 bp of DNA are wrapped around the core particle in one and three quarter turns and follows a left-handed double helix across the surface of the nucleosome. For simplicity, the nucleosome structure can be visualized as a flattened cylinder with a diameter of 11 nm and a height of 5.5 nm (Figure 1.1C). Contained within the structure is a two-fold axis of symmetry, or dyad axis, which essentially dissects the nucleosome into two nearly identical halves. Because histone:DNA interactions are disrupted under high salt concentrations (>800 mM), the majority of these interactions appear to be electrostatic.

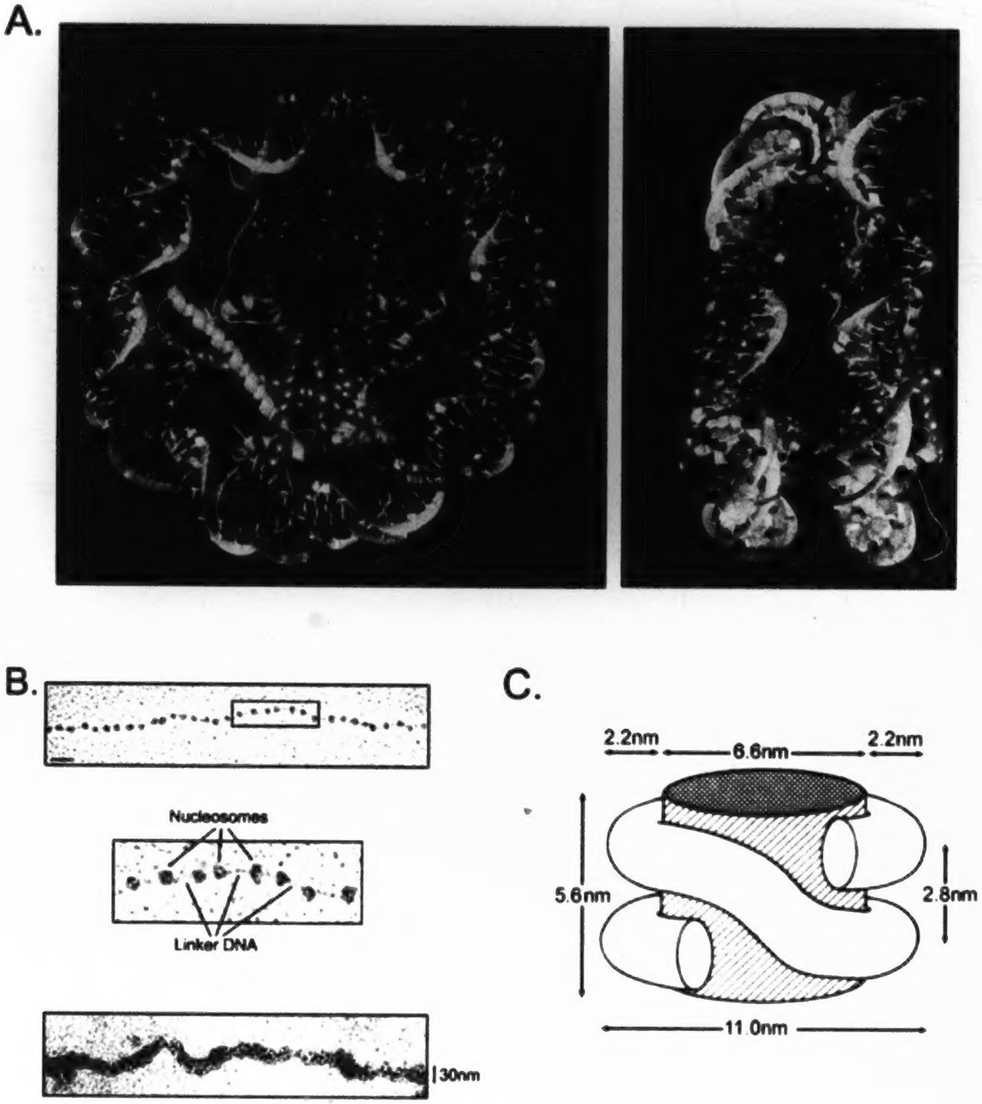

Figure 1.1. Nucleosome and chromatin structure.
Panel A presents a ribbon trace of the 146-bp DNA phosphodiester backbones (brown and turquoise) and eight histone proteins main chains: H3 (blue), H4 (green), H2A (yellow) and H2B (red). The views are down the DNA superhelix axis for the left particle and a 90° rotation for the right. For both particles the dyad axis of symmetry is aligned vertically with the DNA center at the top. Note that the entire NTDs are not included in this crystal structure. (Adapted from (Luger et al., 1997)). Panel B presents electron micrographs depicting the 'beads-on-a-string' motif (top) and 30 nm fiber (bottom). The middle micrograph is a magnification of the region indicated by the black rectangle – it serves to identify the linker DNA and nucleosomes. Scale bar represents 50 nm. The diameter of the fiber shown in the bottom panel is approximately 30 nm. (Adapted from (Alberts et al., 2002)). Panel C displays a schematic representation of the nucleosome core particle comprised of an octomeric core particle (hatched cylinder) and DNA (white cylinder). Approximate dimensions are indicated. (Adapted from (Wolffe, 1998)).

Histones were originally described by Albrecht Kossel in 1884 and have since been identified in almost all eukaryotic cells – they are notably absent from dinoflagellates (Vernet et al., 1990). Although the histones are the predominant nuclear proteins comprising approximately 50% of the total nuclear proteome by mass, they are relatively small proteins ranging between 12 kDa and 23 kDa (Table 1.1). They also contain disproportionately high percentages of arginine (R) and lysine (K) residues rendering them highly basic (Table 1.1). Based on size, net charge and solubility properties, five distinct subtypes have been identified that can be classified into two major types. The core histones, H2A, H2B, H3 and H4, form the octameric core particle while histone H1 or the 'linker-histone', binds linker DNA joining adjacent nucleosomes. Histone H1 is not required for nucleosome formation, but rather appears to be essential for the formation and maintenance of higher-order chromatin structure (Gunjan et al., 2001). The association of H1 with the nucleosome effectively protects an additional 20 bp of linker DNA from micrococcal nuclease digestion and forms a structure referred to as a chromatasome. The structure of histone H1 differs from those of the core histones in that it is a tripartite structure. It contains a central globular domain (see below) and 'unstructured' amino- and carboxy-terminal domains (NTD and CTD). The four core histones only contain two major domains, an 'unstructured' NTD (see below) and a highly structured globular domain similar to that found in H1. The globular domain is comprised of three alpha- (α-) helices (one long and two short) and two intervening non-helical 'loop' regions that are collectively referred to as the histone fold domain (HFD) (Figure 1.2, A). X-ray crystallographic data demonstrated that the three α-helices from the four core histones are specifically arranged to give a tertiary structure

Table 1.1: Properties of mammalian histones.

Histone	Type	Length	MW[a]	Lysine[b]	Arginine[c]	Net Charge
H2A	Core	129	13960	14 (10.9%)	12 (9.3%)	+15
H2B	Core	125	13774	20 (16.0%)	8 (6.4%)	+19
H3	Core	135	15273	13 (9.6%)	18 (13.3%)	+20
H4	Core	102	11236	11 (10.8%)	14 (13.7%)	+16
H1	Linker	224	22500	66 (29.5%)	3 (1.3%)	+58

[a] MW represents molecular weight
[b] number of lysine residues per molecule (percentage of total residues that are lysines)
[c] number of arginine residues per molecule (percentage of total residues that are arginines)

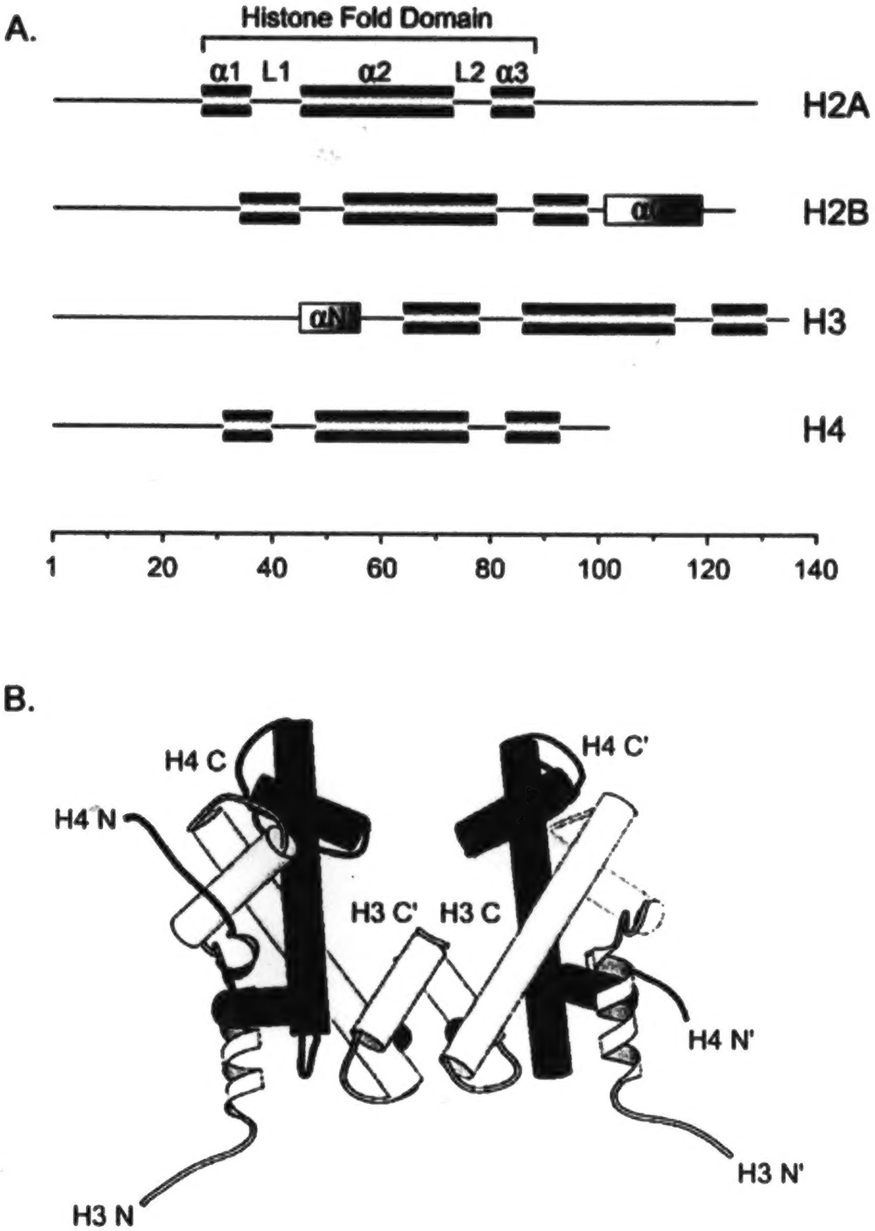
A.
Histone Fold Domain
α1
L1
α2
L2
α3
H2A
H2B
αC
H3
αN
H4
1
20
40
60
80
100
120
140
B.
H4 C
H4 C'
H4 N
H3 C'
H3 C
H4 N'
H3 N'
H3 N

Figure 1.2. Structural elements of the core histones.
Schematic representation of the four core histone (A) where the positions of the three α-helical regions (α1, α2 and α3) comprising the histone fold domain (HFD) are indicated by gray rectangles. The position of the two linker regions (L1 and L2) are indicated as are the two additional helices αC (H2B) and αN (H3). A scale bar indicating the relative amino acid positions is indicated at the bottom. Panel B illustrates the approximate 3D positions of the three α-helices of the histone fold for histones H3 and H4. The interface, or the 'histone-handshake' between both sets of histones H3 and H4 (H3:H4 and H3':H4') within the same nucleosome are shown. (Adapted from (Wolffe, 1998)).

known as the histone fold (Figure 1.2, B). The HFDs of H3 and H4, and H2A and H2B form the primary interface between histones within the same nucleosome and interlock to form the 'histone handshake' (Figure 1.2, B) (Wolffe, 1998). The histone handshake interaction gives rise to the stable H2A-H2B and H3-H4 dimers, primarily through ionic interactions, that are fundamental to core octamer assembly. Chemical cross-linking and X-ray crystallographic studies indicate that the globular domains are responsible for binding the predominant proportion of the DNA (~121 bp) within the nucleosome, with each heterodimer (i.e. H2A-H2B or H3-H4) binding approximately 30 bp of DNA (Arents et al., 1991; Luger et al., 1997). Interactions between the histones and DNA occur between residues located in the α-helices or the intervening loop regions of the HFD and the phosphodiester backbone of the DNA. It is for this reason that nucleosome assembly is considered DNA sequence independent.

1.2 THE NUCLEOSOME – A HISTORICAL PERSPECTIVE

Although the basic repeating unit of chromatin is now known to be the nucleosome, this wasn't always the case. Initial insights into a repeating chromatin structure were obtained from limited mircrococcal nuclease digestions of DNA and electron microscopy performed under variable denaturing conditions. Micrococcal nuclease digestion of chromatin followed by gel electrophoreses resulted in the identification of a repeating fragment of 180-200 bp (Hewish and Burgoyne, 1973; Williamson, 1970). This repeating fragment is now known to represent the DNA associated with a single nucleosome. The principle of a repeating chromatin structure was further supported in the 1970's by EM images identifying a highly repetitive, 'beads-on-a-string', conformation (Figure 1.1, B) (Olins and Olins, 1974; Woodcock et al., 1976a; Woodcock et al., 1976b). The diameter of these 'beads' were approximately 10 nm, giving rise to the term '10 nm fiber'. As a direct result of these investigations, Kornberg proposed the 'nucleosome model', which postulated that each particle or bead was comprised of DNA wrapped around an octamer of core histones (Kornberg, 1974; Kornberg and Thomas, 1974). Early in its infancy, the 'nucleosomal model' was thought to only persist within a small subfraction of chromatin. However, subsequent analyses have demonstrated that more than 80% of nuclear eukaryotic DNA is complexed in this fashion (Noll, 1974) and thereby solidified a role for the nucleosome in DNA compaction.

1.3 NUCLEOSOME DIVERSITY AND HETEROGENEITY

Nucleosome diversity or heterogeneity is brought about by at least three different, yet interrelated, mechanisms. First, variability within each of the core histone subtypes (e.g. H2A, H2B, H3 and H4) exists that is highly conserved across species (Sullivan et al., 2002). Genes encoding supplemental core histone variants within each of those subtypes, with the possible exception of histone H4 (see below), have been identified. Moreover, only a few amino acid (aa) substitutions in these minor variants typically distinguish them from their prototypic subtype. However, some histone variants differ from their prototypic histone subtype through the inclusion of an extended CTD. In humans for example, H2AX and macroH2A differ from the major H2A subtype through the inclusion of an additional 13 and 200 aa residues within their respective CTDs. A second mechanism that increases nucleosome diversity is the incorporation of minor histone variants into chromatin in a DNA replication-independent manner. Replication-independent nucleosome assembly (RINA) presumably occurs when chromatin is in a more 'relaxed' structural state and is exclusively associated with transcription (Ahmad and Henikoff, 2002b). Correspondingly, many of the minor histone variants that are incorporated during RINA are constitutively expressed at low levels throughout the entire cell cycle whereas the expression of the major histone subtypes is tightly regulated and coupled to DNA synthesis. It is the combination of strict temporal regulation and dramatic increases in expression levels of the major histone subtypes that ensures they are the predominant histone incorporated during replication-dependent nucleosome assembly (RDNA) (Turner, 2002b; Wolffe, 1998). Conversely, the apparent lack of temporal regulation and their presence outside of S-phase ensures that the minor histone variants form the predominant pool of non-chromatinized histone outside of S-phase (Jackson and Chalkley, 1985). Their 'elevated' levels (as compared with the major histone subtypes) outside of S-phase, virtually guarantees their inclusion into chromatin (Turner, 2002b). The final mechanism underlying increased nucleosome diversity is that of posttranslational histone modifications. To date, well over 65 different modifications have been identified which in various combinations and permutations, could produce well over 6×10^{64} uniquely modified nucleosomes. It is certainly true that many of these modifications are rare, while others only occur under certain circumstances. Nevertheless, the huge combinatorial repertoire of posttranslational modifications remaining means that it is possible that most, if not all, nucleosomes could be unique. Because posttranslational modifications form the basis of this thesis, they are described in greater detail below. Overall, it is the complexity inherent in each of these three mechanisms that when found in various combinations ensures that nucleosomes are extremely heterogeneous. An important corollary of the inclusion of histone variants and posttranslational modifications at various stages of the cell cycle, is that different chromatin states (i.e. highly compacted or less compacted and transcriptionally active or silent) can occur that have critical functional roles in nuclear and cellular processes.

1.4 HISTONE VARIANTS

In addition to core histone variants acting to increase the diversity of the nucleosome, many minor variants have evolved specialized functions within specific chromatin subtypes (see below). Major histone subtypes can often be distinguished from minor variants by both their timing of expression and their pattern of incorporation into newly synthesized DNA. The expression patterns of the major histone subtypes are highly regulated and tightly coupled with S-phase (Schumperli, 1986; van Wijnen et al., 1994). This fixed temporal regulation pattern assures that major variants represent the predominant histone pools that are incorporated following DNA replication. In most metazoans, the major histone subtypes are most frequently present as multi-gene families, with each gene cluster typically encoding all four core histones (Albig and Doenecke, 1997; Doenecke et al., 1997; Marzluff et al., 2002; Sullivan et al., 2002). In contrast, genes encoding minor histone variants frequently localize within chromosomal regions outside those containing histone gene clusters and are referred to as 'orphan' histones. Many minor variants are constitutively expressed in an S-phase independent fashion although some variants do exhibit S-phase dependent expression patterns (see below). As a result, minor histone variants represent the predominant histone species outside of S-phase. Importantly, it is the constitutively expressed minor variants that are critical for the replacement of histones lost during specific physiologic processes such as transcription and DNA repair.

1.4.1 *Histone H2A and H2A Variants*

Histone H2A is the second largest core histone in humans (Table 1.1) and contains a slightly extended CTD as compared with other three core histones (Figure 1.2, A). Importantly, a section of the H2A CTD (residues 105-117) links it to the underlying H3:H4 HFD and is believed to further stabilize the nucleosome structure (Luger et al., 1997). Currently there are at least five histone H2A variants that have been identified including; macroH2A1, macroH2A2, H2ABbd, H2AX and H2AZ (reviewed in (Dryhurst et al., 2004; Pilch et al., 2003; Redon et al., 2002)). Histone H2AX is a minor histone H2A variant that is found in species ranging from *Giardia intestinalis* to *Homo sapiens* where it comprises either 95% or between 2% and 25% of the total H2A pools, respectively (Rogakou et al., 1998). H2AX contains an invariant sequence motif that is highly conserved both with respect to position and sequence – the serine-glutamine-(aspartic acid/glutamic acid)-Φ motif (SQ(D/E)Φ), where Φ represents a hydrophobic residue, localizes to the extreme CTD of H2AX. However, between species some variability does exist as the distance between the globular domain and the SQ(D/E)Φ motif is 16 aa residues longer in mammals than in *G intestinalis* (reviewed in (Pilch et al., 2003)). In many organisms including *Saccharomyces cerevisiae, Drosophila melanogaster*, *Xenopus laevis*, and mammals, H2AX can be phosphorylated at the S residue within the SQ(D/E)Φ motif. This phosphorylation event typically occurs in response to DNA double strand breaks (DSBs) arising naturally or induced under certain experimental conditions (see Chapter 4 for additional details). It is this phosphorylated form of H2AX that is commonly referred to as γ-H2AX. Since γ-H2AX was studied in detail in this thesis, additional characteristics are provided in Chapter 4.

Histone H2AZ is another minor histone H2A variant that is found in species ranging from *S. cerevisiae* to *H sapiens*. Unlike H2AX, H2AZ exhibits substantial sequence variability between species. For instance, H2AZ orthologs from *S. cerevisiae* and *Mus musculus* are only 64.3% identical or 79.1% similar, although H2AZ is more highly conserved among metazoan species (Rangasamy et al., 2004). The observation that H2AZ is essential for viability in *D. melanogaster*, *Tetrahymena thermophila* and *M. musculus* (Brown, 2001; Faast et al., 2001; Liu et al., 1996; van Daal and Elgin, 1992) suggests that H2AZ exhibits a major functional role within the nucleus. However, this trait is not evolutionarily conserved as H2AZ is not essential in yeast (Santisteban et al., 2000). The disparity between its requirement within various species is perhaps due to the sequence divergence observed between distantly-related species, or the observation that H2AZ represents only a small fraction of the total H2A pool. For example in *S. cerevisiae*, H2AX is the predominant H2A subtype comprising approximately 95% of the total H2A pool (Pilch et al., 2003). Unlike H2AX however, H2AZ appears to exhibit a role in gene activation (Santisteban et al., 2000), while knockdown studies have suggested it may play an undefined role in genomic stability (Rangasamy et al., 2004). Interestingly, in *D. melanogaster* and in response to DNA DSBs, H2AZ (or H2Av) accomplishes the same role that H2AX does in most other species (Madigan et al., 2002).

1.4.2 *Histone H2B and H2B Variants*

Histone H2B is a highly conserved histone species with nearly identical sequences having been identified in fungi, plants and metazoans. Some divergent sequences have been observed but only from highly divergent species. H2B differs from H2A and H3 in that it contains an additional C-terminal α-helix that appears to mediate its interaction with nucleosomal DNA (Figure 1.2, A) (Luger et al., 1997). The extra α-helix localizes to the outer plane of the nucleosomal disc and is suggested to have a role in nucleosomal stacking and the generation of higher-order chromatin structure (Luger et al., 1997). Like histones H2A and H3, a pollen-specific H2B variant has been identified in lily (*Lilium longiflorum*) that specializes in chromatin compaction within pollen (Ueda et al., 2000). Furthermore, a sperm-specific histone, SubH2Bv, found in vertebrates such as rodents and bovine, has also been identified (Aul and Oko, 2002).

1.4.3 *Histone H3 and H3 Variants*

Histone H3 (or H3.1) is a replication-dependent histone. It is encoded by nine intronless genes (*H3/a, H3/b, H3/c, H3/d, H3/f, H3/I, H3/j, H3/k* and *H3/l*) clustered on the short arm of chromosome 6 (Albig and Doenecke, 1997; Doenecke et al., 1997; Marzluff et al., 2002; Sullivan et al., 2002). From a structural perspective histone H3 (or H3.1) is instrumental in organizing the nucleosome – the dyad axis, or two-fold axis of symmetry, is organized along the dimerization interface of the two H3 molecules (Arents et al., 1991; Luger et al., 1997). Apart from the previously described interactions with histone H4, H3 also interacts with H2A and makes at least two specific contacts with the nucleosomal DNA. In higher eukaryotes there are at least four different histone H3 isoforms that include the prototypic H3.1, H3.2, H3.3 and centromeric protein-A (CENP-A). Additional H3 variants have been identified and include a pollen-specific form from lily (Ueda et al., 2000) and at least four non-orthologous variants from *Caenorhabditis elegans* and *Caenorhabditis briggsae* whose function(s) remain to be determined (Malik and Henikoff, 2003).

Histone H3.2 (Entrez accession number S06743) is a replication-dependent histone H3 variant encoded by *H3/m*. It differs from the canonical H3 sequence (Entrez accession number JH0304) by only 1 aa. Located upstream of the murine *H3/m* gene is a coding region activating sequence (CRAS) that up-regulates the expression of H3.2 specifically at the G_1/S transition (Hurt et al., 1991; Hurt et al., 1989). Subsequent investigations have identified two specific DNA sequence elements (α and Ω) within the CRAS that bind nuclear factors to induce its expression. Consistent with a specific role in regulating the replication-associated expression pattern, α and Ω elements have been identified upstream of all four major core histone subtypes whose expression patterns are also replication-dependent (Bowman and Hurt, 1995; Kaludov et al., 1996). Mutation of either of these sequence elements (i.e. α or Ω) resulted in a four-fold decrease in expression levels and strongly implicates them in restricting H3.2 expression to the G_1/S boundary. Although H3.2 expression is restricted to S-phase, it is incorporated primarily within the pericentromeric heterochromatin (Russanova et al., 1989) presumably by some unknown targeting mechanism.

Histone H3.3 is a constitutively-expressed replacement H3 variant that is encoded by 'orphan' genes devoid of the strict transcriptional (e.g. α and Ω sequence elements) and post-transcriptional controls that regulate the expression pattern of H3.1 and H3.2. All eukaryotic organisms examined to date express both histone H3.1 and H3.3. The H3.3 protein sequence differs from that of H3.1 at only a few aa positions – the sequence divergence occurs at four distinct positions, one within the NTD and three within the HFD. Each of the four divergent positions appears to impart variable degrees of functional consequence. For instance, in *Drosophila melanogaster*, the three substitutions in the HFD are essential for replication-independent nucleosome assembly (Ahmad and Henikoff, 2002b). However, whether these three positions affect the deposition of nucleosomes or their strength of packing still remains to be determined. Nevertheless, the correlation between H3.3 deposition and transcriptional activity *in vivo* argues that chromatinized H3.3 may be more transcriptionally permissive, and may function in a similar fashion to H2A.Z (see above). Although histone H3.3 expression levels are overwhelmed by H3.1 in S-phase, it is constitutively expressed throughout the entire cell cycle. Therefore, it represents the major H3 isoform available for deposition or replacement outside of S-phase (Wu et al., 1982). In fact, Bosch and Suau (1995) noted that in dividing rat neuroblasts, histones H3.1 and H3.2 were the predominant histones incorporated into chromatin, while in non-dividing and long-lived neurons, H3.1 and H3.2 were gradually replaced by H3.3.

CENP-A is another highly specialized histone H3 variant that localizes to eukaryotic centromeres (Palmer et al., 1991; Palmer et al., 1987) where it is believed to regulate the packaging of centromeric chromatin. CENP-A is unique amongst all H3 variants in that it does not exhibit any sequence similarity with the NTD of H3.1 (Ahmad and Henikoff, 2002a). In fact, CENP-A only exhibits about 50% sequence identity with H3.1, almost all of which occurs within the HFD (Henikoff et al., 2001). Moreover, the overall length of the various CENP-A orthologs from different species varies tremendously and ranges between 20 and 200 aa in length (Ahmad and Henikoff, 2002a).

1.4.4 *Histone H4 and H4 Variants*

Unlike histone H2A or H3, H4 is one of the most slowly evolving histones, with hardly any aa substitutions evident between fungi, plants and animals (Turner, 2002b; Wolffe, 1998). The lack of sequence divergence is not entirely unexpected as H4 makes critical protein-protein contacts with the other core histones. However, unlike histone H2A, the H4 NTD contains many residues that are capable of being posttranslationally modified (see below). Those residues capable of being modified are highly conserved between species. This suggests that the underlying evolution of H4 is tightly conserved amongst species. In mammals, two H4 variants have been identified and are the products of alternative processing of the same primary transcript (Marzluff et al., 2002). Collectively, these data underscore the functional conservation existing within H4.

1.5 HISTONE AMINO-TERMINAL DOMAINS – STRUCTURE AND FUNCTION

As detailed above the core histones are comprised of two major domains – a globular CTD and an 'unstructured' NTD. The NTDs constitute a major proportion of the total length of each core histone and represent as much as 28% of the total length (Figure 1.3). In humans the core histone NTDs range from 16 to 44 aa in length (H2A = 16, H2B = 32, H3 = 44, and H4 = 26). The NTDs are classically considered to be 'unstructured' or exhibit a 'random coil' structure, as they have not been fully detected by X-ray crystallography. This presumably results from the lack of a single fixed structure within nucleosome crystals (Arents et al., 1991; Luger et al., 1997). The lack of evidence for a single structure suggests that the NTDs may remain relatively mobile or, alternatively, they may adopt a variety of different structures with no single predominating structure. Examination of the primary sequences of all four core histones

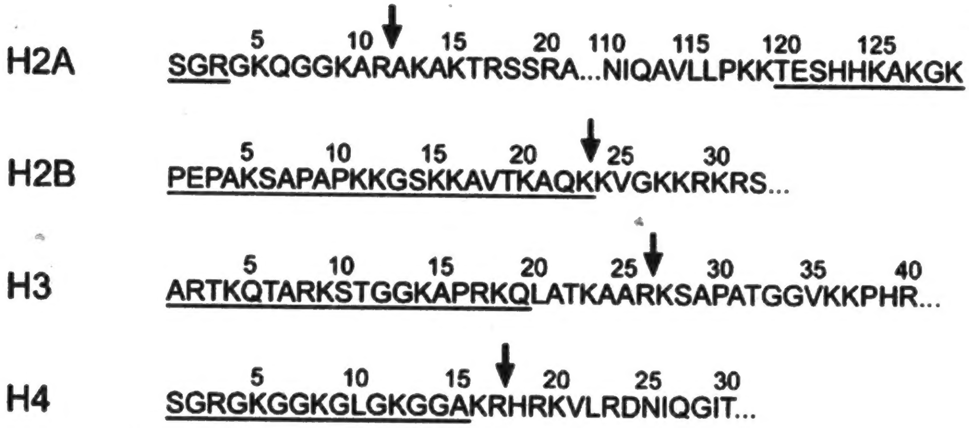
H2A
5 10 15 20 110 115 120 125
SGRGKQGGKARAKAKTRSSRA...NIQAVLLPKKTESHHKAKGK
H2B
5 10 15 20 25 30
PEPAKSAPAPKKGSKKAVTKAQKKVGKKRKRS...
H3
5 10 15 20 25 30 35 40
ARTKQTARKSTGGKAPRKQLATKAARKSAPATGGVKKPHR...
H4
5 10 15 20 25 30
SGRGKGGKGLGKGGAKRHRKVLRDNIQGIT...

Figure 1.3. Single amino acid sequences of the core histone NTDs.
Residue numbers are indicated above each sequence. The arrows indicates the locations nearest the HFDs at which the trypsin can cleave the tails in chromatin, while the underlined sequences are those that were not included in X-ray analyses of nucleosome core particles (Arents et al., 1991; Luger et al., 1997). A small portion of the CTD from H2A has also been included.

reveals a disproportionately high percentage of lysine and arginine residues resulting in an overall positive charge at near neutral pH (Table 1.1). Surprisingly, the aa composition does not favor any single extensive secondary sequence elements such as α-helices or β-sheets. However, based on more rigorous primary sequence analyses, short regions have been identified that appear capable of adopting an α-helical structure. Circular dichroism (CD) experiments performed on isolated nucleosomes demonstrated that the NTDs of H3 and H4, but not those of H2A and H2B, are highly organized as DNA-bound peptide segments with half of the residues adopting an α-helical structure (Baneres et al., 1997). Furthermore, the presence and amount of specific posttranslational modifications also appears to influence the α-helical nature of the NTDs. For example, Wang and colleagues (Wang et al., 2000) employed CD to demonstrate that increases in the α-helical content of the NTD from H4 accompanied and overall increase in the level of H4 acetylation. It is also conceivable that the secondary structure of the histone NTDs may be influenced by their close association with the DNA encompassing the core particle. This spatial proximity may impart certain structural restraints, even where the primary sequence is not favorable. High-resolution (2.8Å) images obtained from crystallographic data of nucleosome structures have revealed some structural details within the NTDs proximal to the globular HFDs. For instance, H2B and H3 NTDs extend from the nucleosome in the narrow channels between the two DNA strands (Luger et al., 1997), while H2A and H4 NTDs exit through minor grooves on the top or bottom of the nucleosome. In any case, it appears that although the core histone NTDs are often considered 'unstructured' they do exhibit short regions of secondary structure. These short regions however, appear to be dynamic rather than static and are likely influenced by the amount, levels (mono-, di-, tri-, etc.) and types of posttranslational modifications, which are in constant flux throughout the cell cycle.

Additional structural constraints may be placed on the histone NTDs through the myriad protein-histone interactions that have been identified. Many non-histone proteins have been shown to interact with the NTDs of histones H3 and H4 to generate transcriptionally active or repressed chromatin states. For example, binding of high mobility group (HMG) proteins, HMG-14 and -17, to nucleosomes results in the unfolding of higher-order chromatin structure, thereby facilitating transcription (Trieschmann et al., 1998). Alternatively, the *trans*-acting repressors from yeast, Sir3 and Sir4 (Grunstein, 1998), along with the global repressor Ssn6/Tup1 (Edmondson et al., 1996), bind H3 and/or H4 NTDs and render the chromatin transcriptionally silent.

In addition to the histone NTDs influencing gene transcription or silencing, they also appear to exhibit functional roles in establishing the hierarchy of higher-order chromatin structure. The apparent lack of structural roles assigned to the highly conserved NTDs suggests that the histone tails must be conserved for a different, perhaps functional role. Controlled enzymatic digestion of the core histones (e.g. trypsin cleavage of the NTDs) has demonstrated that the tails themselves are not essential for nucleosome assembly or maintenance of nucleosome integrity (Ausio et al., 1989; Hayes et al., 1991a; Hayes et al., 1991b). Perhaps the first insights into their function(s) come from the observations that the nucleosomes themselves, as 10 nm fibers, cannot achieve the 10,000-fold increase in DNA compaction that occurs in mammalian cells. Necessarily, much higher levels of chromatin compaction are required to efficiently compact the two meters of human DNA within each nucleus with a diameter of approximately 10 μm. EM investigations have revealed that the overall length of chromatin can be altered from the 'beads-on-a-string' conformation to higher levels of folding only if the tails remain intact (Allan et al., 1982). Consistent with this observation is the finding that one of the two H4 NTDs (residues 16-24) makes contact with a negatively charged patch formed by H2A and H2B residues in an adjacent nucleosome (Luger et al., 1997). This observation suggests that the histone NTDs may function to promote internucleosomal interactions that, in turn, facilitate higher-order chromatin compaction (Lenfant et al., 1996; Luger et al., 1997).

1.6 POSTTRANSLATIONAL MODIFICATIONS OF THE CORE HISTONES

Beyond the primary function of packaging DNA, nucleosomes have evolved much more dynamic functions in regulating chromatin structure through epigenetic or posttranslational modifications. Understanding how many of these modifications influence and regulate chromatin structure and gene silencing or activation has been of major interest since the mid 1960's. A recent resurgence in research interest surrounding posttranslational modifications has occurred that was, and is primarily stimulated by the development of immunoreagents (i.e. antibodies) that specifically recognize the various types of posttranslational histone modifications. Not only are these modification-specific antibodies capable of distinguishing different posttranslational modifications occurring at specific aa residues within each of the four core histones, but they also are capable discerning between various levels of particular modifications (e.g. mono-, di- and tri-methylation).

As mentioned above, posttranslational histone modifications lead to increased nucleosomal diversity or heterogeneity. Since the initial discovery that histone lysine residues could be acetylated (Phillips, 1963) many additional posttranslational histone modifications have been identified; phosphorylation (Gutierrez and Hnilica, 1967; Langan, 1968), methylation (Murray, 1964), adenosine diphosphate (ADP)-ribosylation (Nishizuka et al., 1968), ubiquitination (Goldknopf et al., 1975), sumoylation (Shiio and Eisenman, 2003) and biotinylation (Camporeale et al., 2004; Hymes et al., 1995). Based on the knowledge that cells expend a tremendous amount of energy modifying and regulating posttranslational modifications, it is reasonable to suggest that these modifications play critical roles in regulating chromatin structure and function. Not surprisingly, most posttranslational modifications occur outside the globular domains, within the NTDs (Figure 1.4). Intuitively, modifications within the globular regions could potentially destroy critical histone:histone or histone:DNA interactions, thereby disrupting nucleosome structure. A prevailing characteristic of most posttranslational histone modifications is that they are reversible – only methylation appears to be stable. As a result, the basal steady-state level of any of these modifications reflects the net balance between activities of enzymes catalyzing their addition or removal. Like the histones themselves, these modifications are highly conserved throughout evolution and have been implicated in regulating histone structure and/or function. However, the degree of variation, or nucleosome heterogeneity imparted by posttranslational modifications is orders of magnitude greater than those imparted by histone variants. Numerous studies have established that the presence or absence of particular modifications often correlates with specific types of chromatin or the transcriptional status of specific genes (see below and Table 1.2). These characteristics are perhaps the

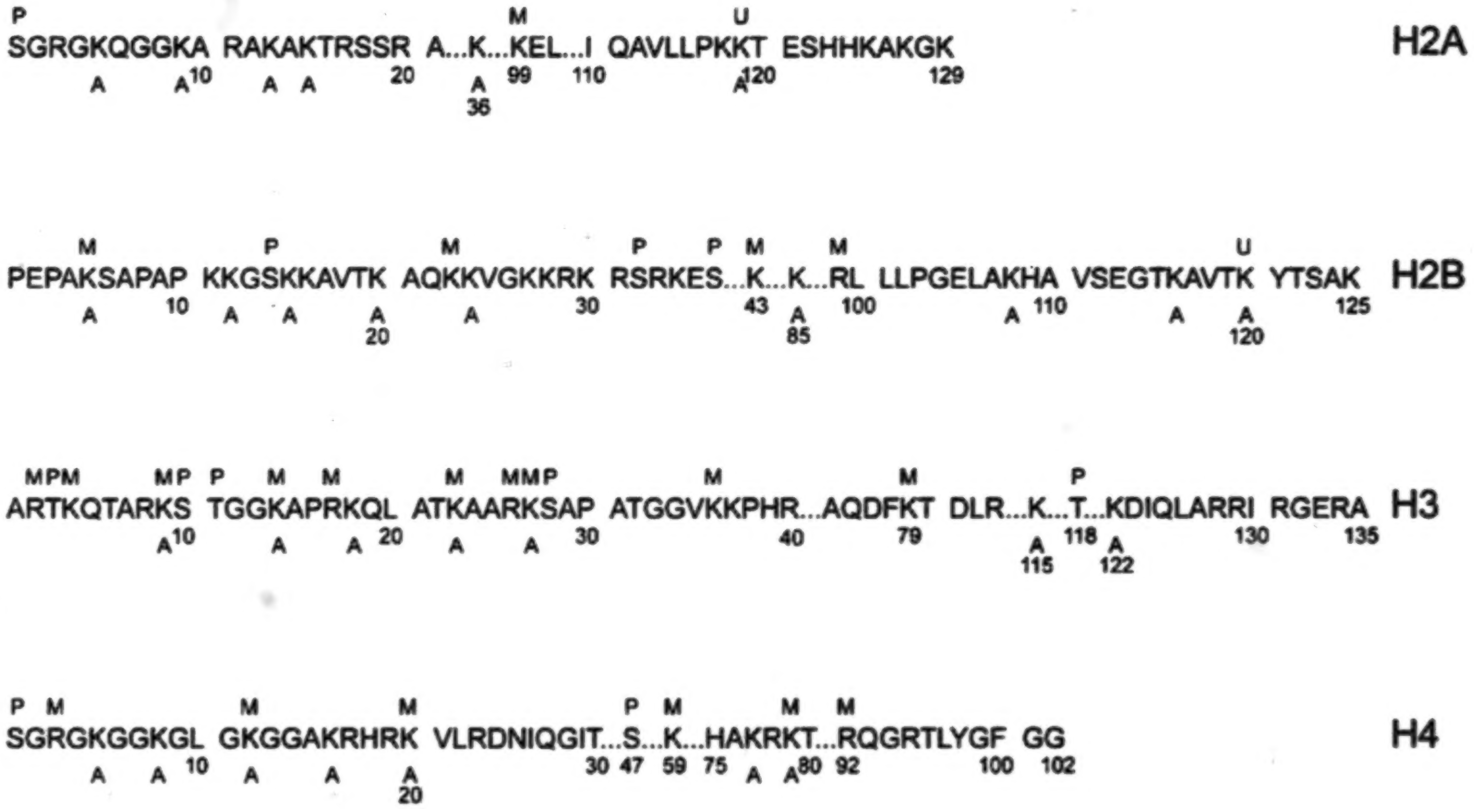
H2A
SGRGKQGGKA RAKAKTRSSR A...K...KEL...I QAVLLPKKT ESHHKAKGK
P M U
A A10 A A 20 A 36 99 110 A120 129
H2B
PEPAKSAPAP KKGSKKAVTK AQKKVGKKRK RSRKES...K...K...RL LLPGELAKHA VSEGTKAVTK YTSAK
M P M P P M M U
A 10 A A A 20 A 30 43 A 85 100 A 110 A A 120 125
H3
ARTKQTARKS TGGKAPRKQL ATKAARKSAP ATGGVKKPHR...AQDFKT DLR...K...T...KDIQLARRI RGERA
MPM MP P M M M MMP M M P
A10 A A 20 A A 30 40 79 A 115 118 A 122 130 135
H4
SGRGKGGKGL GKGGAKRHRK VLRDNIQGIT...S...K...HAKRKT...RQGRTLYGF GG
P M M M P M M M
A A 10 A A A 20 30 47 59 75 A A80 92 100 102

Figure 1.4. Location of various posttranslational histone modifications.
Single amino acid sequences of specific regions of the core histones with the residue number indicated below key residues. Residues capable of being posttranslationally modified by acetylation (A), phosphorylation (P), methylation (M) or ubiquitination (U) are identified by symbols above or below that specific residue.

Table 1.2: Histone modifications and their general effects on gene transcription.

Modification	Modifying Enzymes	Demodifying Enzymes	Primary Transcriptional Effect
Acetylation	HATs	HDACs	Activation
Phosphorylation	kinases	protein phosphatases	Activation[a]
	kinases	protein phosphatases	Silencing[b]
Methylation	HMTs	HDMs[c]	Repression
Ubiquitination	E3[d]	isopeptidases[e]	Activation
Sumoylation	E3[f]	ULP-related proteases[g]	Repression

[a] in response to mitogenic treatment

[b] mitosis-associated phosphorylation – silencing is due primarily to chromosome compaction

[c] the existence of HDMs is controversial as none have been purified to date and the modification is generally accepted to be static

[d] yeast Rad6 is the only ubiquitin E2 known to monoubiquitinate histones *in vivo*

[e] isopeptidases or ubiquitin proteases (UBPs) are known to remove ubiquitin

[f] UBC9 is the only known E2 SUMO-conjugating enzyme identified in species ranging from yeast through humans

[g] although histone desumoylation has yet to be identified, studies of other sumoylated proteins demonstrates that SUMO removal by ULP proteases is likely to occur with histones

principal reasons why initial X-ray crystallographic efforts employing a mixed population of nucleosomes could not accurately resolve its structure.

1.6.1 *Histone Acetylation*

Histone acetylation is arguably the best-studied posttranslational histone modification. It has been identified in all animal and plant species examined and occurs on all four core histones (Figure 1.4) (Csordas, 1990). At least 29 different histone lysine residues are targets for acetylation (Figure 1.4), most of which localize within the NTDs. Histone acetylation occurs when an acetyl group from acetyl-coenzyme-A (Acetyl-CoA) is covalently attached to the ε-amino group of a lysine side chain (Figure 1.5) by a group of acetyltransferases collectively referred to as histone acetyltransferases (HATs). The reverse reaction, or removal of the acetyl group, is performed by a group of enzymes collectively referred to as histone deacetylases (HDACs). The net result of the addition of a single acetyl group is that the positive charge associated with a lysine residue is neutralized, effectively decreasing the overall charge by one (Figure 1.5). Steady state levels of acetylation depend on the equilibrium between HATs and HDACs. However, consistent amongst many of these studies is that two dynamic populations exist – one that turns over rapidly on the order of minutes (3 to 7 min) and one that is much more stable with a half-life ($t_{\frac{1}{2}}$) of approximately 2 hrs (Covault and Chalkley, 1980). The dynamic nature of histone acetylation turnover is further emphasized by the ability of HDAC inhibitors (e.g. sodium butyrate, trichostain A [TSA], suberolylanilide hydroxamic acid [SAHA], etc.) to rapidly induce hyperacetylation of the core histones.

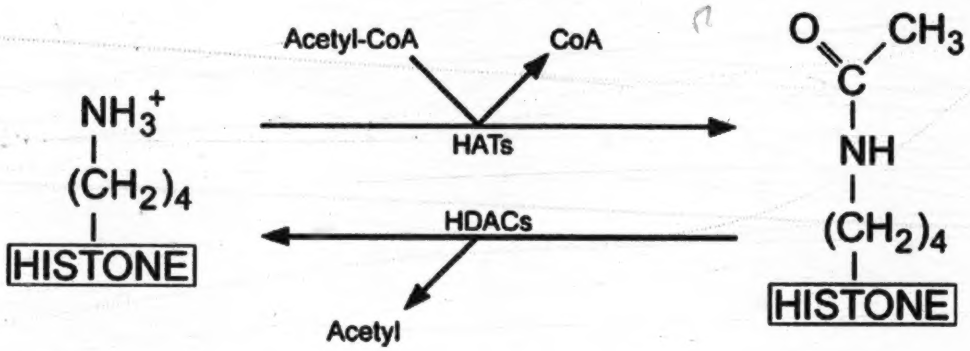
Acetyl-CoA
CoA
HATs
HDACs
Acetyl
NH_3^+
$(CH_2)_4$
HISTONE
O
CH_3
C
NH
$(CH_2)_4$
HISTONE

Figure 1.5. The histone acetylation and deacetylation reactions.
Shown here is the chemical reaction for the addition and removal of an acetate group from a lysine residue contained within a core histone. The acetyl group is covalently transferred from acetyl-CoA through HAT activity to the ε-amino group of an acceptor lysine residue contained within a core histone, while HDAC activity removes the acetyl group. Note that the addition of an acetyl group decreases the overall charge of the lysine residue.

Acetylation, like most posttranslational modifications, is tightly regulated. Not every lysine residue within all four core histones serves as a suitable *in vivo* substrate. In fact, several lysine residues within the NTDs of histones H2B and H3 do not appear to be utilized, strongly suggesting that lysine acetylation is not purely a random event. In addition, the site utilization also appears to be non-random as specific modifications are associated with distinct cell cycle stages (McManus-KJ Submitted). For example, newly synthesized histones are acetylated prior to replication-dependent nucleosome assembly (RDNA) at K9 (H3), K5 (H4) and K12 (H4) (Chang et al., 1997; Ruiz-Carrillo et al., 1975; Sobel et al., 1994) and are rapidly erased by various HDACs following deposition (Jackson et al., 1976a; Jackson et al., 1976b). The acetylation site utilization patterns outside of RDNA also appear to be non-random and exhibit strict orders of site occupancies that can differ significantly between organisms. For example, in cuttlefish, the mono-acetylated histone H4 subtype is acetylated exclusively at K12 (Couppez et al., 1987). As levels of acetylation are artificially increased through treatment with HDAC inhibitors (e.g. sodium butyrate), the order in which the subsequent sites are utilized also appears to be regulated and invariant. Acetylation of K5 precedes that of K16 and K8. In humans and pigs however, H4 is almost exclusively mono-acetylated at K16 (Thorne et al., 1990). The di-acetylated form includes either K8 or K12 while the most highly acetylated form includes K5. Additional site utilization preferences for histone H4 have also been documented for Tetrahymena and differ slightly to those of cuttlefish and humans (Chicoine et al., 1986). Similar observations have been made for histone H3 – human and pig H3 exhibit a strict order of site occupancy where K14 acetylation is followed by K23 which is followed by K18 (Thorne et al., 1990). Because the sequence of the nucleosomes is nearly identical between cuttlefish, humans and *Tetrahymena*, the distinctive order of site utilization appears to reflect the properties of the HATs and HDACs involved rather than gross differences in nucleosome structure.

Over 40 years ago, Vincent Allfrey proposed that histone acetylation in eukaryotes was associated with transcriptional activity (Allfrey et al., 1964). Since then, numerous research groups have demonstrated that active or transcribing chromatin is associated with acetylated core histones (see (Hebbes et al., 1988; Sealy and Chalkley, 1978a; Sealy and Chalkley, 1978b; Vidali et al., 1978)). Currently, most studies emphasize the role of histone acetylation in activating and repressing gene structure locally and typically at the level of the promoter. Although histone acetylation can alter nucleosome structure, the results published to date can be considered to reflect subtle structural changes (Ausio, 1992; Libertini et al., 1988). These observations are in stark contrast with the effects of histone acetylation on higher-order chromatin folding, where the documented effects are often more dramatic (Garcia-Ramirez et al., 1995; Schwarz and Hansen, 1994; Tse et al., 1998). Histone acetylation clearly reduces nucleosome-nucleosome interactions which appears to be an underlying mechanism regulating folding to and beyond the 30 nm fiber. Changes in higher-order chromatin structure, however, require acetylation modifications to extend beyond single nucleosomes. Indeed, chromatin is often highly acetylated over vast expanses of DNA *in vivo*, both within and flanking gene loci (Hebbes and Allen, 2000; Madisen et al., 1998; Turner et al., 1990; van Holde and Zlatanova, 1996). Disruption of the higher-order chromatin folding by histone acetylation is sufficient to promote and maintain the unfolded structure required for gene transcription to occur (Tse et al., 1998) and is reviewed elsewhere (Davie and

Spencer, 1999). Furthermore, histone lysine acetylation neutralizes the lysine-imparted positive charge of the NTDs and has been shown to directly affect its affinity for DNA (Hong et al., 1993). In 1998, Tse et al (1998) demonstrated that acetylation of 46% of maximal site occupancy is sufficient to prevent higher-order folding. This seminal paper established that histone acetylation functions quantitatively and as a sensitive mechanism for modulating higher-order folding and transcriptional initiation and elongation *in vitro*.

As described above, the balance of HAT and HDAC activities regulate the dynamics of histone acetylation. Currently, two major HAT families exist – one whose members localize to the cytoplasm (Type B), and one whose members localize to the nucleoplasm (Type A). Cytoplasmic type-B HATs acetylate newly synthesized histones prior to RDNA (Allis et al., 1985; Ruiz-Carrillo et al., 1975), while nucleoplasmic type-A HATs generally catalyze transcription-related acetylation events (Brownell and Allis, 1996). HAT members from both types have been investigated extensively and are reviewed in detail elsewhere (Roth et al., 2001). However, at least five different HAT sub-groups exist within the two HAT families and are based primarily on sequence similarities, rather than substrate specificities. These sub-types include; 1) GNAT (Gcn5-related *N*-acetyltransferase) (e.g. Gcn5, PCAF, Hat1, etc.), 2) MYST (MOZ, YBF2/Sas3, Sas2 and TIP60) (e.g. Esa1, MOF, MORF, etc.), 3) p300/CBP (cAMP response element binding protein [CREB] binding protein [CBP]), 4) basal transcription factors (e.g. TAFII250 and TFIIC) and, 5) nuclear receptor cofactors (e.g. activator of retinoic acid receptor [ACTR] and steroid receptor coactivator 1 [SRC1]). Surprisingly members of different sub-types often exhibit overlapping substrate specificities (Roth et al., 2001). More recently, HATs have been shown to acetylate non-histone proteins and are more generally referred to as factor acetyltransferases (FATs). For example, *in vitro* biochemical studies have shown that CBP and/or P300 can acetylate numerous non-histone proteins (Table 1.3). In either context, histone or non-histone acetylation appears to function in an analogous fashion to that of phosphorylation involving signal-transduction molecules containing src homology domains (e.g. SH2 or SH3) – it either promotes or reduces intermolecular interactions allowing for signal propagation and transduction ultimately leading to transcriptional activation of specific genes.

To date, more than 45 HDACs have been identified in organisms ranging from *S. cerevisiae* to *H. sapiens* (reviewed in (Marmorstein, 2004)). Based on primary sequence similarities individual HDACs can be placed in one of three families; class I, class II or class III (Marmorstein and Roth, 2001). Interestingly, class III HDACs are distinct from class I and II HDACs in that they require nicotinamide adenine dinucleotide (NAD^+) as a cofactor and are resistant to inhibition by HDAC inhibitors such as TSA or sodium butyrate (Imai et al., 2000; Smith et al., 2000). Class I HDACs (HDAC-1, -2, -3 and -8) are predominantly nuclear and are most closely related to the *S. cerevisiae* transcriptional regulator, RPD3, while class II HDACs (HDAC-4, -5, -6, -7, -9, and -10) can shuttle in and out of nuclei and share similar domains/motifs to that of HDA1 from yeast (Bjerling et al., 2002). As with HATs, HDACs also exhibit activities towards non-histone proteins including p53, E2F, α-tubulin and MyoD (Hubbert et al., 2002; Juan et al., 2000). Furthermore, the observation that HDACs are frequently observed in the cytoplasm and in bacteria, which do not contain histones, strongly suggests that histones may not be their predominant targets.

Table 1.3. Targets of CBP and P300 acetylation activities

Acetyltransferase	Target Protein	Reference
CBP	HMG[a] I(Y) and HMG IC	(Munshi et al., 1998)
CBP	E2F1	(Martinez-Balbas et al., 2000)
CBP	TCF[b]	(Waltzer and Bienz, 1998)
CBP	Human importin-alpha (Rch1)	(Bannister et al., 2000)
CBP	Importin-alpha 7	(Bannister et al., 2000)
CBP	MafG	(Hung et al., 2001)
CBP	Ku70	(Cohen et al., 2004)
p300	p53	(Gu et al., 1997)
p300	Tat	(Kiernan et al., 1999)
p300	TFIIeβ[c] or TFIIF	(Ott et al., 1999)
p300	ACTR[d]	(Chen et al., 1997)
p300	NF-Y[e]	(Li et al., 1998)
p300	MyoD	(Polesskaya et al., 2000)
p300	E1A	(Zhang et al., 2000)
p300/CBP	H2A, H2B, H3 and H4	(Bannister and Kouzarides, 1996; Ogryzko et al., 1996; Schiltz et al., 1999)
p300/CBP	GATA-1	(Boyes et al., 1998; Hung et al., 1999)
p300/CBP	EKLF[f]	(Zhang and Bieker, 1998)

[a] high mobility group (HMG)
[b] T-cell factor (TCF)
[c] transcription factor (TF)
[d] activator of retinoic acid receptor (ACTR)
[e] nuclear factor (NF)
[f] erythroid Krüppel-like factor (EKLF)

1.6.2 *Histone Phosphorylation*

Histone phosphorylation occurs on at least eight different S residues (Figure 1.4) and was recently detected on two threonine (T) residues contained within the histone H3 NTD (Polioudaki et al., 2004; Preuss et al., 2003). Phosphorylation of S and T residues is mediated through the activities of histone kinases. These kinases covalently attach a phosphate moiety from a nucleotide triphosphate (TP), such as adenosine TP (ATP), guanosine TP (GTP) or cyclic adenosine monophosphate (cAMP) (Figure 1.6). The loss of phosphorylation is regulated by histone phosphatases and results in the removal of inorganic phosphate.

Histone phosphorylation occurring at S10 (H3) is perhaps the best-studied core histone phosphorylation event. Many studies examining phosphorylated S10 (PhosS10) have been conducted and established that it is essential for two very different functions, mitosis and transcription. In mammalian cells (e.g. Chinese hamster ovary [CHO] and HeLa cells), the correlation between PhosS10 dynamics and the cell cycle have been known for decades (Gurley et al., 1973; Gurley et al., 1974; Paulson and Taylor, 1982) and its temporal progression pattern has been well documented (Gurley et al., 1974; Hendzel et al., 1997). Briefly, PhosS10 initiates within pericentromeric heterochromatin presumably following DNA replication. It is rapidly induced during the later stages of G_2, peaks at metaphase and is rapidly dephosphorylated until it is nearly absent in early G_1 (Hendzel et al., 1997). Since these original studies, it is now well established that mitosis-specific phosphorylation of S10 is essential for proper chromosome condensation and segregation during mitosis and meiosis in a variety of organisms including *Schizosaccharomyces pombe*, *T. thermophila* and mammals (Bui et al., 2004;

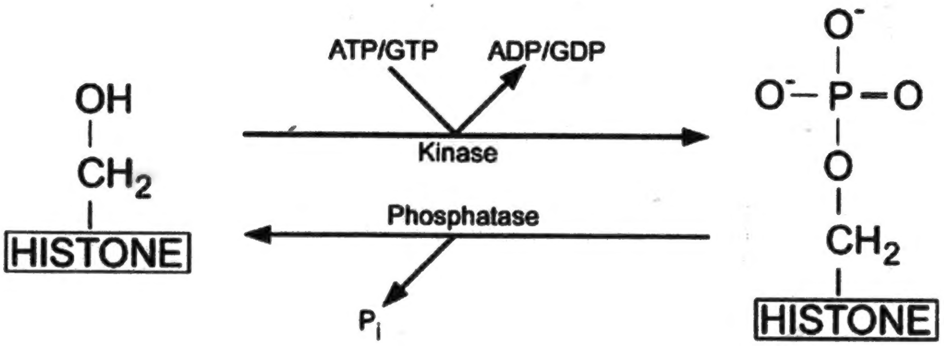
ATP/GTP
ADP/GDP
Kinase
Phosphatase
P_i
OH
CH_2
HISTONE
O^-
O^-
P
O
O
CH_2
HISTONE

Figure 1.6. The histone phosphorylation and dephosphorylation reactions.
Depicted here is the chemical reaction for the addition and removal of a phosphate group to the β-hydroxyl group of serine by a histone kinase and phosphatase respectively. A nucleotide triphosphate (e.g. ATP or GTP) serves as the donor, while inorganic phosphate (Pi) is released. Note that the addition of a phosphate groups results in a negative charge associated with the serine residue.

Petersen et al., 2001; Wei et al., 1999). Evidence strongly implicates Aurora B kinase in humans, and its orthologs in other organisms, in the mitosis-associated phosphorylation of S10 (de la Barre et al., 2000; De Souza et al., 2000; Giet and Glover, 2001). Removal of PhosS10 during the later stages of mitosis appears to be regulated by type 1 phosphatases, such as Glc7 in yeast (Hsu et al., 2000; Murnion et al., 2001). In mammals however, the true identity of the *in vivo* phosphatase still remains unresolved. Similar investigations conducted in various organisms clearly demonstrate that identical modifications (i.e. PhosS10) do not exhibit identical temporal progression patterns. In maize for example, the onset of PhosS10 in mitosis and meiosis begins in late prophase, after chromosome condensation has already initiated (Kaszas and Cande, 2000). Furthermore, PhosS10 in maize appears to be associated with chromosome cohesion (Kaszas and Cande, 2000) rather than with chromosome condensation. Surprisingly however, PhosS10 is not required for cell cycle progression in *S. cerevisiae* (Hsu et al., 2000). Rather, evidence suggests that phosphorylation of H2B may perform a redundant role, as its temporal progression pattern mimics that of PhosS10 from other organisms (Hsu et al., 2000).

Subsequent immunofluorescent, immunoblotting and radiolabeling studies have identified additional histone phosphorylation events that also exhibit mitosis-associated dynamics such as T11 (H3) (Preuss et al., 2003) and S28 (H3) (Goto et al., 1999). The temporal progression for PhosS28 has recently been detailed in plants where it was reported to exhibit the identical temporal progression pattern as PhosS10 (Gernand et al., 2003). However, it still remains to be determined whether these phosphorylation events are causally linked with mitosis. These observations firmly establish that distinct temporal progression patterns have emerged separately throughout evolution and that the function(s) of identical posttranslational modifications occurring in different organisms are not universally conserved.

PhosS10 levels also increase dramatically in response to stimulation by growth factors, phorbol esters, protein synthesis inhibitors (e.g. anisomycin and cycloheximide) or protein phosphatase inhibitors (e.g. okadaic acid). This increase is particularly pronounced for nucleosomes contained within immediate-early gene loci, such as c-jun, c-fos and c-myc, where it is associated with transcriptional activation (Barratt et al., 1994; Chadee et al., 1999; Clayton et al., 2000; Mahadevan et al., 1991; Thomson et al., 1999). Interestingly, under such conditions the small H3 fraction subjected to phosphorylation is also extremely sensitive to hyperacetylation induced by sodium butyrate treatment, whereas the bulk H3 fraction is not (Barratt et al., 1994). Barratt and colleagues (Barratt et al., 1994) also established that S10 phosphorylation is not based on preferential modification of a specific H3 variant localizing within the immediate-early gene loci nor does phosphorylation predispose nucleosomes to hyperacetylation. Thus they conclude that the mitogen-regulated kinase that phosphorylates S10 is restricted to a small subset of nucleosomes that is particularly susceptible to hyperacetylation. Although the identity of the ultimate kinase regulating S10 phosphorylation has been controversial (see (Davie, 2003)), it is now apparent that the mitogen- and stress-response kinases 1 and 2 (MSK1 and MSK2) are the *bone fide* kinases (Soloaga et al., 2003).

The observations detailed above present a paradox – PhosS10 is associated with regulating chromatin compaction and presumably transcriptional silencing during mitosis, and with transcriptionally active chromatin presumably residing within remodeled chromatin during interphase. One possible explanation for the paradoxical functional dichotomy is the presence or absence of additional posttranslational modifications such as acetylation. The mitosis-associated increase in PhosS10 correlates with an overall decrease in histone acetylation, specifically at K9 (H3) (Kruhlak et al., 2001) (McManus and Hendzel, Submitted), while the growth factor-stimulated increase occurs in a small H3 fraction that is particularly sensitive to hyperacetylation (Barratt et al., 1994). Until recently however, it was unclear whether the association of hyperacetylation within the small phosphorylated H3 fraction observed by Barratt and colleagues (Barratt et al., 1994) occurred within the same or adjacent H3 NTDs. Only through the generation of antibodies that specifically recognize di-modified H3 species (i.e. acetylated K9 with PhosS10 [AcK9/PhosS10]) was the first direct *in situ* proof provided that these modifications do exist on the same NTD (Cheung et al., 2000; Clayton et al., 2000). These observations, coupled with the knowledge that certain HATs (e.g. GCN5) exhibit a preference for binding to H3 when it is phosphorylated at S10 (Cheung et al., 2000; Clayton et al., 2000; Lo et al., 2000), provide a mechanism for the functional difference observed between the mitosis-associated and the mitogen-stimulated S10 phosphorylation events.

1.6.3 *Histone Methylation*

Histone methylation occurs on all four core histones and on both arginine and lysine residues (Figure 1.4). The catalytic addition of methyl moieties to R or K residues is regulated by histone methyltransferases (HMTs). Unlike K acetylation, K methylation leaves the positive charge associated with the K residue intact (Figure 1.7). Histone methylation represents a unique posttranslational modification in two regards.

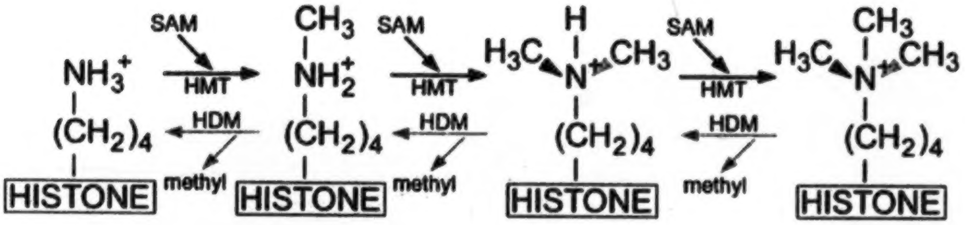

Figure 1.7. The histone lysine methylation reactions.
Shown here is a sequential series of reaction steps that generates, mono-, di- and tri-methylated lysines. HDMs catalyze the covalent addition of a methyl group from the S-adenosyl methionine (SAM) donor to the ε-amino group of the recipient lysine residue. Methylation is generally considered to be a stable epigenetic imprint, however, evidence suggests that histone demethylases (HDMs) may exist and that the reverse reaction may occur. Because HDMs have not been identified to date, the reverse reaction is only hypothetical and is indicated by gray arrows. Note that the positive charge associated with a lysine residue remains intact following the addition of a methyl group.

First, multiple methylations can occur at the same site. For example, R residues can be mono- or di-methylated while K residues can be mono-, di- or tri-methylated. Furthermore, depending on how the methyl moieties are attached, the di-methylated arginine residues can exist in either a symmetrical or asymmetric form. The fact that different levels of methylation can exist at a single site adds an additional layer of complexity that is unrivaled by other posttranslational modifications. Second, in contrast to all other posttranslational modifications, methylation appears to be much more stable. Because no histone demethylases (HDMs) have been identified to date, methylation is considered irreversible. A corollary of this stability is that histone methylation is believed to impart a heritable genetic imprint that can be passed on to successive generations. However, evidence from the 1970's and 1990's suggests that histone demethylation may indeed occur (detailed in Chapter 3). More recently, Wang and colleagues (Wang et al., 2004b) demonstrated that arginine methylation could be altered through demethylimination by human peptidylarginine deiminase 4 (PAD4). In human HL-60 granulocytes and MCF-7 cells, PAD4 converts methylarginine to citrulline by releasing methylamine (Wang et al., 2004b). Moreover, PAD4 activity in MCF-7 cells is linked with transcriptional regulation of estrogen responsive genes.

Like acetylation, methylation also exhibits preferred site utilizations. The primary sites of lysine methylation in vertebrates are K9 and K27 of H3, and K20 of histone H4. Although many additional sites exist (see Figure 1.4) their preferred order of addition remains to be characterized and is likely to be complicated by the existence of multiple levels of methylation (e.g. mono-, di- and tri-). Radiolabeling studies involving isotopically labeled S-adenosyl methionine (SAM) have shown that methylation begins shortly after RDNA (Borun et al., 1972). However, it should be noted that not all organisms exhibit identical methylation patterns. In yeast for example, a dichotomy exists whereby K9 (H3) in *S. cerevisiae* is never methylated while in *S. pombe* it is.

HMTs regulate the covalent addition of one, two, or three methyl moieties onto the ε-amino group of lysine. It is not a requirement that the addition of methyl moieties be a sequential series of reactions regulated by different HMTs. Individual HMTs exist that can di- or tri-methylate previously unmodified lysine residues. The first HMT to be identified was Suppressor of Variegation 3-9 [Su(var)3-9] from *D. melanogaster* (Reuter and Spierer, 1992; Schotta et al., 2002; Tschiersch et al., 1994). It is a ubiquitously expressed protein that has orthologs in organisms ranging from *S. pombe* (Cryptic loci regulator 4 [Clr4]) (Ekwall and Ruusala, 1994; Ivanova et al., 1998) to mice (Suv39h1) (Aagaard et al., 1999) to humans (SUV39H1) (Rea et al., 2000). Su(var)3-9 and almost all other HMTs contain a prototypic SET (Su(var)3-9, Enhancer of zeste and Trithorax) domain that was identified through sequence comparisons. To date, the disruptor of telomere silencing 1 (Dot1) is the only HMT that does not contain the canonical SET domain (Feng et al., 2002). Rather, Dot1 contains a methylase fold that is more frequently observed in other non-histone methyltransferases (Dlakic, 2001; Ng et al., 2002a; van Leeuwen et al., 2002). To date, more that 60 human sequences have been identified that contain a SET domain (http://www.sanger.ac.uk/cgi-bin/Pfam/getacc?PF00856). In general terms, the SET domain is comprised of three distinct regions, N-SET (amino), I-SET (intervening) and C-SET (carboxy). The N- and C-SET regions are typically of fixed lengths with the C-SET region harboring critical aa residues that define the active site. The size of the I-SET region varies and its size is proposed to limit the level of methylation (i.e. mono, di or tri) each specific HMT can catalyze (reviewed in (Marmorstein, 2003)). Furthermore, the abilities of specific HMTs to mono-, di- or trimethylate histones appear to be directly related to the structure and/or size of their catalytic sites. In mono-methylating HMTs such as Set7/9, the ε-amino group is bound so tightly within the active site that it is sterically impossible for an additional bulky methyl group to be incorporated. Moreover, the compact nature of the active site prohibits rotation about the C-N bond that is essential for subsequent additions (Kwon et al., 2003; Xiao et al., 2003). On the other hand, di- and tri-HMTs (e.g. defective in methylation-5 [DIM-5]) (Tamaru et al., 2003) exhibit far more flexibility in their active sites, presumably due to the extended I-SET region and can easily accommodate one or two additional methyl groups (Zhang et al., 2002; Zhang et al., 2003).

Functionally speaking, histone methylation is frequently considered the antithesis of acetylation. It is most often associated with silenced or heterochromatin, although this is a gross oversimplification – methylation, specifically trimethylated K4 (tMeK4 [H4]) localizes predominantly within euchromatin or actively transcribing genes. Although chromatin immunoprecipitation (ChIP) assays have demonstrated that methylated K9 of H3 and K20 of H4 are associated with transcriptional silencing (Hall et al., 2002; Nishioka et al., 2002; Noma et al., 2001; Schotta et al., 2004b), they have also demonstrated that K4, K36 and K79 of H3 are generally associated with transcriptional activity (Im et al., 2003; Ng et al., 2003; Noma et al., 2001; Schaft et al., 2003). Correspondingly within mammalian cells, many of these modifications partition within either heterochromatic (e.g. trimethylated K9 of H3 [tMeK9]) or euchromatic (e.g.

tMeK4) regions as identified by immunofluorescent staining (reviewed in (Lachner et al., 2003; Schotta et al., 2004a; Vaquero et al., 2003)). Unfortunately, many of the cytological and ChIP studies performed in the past failed to distinguish between the different levels (i.e. mono, di or tri) of methylation that can occur thereby complicating the direct interpretation of results. It is now known that distinct variations in localization and/or association within active or inactive chromatin can occur with various levels of modifications occurring at the identical residue. In 2002, Santos-Rosa and colleagues (Santos-Rosa et al., 2002) employed ChIP assays to demonstrate that dimethylated K4 (H3) localized within both active and inactive genes, while tri-methylated K4 (H3) only localizes within active genes in *S. cerevisiae*. Therefore, based on this work it is apparent that histone K methylation can partition within both heterochromatin and euchromatin and may be functionally involved in both gene silencing and activation.

1.6.4 *Histone Ubiquitination*

Histone ubiquitination is a reversible modification whose steady-state levels are dependent upon the availability of free ubiquitin and the enzymes catalyzing its addition or removal. Ubiquitin is a 76 aa protein that is covalently attached to lysine residues through an isopeptide bond between the C-terminal glycine of ubiquitin and the ε-amino group of a lysine residue on the acceptor molecule (e.g. core histone). Ubiquitin attachment is mediated through a cascade of three successive reactions involving E1 activating, E2 conjugating and E3 ligating enzymes. The E3 ligase both recognizes and ligates ubiquitin to the target molecule (reviewed in (Pickart, 2001)), while its removal is regulated by isopeptidases (Wilkinson, 2000). Interestingly, protein ubiquitination was first identified through studies involving histones (Goldknopf et al., 1975) and differs from non-histone protein ubiquitination in two significant ways; 1) histones are predominantly mono-ubiquitinated, rather than poly-ubiquitinated, and 2) ubiquitination does not target histones for proteolytic degradation by the 26S proteasome (see (Hochstrasser, 1996; Pickart, 2001)). Currently, H2A (Goldknopf et al., 1975), H2B (West and Bonner, 1980), H3 (West and Bonner, 1980) and H1 (Pham and Sauer, 2000) have been identified as *in vivo* ubiquitination targets.

The exact function of histone ubiquitination remains controversial although many studies suggest that ubiquitination of histones H2A and H2B may be functionally involved in transcription (reviewed in (Zhang, 2003)). For example, Varshavsky and colleagues (Levinger and Varshavsky, 1982) demonstrated that approximately 50% of H2A is ubiquitinated in nucleosomes localizing to transcriptionally poised heat shock protein 70 (Hsp70) genes compared to an average of one ubiquitinated H2A molecule per 25 nucleosomes in untranscribed satellite DNA. They subsequently showed that di-ubiquitinated H2A was preferentially enriched around the first exon of an actively transcribing mouse dihydrofolate reductase (*DHFR*) gene (Barsoum and Varshavsky, 1985). Although most studies suggest a strong positive correlation between histone ubiquitination and transcription, an inverse relationship has also been reported. For example, ubiquitinated histones have been identified in transcriptionally silent or repressed domains such as the transcriptionally silent macronuclei of *Tetrahymena* (Nickel et al., 1989) or the sex body of mouse spermatids (Baarends et al., 1999). Therefore, the exact influence histone ubiquitination has on transcription remains to be established.

Currently there are three putative mechanisms describing how histone ubiquitination affects transcription. First, histone ubiquitination may alter higher order chromatin structure, thereby rendering the genome more accessible to regulatory and transcription factors. This hypothesis is consistent with the observation that levels of ubiquitinated histones vary throughout the cell cycle. For example, ubiquitinated H2A and H2B have been shown to decrease dramatically in G_2 and mitosis, when the chromatin is most condensed and reappears as chromatin begins to decondense in G_1 (Wu et al., 1981). Second, ubiquitination may signal regulatory factors that affect transcription in much the same manner that tMeK9 (H3) recruits HP1 (Bannister et al., 2001; Lachner et al., 2001). For example, Seigneurin-Berny *et al* (2001) demonstrated that murine HDAC6 associates with two proteins implicated in ubiquitination, and that a zinc-finger domain located in the CTD can bind directly to ubiquitin. This observation implies the existence of a mechanism to selectively target HDAC6 to ubiquitinated chromatin. Third, histone ubiquitination may affect transcription through its influence on other subsequent post-translational histone modifications. Recently, two research groups discovered that Set1/COMPASS-mediated methylation of K4 (H3) leading to telomeric gene silencing in *S. cerevisiae* requires functional Rad6 (a ubiquitin-conjugating enzyme) and intact ubiquitinated K123 (H2B) (Dover et al., 2002; Sun and Allis, 2002). Moreover, the fact that deletion of *SET1* or substitution of K4 (H3) with arginine did not affect K123 ubiquitination, suggests a unidirectional regulatory pathway in which H2B ubiquitination is upstream of K4 methylation (Sun and Allis, 2002). Subsequent studies have also found that K79 (H3) methylation is dependent on Rad6-mediated ubiquitination of H2B (Briggs et al., 2002; Ng et al., 2002b).

1.6.5 *Histone Biotinylation*

Like other post-translational modifications, histone biotinylation is a reversible reaction whose levels are regulated by the availability of a biotinyl moiety, and the enzymes catalyzing its addition (e.g. biotinidase (Hymes et al., 1995) or holocarboxylase synthetase (Narang et al., 2004)) or removal (e.g. biotinidase (Ballard et al., 2002)). Although only K8 and K12 of H4 have been identified as *in vivo* target substrates to date (Camporeale et al., 2004), all four core histones can be biotinylated *in vitro* and therefore may serve as biotinylation substrates *in vivo* (Stanley et al., 2001). Histone biotinylation appears to be physiologically important where it may function in cellular proliferation, DNA damage responses, and in gene silencing. In human cells, histone biotinylation levels are dynamic and begin to increase in early G_1 and remain at relatively high levels throughout G_2 and M-phase. High levels of histone biotinylation are observed in proliferating cell such as peripheral blood mononuclear cells, but are absent or extremely low in quiescent cells (Stanley et al., 2001). Elevated biotinylation levels are also observed following ultra violet (UV) induced DNA damage in human lymphoid cells (Peters et al., 2002). Interestingly, in these UV-damaged cells, biotinylation localizes to both damaged, yet unrepaired loci and transcriptionally silent regions. Although these observations suggest that biotinylation may participate in DNA damage recognition/repair and/or transcriptional silencing, it was observed that these cells underwent apoptosis and histone biotinylation may be involved in something other than DNA repair. In addition, the association of biotinylation with transcriptionally silent loci in these dying cells is correlative at best, and may only reflect the increased availability of substrates resulting from decreased mitochondrial integrity and the subsequent diffusion of biotinyl moieties into the nucleus.

1.6.6 *Histone Sumoylation*

One of the most recently identified posttranslational histone modifications is the small ubiquitin-related modifier (SUMO). SUMO is a 9 kDa protein that is a well-characterized member of a growing family of ubiquitin-like proteins involved in posttranslational modifications (reviewed in (Melchior, 2000; Muller et al., 2001; Seeler and Dejean, 2003)). Recently, Siino and Eisenmann (2003) demonstrated that histone H4 can be sumoylated both *in vitro* and *in vivo*, however the targeted K residue(s) remains to be identified. It also remains to be determined whether other core histones can be sumoylated *in vivo*.

Sumoylation has been identified in organisms ranging from yeast to humans and on dozens of different proteins such as the Ran-GTPase-activating protein 1 (RanGAP1) (Mahajan et al., 1997), promyelocytic leukemia (PML) bodies (Muller et al., 1998), IκBα (Desterro et al., 1998), p53 (Gostissa et al., 1999; Rodriguez et al., 1999) and mouse double minute 2 (MDM2) (Buschmann et al., 2000). Like ubiquitination, SUMO moieties are covalently attached to proteins through a cascade of enzyme (e.g. E1, E2 and E3) activities. Unlike ubiquitination however, sumoylation appears to have four known functions, none of which target SUMO-modified proteins for degradation. First, sumoylation is proposed to regulate protein targeting. For example, sumoylation of RanGAP1 results in its relocalization from the cytoplasm to the nuclear pore complex (Mahajan et al., 1997; Mahajan et al., 1998; Matunis et al., 1996; Matunis et al., 1998). To date, SUMO-mediated regulation of histone targeting has not been identified, particularly during nucleosome deposition during S-phase. Second, sumoylation appears to prolong the lifespan of a protein by effectively functioning as a ubiquitination antagonist. For instance, sumoylation of IκBα stabilizes this NF-κB inhibitor by blocking ubiquitination at the same acceptor site (Desterro et al., 1998). In the context of histones however, this function does not appear to be relevant because ubiquitination does not target histones for proteolysis. Third, sumoylation has been proposed to regulate protein interactions by virtue of an unstructured 22 aa NTD (Seeler and Dejean, 2003). This additional domain could theoretically serve as a molecular beacon thereby recruiting factors to chromatin that could affect transcription. Finally, sumoylation has been shown to both positively and negatively regulate transcriptional activity. For example, heat shock factor HSF1 and p53 (Gostissa et al., 1999; Rodriguez et al., 1999; Verger et al., 2003) become stimulated upon sumoylation, while sumoylation of Elk1, Sp3, c-Myb and c-Jun correlates with transcriptional repression (Verger et al., 2003). In 2003, Shiio and Eisenman (Shiio and Eisenman, 2003) demonstrated that sumoylated H4 associates with chromatin and known transcriptional silencers, namely HDAC1 and HP1, which suggests that H4 sumoylation could mediate transcriptional repression. As with many posttranslational modifications H4 sumoylation also exhibit interrelationship with other types of posttranslational modifications. For instance, H4 sumoylation has been observed to increase following acetylation (Shiio and Eisenman, 2003) and suggests that acetylation may serve as the targeting mechanisms of the sumoylating enzyme itself, which in turn, may downregulate transcription of that specific gene. If this proves true, this could provide an additional mechanism for silencing actively transcribing genes or a way to regulate the epigenetic silencing of specific genetic loci.

1.6.7 *Histone ADP-Ribosylation*

Poly-ADP-ribosylation is a reversible reaction whereby homopolymers of ADP-ribose (ADPr) from NAD$^+$ are either covalently attached to, or non-covalently associated with a specific protein. The net amount of covalently attached ADPr depends on the balance between poly-ADP-ribose polymerase (PARP) and poly-ADP-ribose glycohydrolase (PARG), which add or remove ADPr, respectively. All histones are potential PARP substrates, however H1 and H2B appear to be the primary targets (Adamietz and Rudolph, 1984; D'Amours et al., 1999; Krupitza and Cerutti, 1989). These non-covalent associations of poly-ADPr with histones appear to be specific rather than the result of stochastic electrostatic interactions and a specific order of associations has been determined (H1 > H2B > H2A > H3 > H4) (Realini and Althaus, 1992).

The correlation between histone poly-ADPr and transcription remains controversial. Many investigations have suggested a link between poly-ADPr and transcription. Ota *et al* (2003) demonstrated that in a PARP-1 deficient murine cell line, the expression levels of various HATs, that positively regulate transcription (e.g. CBP, P300 and PCAF), are decreased dramatically and leads to a significant decrease in global acetylation levels. Although PARP interacts with transcription factor activator protein-2 (AP-2), there is no direct evidence that histone ADPr is involved in positively regulating transcription in either of these instances.

Overall there is no direct *in vivo* evidence that clearly demonstrates core histone ADPr regulates chromatin remodeling. *In vitro* evidence suggests that H1 ADPr may prevent chromatin condensation by promoting a relaxed chromatin structure without the requirement for complete H1 dissociation (de Murcia et al., 1986; Poirier et al., 1982).

Alternatively, it is plausible that ADPr may also be involved in chromatin compaction. Conceivably, ADPr could potentially serve as a cross-linking agent between chromatinized H1 molecules, and would explain its presence within transcriptionally silenced DNA regions (Lorimer et al., 1977; Stone et al., 1977; Wong et al., 1983).

1.7 HIGHER ORDER CHROMATIN STRUCTURE

One of the primary characteristics of chromatin is that its structure must be dynamic. Chromatin structure must remain pliable so that it can accommodate required structural changes associated with efficiently distributing genes within euchromatin and heterochromatin as well as package the genome so that it can be accurately replicated and segregated. It must also remain dynamic so that it can adapt to various stresses, stimuli or cellular events that a typical cell routinely encounters. In turn, this fundamental characteristic regulates the accessibility of specific nuclear factors (e.g. co-activators, transcription factors, repressors, etc.) to the genomic template (Rattner, 1992). Currently the structure of higher-order chromatin is only poorly understood. There are numerous proposed models that are primarily based on a series of hierarchical folding steps with several intermediate stages or structures (Figure 1.8). While the exact structure of both interphase and mitotic higher-order chromatin structure remains elusive, it is clear that many supplementary proteins (e.g. histone H1 and HMG proteins) are required for its generation and stability.

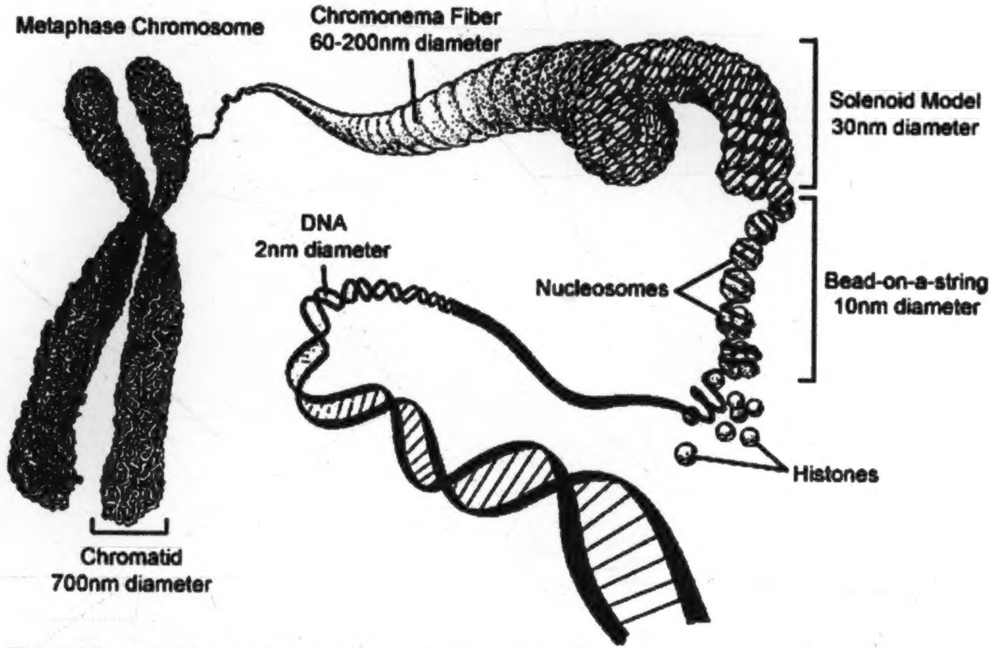
Metaphase Chromosome
Chromonema Fiber
60-200nm diameter
Solenoid Model
30nm diameter
DNA
2nm diameter
Nucleosomes
Bead-on-a-string
10nm diameter
Histones
Chromatid
700nm diameter

Figure 1.8. A putative model depicting the hierarchical series of folding events involved in the generation of higher-order chromatin structure.
Shown here are various proposed steps required for the generation of chromatin compaction and folding that are present within a metaphase chromosome. Intermediates in the folding process are indicated with the approximate diameters indicated. (Adapted from Dr. Jeff Hansen's home page [http://www.bmb.colostate.edu/faculty_detailed.cfm?lastname=Hansen&firstname=Jeffrey%20C]).

Presumably, higher-order chromatin structure is initiated through nucleosome-nucleosome interactions occurring between adjacent and non-adjacent nucleosomes. The potential resulting structures are defined by the physical constraints inherent in the linker and nucleosomal DNA. As a result many models of higher-order chromatin structure attempt to accommodate the preferred DNA path through two sequential nucleosomes or di-nucleosomes. Di-nucleosomes exert specific conformational and structural constraints on the DNA entering and exiting the nucleosome. Consequently at low salt concentrations, the 10 nm fiber cannot favor a completely linear structure and the DNA is known to follow a 'zig-zag' or 'saw-tooth' pathway in electron micrograph images (Bednar et al., 1998; Leuba et al., 1994; Woodcock et al., 1993).

Another feature common to many models is the existence of a 30 nm fiber. Many models have been suggested but are generally based upon three variations, namely the 'twisted-ribbon', the 'crossed-linker' and the 'solenoid' models. The 'twisted-ribbon' and the 'crossed-linker' models in particular, attempt to accommodate the structural constraints imparted by the DNA discussed above. The twisted-ribbon model (Sperling and Amos, 1977) compacts the nucleosomes in a zig-zag pattern that is twisted around an imaginary cylinder thereby creating two parallel helices containing either even or odd numbered nucleosomes (Figure 1.9, A). In this model there are 18 nucleosomes per turn, the diameter of the helix is approximately 30 nm and the pitch is approximately 32 nm. The primary advantage of this model is that it nicely accommodates the preferred path of the linker DNA. However this model places the linker DNA and linker histones on the outside of the fiber. Most nuclease and protease data argues that both are protected and primarily internal (Yao et al., 1990; Yao et al., 1991). The crossed-linker

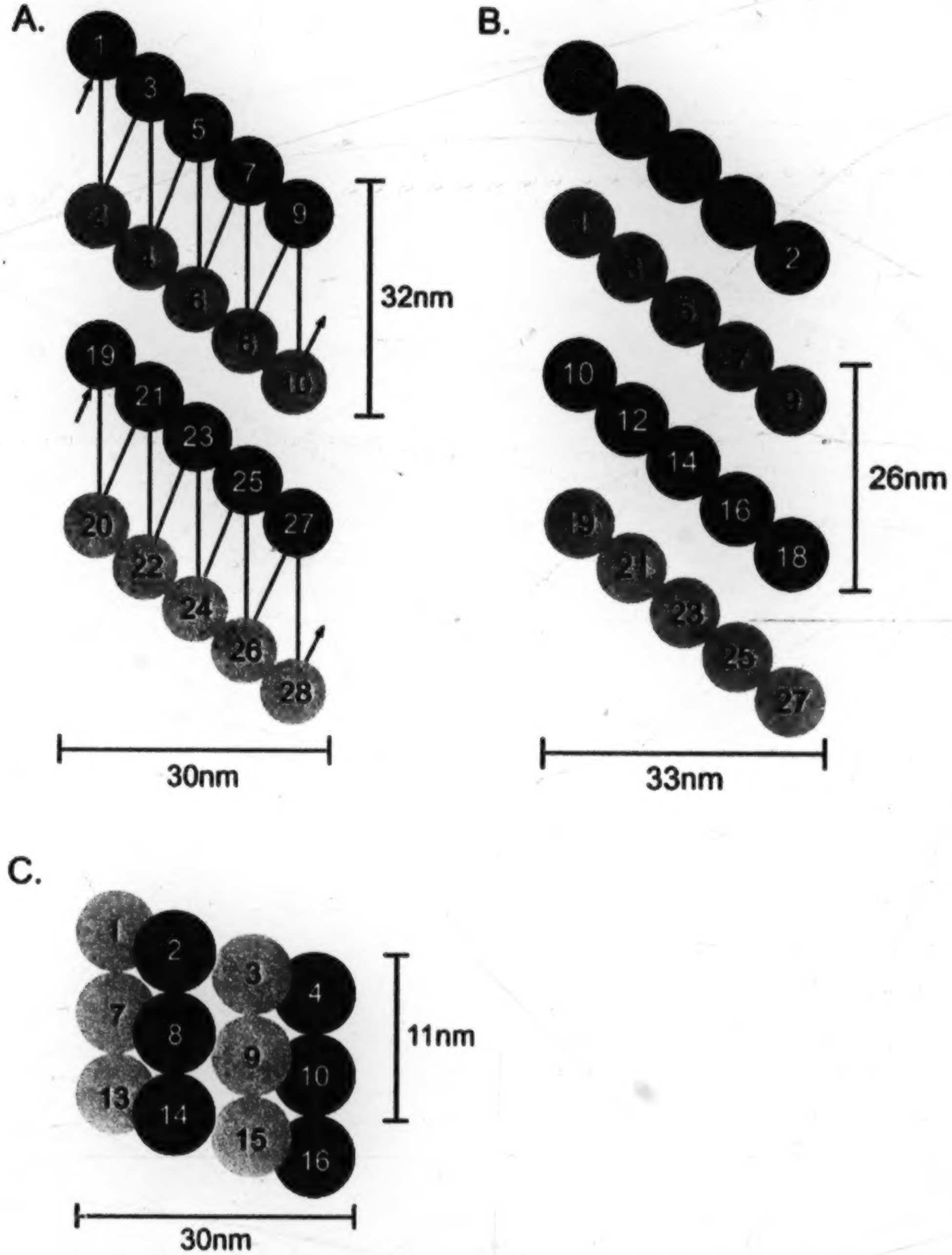
A.
1
3
5
7
9
2
4
6
8
10
32nm
19
21
23
25
27
20
22
24
26
28
30nm
B.
2
1
3
5
7
9
10
12
14
16
18
26nm
19
21
23
25
27
33nm
C.
1
2
3
4
7
8
9
10
11nm
13
14
15
16
30nm

Figure 1.9. Side views of three putative 30 nm fiber models.
Circles and numbers indicate identify the positions and locations of sequentially adjacent nucleosomes within each of the models. The approximate dimensions are indicated. Panel A presents one side of the cylinder from the twisted-ribbon model. Lines and arrows indicate the position and direction of the linker DNA. Panel B depicts the positions of nucleosomes from one side of the crossed-linker model while Panel C depicts the solenoid model. (Adapted from (Turner, 2002b)).

model (Williams et al., 1986) is similar to the twisted-ribbon model in that it contains two parallel helices of alternating even or odd numbered nucleosomes (Figure 1.9, B). It also contains 18 nucleosomes per turn, but the path of the linker DNA differs substantially. Linearly sequential nucleosomes are located on opposite sides of the helix with the linker DNA spanning the imaginary cylinder. This model predicts that the diameter of the central cylinder is proportional to the lengths of the linker DNAs and correctly positions the linker DNA and histone H1 within the protected central cylinder.

More recent chromatin fiber analyses have identified a spectrum of chromatin states that range from unfolded to moderately folded to highly folded conformations (Fletcher and Hansen, 1996; Zlatanova et al., 1998). Several approaches have been employed to investigate the folding and unfolding of the chromatin fiber, including EM, X-ray diffraction, CD and hydrodynamic measurements (i.e. ultra-centrifugation). For example, EM has been used to examine the folding dynamics of artificial fibers comprised of several kilobase pairs of DNA, in varying ionic conditions (Thoma et al., 1979). Based on this work, a third model for the 30 nm fiber was proposed and is generally accepted to be the actual *in vivo* structure although this remains to be demonstrated conclusively. The solenoid model (Finch and Klug, 1976) is comprised of a chain of nucleosomes in the form of a solenoid, with a pitch of 11 nm and six nucleosomes per helical turn (Figure 1.9, C). Each turn is thought to correspond to the nucleosomes stacking with their long axes parallel to the fiber, since individual nucleosomes are 11 nm wide discs (Thoma et al., 1979). Implicit in this model is that the nucleosomes form the outer shell, while the linker histones align down the central core of the solenoid. This model also predicts that the linker histones may serve as a nucleating agent for the formation of the 30 nm fiber as they interact with adjacent linker histones thereby shaping the chromatin fiber. Exactly how the fiber is initiated and whether or not directionality plays a role in its propagation are still areas of debate. Evidence for and against these points have been presented (Clark and Thomas, 1986; Hayes and Wolffe, 1993; Thomas et al., 1992). What is clear however, is that its propagation is likely to be directional based on the observation that polarity within a chromatin fiber is observed with respect to histone H1 found in chromatin fragments greater than 1 kb in length (Lennard and Thomas, 1985). Whether or not it is mediated through interactions between adjacent linker histones or linker histones and adjacent 'naked' DNA stretches, or even if it is localized or co-operative in nature, still remain to be determined. A major detractor of the solenoid model however, is the linker DNA must curve sharply between adjacent nucleosomes, a concession that is difficult to resolve.

Although it is known that DNA and nucleosomes are organized into structures *in vivo* with diameters well beyond that of the 10 or 30 nm fibers, the detailed folding of nucleosomes into interphase or mitotic structures is only poorly understood. Many models have been proposed for both interphase and mitotic chromatin architecture (Rattner and Lin, 1987; Woodcock et al., 1984). The models for interphase chromatin are frequently gleaned from topographical data investigating the unfolding of mitotic chromosomes into 'interphase' chromatin, rather than how interphase chromatin compacts to form mitotic chromosomes. In any case, the operational model of interphase or mitotic chromosome structure must present a plausible pathway for chromatin compaction during G_2 through prophase and decondensation from telophase through mid-G_1. The direct verification or contradiction of any model requires 3D reconstructions of native interphase or mitotic chromosomes with sufficient resolution to trace the folding of tightly packed, individual 30 nm chromatin fibers throughout large chromosomal regions (Belmont and Bruce, 1994).

Digital and electron microscopy of Drosophila and human cells established that large-scale chromatin domains are prominent components of both mitotic chromosomes and interphase chromatin (Belmont et al., 1989; Belmont and Bruce, 1994). Belmont and colleagues (Belmont and Bruce, 1994) have performed critical cytological and EM experiments that focus primarily on changes within interphase chromosome structure that accompany cell cycle progression. This seminal study identified discrete and tightly coiled chromatin fibers within partially decondensed chromatin masses. These interphase fibers are referred to as chromonema fibers and have diameters typically ranging between 100 and 130 nm. Importantly, this study reaffirmed that chromatin is rarely found as 30 nm fibers and reconfirmed that the 10 nm fiber is rare, if present at all *in vivo*. They also noted that an uncoiling and straightening of the chromonema fibers accompanies the transition from early G_1 (200 to 400 nm fibers) to late G_1 (100 to 130 nm fibers) and into early S-phase (60 to 80 nm fibers) (Belmont and Bruce, 1994). Although these more extended S-phase chromonema fibers could be traced over distances greater than 2 μm, localized regions of unfolding were occasionally observed and revealed loosely folded 30 nm fibers. This suggests that the 60-80 nm fibers are primarily comprised of tightly folded 30 nm fibers. The working model proposed by Belmont and colleagues to explain the observed large-scale chromatin structure is presented in Figure 1.10A (Belmont and Bruce, 1994). The model proposes that higher-order 30 nm fibers fold into 60-80 nm chromonema fibers that undergo additional levels of compaction either through folding into 100-130 nm fibers or through a continuous remodeling processes. In turn, these 100-

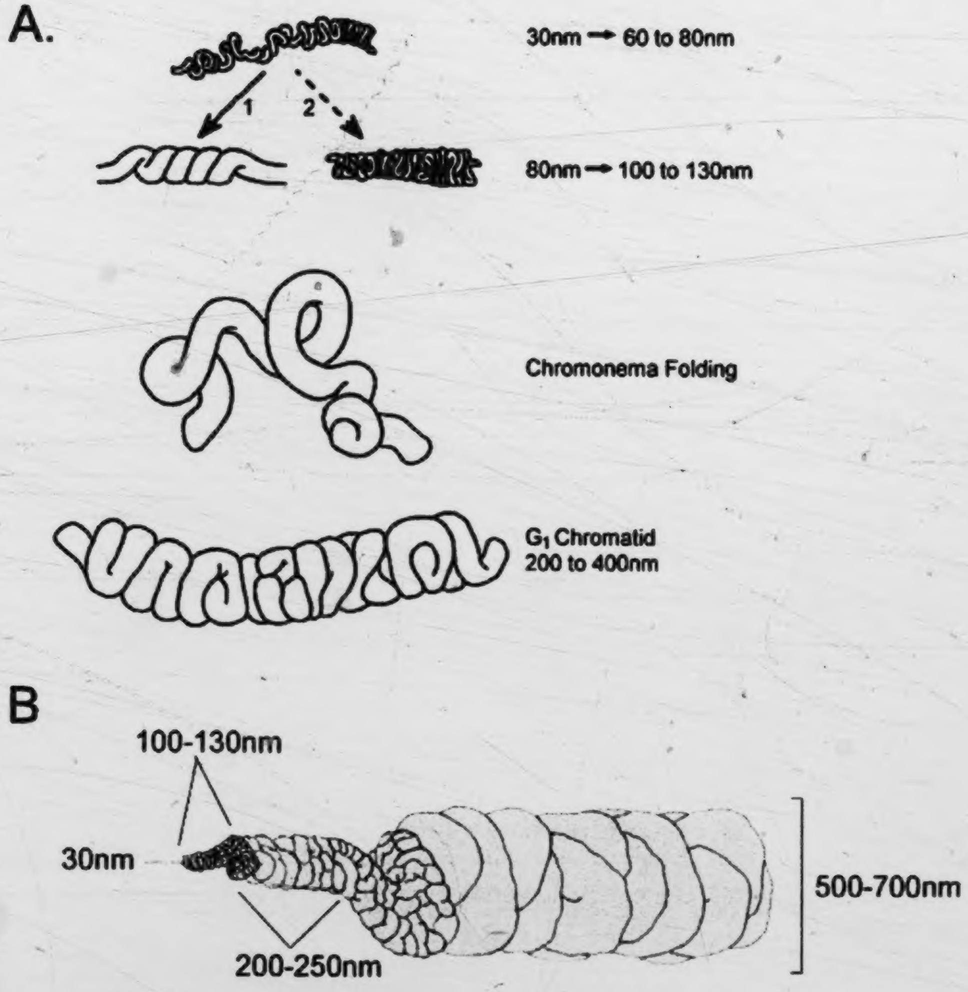
A.
30nm → 60 to 80nm
1
2
80nm → 100 to 130nm
Chromonema Folding
G₁ Chromatid
200 to 400nm
B
100-130nm
30nm
200-250nm
500-700nm

Figure 1.10. Putative mModels of higher-order chromatin structure.
Panel A presents a working model for interphase chromatin organization. It depicts a series of folding events that ultimately leads to the formation of interphase chromatin structure. The arrows and numbers indicate that the transition between the 60-80 nm chromonema fibers and the 100-130 nm fibers may occur by; 1) the successive coiling of chromonema fibers or, 2) the continuous remodeling of the folded 30nm chromatin fibers to form a thicker chromonema fiber. (Adapted from (Belmont and Bruce, 1994)).
Panel B presents the 'Hierarchical folding, axial glue' model of metaphase chromosome structure proposed by Belmont and colleagues. The 30 nm fiber folds into 100-130 nm chromonema fibers, which in turn fold into 200-250 nm middle prophase chromatids, which eventually fold into 500-700 nm metaphase chromatids. (Adapted from (Kireeva et al., 2004)).

130 nm fibers fold and kink into condensed chromatin masses over larger chromosomal regions that give rise to contiguous condensed regions or chromatids (Belmont and Bruce, 1994). This hierarchical model of chromatin compaction is now referred to as the 'hierarchical folding, axial glue' model and is presented in Figure 1.10, B (Kireeva et al., 2004; Strukov et al., 2003). For a size perspective, consider that a 30 nm fiber spanning the 100 nm diameter of a chromonema fiber would include approximately 1×10^5 bp of DNA (Gerchman and Ramakrishnan, 1987). Thus in the context of transcription, the diameter of a single chromonema fiber could conceivably contain the entire enhancer and promoter sequence elements of a mammalian gene (Horn and Peterson, 2002). Subsequent *in vivo* studies have unequivocally demonstrated that transcribing chromatin does not exist as 10 nm fibers but rather occurs in chromonema fibers with diameters of approximately 100 nm. In 1999, Tumbar *et al* (1999) introduced a tandem array of LacI-sequences (~90 mega-bp) upstream of a dihydrofolate reductase (*DHFR*) gene in a mammalian genome. Cells were transfected with either an activator (GFP-LacI-VP16) or a repressor (LacI-GFP) construct. Measurements of the GFP signal lengths were then made and it was estimated that in the activator system (GFP-LacI-VP16) the diameter of the transcribing chromatin fiber was approximately 100 nm (Tumbar et al., 1999). Together these studies lay the foundation for the hierarchical series of chromatin folding events and challenge a long-held dogma that the oscillation between 10 and 30 nm fibers is the mechanism regulating transcriptional activation or silencing.

1.8 HISTONE CODE HYPOTHESIS

Early on in the investigation of histone modifications, Vincent Allfrey and colleagues (Allfrey et al., 1964) suggested that acetylation, or more specifically hyperacetylation, could positively influence the transcriptional competency of specific genetic loci. It is now clear that regulatory signals, either extracellular or intracellular, directly influence chromatin structure and function (reviewed in (Cheung et al., 2000)). In fact, physical models have been proposed that suggest posttranslational histone modifications disrupt histone:histone and histone:DNA interactions thereby altering chromatin structure (Hansen et al., 1998; Wolffe and Hayes, 1999). The dynamic changes in chromatin architecture that accompany various cellular processes or stimuli, directly influence the accessibility of genes to nuclear factors (i.e. transcription factors, co-activators, co-repressors, etc.) that engage the genomic template (Lomvardas and Thanos, 2002). It is now well appreciated that the epigenomic information contained within chromatin directly influences most chromatin-regulated processes and has far-reaching consequences that impact cellular decisions and ultimately, their fate (Figure 1.11, A).

A growing awareness of the biological outcomes surrounding epigenetic modifications has led many researchers to propose that an epigenetic indexing system for genomes must exist that functions in addition to the genetic information encoded by the genome itself (reviewed in (Agalioti et al., 2002; Berger, 2002; Fischle et al., 2003a; Fischle et al., 2003b; Hake et al., 2004; Jenuwein and Allis, 2001; Loidl, 2004; Rice and Allis, 2001; Schreiber and Bernstein, 2002; Strahl and Allis, 2000; Turner, 2000; Turner, 2002a; Wang et al., 2004a)). The numerous observed correlations identified between

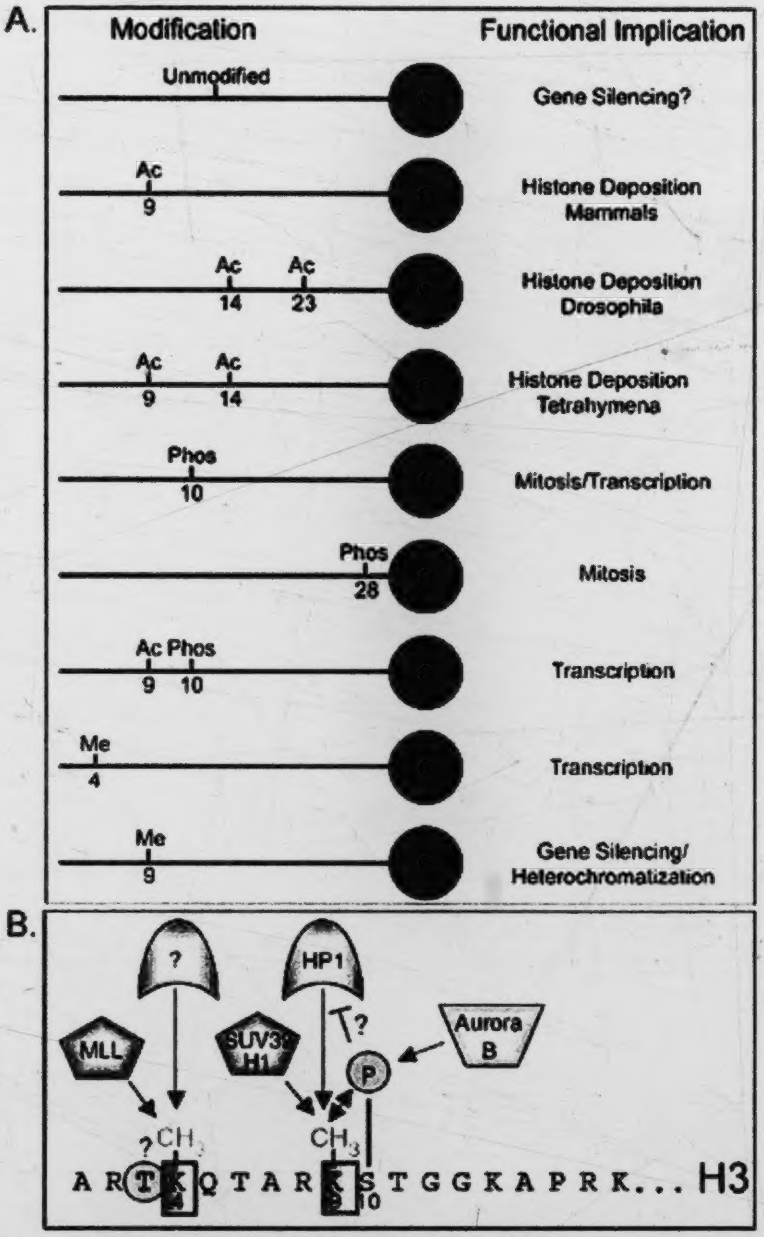
A.
Modification
Functional Implication
Unmodified
Gene Silencing?
Ac
9
Histone Deposition
Mammals
Ac
Ac
14
23
Histone Deposition
Drosophila
Ac
Ac
9
14
Histone Deposition
Tetrahymena
Phos
10
Mitosis/Transcription
Phos
28
Mitosis
Ac Phos
9 10
Transcription
Me
4
Transcription
Me
9
Gene Silencing/
Heterochromatization
B.
?
HP1
MLL
SUV39
H1
?
Aurora
B
P
?CH3
CH3
A R T K Q T A R K S T G G K A P R K . . . H3
4
9
10

Figure 1.11. Histone Code hypothesis and binary switches.
Some specific histone H3 posttranslational modifications including acetylation (Ac), phosphorylation (Phos) and methylation (Me) and the various functional outcomes associated with each (A). The amino acid positions are indicated below the specific modification. Panel B presents a specific example of the Binary Switch proposed by the Allis group involving H3. Suv39H1 methylase activity results in the generation of an HP1 binding site (i.e. tMeK9). The HP1/tMeK9 interaction is ablated by S10 phosphorylation that occurs via Aurora B kinase activity. A similar mechanism is proposed for K4 methylation by MLL although the tMeK4 interacting protein has yet to be identified. Presumably threonine 3 phosphorylation could ablate the proposed tMeK4 interaction. (Adapted from (Hake et al., 2004)).

residue-specific posttranslational modifications and the transcriptional competency at specific genetic loci forms the basis of the 'Histone Code Hypothesis'. The hypothesis posits that specific posttranslational modifications occurring at distinct residues contained within the four core histones results in a code that can be read and interpreted by numerous nuclear proteins to evoke defined functional outcomes. Support for this idea is drawn from a wealth of biochemical and structural data demonstrating that many modifications efficiently regulate chromatin structure by altering the charge of nucleosomes or disrupting histone-histone and histone-DNA interactions. More recent molecular and cytological data have demonstrated that specific posttranslational modifications serve to regulate such cellular processes as chromosome condensation (Bui et al., 2004; Wei et al., 1999), chromosome segregation (Petersen et al., 2001; Wei et al., 1999), DNA repair (Bassing et al., 2002; Celeste et al., 2002; Nazarov et al., 2003) and apoptosis (Cheung et al., 2003; Fernandez-Capetillo et al., 2004). Only now that it has been realized that posttranslational modifications regulate many different cellular processes including transcription and mitosis, are they being exploited as potential therapeutic targets.

In order for the Histone Code Hypothesis to function as proposed, at least four interrelated and fundamental requirements must exist. It is the combination of these various characteristics that ensures that numerous outcomes are possible, which can be erased at any stage of the cell cycle. First, numerous proteins must exist with enzymatic activities that covalently attach a diverse array of posttranslational modifications to the histone template. As indicated in previous sections, at least seven different core enzyme families exist that regulate the addition of seven different posttranslational modifications

– HATs (acetylation), kinases (phosphorylation), HMTs (methylation), PARP (ADP-ribosylation), holocarboxylase synthetase (biotinylation), E3 ligase (ubiquitination) and E3 ligase (sumoylation). Second, based on the total number of a specific type of a particular modification (e.g. 29 different sites of acetylation) coupled with the observations that not all enzymes within a particular family modify each possible residue, numerous enzymes must exist within each of those seven core families. This is indeed the case as numerous different HATs, kinases, HMTs, etc., have been identified. Moreover, a myriad of *in vitro* radioactive labeling experiments has clearly established that similar enzymes (e.g. HATs) can exhibit both overlapping and more importantly, distinct specificity preferences (see Chapter 5 for more detail).

The third requirement of the Histone Code Hypothesis is that a mechanism must exist whereby specific modifications can be recognized and differentially interpreted. Accordingly, two independent posttranslational histone modification protein-docking modules have been identified in a wide array of chromatin interacting proteins. Bromodomains and chromatin-organization modifier (chromo) domains contained within these proteins recognize and bind acetylated and methylated K residues, respectively. Currently, in yeast, Drosophila, and mammals, there are more than 350 proteins that contain bromodomains (http://www.sanger.ac.uk/cgi-bin/Pfam/getacc?PF00439), while more than 190 proteins contain chromodomains (http://www.sanger.ac.uk/cgi-bin/Pfam/getacc?PF00385). The bromodomain is a conserved sequence that is approximately 110 aa residues in length (Haynes et al., 1992). Although most proteins contain a single bromodomain, up to five repeats have been identified in some proteins (Jeanmougin et al., 1997). Surprisingly, nearly all HATs contain bromodomains suggesting that different acetylated residues or variable levels of acetylation may affect a diverse array of functional outcomes (Dhalluin et al., 1999). Bromodomains have also been shown to be indispensable for *in vivo* function – deletion of the yeast GCN5 bromodomain ablates its acetylase activity directly impinging on its ability to upregulate gene expression (Georgakopoulos et al., 1995). This observation supports the argument that bromodomains contribute to highly specific histone acetylation by tethering transcriptional HATs to specific genetic loci (Brownell and Allis, 1996). The chromodomain is a conserved sequence comprised of approximately 60 aa residues that was first identified in Drosophila screens for modifiers of variegation. Chromodomain-containing proteins can be classified generally into one of three categories; 1) those that have a N-terminal chromodomain followed by a chromoshadow domain (e.g. HP1 and mammalian modifier (MOD) 1 and MOD2) (Ball et al., 1997; Cowieson et al., 2000; Singh et al., 1991), 2) those with a single chromodomain (e.g. Polycomb (Pc), MOD3 and Mi-2β) (Bouazoune et al., 2002; Messmer et al., 1992; Pearce et al., 1992; Saunders et al., 1993) and, 3) those with paired or tandem chromodomains (e.g. chromodomain-helicase-DNA-binding proteins 1 to 3 [CHD-1 to 3]) (Delmas et al., 1993). In either case (bromodomains or chromodomains), the large number and vast types of proteins harboring these domains implies that numerous functional outcomes must be associated with acetylation and methylation alone. It further suggests that additional modifications may also have cognate binding domains that regulate many additional functions.

The final requirement of the Histone Code Hypothesis is that the posttranslational modifications encoding specific functional outcomes must necessarily be dynamic and be capable of being reset. This is particularly critical with respect to genes encoding proteins required for cell cycle progression, environmental changes (stimulation, starvation, etc.), embryogenesis, differentiation and development. Under these circumstances, the precise temporal regulation of these genes must be maintained and therefore the modifications must be reversible. Accordingly, three mechanisms are in place that reset the epigenetic imprint or specifically eliminate various posttranslational modifications. These include RDNA, RINA and the enzymatic removal of the posttranslational modification itself. RDNA and RINA effectively remove specific posttranslational modifications by incorporating histones into newly synthesized or transcribing DNA respectively. The enzymatic removal of specific posttranslational modifications is accomplished by numerous different enzymes such as HDACs, phosphatases, biotinidases, etc. With the possible exception of methylation, large families of enzymes exist that can remove all remaining posttranslational modifications. Nevertheless, the various combinations of these three different mechanisms virtually guarantee that all epigenetic imprints, including methylation, can be reset at various points of the cell cycle.

1.8.1 *Binary Switches*

During the past few years, the Allis research group has proposed an additional layer of complexity that functions under the auspices of the Histone Code Hypothesis. They suggest that binary on/off switches exist that regulate the on/off rates of effector molecules required to alter or reset distinct functional outcomes that accompany specific epigenetic marks (Fischle et al., 2003a). These effector molecules contain cognate binding modules (e.g. bromo- and chromo-domains) that recognize and interact with a specific epigenetic mark. Accordingly, following the initial interaction between a posttranslational modification and its cognate interacting protein, a supplemental posttranslational modification occurring at an adjacent or nearby site, disrupts the initial interaction. For example, Fischle *et al* (2003a) postulate that the heterochromatic or repressed state imparted by HP1 binding of tMeK9 (H3) can be ablated through subsequent phosphorylation of serine 10 (H3) (Figure 1.11, B). In essence, PhosS10 prohibits HP1 binding to tMeK9 and effectively 'turns off' the heterochromatic imprint that its binding imparts. In other words, this binary switch successfully resets the genomic imprint so that a particular gene is altered. This specific example is based upon the structural examination of the HP1 chromodomain interaction with tMeK9 (Jacobs and Khorasanizadeh, 2002; Nielsen et al., 2002), which predicts that PhosS10 could sufficiently diminish the affinity of HP1 for tMeK9. In fact, *in vitro* data confirm that HP1 binding is nearly completely abolished when S10 is phosphorylated and that methylated K9 and PhosS10 can co-exist within the same H3 NTD (Fischle et al., 2003a; Mateescu et al., 2004; Wang et al., 2004a). Coincidentally, many of the known methylation sites existing within the H3 and H4 NTDs have adjacent residues that are, or may be, capable of being phosphorylated (Figure 1.4). Although this working model was designed to account for a methyl/phos switch, the Allis group contends that it could conceivably be extrapolated to include additional switching pairs such as acetyl/phos or ubiquitin/phos (Fischle et al., 2003a).

1.9 RESEARCH OBJECTIVES

1.9.1 *Chapter 3 – Dynamic Changes in Histone Lysine Methylations: Identification of a Mitosis-specific Function for Dynamic Methylation in Chromosome Congression and Segregation*

Histone methylation is unique amongst post-translational histone modifications by virtue of its stability. It is believed to represent a permanent and heritable epigenetic mark for gene-specific regulation. In this study, we use quantitative *in situ* approaches to investigate the cell cycle and spatial dynamics of various methylated isoforms present at lysines (K) 4 and 9 (histone H3) and K20 (histone H4). Contrary to the expected stability of trimethylated lysines, our results for tMeK9 (H3) demonstrate that methylations can be lost rapidly and in a cell cycle-specific manner. Loss of tMeK9 appears to reflect a robust demethylase activity that is restricted to the period between anaphase and cytokinesis. Subsequent investigations of mitoses in tMeK9-deficient cells revealed defects in chromosome congression and segregation. Collectively, these results identify a mitosis-specific trimethylation of K9 in pericentromeric heterochromatin that functions in the faithful segregation of chromosomes.

1.9.2 *Chapter 4 – ATM-dependent Mitotic Phosphorylation of H2AX in Normally Growing Mammalian Cells*

H2AX is a core histone H2A variant that contains an invariant serine/glutamine (SQ) motif within an extended carboxy-terminal tail. H2AX phosphorylation at the SQ motif (γ-H2AX) has been shown to increase dramatically upon exogenously introduced DNA double-strand breaks (DSBs). In this study, we employ quantitative *in situ* approaches to investigate the spatial patterning and cell cycle dynamics of γ-H2AX in a panel of normally growing (unirradiated) mammalian cell lines. We provide the first evidence for the existence of two distinct yet highly discernable γ-H2AX focal populations: a small population of large amorphous foci that colocalize with numerous repair proteins and a previously unidentified predominant population of small foci that does not colocalize with the same repair proteins. Our results also describe novel cell cycle-dependent dynamics for γ-H2AX in unirradiated mammalian cells that are dependent on functional ATM expression. Furthermore, based on similarities drawn from other histone posttranslational modifications and previous observations in haploinsufficient ($\mathit{H2AX}^{-/+}$) and null mice ($\mathit{H2AX}^{-/-}$), γ-H2AX may be essential for the fidelity of the mitotic process thereby ensuring the faithful transmission of genetic information from one generation to the next.

1.9.3 *Chapter 5 – Quantitative Analysis of CBP- and P300-Induced Histone Acetylations In Situ Using a Native Chromatin Template*

Histone tails are involved in numerous *in vivo* interactions, including those with DNA, adjacent histones, and other nonhistone proteins. The amino termini are also the substrates for a number of enzymes, including histone acetyltransferases (HATs) and histone deacetylases (HDACs). Traditional biochemical approaches defining the substrate specificity profiles of HATs have been performed using purified histone tails, recombinant histones, or purified mononucleosomes as substrates. It is clear that the in vivo presentation of the substrate cannot be accurately represented by using these in vitro approaches. Because of the difficulty in translating in vitro results into in vivo situations, we developed a novel single-cell HAT assay that provides quantitative measurements of endogenous HAT activity. The HAT assay is performed under in vivo conditions by using the native chromatin structure as the physiological substrate. The assay combines the spatial resolving power of laser scanning confocal microscopy with simple statistical analyses to characterize CREB binding protein (CBP)- and P300-induced changes in global histone acetylation levels at specific lysine residues. Here we show that CBP and P300 exhibit unique substrate specificity profiles, consistent with the developmental and functional differences between the two HATs.

1.10 REFERENCES

Aagaard, L., G. Laible, P. Selenko, M. Schmid, R. Dorn, G. Schotta, S. Kuhfittig, A. Wolf, A. Lebersorger, P.B. Singh, G. Reuter, and T. Jenuwein. 1999. Functional mammalian homologues of the Drosophila PEV-modifier Su(var)3-9 encode centromere-associated proteins which complex with the heterochromatin component M31. *Embo J.* 18:1923-38.

Adamietz, P., and A. Rudolph. 1984. ADP-ribosylation of nuclear proteins in vivo. Identification of histone H2B as a major acceptor for mono- and poly(ADP-ribose) in dimethyl sulfate-treated hepatoma AH 7974 cells. *J Biol Chem.* 259:6841-6.

Agalioti, T., G. Chen, and D. Thanos. 2002. Deciphering the transcriptional histone acetylation code for a human gene. *Cell.* 111:381-92.

Ahmad, K., and S. Henikoff. 2002a. Epigenetic consequences of nucleosome dynamics. *Cell.* 111:281-4.

Ahmad, K., and S. Henikoff. 2002b. The histone variant H3.3 marks active chromatin by replication-independent nucleosome assembly. *Mol Cell.* 9:1191-200.

Alberts, B., A. Johnson, J. Lewis, K. Roberts, and P. Walter. 2002. Molecular Biology of the Cell. Garland Science Publishing. 1400 pp.

Albig, W., and D. Doenecke. 1997. The human histone gene cluster at the D6S105 locus. *Hum Genet.* 101:284-94.

Allan, J., N. Harborne, D.C. Rau, and H. Gould. 1982. Participation of core histone "tails" in the stabilization of the chromatin solenoid. *J Cell Biol.* 93:285-97.

Allfrey, V.G., R. Faulkner, and A.E. Mirsky. 1964. Acetylation and Methylation of Histones and Their Possible Role in the Regulation of Rna Synthesis. *Proc Natl Acad Sci U S A.* 51:786-94.

Allis, C.D., L.G. Chicoine, R. Richman, and I.G. Schulman. 1985. Deposition-related histone acetylation in micronuclei of conjugating Tetrahymena. *Proc Natl Acad Sci U S A.* 82:8048-52.

Arents, G., R.W. Burlingame, B.C. Wang, W.E. Love, and E.N. Moudrianakis. 1991. The nucleosomal core histone octamer at 3.1 A resolution: a tripartite protein assembly and a left-handed superhelix. *Proc Natl Acad Sci U S A.* 88:10148-52.

Aul, R.B., and R.J. Oko. 2002. The major subacrosomal occupant of bull spermatozoa is a novel histone H2B variant associated with the forming acrosome during spermiogenesis. *Dev Biol.* 242:376-87.

Ausio, J. 1992. Structure and dynamics of transcriptionally active chromatin. *J Cell Sci.* 102 (Pt 1):1-5.

Ausio, J., F. Dong, and K.E. van Holde. 1989. Use of selectively trypsinized nucleosome core particles to analyze the role of the histone "tails" in the stabilization of the nucleosome. *J Mol Biol*. 206:451-63.

Baarends, W.M., J.W. Hoogerbrugge, H.P. Roest, M. Ooms, J. Vreeburg, J.H. Hoeijmakers, and J.A. Grootegoed. 1999. Histone ubiquitination and chromatin remodeling in mouse spermatogenesis. *Dev Biol*. 207:322-33.

Ball, L.J., N.V. Murzina, R.W. Broadhurst, A.R. Raine, S.J. Archer, F.J. Stott, A.G. Murzin, P.B. Singh, P.J. Domaille, and E.D. Laue. 1997. Structure of the chromatin binding (chromo) domain from mouse modifier protein 1. *Embo J.* 16:2473-81.

Ballard, T.D., J. Wolff, J.B. Griffin, J.S. Stanley, S. van Calcar, and J. Zempleni. 2002. Biotinidase catalyzes debiotinylation of histones. *Eur J Nutr*. 41:78-84.

Baneres, J.L., A. Martin, and J. Parello. 1997. The N tails of histones H3 and H4 adopt a highly structured conformation in the nucleosome. *J Mol Biol*. 273:503-8.

Bannister, A.J., and T. Kouzarides. 1996. The CBP co-activator is a histone acetyltransferase. *Nature*. 384:641-3.

Bannister, A.J., E.A. Miska, D. Gorlich, and T. Kouzarides. 2000. Acetylation of importin-alpha nuclear import factors by CBP/p300. *Curr Biol*. 10:467-70.

Bannister, A.J., P. Zegerman, J.F. Partridge, E.A. Miska, J.O. Thomas, R.C. Allshire, and T. Kouzarides. 2001. Selective recognition of methylated lysine 9 on histone H3 by the HP1 chromo domain. *Nature*. 410:120-4.

Barratt, M.J., C.A. Hazzalin, E. Cano, and L.C. Mahadevan. 1994. Mitogen-stimulated phosphorylation of histone H3 is targeted to a small hyperacetylation-sensitive fraction. *Proc Natl Acad Sci U S A*. 91:4781-5.

Barsoum, J., and A. Varshavsky. 1985. Preferential localization of variant nucleosomes near the 5'-end of the mouse dihydrofolate reductase gene. *J Biol Chem.* 260:7688-97.

Bassing, C.H., K.F. Chua, J. Sekiguchi, H. Suh, S.R. Whitlow, J.C. Fleming, B.C. Monroe, D.N. Ciccone, C. Yan, K. Vlasakova, D.M. Livingston, D.O. Ferguson, R. Scully, and F.W. Alt. 2002. Increased ionizing radiation sensitivity and genomic instability in the absence of histone H2AX. *Proc Natl Acad Sci U S A*. 99:8173-8.

Bednar, J., R.A. Horowitz, S.A. Grigoryev, L.M. Carruthers, J.C. Hansen, A.J. Koster, and C.L. Woodcock. 1998. Nucleosomes, linker DNA, and linker histone form a unique structural motif that directs the higher-order folding and compaction of chromatin. *Proc Natl Acad Sci U S A*. 95:14173-8.

Belmont, A.S., M.B. Braunfeld, J.W. Sedat, and D.A. Agard. 1989. Large-scale chromatin structural domains within mitotic and interphase chromosomes in vivo and in vitro. *Chromosoma*. 98:129-43.

Belmont, A.S., and K. Bruce. 1994. Visualization of G1 chromosomes: a folded, twisted, supercoiled chromonema model of interphase chromatid structure. *J Cell Biol*. 127:287-302.

Berger, S.L. 2002. Histone modifications in transcriptional regulation. *Curr Opin Genet Dev*. 12:142-8.

Bjerling, P., R.A. Silverstein, G. Thon, A. Caudy, S. Grewal, and K. Ekwall. 2002. Functional divergence between histone deacetylases in fission yeast by distinct cellular localization and in vivo specificity. *Mol Cell Biol*. 22:2170-81.

Borun, T.W., D. Pearson, and W.K. Paik. 1972. Studies of histone methylation during the HeLa S-3 cell cycle. *J Biol Chem*. 247:4288-98.

Bosch, A., and P. Suau. 1995. Changes in core histone variant composition in differentiating neurons: the roles of differential turnover and synthesis rates. *Eur J Cell Biol*. 68:220-5.

Bouazoune, K., A. Mitterweger, G. Langst, A. Imhof, A. Akhtar, P.B. Becker, and A. Brehm. 2002. The dMi-2 chromodomains are DNA binding modules important for ATP-dependent nucleosome mobilization. *Embo J*. 21:2430-40.

Bowman, T.L., and M.M. Hurt. 1995. The coding sequences of mouse H2A and H3 histone genes contains a conserved seven nucleotide element that interacts with nuclear factors and is necessary for normal expression. *Nucleic Acids Res*. 23:3083-92.

Boyes, J., P. Byfield, Y. Nakatani, and V. Ogryzko. 1998. Regulation of activity of the transcription factor GATA-1 by acetylation. *Nature*. 396:594-8.

Briggs, S.D., T. Xiao, Z.W. Sun, J.A. Caldwell, J. Shabanowitz, D.F. Hunt, C.D. Allis, and B.D. Strahl. 2002. Gene silencing: trans-histone regulatory pathway in chromatin. *Nature*. 418:498.

Brown, D.T. 2001. Histone variants: are they functionally heterogeneous? *Genome Biol*. 2:REVIEWS0006.

Brownell, J.E., and C.D. Allis. 1996. Special HATs for special occasions: linking histone acetylation to chromatin assembly and gene activation. *Curr Opin Genet Dev.* 6:176-84.

Bui, H.T., E. Yamaoka, and T. Miyano. 2004. Involvement of histone H3 (Ser10) phosphorylation in chromosome condensation without CDC2 kinase and mitogen-activated protein kinase activation in pig oocytes. *Biol Reprod.* 70:1843-51.

Buschmann, T., S.Y. Fuchs, C.G. Lee, Z.Q. Pan, and Z. Ronai. 2000. SUMO-1 modification of Mdm2 prevents its self-ubiquitination and increases Mdm2 ability to ubiquitinate p53. *Cell.* 101:753-62.

Camporeale, G., E.E. Shubert, G. Sarath, R. Cerny, and J. Zempleni. 2004. K8 and K12 are biotinylated in human histone H4. *Eur J Biochem.* 271:2257-63.

Celeste, A., S. Petersen, P.J. Romanienko, O. Fernandez-Capetillo, H.T. Chen, O.A. Sedelnikova, B. Reina-San-Martin, V. Coppola, E. Meffre, M.J. Difilippantonio, C. Redon, D.R. Pilch, A. Olaru, M. Eckhaus, R.D. Camerini-Otero, L. Tessarollo, F. Livak, K. Manova, W.M. Bonner, M.C. Nussenzweig, and A. Nussenzweig. 2002. Genomic instability in mice lacking histone H2AX. *Science.* 296:922-7.

Chadee, D.N., M.J. Hendzel, C.P. Tylipski, C.D. Allis, D.P. Bazett-Jones, J.A. Wright, and J.R. Davie. 1999. Increased Ser-10 phosphorylation of histone H3 in mitogen-stimulated and oncogene-transformed mouse fibroblasts. *J Biol Chem.* 274:24914-20.

Chang, L., S.S. Loranger, C. Mizzen, S.G. Ernst, C.D. Allis, and A.T. Annunziato. 1997. Histones in transit: cytosolic histone complexes and diacetylation of H4 during nucleosome assembly in human cells. *Biochemistry.* 36:469-80.

Chen, H., R.J. Lin, R.L. Schiltz, D. Chakravarti, A. Nash, L. Nagy, M.L. Privalsky, Y. Nakatani, and R.M. Evans. 1997. Nuclear receptor coactivator ACTR is a novel histone acetyltransferase and forms a multimeric activation complex with P/CAF and CBP/p300. *Cell.* 90:569-80.

Cheung, P., K.G. Tanner, W.L. Cheung, P. Sassone-Corsi, J.M. Denu, and C.D. Allis. 2000. Synergistic coupling of histone H3 phosphorylation and acetylation in response to epidermal growth factor stimulation. *Mol Cell.* 5:905-15.

Cheung, W.L., K. Ajiro, K. Samejima, M. Kloc, P. Cheung, C.A. Mizzen, A. Beeser, L.D. Etkin, J. Chernoff, W.C. Earnshaw, and C.D. Allis. 2003. Apoptotic phosphorylation of histone H2B is mediated by mammalian sterile twenty kinase. *Cell.* 113:507-17.

Chicoine, L.G., I.G. Schulman, R. Richman, R.G. Cook, and C.D. Allis. 1986. Nonrandom utilization of acetylation sites in histones isolated from Tetrahymena. Evidence for functionally distinct H4 acetylation sites. *J Biol Chem*. 261:1071-6.

Clark, D.J., and J.O. Thomas. 1986. Salt-dependent co-operative interaction of histone H1 with linear DNA. *J Mol Biol*. 187:569-80.

Clayton, A.L., S. Rose, M.J. Barratt, and L.C. Mahadevan. 2000. Phosphoacetylation of histone H3 on c-fos- and c-jun-associated nucleosomes upon gene activation. *Embo J*. 19:3714-26.

Cohen, H.Y., S. Lavu, K.J. Bitterman, B. Hekking, T.A. Imahiyerobo, C. Miller, R. Frye, H. Ploegh, B.M. Kessler, and D.A. Sinclair. 2004. Acetylation of the C terminus of Ku70 by CBP and PCAF controls Bax-mediated apoptosis. *Mol Cell*. 13:627-38.

Couppez, M., A. Martin-Ponthieu, and P. Sautiere. 1987. Histone H4 from cuttlefish testis is sequentially acetylated. Comparison with acetylation of calf thymus histone H4. *J Biol Chem*. 262:2854-60.

Covault, J., and R. Chalkley. 1980. The identification of distinct populations of acetylated histone. *J Biol Chem*. 255:9110-6.

Cowieson, N.P., J.F. Partridge, R.C. Allshire, and P.J. McLaughlin. 2000. Dimerisation of a chromo shadow domain and distinctions from the chromodomain as revealed by structural analysis. *Curr Biol*. 10:517-25.

Csordas, A. 1990. On the biological role of histone acetylation. *Biochem J*. 265:23-38.

D'Amours, D., S. Desnoyers, I. D'Silva, and G.G. Poirier. 1999. Poly(ADP-ribosyl)ation reactions in the regulation of nuclear functions. *Biochem J*. 342 (Pt 2):249-68.

Davie, J.R. 2003. MSK1 and MSK2 mediate mitogen- and stress-induced phosphorylation of histone H3: a controversy resolved. *Sci STKE*. 2003:PE33.

Davie, J.R., and V.A. Spencer. 1999. Control of histone modifications. *J Cell Biochem*. Suppl 32-33:141-8.

de la Barre, A.E., V. Gerson, S. Gout, M. Creaven, C.D. Allis, and S. Dimitrov. 2000. Core histone N-termini play an essential role in mitotic chromosome condensation. *Embo J*. 19:379-91.

de Murcia, G., A. Huletsky, D. Lamarre, A. Gaudreau, J. Pouyet, M. Daune, and G.G. Poirier. 1986. Modulation of chromatin superstructure induced by poly(ADP-ribose) synthesis and degradation. *J Biol Chem*. 261:7011-7.

De Souza, C.P., A.H. Osmani, L.P. Wu, J.L. Spotts, and S.A. Osmani. 2000. Mitotic histone H3 phosphorylation by the NIMA kinase in Aspergillus nidulans. *Cell.* 102:293-302.

Delmas, V., D.G. Stokes, and R.P. Perry. 1993. A mammalian DNA-binding protein that contains a chromodomain and an SNF2/SWI2-like helicase domain. *Proc Natl Acad Sci U S A.* 90:2414-8.

Desterro, J.M., M.S. Rodriguez, and R.T. Hay. 1998. SUMO-1 modification of IkappaBalpha inhibits NF-kappaB activation. *Mol Cell.* 2:233-9.

Dhalluin, C., J.E. Carlson, L. Zeng, C. He, A.K. Aggarwal, and M.M. Zhou. 1999. Structure and ligand of a histone acetyltransferase bromodomain. *Nature.* 399:491-6.

Dlakic, M. 2001. Chromatin silencing protein and pachytene checkpoint regulator Dot1p has a methyltransferase fold. *Trends Biochem Sci.* 26:405-7.

Doenecke, D., W. Albig, C. Bode, B. Drabent, K. Franke, K. Gavenis, and O. Witt. 1997. Histones: genetic diversity and tissue-specific gene expression. *Histochem Cell Biol.* 107:1-10.

Dover, J., J. Schneider, M.A. Tawiah-Boateng, A. Wood, K. Dean, M. Johnston, and A. Shilatifard. 2002. Methylation of histone H3 by COMPASS requires ubiquitination of histone H2B by Rad6. *J Biol Chem.* 277:28368-71.

Dryhurst, D., A.A. Thambirajah, and J. Ausio. 2004. New twists on H2A.Z: a histone variant with a controversial structural and functional past. *Biochem Cell Biol.* 82:490-7.

Edmondson, D.G., M.M. Smith, and S.Y. Roth. 1996. Repression domain of the yeast global repressor Tup1 interacts directly with histones H3 and H4. *Genes Dev.* 10:1247-59.

Ekwall, K., and T. Ruusala. 1994. Mutations in rik1, clr2, clr3 and clr4 genes asymmetrically derepress the silent mating-type loci in fission yeast. *Genetics.* 136:53-64.

Faast, R., V. Thonglairoam, T.C. Schulz, J. Beall, J.R. Wells, H. Taylor, K. Matthaei, P.D. Rathjen, D.J. Tremethick, and I. Lyons. 2001. Histone variant H2A.Z is required for early mammalian development. *Curr Biol.* 11:1183-7.

Feng, Q., H. Wang, H.H. Ng, H. Erdjument-Bromage, P. Tempst, K. Struhl, and Y. Zhang. 2002. Methylation of H3-lysine 79 is mediated by a new family of HMTases without a SET domain. *Curr Biol.* 12:1052-8.

Fernandez-Capetillo, O., C.D. Allis, and A. Nussenzweig. 2004. Phosphorylation of histone H2B at DNA double-strand breaks. *J Exp Med*. 199:1671-7.

Finch, J.T., and A. Klug. 1976. Solenoidal model for superstructure in chromatin. *Proc Natl Acad Sci U S A*. 73:1897-901.

Fischle, W., Y. Wang, and C.D. Allis. 2003a. Binary switches and modification cassettes in histone biology and beyond. *Nature*. 425:475-9.

Fischle, W., Y. Wang, and C.D. Allis. 2003b. Histone and chromatin cross-talk. *Curr Opin Cell Biol*. 15:172-83.

Fletcher, T.M., and J.C. Hansen. 1996. The nucleosomal array: structure/function relationships. *Crit Rev Eukaryot Gene Expr*. 6:149-88.

Garcia-Ramirez, M., C. Rocchini, and J. Ausio. 1995. Modulation of chromatin folding by histone acetylation. *J Biol Chem*. 270:17923-8.

Georgakopoulos, T., N. Gounalaki, and G. Thireos. 1995. Genetic evidence for the interaction of the yeast transcriptional co-activator proteins GCN5 and ADA2. *Mol Gen Genet*. 246:723-8.

Gerchman, S.E., and V. Ramakrishnan. 1987. Chromatin higher-order structure studied by neutron scattering and scanning transmission electron microscopy. *Proc Natl Acad Sci U S A*. 84:7802-6.

Gernand, D., D. Demidov, and A. Houben. 2003. The temporal and spatial pattern of histone H3 phosphorylation at serine 28 and serine 10 is similar in plants but differs between mono- and polycentric chromosomes. *Cytogenet Genome Res*. 101:172-6.

Giet, R., and D.M. Glover. 2001. Drosophila aurora B kinase is required for histone H3 phosphorylation and condensin recruitment during chromosome condensation and to organize the central spindle during cytokinesis. *J Cell Biol*. 152:669-82.

Goldknopf, I.L., C.W. Taylor, R.M. Baum, L.C. Yeoman, M.O. Olson, A.W. Prestayko, and H. Busch. 1975. Isolation and characterization of protein A24, a "histone-like" non-histone chromosomal protein. *J Biol Chem*. 250:7182-7.

Gostissa, M., A. Hengstermann, V. Fogal, P. Sandy, S.E. Schwarz, M. Scheffner, and G. Del Sal. 1999. Activation of p53 by conjugation to the ubiquitin-like protein SUMO-1. *Embo J*. 18:6462-71.

Goto, H., Y. Tomono, K. Ajiro, H. Kosako, M. Fujita, M. Sakurai, K. Okawa, A. Iwamatsu, T. Okigaki, T. Takahashi, and M. Inagaki. 1999. Identification of a novel phosphorylation site on histone H3 coupled with mitotic chromosome condensation. *J Biol Chem*. 274:25543-9.

Grunstein, M. 1998. Yeast heterochromatin: regulation of its assembly and inheritance by histones. *Cell*. 93:325-8.

Gu, W., X.L. Shi, and R.G. Roeder. 1997. Synergistic activation of transcription by CBP and p53. *Nature*. 387:819-23.

Gunjan, A., D.B. Sittman, and D.T. Brown. 2001. Core histone acetylation is regulated by linker histone stoichiometry in vivo. *J Biol Chem*. 276:3635-40.

Gurley, L.R., R.A. Walters, and R.A. Tobey. 1973. Histone phosphorylation in late interphase and mitosis. *Biochem Biophys Res Commun*. 50:744-50.

Gurley, L.R., R.A. Walters, and R.A. Tobey. 1974. Cell cycle-specific changes in histone phosphorylation associated with cell proliferation and chromosome condensation. *J Cell Biol*. 60:356-64.

Gutierrez, R.M., and L.S. Hnilica. 1967. Tissue specificity of histone phosphorylation. *Science*. 157:1324-5.

Hake, S.B., A. Xiao, and C.D. Allis. 2004. Linking the epigenetic 'language' of covalent histone modifications to cancer. *Br J Cancer*. 90:761-9.

Hall, I.M., G.D. Shankaranarayana, K. Noma, N. Ayoub, A. Cohen, and S.I. Grewal. 2002. Establishment and maintenance of a heterochromatin domain. *Science*. 297:2232-7.

Hansen, J.C., C. Tse, and A.P. Wolffe. 1998. Structure and function of the core histone N-termini: more than meets the eye. *Biochemistry*. 37:17637-41.

Hayes, J.J., J. Bashkin, T.D. Tullius, and A.P. Wolffe. 1991a. The histone core exerts a dominant constraint on the structure of DNA in a nucleosome. *Biochemistry*. 30:8434-40.

Hayes, J.J., D.J. Clark, and A.P. Wolffe. 1991b. Histone contributions to the structure of DNA in the nucleosome. *Proc Natl Acad Sci U S A*. 88:6829-33.

Hayes, J.J., and A.P. Wolffe. 1993. Preferential and asymmetric interaction of linker histones with 5S DNA in the nucleosome. *Proc Natl Acad Sci U S A*. 90:6415-9.

Haynes, S.R., C. Dollard, F. Winston, S. Beck, J. Trowsdale, and I.B. Dawid. 1992. The bromodomain: a conserved sequence found in human, Drosophila and yeast proteins. *Nucleic Acids Res*. 20:2603.

Hebbes, T.R., and S.C. Allen. 2000. Multiple histone acetyltransferases are associated with a chicken erythrocyte chromatin fraction enriched in active genes. *J Biol Chem*. 275:31347-52.

Hebbes, T.R., A.W. Thorne, and C. Crane-Robinson. 1988. A direct link between core histone acetylation and transcriptionally active chromatin. *Embo J*. 7:1395-402.

Hendzel, M.J., Y. Wei, M.A. Mancini, A. Van Hooser, T. Ranalli, B.R. Brinkley, D.P. Bazett-Jones, and C.D. Allis. 1997. Mitosis-specific phosphorylation of histone H3 initiates primarily within pericentromeric heterochromatin during G2 and spreads in an ordered fashion coincident with mitotic chromosome condensation. *Chromosoma*. 106:348-60.

Henikoff, S., K. Ahmad, and H.S. Malik. 2001. The centromere paradox: stable inheritance with rapidly evolving DNA. *Science*. 293:1098-102.

Hewish, D.R., and L.A. Burgoyne. 1973. Chromatin sub-structure. The digestion of chromatin DNA at regularly spaced sites by a nuclear deoxyribonuclease. *Biochem Biophys Res Commun*. 52:504-10.

Hochstrasser, M. 1996. Ubiquitin-dependent protein degradation. *Annu Rev Genet*. 30:405-39.

Hong, L., G.P. Schroth, H.R. Matthews, P. Yau, and E.M. Bradbury. 1993. Studies of the DNA binding properties of histone H4 amino terminus. Thermal denaturation studies reveal that acetylation markedly reduces the binding constant of the H4 "tail" to DNA. *J Biol Chem*. 268:305-14.

Horn, P.J., and C.L. Peterson. 2002. Molecular biology. Chromatin higher order folding--wrapping up transcription. *Science*. 297:1824-7.

Hsu, J.Y., Z.W. Sun, X. Li, M. Reuben, K. Tatchell, D.K. Bishop, J.M. Grushcow, C.J. Brame, J.A. Caldwell, D.F. Hunt, R. Lin, M.M. Smith, and C.D. Allis. 2000. Mitotic phosphorylation of histone H3 is governed by Ipl1/aurora kinase and Glc7/PP1 phosphatase in budding yeast and nematodes. *Cell*. 102:279-91.

Hubbert, C., A. Guardiola, R. Shao, Y. Kawaguchi, A. Ito, A. Nixon, M. Yoshida, X.F. Wang, and T.P. Yao. 2002. HDAC6 is a microtubule-associated deacetylase. *Nature*. 417:455-8.

Hung, H.L., A.Y. Kim, W. Hong, C. Rakowski, and G.A. Blobel. 2001. Stimulation of NF-E2 DNA binding by CREB-binding protein (CBP)-mediated acetylation. *J Biol Chem*. 276:10715-21.

Hung, H.L., J. Lau, A.Y. Kim, M.J. Weiss, and G.A. Blobel. 1999. CREB-Binding protein acetylates hematopoietic transcription factor GATA-1 at functionally important sites. *Mol Cell Biol*. 19:3496-505.

Hurt, M.M., T.L. Bowman, and W.F. Marzluff. 1991. A common transcriptional activator is located in the coding region of two replication-dependent mouse histone genes. *Mol Cell Biol*. 11:2929-36.

Hurt, M.M., N.B. Pandey, and W.F. Marzluff. 1989. A region in the coding sequence is required for high-level expression of murine histone H3 gene. *Proc Natl Acad Sci U S A*. 86:4450-4.

Hymes, J., K. Fleischhauer, and B. Wolf. 1995. Biotinylation of histones by human serum biotinidase: assessment of biotinyl-transferase activity in sera from normal individuals and children with biotinidase deficiency. *Biochem Mol Med*. 56:76-83.

Im, H., C. Park, Q. Feng, K.D. Johnson, C.M. Kiekhaefer, K. Choi, Y. Zhang, and E.H. Bresnick. 2003. Dynamic regulation of histone H3 methylated at lysine 79 within a tissue-specific chromatin domain. *J Biol Chem*. 278:18346-52.

Imai, S., C.M. Armstrong, M. Kaeberlein, and L. Guarente. 2000. Transcriptional silencing and longevity protein Sir2 is an NAD-dependent histone deacetylase. *Nature*. 403:795-800.

Ivanova, A.V., M.J. Bonaduce, S.V. Ivanov, and A.J. Klar. 1998. The chromo and SET domains of the Clr4 protein are essential for silencing in fission yeast. *Nat Genet*. 19:192-5.

Jackson, V., and R. Chalkley. 1985. Histone synthesis and deposition in the G1 and S phases of hepatoma tissue culture cells. *Biochemistry*. 24:6921-30.

Jackson, V., D. Granner, and R. Chalkley. 1976a. Deposition of histone onto the replicating chromosome: newly synthesized histone is not found near the replication fork. *Proc Natl Acad Sci U S A*. 73:2266-9.

Jackson, V., A. Shires, N. Tanphaichitr, and R. Chalkley. 1976b. Modifications to histones immediately after synthesis. *J Mol Biol*. 104:471-83.

Jacobs, S.A., and S. Khorasanizadeh. 2002. Structure of HP1 chromodomain bound to a lysine 9-methylated histone H3 tail. *Science*. 295:2080-3.

Jeanmougin, F., J.M. Wurtz, B. Le Douarin, P. Chambon, and R. Losson. 1997. The bromodomain revisited. *Trends Biochem Sci*. 22:151-3.

Jenuwein, T., and C.D. Allis. 2001. Translating the histone code. *Science*. 293:1074-80.

Juan, L.J., W.J. Shia, M.H. Chen, W.M. Yang, E. Seto, Y.S. Lin, and C.W. Wu. 2000. Histone deacetylases specifically down-regulate p53-dependent gene activation. *J Biol Chem*. 275:20436-43.

Kaludov, N.K., T.L. Bowman, E.M. Sikorski, and M.M. Hurt. 1996. Cell cycle-regulated binding of nuclear proteins to elements within a mouse H3.2 histone gene. *Proc Natl Acad Sci U S A*. 93:4465-70.

Kaszas, E., and W.Z. Cande. 2000. Phosphorylation of histone H3 is correlated with changes in the maintenance of sister chromatid cohesion during meiosis in maize, rather than the condensation of the chromatin. *J Cell Sci*. 113 (Pt 18):3217-26.

Kiernan, R.E., C. Vanhulle, L. Schiltz, E. Adam, H. Xiao, F. Maudoux, C. Calomme, A. Burny, Y. Nakatani, K.T. Jeang, M. Benkirane, and C. Van Lint. 1999. HIV-1 tat transcriptional activity is regulated by acetylation. *Embo J*. 18:6106-18.

Kireeva, N., M. Lakonishok, I. Kireev, T. Hirano, and A.S. Belmont. 2004. Visualization of early chromosome condensation: a hierarchical folding, axial glue model of chromosome structure. *J Cell Biol*. 166:775-85.

Kornberg, R.D. 1974. Chromatin structure: a repeating unit of histones and DNA. *Science*. 184:868-71.

Kornberg, R.D., and J.O. Thomas. 1974. Chromatin structure; oligomers of the histones. *Science*. 184:865-8.

Kruhlak, M.J., M.J. Hendzel, W. Fischle, N.R. Bertos, S. Hameed, X.J. Yang, E. Verdin, and D.P. Bazett-Jones. 2001. Regulation of global acetylation in mitosis through loss of histone acetyltransferases and deacetylases from chromatin. *J Biol Chem*. 276:38307-19.

Krupitza, G., and P. Cerutti. 1989. Poly(ADP-ribosylation) of histones in intact human keratinocytes. *Biochemistry*. 28:4054-60.

Kwon, T., J.H. Chang, E. Kwak, C.W. Lee, A. Joachimiak, Y.C. Kim, J. Lee, and Y. Cho. 2003. Mechanism of histone lysine methyl transfer revealed by the structure of SET7/9-AdoMet. *Embo J*. 22:292-303.

Lachner, M., D. O'Carroll, S. Rea, K. Mechtler, and T. Jenuwein. 2001. Methylation of histone H3 lysine 9 creates a binding site for HP1 proteins. *Nature*. 410:116-20.

Lachner, M., R.J. O'Sullivan, and T. Jenuwein. 2003. An epigenetic road map for histone lysine methylation. *J Cell Sci*. 116:2117-24.

Langan, T.A. 1968. Histone phosphorylation: stimulation by adenosine 3',5'-monophosphate. *Science*. 162:579-80.

Lenfant, F., R.K. Mann, B. Thomsen, X. Ling, and M. Grunstein. 1996. All four core histone N-termini contain sequences required for the repression of basal transcription in yeast. *Embo J.* 15:3974-85.

Lennard, A.C., and J.O. Thomas. 1985. The arrangement of H5 molecules in extended and condensed chicken erythrocyte chromatin. *Embo J.* 4:3455-62.

Leuba, S.H., G. Yang, C. Robert, B. Samori, K. van Holde, J. Zlatanova, and C. Bustamante. 1994. Three-dimensional structure of extended chromatin fibers as revealed by tapping-mode scanning force microscopy. *Proc Natl Acad Sci U S A.* 91:11621-5.

Levinger, L., and A. Varshavsky. 1982. Selective arrangement of ubiquitinated and D1 protein-containing nucleosomes within the Drosophila genome. *Cell.* 28:375-85.

Li, Q., M. Herrler, N. Landsberger, N. Kaludov, V.V. Ogryzko, Y. Nakatani, and A.P. Wolffe. 1998. Xenopus NF-Y pre-sets chromatin to potentiate p300 and acetylation-responsive transcription from the Xenopus hsp70 promoter in vivo. *Embo J.* 17:6300-15.

Libertini, L.J., J. Ausio, K.E. van Holde, and E.W. Small. 1988. Histone hyperacetylation. Its effects on nucleosome core particle transitions. *Biophys J.* 53:477-87.

Liu, X., B. Li, and GorovskyMa. 1996. Essential and nonessential histone H2A variants in Tetrahymena thermophila. *Mol Cell Biol.* 16:4305-11.

Lo, W.S., R.C. Trievel, J.R. Rojas, L. Duggan, J.Y. Hsu, C.D. Allis, R. Marmorstein, and S.L. Berger. 2000. Phosphorylation of serine 10 in histone H3 is functionally linked in vitro and in vivo to Gcn5-mediated acetylation at lysine 14. *Mol Cell.* 5:917-26.

Loidl, P. 2004. A plant dialect of the histone language. *Trends Plant Sci.* 9:84-90.

Lomvardas, S., and D. Thanos. 2002. Modifying gene expression programs by altering core promoter chromatin architecture. *Cell.* 110:261-71.

Lorimer, W.S., 3rd, P.R. Stone, and W.R. Kidwell. 1977. Control of histone H1 dimer-poly(ADP-ribose) complex formation by poly(ADP-ribose) glycohydrolase. *Exp Cell Res.* 106:261-6.

Luger, K., A.W. Mader, R.K. Richmond, D.F. Sargent, and T.J. Richmond. 1997. Crystal structure of the nucleosome core particle at 2.8 A resolution. *Nature.* 389:251-60.

Madigan, J.P., H.L. Chotkowski, and R.L. Glaser. 2002. DNA double-strand break-induced phosphorylation of Drosophila histone variant H2Av helps prevent radiation-induced apoptosis. *Nucleic Acids Res*. 30:3698-705.

Madisen, L., A. Krumm, T.R. Hebbes, and M. Groudine. 1998. The immunoglobulin heavy chain locus control region increases histone acetylation along linked c-myc genes. *Mol Cell Biol*. 18:6281-92.

Mahadevan, L.C., A.C. Willis, and M.J. Barratt. 1991. Rapid histone H3 phosphorylation in response to growth factors, phorbol esters, okadaic acid, and protein synthesis inhibitors. *Cell*. 65:775-83.

Mahajan, R., C. Delphin, T. Guan, L. Gerace, and F. Melchior. 1997. A small ubiquitin-related polypeptide involved in targeting RanGAP1 to nuclear pore complex protein RanBP2. *Cell*. 88:97-107.

Mahajan, R., L. Gerace, and F. Melchior. 1998. Molecular characterization of the SUMO-1 modification of RanGAP1 and its role in nuclear envelope association. *J Cell Biol*. 140:259-70.

Malik, H.S., and S. Henikoff. 2003. Phylogenomics of the nucleosome. *Nat Struct Biol*. 10:882-91.

Marmorstein, R. 2003. Structure of SET domain proteins: a new twist on histone methylation. *Trends Biochem Sci*. 28:59-62.

Marmorstein, R. 2004. Structural and chemical basis of histone acetylation. *Novartis Found Symp*. 259:78-98; discussion 98-101, 163-9.

Marmorstein, R., and S.Y. Roth. 2001. Histone acetyltransferases: function, structure, and catalysis. *Curr Opin Genet Dev*. 11:155-61.

Martinez-Balbas, M.A., U.M. Bauer, S.J. Nielsen, A. Brehm, and T. Kouzarides. 2000. Regulation of E2F1 activity by acetylation. *Embo J*. 19:662-71.

Marzluff, W.F., P. Gongidi, K.R. Woods, J. Jin, and L.J. Maltais. 2002. The human and mouse replication-dependent histone genes. *Genomics*. 80:487-98.

Mateescu, B., P. England, F. Halgand, M. Yaniv, and C. Muchardt. 2004. Tethering of HP1 proteins to chromatin is relieved by phosphoacetylation of histone H3. *EMBO Rep*. 5:490-6.

Matunis, M.J., E. Coutavas, and G. Blobel. 1996. A novel ubiquitin-like modification modulates the partitioning of the Ran-GTPase-activating protein RanGAP1 between the cytosol and the nuclear pore complex. *J Cell Biol*. 135:1457-70.

Matunis, M.J., J. Wu, and G. Blobel. 1998. SUMO-1 modification and its role in targeting the Ran GTPase-activating protein, RanGAP1, to the nuclear pore complex. *J Cell Biol*. 140:499-509.

Melchior, F. 2000. SUMO--nonclassical ubiquitin. *Annu Rev Cell Dev Biol*. 16:591-626.

Messmer, S., A. Franke, and R. Paro. 1992. Analysis of the functional role of the Polycomb chromo domain in Drosophila melanogaster. *Genes Dev*. 6:1241-54.

Muller, S., C. Hoege, G. Pyrowolakis, and S. Jentsch. 2001. SUMO, ubiquitin's mysterious cousin. *Nat Rev Mol Cell Biol*. 2:202-10.

Muller, S., M.J. Matunis, and A. Dejean. 1998. Conjugation with the ubiquitin-related modifier SUMO-1 regulates the partitioning of PML within the nucleus. *Embo J*. 17:61-70.

Munshi, N., M. Merika, J. Yie, K. Senger, G. Chen, and D. Thanos. 1998. Acetylation of HMG I(Y) by CBP turns off IFN beta expression by disrupting the enhanceosome. *Mol Cell*. 2:457-67.

Murnion, M.E., R.R. Adams, D.M. Callister, C.D. Allis, W.C. Earnshaw, and J.R. Swedlow. 2001. Chromatin-associated protein phosphatase 1 regulates aurora-B and histone H3 phosphorylation. *J Biol Chem*. 276:26656-65.

Murray, K. 1964. The Occurrence of Epsilon-N-Methyl Lysine in Histones. *Biochemistry*. 127:10-5.

Narang, M.A., R. Dumas, L.M. Ayer, and R.A. Gravel. 2004. Reduced histone biotinylation in multiple carboxylase deficiency patients: a nuclear role for holocarboxylase synthetase. *Hum Mol Genet*. 13:15-23.

Nazarov, I.B., A.N. Smirnova, R.I. Krutilina, M.P. Svetlova, L.V. Solovjeva, A.A. Nikiforov, S.L. Oei, I.A. Zalenskaya, P.M. Yau, E.M. Bradbury, and N.V. Tomilin. 2003. Dephosphorylation of histone gamma-H2AX during repair of DNA double-strand breaks in mammalian cells and its inhibition by calyculin A. *Radiat Res*. 160:309-17.

Ng, H.H., D.N. Ciccone, K.B. Morshead, M.A. Oettinger, and K. Struhl. 2003. Lysine-79 of histone H3 is hypomethylated at silenced loci in yeast and mammalian cells: a potential mechanism for position-effect variegation. *Proc Natl Acad Sci U S A*. 100:1820-5.

Ng, H.H., Q. Feng, H. Wang, H. Erdjument-Bromage, P. Tempst, Y. Zhang, and K. Struhl. 2002a. Lysine methylation within the globular domain of histone H3 by Dot1 is important for telomeric silencing and Sir protein association. *Genes Dev*. 16:1518-27.

Ng, H.H., R.M. Xu, Y. Zhang, and K. Struhl. 2002b. Ubiquitination of histone H2B by Rad6 is required for efficient Dot1-mediated methylation of histone H3 lysine 79. *J Biol Chem*. 277:34655-7.

Nickel, B.E., C.D. Allis, and J.R. Davie. 1989. Ubiquitinated histone H2B is preferentially located in transcriptionally active chromatin. *Biochemistry*. 28:958-63.

Nielsen, P.R., D. Nietlispach, H.R. Mott, J. Callaghan, A. Bannister, T. Kouzarides, A.G. Murzin, N.V. Murzina, and E.D. Laue. 2002. Structure of the HP1 chromodomain bound to histone H3 methylated at lysine 9. *Nature*. 416:103-7.

Nishioka, K., J.C. Rice, K. Sarma, H. Erdjument-Bromage, J. Werner, Y. Wang, S. Chuikov, P. Valenzuela, P. Tempst, R. Steward, J.T. Lis, C.D. Allis, and D. Reinberg. 2002. PR-Set7 is a nucleosome-specific methyltransferase that modifies lysine 20 of histone H4 and is associated with silent chromatin. *Mol Cell*. 9:1201-13.

Nishizuka, Y., K. Ueda, T. Honjo, and O. Hayaishi. 1968. Enzymic adenosine diphosphate ribosylation of histone and poly adenosine diphosphate ribose synthesis in rat liver nuclei. *J Biol Chem*. 243:3765-7.

Noll, M. 1974. Subunit structure of chromatin. *Nature*. 251:249-51.

Noma, K., C.D. Allis, and S.I. Grewal. 2001. Transitions in distinct histone H3 methylation patterns at the heterochromatin domain boundaries. *Science*. 293:1150-5.

Ogryzko, V.V., R.L. Schiltz, V. Russanova, B.H. Howard, and Y. Nakatani. 1996. The transcriptional coactivators p300 and CBP are histone acetyltransferases. *Cell*. 87:953-9.

Olins, A.L., and D.E. Olins. 1974. Spheroid chromatin units (v bodies). *Science*. 183:330-2.

Ota, K., M. Kameoka, Y. Tanaka, A. Itaya, and K. Yoshihara. 2003. Expression of histone acetyltransferases was down-regulated in poly(ADP-ribose) polymerase-1-deficient murine cells. *Biochem Biophys Res Commun*. 310:312-7.

Ott, M., M. Schnolzer, J. Garnica, W. Fischle, S. Emiliani, H.R. Rackwitz, and E. Verdin. 1999. Acetylation of the HIV-1 Tat protein by p300 is important for its transcriptional activity. *Curr Biol*. 9:1489-92.

Palmer, D.K., K. O'Day, H.L. Trong, H. Charbonneau, and R.L. Margolis. 1991. Purification of the centromere-specific protein CENP-A and demonstration that it is a distinctive histone. *Proc Natl Acad Sci U S A*. 88:3734-8.

Palmer, D.K., K. O'Day, M.H. Wener, B.S. Andrews, and R.L. Margolis. 1987. A 17-kD centromere protein (CENP-A) copurifies with nucleosome core particles and with histones. *J Cell Biol*. 104:805-15.

Paulson, J.R., and S.S. Taylor. 1982. Phosphorylation of histones 1 and 3 and nonhistone high mobility group 14 by an endogenous kinase in HeLa metaphase chromosomes. *J Biol Chem*. 257:6064-72.

Pearce, J.J., P.B. Singh, and S.J. Gaunt. 1992. The mouse has a Polycomb-like chromobox gene. *Development*. 114:921-9.

Peters, D.M., J.B. Griffin, J.S. Stanley, M.M. Beck, and J. Zempleni. 2002. Exposure to UV light causes increased biotinylation of histones in Jurkat cells. *Am J Physiol Cell Physiol*. 283:C878-84.

Petersen, J., J. Paris, M. Willer, M. Philippe, and I.M. Hagan. 2001. The S. pombe aurora-related kinase Ark1 associates with mitotic structures in a stage dependent manner and is required for chromosome segregation. *J Cell Sci*. 114:4371-84.

Pham, A.D., and F. Sauer. 2000. Ubiquitin-activating/conjugating activity of TAFII250, a mediator of activation of gene expression in Drosophila. *Science*. 289:2357-60.

Phillips, D.M. 1963. The presence of acetyl groups of histones. *Biochem J*. 87:258-63.

Pickart, C.M. 2001. Mechanisms underlying ubiquitination. *Annu Rev Biochem*. 70:503-33.

Pilch, D.R., O.A. Sedelnikova, C. Redon, A. Celeste, A. Nussenzweig, and W.M. Bonner. 2003. Characteristics of gamma-H2AX foci at DNA double-strand breaks sites. *Biochem Cell Biol*. 81:123-9.

Poirier, G.G., G. de Murcia, J. Jongstra-Bilen, C. Niedergang, and P. Mandel. 1982. Poly(ADP-ribosyl)ation of polynucleosomes causes relaxation of chromatin structure. *Proc Natl Acad Sci U S A*. 79:3423-7.

Polesskaya, A., A. Duquet, I. Naguibneva, C. Weise, A. Vervisch, E. Bengal, F. Hucho, P. Robin, and A. Harel-Bellan. 2000. CREB-binding protein/p300 activates MyoD by acetylation. *J Biol Chem*. 275:34359-64.

Polioudaki, H., Y. Markaki, N. Kourmouli, G. Dialynas, P.A. Theodoropoulos, P.B. Singh, and S.D. Georgatos. 2004. Mitotic phosphorylation of histone H3 at threonine 3. *FEBS Lett*. 560:39-44.

Preuss, U., G. Landsberg, and K.H. Scheidtmann. 2003. Novel mitosis-specific phosphorylation of histone H3 at Thr11 mediated by Dlk/ZIP kinase. *Nucleic Acids Res*. 31:878-85.

Rangasamy, D., I. Greaves, and D.J. Tremethick. 2004. RNA interference demonstrates a novel role for H2A.Z in chromosome segregation. *Nat Struct Mol Biol*. 11:650-5.

Rattner, J.B. 1992. Integrating chromosome structure with function. *Chromosoma*. 101:259-64.

Rattner, J.B. and C.C. Lin. The higher order structure of the centromere. *Genome*. 29:588-93.

Rea, S., F. Eisenhaber, D. O'Carroll, B.D. Strahl, Z.W. Sun, M. Schmid, S. Opravil, K. Mechtler, C.P. Ponting, C.D. Allis, and T. Jenuwein. 2000. Regulation of chromatin structure by site-specific histone H3 methyltransferases. *Nature*. 406:593-9.

Realini, C.A., and F.R. Althaus. 1992. Histone shuttling by poly(ADP-ribosylation). *J Biol Chem*. 267:18858-65.

Redon, C., D. Pilch, E. Rogakou, O. Sedelnikova, K. Newrock, and W. Bonner. 2002. Histone H2A variants H2AX and H2AZ. *Curr Opin Genet Dev*. 12:162-9.

Reuter, G., and P. Spierer. 1992. Position effect variegation and chromatin proteins. *Bioessays*. 14:605-12.

Rice, J.C., and C.D. Allis. 2001. Code of silence. *Nature*. 414:258-61.

Rodriguez, M.S., J.M. Desterro, S. Lain, C.A. Midgley, D.P. Lane, and R.T. Hay. 1999. SUMO-1 modification activates the transcriptional response of p53. *Embo J*. 18:6455-61.

Rogakou, E.P., D.R. Pilch, A.H. Orr, V.S. Ivanova, and W.M. Bonner. 1998. DNA double-stranded breaks induce histone H2AX phosphorylation on serine 139. *J Biol Chem*. 273:5858-68.

Roth, S.Y., J.M. Denu, and C.D. Allis. 2001. Histone acetyltransferases. *Annu Rev Biochem*. 70:81-120.

Ruiz-Carrillo, A., L.J. Wangh, and V.G. Allfrey. 1975. Processing of newly synthesized histone molecules. *Science*. 190:117-28.

Russanova, V., E. Stephanova, I. Pashev, and R. Tsanev. 1989. Histone variants in mouse centromeric chromatin. *Mol Cell Biochem*. 90:1-7.

Santisteban, M.S., T. Kalashnikova, and M.M. Smith. 2000. Histone H2A.Z regulats transcription and is partially redundant with nucleosome remodeling complexes. *Cell*. 103:411-22.

Santos-Rosa, H., R. Schneider, A.J. Bannister, J. Sherriff, B.E. Bernstein, N.C. Emre, S.L. Schreiber, J. Mellor, and T. Kouzarides. 2002. Active genes are tri-methylated at K4 of histone H3. *Nature*. 419:407-11.

Saunders, W.S., C. Chue, M. Goebl, C. Craig, R.F. Clark, J.A. Powers, J.C. Eissenberg, S.C. Elgin, N.F. Rothfield, and W.C. Earnshaw. 1993. Molecular cloning of a human homologue of Drosophila heterochromatin protein HP1 using anti-centromere autoantibodies with anti-chromo specificity. *J Cell Sci*. 104 (Pt 2):573-82.

Schaft, D., A. Roguev, K.M. Kotovic, A. Shevchenko, M. Sarov, K.M. Neugebauer, and A.F. Stewart. 2003. The histone 3 lysine 36 methyltransferase, SET2, is involved in transcriptional elongation. *Nucleic Acids Res*. 31:2475-82.

Schiltz, R.L., C.A. Mizzen, A. Vassilev, R.G. Cook, C.D. Allis, and Y. Nakatani. 1999. Overlapping but distinct patterns of histone acetylation by the human coactivators p300 and PCAF within nucleosomal substrates. *J Biol Chem*. 274:1189-92.

Schotta, G., A. Ebert, V. Krauss, A. Fischer, J. Hoffmann, S. Rea, T. Jenuwein, R. Dorn, and G. Reuter. 2002. Central role of Drosophila SU(VAR)3-9 in histone H3-K9 methylation and heterochromatic gene silencing. *Embo J*. 21:1121-31.

Schotta, G., M. Lachner, A.H. Peters, and T. Jenuwein. 2004a. The indexing potential of histone lysine methylation. *Novartis Found Symp*. 259:22-37; discussion 37-47, 163-9.

Schotta, G., M. Lachner, K. Sarma, A. Ebert, R. Sengupta, G. Reuter, D. Reinberg, and T. Jenuwein. 2004b. A silencing pathway to induce H3-K9 and H4-K20 trimethylation at constitutive heterochromatin. *Genes Dev*. 18:1251-62.

Schreiber, S.L., and B.E. Bernstein. 2002. Signaling network model of chromatin. *Cell*. 111:771-8.

Schumperli, D. 1986. Cell-cycle regulation of histone gene expression. *Cell*. 45:471-2.

Schwarz, P.M., and J.C. Hansen. 1994. Formation and stability of higher order chromatin structures. Contributions of the histone octamer. *J Biol Chem*. 269:16284-9.

Sealy, L., and R. Chalkley. 1978a. DNA associated with hyperacetylated histone is preferentially digested by DNase I. *Nucleic Acids Res*. 5:1863-76.

Sealy, L., and R. Chalkley. 1978b. The effect of sodium butyrate on histone modification. *Cell*. 14:115-21.

Seeler, J.S., and A. Dejean. 2003. Nuclear and unclear functions of SUMO. *Nat Rev Mol Cell Biol*. 4:690-9.

Seigneurin-Berny, D., A. Verdel, S. Curtet, C. Lemercier, J. Garin, S. Rousseaux, and S. Khochbin. 2001. Identification of components of the murine histone deacetylase 6 complex: link between acetylation and ubiquitination signaling pathways. *Mol Cell Biol*. 21:8035-44.

Shiio, Y., and R.N. Eisenman. 2003. Histone sumoylation is associated with transcriptional repression. *Proc Natl Acad Sci U S A*. 100:13225-30.

Singh, P.B., J.R. Miller, J. Pearce, R. Kothary, R.D. Burton, R. Paro, T.C. James, and S.J. Gaunt. 1991. A sequence motif found in a Drosophila heterochromatin protein is conserved in animals and plants. *Nucleic Acids Res*. 19:789-94.

Smith, J.S., C.B. Brachmann, I. Celic, M.A. Kenna, S. Muhammad, V.J. Starai, J.L. Avalos, J.C. Escalante-Semerena, C. Grubmeyer, C. Wolberger, and J.D. Boeke. 2000. A phylogenetically conserved NAD+-dependent protein deacetylase activity in the Sir2 protein family. *Proc Natl Acad Sci U S A*. 97:6658-63.

Sobel, R.E., R.G. Cook, and C.D. Allis. 1994. Non-random acetylation of histone H4 by a cytoplasmic histone acetyltransferase as determined by novel methodology. *J Biol Chem*. 269:18576-82.

Soloaga, A., S. Thomson, G.R. Wiggin, N. Rampersaud, M.H. Dyson, C.A. Hazzalin, L.C. Mahadevan, and J.S. Arthur. 2003. MSK2 and MSK1 mediate the mitogen- and stress-induced phosphorylation of histone H3 and HMG-14. *Embo J*. 22:2788-97.

Sperling, R., and L.A. Amos. 1977. Arrangement of subunits in assembled histone H4 fibers. *Proc Natl Acad Sci U S A*. 74:3772-6.

Stanley, J.S., J.B. Griffin, and J. Zempleni. 2001. Biotinylation of histones in human cells. Effects of cell proliferation. *Eur J Biochem*. 268:5424-9.

Stone, P.R., W.S. Lorimer, 3rd, and W.R. Kidwell. 1977. Properties of the complex between histone H1 and poly(ADP-ribose synthesised in HeLa cell nuclei. *Eur J Biochem*. 81:9-18.

Strahl, B.D., and C.D. Allis. 2000. The language of covalent histone modifications. *Nature*. 403:41-5.

Strukov, Y.G., Y. Wang, and A.S. Belmont. 2003. Engineered chromosome regions with altered sequence composition demonstrate hierarchical large-scale folding within metaphase chromosomes. *J Cell Biol*. 162:23-35.

Sullivan, S., D.W. Sink, K.L. Trout, I. Makalowska, P.M. Taylor, A.D. Baxevanis, and D. Landsman. 2002. The Histone Database. *Nucleic Acids Res*. 30:341-2.

Sun, Z.W., and C.D. Allis. 2002. Ubiquitination of histone H2B regulates H3 methylation and gene silencing in yeast. *Nature*. 418:104-8.

Tamaru, H., X. Zhang, D. McMillen, P.B. Singh, J. Nakayama, S.I. Grewal, C.D. Allis, X. Cheng, and E.U. Selker. 2003. Trimethylated lysine 9 of histone H3 is a mark for DNA methylation in Neurospora crassa. *Nat Genet*. 34:75-9.

Thoma, F., T. Koller, and A. Klug. 1979. Involvement of histone H1 in the organization of the nucleosome and of the salt-dependent superstructures of chromatin. *J Cell Biol*. 83:403-27.

Thomas, J.O., C. Rees, and J.T. Finch. 1992. Cooperative binding of the globular domains of histones H1 and H5 to DNA. *Nucleic Acids Res*. 20:187-94.

Thomson, S., L.C. Mahadevan, and A.L. Clayton. 1999. MAP kinase-mediated signalling to nucleosomes and immediate-early gene induction. *Sem Cell Dev Biol*. 10:205-14.

Thorne, A.W., D. Kmiciek, K. Mitchelson, P. Sautiere, and C. Crane-Robinson. 1990. Patterns of histone acetylation. *Eur J Biochem*. 193:701-13.

Trieschmann, L., B. Martin, and M. Bustin. 1998. The chromatin unfolding domain of chromosomal protein HMG-14 targets the N-terminal tail of histone H3 in nucleosomes. *Proc Natl Acad Sci U S A*. 95:5468-73.

Tschiersch, B., A. Hofmann, V. Krauss, R. Dorn, G. Korge, and G. Reuter. 1994. The protein encoded by the Drosophila position-effect variegation suppressor gene Su(var)3-9 combines domains of antagonistic regulators of homeotic gene complexes. *Embo J*. 13:3822-31.

Tse, C., T. Sera, A.P. Wolffe, and J.C. Hansen. 1998. Disruption of higher-order folding by core histone acetylation dramatically enhances transcription of nucleosomal arrays by RNA polymerase III. *Mol Cell Biol*. 18:4629-38.

Tumbar, T., G. Sudlow, and A.S. Belmont. 1999. Large-scale chromatin unfolding and remodeling induced by VP16 acidic activation domain. *J Cell Biol*. 145:1341-54.

Turner, B.M. 2000. Histone acetylation and an epigenetic code. *Bioessays*. 22:836-45.

Turner, B.M. 2002a. Cellular memory and the histone code. *Cell*. 111:285-91.

Turner, B.M. 2002b. Chromatin and gene regulation: Molecular mechanisms in epigenetics. Blackwell Science Inc., Malden. 288 pp.

Turner, B.M., L. Franchi, and H. Wallace. 1990. Islands of acetylated histone H4 in polytene chromosomes and their relationship to chromatin packaging and transcriptional activity. *J Cell Sci.* 96 (Pt 2):335-46.

Ueda, K., Y. Kinoshita, Z.J. Xu, N. Ide, M. Ono, Y. Akahori, I. Tanaka, and M. Inoue. 2000. Unusual core histones specifically expressed in male gametic cells of Lilium longiflorum. *Chromosoma.* 108:491-500.

van Daal, A., and S.C. Elgin. 1992. A histone variant, H2AvD, is essential in Drosophila melanogaster. *Mol Biol Cell.* 3:593-602.

van Holde, K., and J. Zlatanova. 1996. What determines the folding of the chromatin fiber? *Proc Natl Acad Sci U S A.* 93:10548-55.

van Leeuwen, F., P.R. Gafken, and D.E. Gottschling. 2002. Dot1p modulates silencing in yeast by methylation of the nucleosome core. *Cell.* 109:745-56.

van Wijnen, A.J., F. Aziz, X. Grana, A. De Luca, R.K. Desai, K. Jaarsveld, T.J. Last, K. Soprano, A. Giordano, and J.B. Lian. 1994. Transcription of histone H4, H3, and H1 cell cycle genes: promoter factor HiNF-D contains CDC2, cyclin A, and an RB-related protein. *Proc Natl Acad Sci U S A.* 91:12882-6.

Vaquero, A., A. Loyola, and D. Reinberg. 2003. The constantly changing face of chromatin. *Sci Aging Knowledge Environ.* 2003:RE4.

Verger, A., J. Perdomo, and M. Crossley. 2003. Modification with SUMO. A role in transcriptional regulation. *EMBO Rep.* 4:137-42.

Vernet, G., M. Sala-Rovira, M. Maeder, F. Jacques, and M. Herzog. 1990. Basic nuclear proteins of the histone-less eukaryote Crypthecodinium cohnii (Pyrrhophyta): two-dimensional electrophoresis and DNA-binding properties. *Biochim Biophys Acta.* 1048:281-9.

Vidali, G., L.C. Boffa, E.M. Bradbury, and V.G. Allfrey. 1978. Butyrate suppression of histone deacetylation leads to accumulation of multiacetylated forms of histones H3 and H4 and increased DNase I sensitivity of the associated DNA sequences. *Proc Natl Acad Sci U S A.* 75:2239-43.

Waltzer, L., and M. Bienz. 1998. Drosophila CBP represses the transcription factor TCF to antagonize Wingless signalling. *Nature.* 395:521-5.

Wang, X., S.C. Moore, M. Laszckzak, and J. Ausio. 2000. Acetylation increases the alpha-helical content of the histone tails of the nucleosome. *J Biol Chem*. 275:35013-20.

Wang, Y., W. Fischle, W. Cheung, S. Jacobs, S. Khorasanizadeh, and C.D. Allis. 2004a. Beyond the double helix: writing and reading the histone code. *Novartis Found Symp*. 259:3-17; discussion 17-21, 163-9.

Wang, Y., J. Wysocka, J. Sayegh, Y.H. Lee, J.R. Perlin, L. Leonelli, L.S. Sonbuchner, C.H. McDonald, R.G. Cook, Y. Dou, R.G. Roeder, S. Clarke, M.R. Stallcup, C.D. Allis, and S.A. Coonrod. 2004b. Human PAD4 regulates histone arginine methylation levels via demethylimination. *Science*. 306:279-83.

Wei, Y., L. Yu, J. Bowen, M.A. Gorovsky, and C.D. Allis. 1999. Phosphorylation of histone H3 is required for proper chromosome condensation and segregation. *Cell*. 97:99-109.

West, M.H., and W.M. Bonner. 1980. Histone 2B can be modified by the attachment of ubiquitin. *Nucleic Acids Res*. 8:4671-80.

Wilkinson, K.D. 2000. Ubiquitination and deubiquitination: targeting of proteins for degradation by the proteasome. *Semin Cell Dev Biol*. 11:141-8.

Williams, S.P., B.D. Athey, L.J. Muglia, R.S. Schappe, A.H. Gough, and J.P. Langmore. 1986. Chromatin fibers are left-handed double helices with diameter and mass per unit length that depend on linker length. *Biophys J*. 49:233-48.

Williamson, R. 1970. Properties of rapidly labelled deoxyribonucleic acid fragments isolated from the cytoplasm of primary cultures of embryonic mouse liver cells. *J Mol Biol*. 51:157-68.

Wolffe, A.P. 1998. Chromatin: Structure and Function. Academic Press Inc., San Diego. 447 pp.

Wolffe, A.P., and J.J. Hayes. 1999. Chromatin disruption and modification. *Nucleic Acids Res*. 27:711-20.

Wong, M., Y. Kanai, M. Miwa, M. Bustin, and M. Smulson. 1983. Immunological evidence for the in vivo occurrence of a crosslinked complex of poly(ADP-ribosylated) histone H1. *Proc Natl Acad Sci U S A*. 80:205-9.

Woodcock, C.L., L.L. Frado, and J.B. Rattner. 1984 The higher-order structure of chromatin: evidence for a helical ribbon arrangement. *J Cell Biol*. 99:42-52.

Woodcock, C.L., S.A. Grigoryev, R.A. Horowitz, and N. Whitaker. 1993. A chromatin folding model that incorporates linker variability generates fibers resembling the native structures. *Proc Natl Acad Sci U S A*. 90:9021-5.

Woodcock, C.L., J.P. Safer, and J.E. Stanchfield. 1976a. Structural repeating units in chromatin. I. Evidence for their general occurrence. *Exp Cell Res*. 97:101-10.

Woodcock, C.L., H.E. Sweetman, and L.L. Frado. 1976b. Structural repeating units in chromatin. II. Their isolation and partial characterization. *Exp Cell Res*. 97:111-9.

Wu, R.S., K.W. Kohn, and W.M. Bonner. 1981. Metabolism of ubiquitinated histones. *J Biol Chem*. 256:5916-20.

Wu, R.S., S. Tsai, and W.M. Bonner. 1982. Patterns of histone variant synthesis can distinguish G0 from G1 cells. *Cell*. 31:367-74.

Xiao, B., C. Jing, J.R. Wilson, P.A. Walker, N. Vasisht, G. Kelly, S. Howell, I.A. Taylor, G.M. Blackburn, and S.J. Gamblin. 2003. Structure and catalytic mechanism of the human histone methyltransferase SET7/9. *Nature*. 421:652-6.

Yao, J., P.T. Lowary, and J. Widom. 1990. Direct detection of linker DNA bending in defined-length oligomers of chromatin. *Proc Natl Acad Sci U S A*. 87:7603-7.

Yao, J., P.T. Lowary, and J. Widom. 1991. Linker DNA bending induced by the core histones of chromatin. *Biochemistry*. 30:8408-14.

Zhang, Q., H. Yao, N. Vo, and R.H. Goodman. 2000. Acetylation of adenovirus E1A regulates binding of the corepressor CtBP. *Proc Natl Acad Sci U S A*. 97:14323-8.

Zhang, W., and J.J. Bieker. 1998. Acetylation and modulation of erythroid Kruppel-like factor (EKLF) activity by interaction with histone acetyltransferases. *Proc Natl Acad Sci U S A*. 95:9855-60.

Zhang, X., H. Tamaru, S.I. Khan, J.R. Horton, L.J. Keefe, E.U. Selker, and X. Cheng. 2002. Structure of the Neurospora SET domain protein DIM-5, a histone H3 lysine methyltransferase. *Cell*. 111:117-27.

Zhang, X., Z. Yang, S.I. Khan, J.R. Horton, H. Tamaru, E.U. Selker, and X. Cheng. 2003. Structural basis for the product specificity of histone lysine methyltransferases. *Mol Cell*. 12:177-85.

Zhang, Y. 2003. Transcriptional regulation by histone ubiquitination and deubiquitination. *Genes Dev*. 17:2733-40.

Zlatanova, J., S.H. Leuba, and K. van Holde. 1998. Chromatin fiber structure: morphology, molecular determinants, structural transitions. *Biophys J*. 74:2554-66.

CHAPTER 2

Materials and Methods

2.1 REAGENTS

For reference purposes, Appendix A contains a list of solutions used throughout these investigations. All chemicals utilized were of molecular biology grade and were purchased from Gibco, Fisher Scientific, Bio-Rad, BDH, Sigma-Aldrich and Roche.

2.2 CELL LINES AND TISSUE CULTURE

The cell lines employed throughout these studies are listed in Table 2.1. All cellular work was performed in a sterile biological safety cabinet (Nuaire). All cells were maintained at subconfluent levels in a 37°C humidified incubator (Napco) containing 5% CO_2. Cells were passaged as required to maintain subconfluent levels. Briefly, medium was removed by aspiration and cells were washed once with sterile phosphate buffered saline (PBS – Appendix A). Following aspiration of the PBS, an appropriate volume of trypsin (0.05% containing 0.53 mM EDTA [Gibco]) was applied to the adherent cells (e.g. 1 mL for a T25 flask, 2 mL for a 10 cm culture dish, and 3 mL for a 15 cm culture dish). To promote detachment from the plastic culture dishes, cells were placed in an incubator for 5 min at 37°C. Approximately 75 to 90% of the suspended cells were removed by aspiration and an appropriate amount of fresh growth medium was added to the flask/plate (e.g. 5mL for a T25 flask, 10 mL for a 10 cm culture dish, and 20 mL for a 15 cm culture dish).

Table 2.1: Descriptions of the mammalian cell lines utilized.

Cell Line	Species	Description	Medium[a]
HeLa	*Homo sapiens* (human)	epitheliod cervical adenocarcinoma	DMEM[b]
SK-N-SH	*Homo sapiens* (human)	neuroblastoma, metastasis to bone marrow	DMEM
AT2BE[c]	*Homo sapiens* (human)	human fibroblast (ATM defective)	DMEM/F12
AT5BI[c]	*Homo sapiens* (human)	human fibroblast (ATM defective)	DMEM/F12
GM38	*Homo sapiens* (human)	normal human fibroblast	DMEM/F12
M059J[d]	*Homo sapiens* (human)	malignant glioblastoma	DMEM/F12
M059K	*Homo sapiens* (human)	malignant glioblastoma	DMEM/F12
Cos-7	*Cercopithecus aethiops* (African green monkey)	SV40 transformed kidney fibroblast	RPMI
10T1/2	*Mus musculus* (mouse)	C3H mouse embryonic fibroblast	α-MEM
IM	*Muntiacus muntjak* (Indian muntjak)	normal skin fibroblast	F10[e]
D5	*Mus musculus* (mouse)	immortalized male MEF[f] (*Suv39h1/2*$^{-/-}$)	IMEF
W8	*Mus musculus* (mouse)	immortalized male MEF[f] (D5 control)	IMEF

[a] all media are supplemented with 10% fetal bovine serum (FBS) unless otherwise indicated

[b] Dulbecco's Modified Eagle's Medium (DMEM)

[c] lacks ataxia telangiectasia mutated (ATM) kinase activity

[d] lacks DNA-dependent protein catalytic subunit (DNA-PK_{CS}) kinase activity

[e] supplemented with 20% FBS

[f] mouse embryonic fibroblast

2.3 IMMUNOFLUORESCENT LABELING

The immunofluorescent labeling used throughout this thesis can be roughly grouped into two distinct types; 1) indirect immunofluorescent (IIF) labeling with antibodies to reveal endogenous protein or posttranslational histone modification localization patterns, and 2) the incorporation of modified nucleotides into newly synthesized RNA or DNA to reveal spatial relationships involving RNA transcripts or DNA synthesis.

2.3.1 *Indirect Immunofluorescent Labeling*

One day prior to immunofluorescent labeling, cells were seeded onto ethanol-sterilized glass coverslips (18 × 18 mm, No. 1) in a 6-well culture plate so that they were approximately 80% confluent the following day. The next day, the medium was aspirated and cells were fixed with freshly prepared 4% (w/v) paraformaldehyde (Appendix A) in PBS for 10 min at room temperature. Cells transiently transfected with green fluorescent protein (GFP) -CBP, hemagglutinin (HA) -P300 and Alternative splicing factor (ASF) -GFP (i.e. those employed for the HAT assay) were fixed 12 to 18 hr post-transfection to minimize overexpression artifacts and minimize indirect effects of transient increases in HAT expression (see Chapter 5). Cells expressing fluorescent protein fusions (e.g. GFP-CBP and ASF-GFP) were only fixed for 5 min to prevent signal quenching that can occur with prolonged fixation. Once fixed, the paraformaldehyde was removed and the cells washed three times with PBS. Cells were permeabilized with PBS containing 0.5% (v/v) Triton X-100 (Appendix A) for 10 min at room temperature. Following three additional PBS washes, coverslips were inverted onto parafilm containing a 25 μL aliquot of an appropriately diluted primary antibody. A plastic lid was placed over the coverslips to prevent desiccation and the cells were incubated for 30 min at room temperature. Coverslips were returned to the 6-well culture plate and rinsed once with PBS and incubated with PBS containing 0.1% (v/v) Triton X-100 (Appendix A) for 1 min. Coverslips were rinsed three additional times with PBS and placed onto a 25 μL aliquot of an appropriately diluted secondary antibody. Cells were covered as before and incubated at room temperature for 30 min. The coverslips were returned to the 6-well plate and rinsed with PBS. Cells were incubated in PBS containing 0.1% Triton X-100 for 1 min and rinsed three times with PBS. Coverslips were mounted onto glass slides containing approximately 10 μL of a 90% glycerol-PBS-based mounting medium containing 1 mg of paraphenylenediamine/mL containing DAPI (Appendix A). Slides were rinsed once with milli-Q water to remove any residual PBS crystals that could negatively influence image quality. Slides were maintained in the dark at 4°C to prolong their photostability. Images were typically acquired the following day and at most, within one week. Table 2.2 presents all antibodies utilized throughout these studies, their working dilutions and their sources.

Table 2.2: Antibodies their dilutions and sources.

Antibody Type	Antibody	Recognizes	Catalogue No.	Dilution	Species[a]	Source
Methylation	mMeK4	mono-methylated lysine 4 (H3)	ab8895	1:500	R	Abcam
	dMeK4	di-methylated lysine 4 (H3)	ab7766	1:500	R	Abcam
	tMeK4	tri-methylated lysine 4 (H3)	ab8580	1:500	R	Abcam
	mMeK9	mono-methylated lysine 9 (H3)	ab9045	1:500	R	Abcam
	dMeK9	di-methylated lysine 9 (H3)	ab7312	1:500	R	Abcam
	tMeK9	tri-methylated lysine 9 (H3)	ab8898	1:500	R	Abcam
	mMeK20	mono-methylated lysine 20 (H4)	ab9051	1:1,000	R	Abcam
	tMeK20	tri-methylated lysine 20 (H4)	ab9053	1:1,000	R	Abcam
Phosphorylation	γ-H2AX	phospho-serine 139 (H2AX) (JBW301)	05-636	1:4,000	M	Upstate
	γ-H2AX	phospho-serine 139 (H2AX) (ab2893)	ab2893	1:200	R	Abcam
	γ-H2AX	phospho-serine 139 (H2AX) (ab11174)	ab11174	1:200	R	Abcam
	S10	phospho-serine 10 (H3)	05-806	1:500	M	Upstate
	S10	phospho-serine 10 (H3) Oregon green		1:500	R	Dr. C. D. Allis
	S28	phospho-serine 28 (H3)	07-145	1:500	R	Upstate
Acetylation	H2B	acetylated lysines 5, 12, 15 and 20 (H2B)	AHP421	1:800	R	Serotec
	K9	acetylated lysine 9 (H3)	06-942	1:400	R	Upstate
	K14	acetylated lysine 14 (H3)	07-353	1:200	R	Upstate
	Ac3	acetylated lysines 9 and 14 (H3)	AHP412	1:500	R	Serotec
	K5	acetylated lysine 5 (H4)	07-327	1:200	R	Upstate
	K8	acetylated lysine 8 (H4)	06-760	1:8,000	R	Upstate
	K12	acetylated lysine 12 (H4)	AHP416	1:2,000	R	Serotec
	K16	acetylated lysine 16 (H4)	AHP417	1:100	R	Serotec
	AcH4	acetylated lysines 5, 8, 12, 16 and 19 (H4)	06-946	1:15,000	R	Upstate

Histone Acetyl-transferases	CBP	CREB binding protein (CBP)	Ac238	1:500	R	Neomarkers
	MYST	MOZ, YBF2/Sas3, Sas2 and TIP60 (MYST)	06-815	1:200	R	Upstate
	P300	P300	100301176	1:200	M	Rockland
	PCAF	P300/CBP Associated Factor (PCAF)		1:200	R	Dr. X. J. Yang
	$\text{TAF}_{II}250$	TBP-associated factor II 250kDa ($\text{TAF}_{II}250$)	sc-735	1:400	M	Santa Cruz
	TIP60	Tat-interacting protein 60kDa (TIP60)	07-038	1:200	R	Upstate
Histone Deacetylases	HDAC-1	histone deacetylase-1 (HDAC-1)	06-720	1:100	R	Upstate
	HDAC-2	histone deacetylase-2 (HDAC-2)	sc-9959	1:200	M	Santa Cruz
	HDAC-3	histone deacetylase-3 (HDAC-3)		1:100	R	Dr. E. Verdin
	HDAC-4	histone deacetylase-4 (HDAC-4)		1:50	R	Dr. E. Verdin
DNA Repair	Mre11	meiotic recombination-11 (Mre11)		1:500	R	Dr. J. Y. Masson
	Rad51	radiation defective-51 (Rad51)		1:500	R	Dr. J. Y. Masson
	Nbs1	Nijmegen breakage syndrome-1 (Nbs1)		1:200	R	Dr. J. Y. Masson
	53BP1	p53 binding protein-1 (53BP1)	ab4565	1:1,000	R	Abcam
	BRCA1	breast cancer susceptibility gene-1 (BRCA1)	ab2956	1:200	R	Abcam
	ATM	ataxia telangiectasia mutated (ATM)		1:200	R	Dr. G. K. Chan
	p-ATM	phospho-ATM (serine 1981)	ab2888	1:200	R	Abcam
Other	ACA	anti-centromeric antigen (ACA)		1:1,000	H	Dr. G. K. Chan
	BrdU	5-bromo-2'-deoxyuridine (Replication)	1-170-376	1:50	M	Roche
	FU	5-fluorouridine (Transcription)	B2531	1:400	M	Sigma
	SC-35	splicing factor compartment-35 (SC-35)		1:1	M	Dr. M. J. Hendzel
Secondary Antibodies	r488	goat anti-rabbit AlexaFluor 488	A-11034	1:200	G	Molecular Probes
	m488	goat anti-mouse AlexaFluor 488	A-11001	1:200	G	Molecular Probes
	rCy3	goat anti-rabbit Cyanin 3 (Cy3)	111165144	1:200	G	Jackson IR
	mCy3	goat anti-mouse Cy3	115165146	1:200	G	Jackson IR

[a] species; human (H), rabbit (R), mouse (M) and goat (G)

2.3.2 *In Situ Indirect Immunofluorescent Peptide Competition Assay*

Based on the extensive use of IIF techniques throughout these studies, an IIF peptide competition assay was developed that is performed *in situ* on paraformaldehyde-fixed cells. Briefly, 7.5 μg of a competing or control peptide was added to each 25 μL dilution of primary antibody investigated. Table 2.3 presents a list of all blocking peptides used and provides basic sequence information for each. Peptide/antibody preparations were mixed gently and incubated at room temperature for 1 hr prior to IIF labeling of asynchronous cells as detailed above. Each individual antibody investigated was examined for reactivity against corresponding competing peptides as well as control peptides.

2.3.3 *Embryo Indirect Immunofluorescence*

E9.5 embryos were collected from CD1 mice (Charles River Laboratories), washed in PBS and fixed in 4% paraformaldehyde at 4°C for 18 hrs. Embryos were cryoprotected in 30% sucrose-PBS, mounted in O.C.T. (Tissue-Tek) and sectioned at 14 μm intervals using a Leica CM 1900 cryostat. Sections were immediately fixed in 4% paraformaldehyde for 7 min, washed twice in PBS for 10 min, permeabilized in PBS/0.1% Triton X-100 for 30 min, blocked in PBS/0.1% Triton X-100 with 5% heat inactivated sheep serum for 30 min, and incubated overnight at 4°C with an appropriate primary antibody. Sections were washed three times in PBS/0.1% Triton X-100 for 10 min each, blocked for 30 min in PBS/0.1% Triton X-100 with 5% heat inactivated sheep serum, incubated with secondary antibody for 2 hrs at room temperature, washed three times in PBS/0.1% Triton X-100 for 5 min each and mounted with 90% glycerol-PBS-DAPI as above. All embryonic work was conducted in the laboratory of Dr. Alan Underhill by Mr. V. Biron (Department of Medical Genetics, University of Alberta).

Table 2.3: Characteristics of the blocking peptides.

Peptide Type	Name[a]	Amino Acid Sequence[b]	Catalogue No.	Source
Methylation	mMeK4	ARTKmmeQTAR (1-8)	ab1340	Abcam
	dMeK4	ARTKdmeQTARKS (1-10)	ab7768	Abcam
	tMeK4	ARTKtmeQTAR (1-8)	b1342	Abcam
	mMeK9	QTARKmmeST (5-11)	ab1771	Abcam
	dMeK9	QTARKdmeSTGG (5-13)	ab1772	Abcam
	tMeK9	QTARKtmeSTGG (5-13)	ab1773	Abcam
	mMeK20	GGAKRHRKmmeVLRDNIQC (13-27)		Dr. P. B. Singh
	dMeK20	GGAKRHRKdmeVLRDNIQC (13-27)		Dr. P. B. Singh
	tMeK20	GGAKRHRKtmeVLRDNIQC (13-27)		Dr. P. B. Singh
	tMeK27	KAARKtmeSAPATGG (23-34)	ab1782	Abcam
Phosphorylation	PhosS10	QTARKSphosTGG (5-13)	ab11477	Abcam
	H2AXp	CKATQASphosQEY (133-142)	NCA[c]	Abcam
Unmodified	H2AXnp	GGKKATQASQEY (131-142)	NCA[c]	Abcam
	H3 (1-16)	ARTKQTARKSTGGKAP (1-16)	ab7728	Abcam

[a] peptide names correspond to antibody nomenclature used in Table 2.2

[b] the single amino acid letter code is used to identify the primary sequence. Methylated and phosphorylated residues are identified by the single amino acid letter followed by the modification, mme (monomethyl), dme (dimethyl), tme (trimethyl) or phos (phosphorylated), respectively. The amino acid positions of the corresponding histones are shown in brackets.

[c] the peptide is not commercially available (NCA) and was generously provided by Abcam

2.3.4 *In Situ Calf Intestinal Alkaline Phosphatase Assay*

To examine the immunoreactivity that certain antibodies exhibit towards phosphorylated epitopes, an IIF calf intestinal alkaline phosphatase (CIP) assay was developed that is performed *in situ*. Asynchronous 10T1/2 cells were seeded onto sterilized glass coverslips as above. 10T1/2 fibroblasts were purposely selected for this assay as they contain prominent pericentromeric heterochromatic regions that are easily detectable with DAPI counterstaining. Furthermore, pericentromeric heterochromatin in prophase and prometaphase cells exhibits a high abundance of PhosS10 staining (Hendzel et al., 1997). The following day, cells were washed once with PBS and twice with Saponin buffer (Appendix A). Coverslips were gently inverted onto Parafilm containing a 25 μL aliquot of 25 μg/mL Saponin (BioChemika) diluted in Saponin buffer. Cells were permeabilized for exactly 1min, carefully washed three times with Saponin buffer and gently inverted onto a 25 μL aliquot of either 12.5U CIP (Amersham Pharmacia) diluted in buffer, or buffer alone (control). Cells were incubated in a humidified atmosphere for 1 hr at 37°C prior to 4% paraformaldehyde fixation. IIF was conducted as above with anti-PhosS10 and either anti-γ-H2AX or anti-tMeK9. Cells were mounted onto slides containing mounting media (with DAPI) and high-resolution (100×) digital imaging microscopy (DIM) images were collected. Unfortunately due to the harsh Saponin conditions, mitotic cells, prometaphase to telophase, were frequently lost. Fortunately however, prophase cells frequently remained attached to the coverslips and therefore served as the mitotic population. Direct qualitative comparisons were then made between CIP-treated and control cells and the immunoreactivity of the antibodies was established.

2.3.5 *5-Fluorouridine Labeling and Transcription*

5-fluorouridine (FU) labeling was conducted to investigate the spatial relationship between various posttranslational histone modifications and sites of active transcription. One day prior to FU incorporation, cells were seeded onto ethanol-sterilized glass coverslips so that they were approximately 80% confluent the following day. The medium was removed by aspiration and 1 mL of fresh, pre-warmed medium (37°C) was added to the cells. To this, 15 µL of a 134 mM solution of FU (Appendix A) was added. Following 15 min incubation at 37°C, the medium was removed and the cells were fixed with 4% (w/v) paraformaldehyde for 10min at room temperature. Finally, cells were immunofluorescently labeled as detailed above with a mouse anti-BrdU monoclonal antibody (Sigma) that crossreacts with FU (see Table 2.2).

2.3.6 *5-Bromo-2'-deoxyuridine Labeling and DNA Replication*

5-bromo-2'-deoxyuridine labeling was performed to investigate the spatial relationship between various posttranslational modifications and early-, mid- and late-S-phase. One day prior to 5-bromo-2'-deoxyuridine (BrdU) incorporation, cells were seeded onto ethanol-sterilized glass coverslips so that they were approximately 80% confluent the following day. The medium was removed and 1mL of fresh, pre-warmed medium (37°C) was added to the cells. Cells were incubated at 37°C for 30 min in the presence of 5 mM BrdU (Appendix A). The medium was removed and the cells were fixed with 4% paraformaldehyde for 10 min at room temperature. Cells were rinsed twice with milli-Q water and permeabilized for 2 min in glass dishes containing ice-cold (-20°C) acetone. Cells were washed five times in milli-Q water and the DNA was denatured by incubation in 2N HCl at room temperature for 15 min. To neutralize the

HCl, the cells were washed twice in sodium borate (pH 8.5) for 2 min each. The cells were washed two additional times with PBS and allowed to recover in a third wash for 5 min. Finally, the BrdU incorporated into the DNA was immunofluorescently labeled as described above using a mouse anti-BrdU (Boehringer Mannheim [Roche]) monoclonal antibody (see Table 2.2).

2.4 CELL SYNCHRONIZATION AND MITOTIC ENRICHMENT

To demonstrate that epitope accessibility or chromatin structure did not influence the IIF (i.e. DIM, QIM or flow cytometry) results of Chapters 3 and 4, mitotically-enriched cell populations were required for flow cytometry and immunoblotting experiments. Accordingly, three different methodologies were utilized to generate two distinct mitotically-enriched populations – one enriched at prophase/prometaphase and one enriched a metaphase.

2.4.1 *Double Thymidine Block*

To enrich for a G_1/S-phase boundary population, asynchronous HeLa or 10T1/2 cells were treated with 2.5 mM thymidine (Appendix A) for 12 hr at 37°C. Cells were rinsed three times with prewarmed PBS, and once with prewarmed DMEM. Cells were permitted to progress for 10 hr prior to a second 12 hr incubation with DMEM containing 2.5 mM thymidine. Following the second 12 hr incubation, cells were either harvested and processed for immunoblotting, or permitted to grow for 5 hr prior to the addition of a second cell cycle arresting drug (see below)

2.4.2 *Nocodazole Treatment*

To generate cellular populations enriched in M-phase (mitotically-enriched), asynchronous HeLa or 10T1/2 cells were incubated with 15 nM nocodazole (Appendix

A) for 12 hr. Nocodazole is an anti-mitotic agent that disrupts microtubules by binding to β-tubulin and preventing the formation of interchain disulfide linkages required for microtubule polymerization. These mitotically-enriched cells were subsequently analyzed by flow cytometry to determine the proportion of cells arrested in the G_2/M population. Immunoblotting was also conducted to investigate the abundance of specific posttranslational histone modifications. Cells were confirmed to be in G_2/M by flow cytometry and visually confirmed to be in prophase/prometaphase by DIM. Alternatively, mitotically-enriched cells were produced by the double thymidine block (see above). G_1/S-phase enriched cells were released and permitted to grow for 5 hr prior to supplementing the media with 15 nM nocodazole for 4 hr.

2.4.3 *ALLN Treatment*

To generate cellular populations enriched in M-phase (mitotically-enriched), asynchronous HeLa or 10T1/2 cells were first arrested at the G_1/S-phase boundary by a double thymidine block. Cells were permitted to grow for 5 hr prior to the addition of 40 μg/mL ALLN (Appendix A) for 4hr. ALLN or calpain inhibitor-I, prevents cyclin B degradation that is required for the metaphase to anaphase transition. Cells were visually confirmed to be in metaphase by DIM.

2.5 FLOW CYTOMETRY

Cell lines were grown at subconfluent levels on 15 cm tissue culture dishes in parallel with those used for immunoblot analysis (see below). Flow cytometry was employed to investigate the cell cycle associated dynamics of histone methylation (Chapter 3) and phosphorylation (Chapter 4) as well as confirm mitotic enrichment following nocodazole treatment. A major benefit of flow cytometry is that when combined with DNA labeling, it can rapidly evaluate a large number of cells and quickly determine the proportion of cells in various cell cycle stages (e.g. G_0/G_1, S-phase or G_2/M).

2.5.1 *Ethanol Fixation*

Asynchronous or mitotically-enriched cells (as generated above) were grown in triplicate at subconfluent levels on 150 mm tissue culture dishes. Growth media were removed and cells were rinsed once with sterile PBS prior to 5 min incubation with 3 mL of trypsin. Once detached, cells were transferred into a 15 mL conical polyethylene centrifuge tube round (Corning) and suspended in PBS to a total volume of 10 mL. For each of the three replicates, cells from different plates were combined so that enough cells were obtained to perform and the entire antibody staining procedure (i.e. all methylated antibodies). Cells were pelleted by centrifugation (AccuSpin FR - Beckman) at 1,500 RPM for 5 min and the supernatant was removed by aspiration. Cells were washed with 10 mL of PBS followed by centrifugation for 5 min at 1,500 RPM. Following aspiration of the supernatant, cells were resuspended in 10.5 mL of PBS from which 0.5 mL was added to 19.5 mL of isotone and mixed well. Cells were counted using a particle count and size analyzer (Becton Dickinson) and the total number of cells in 10 mL were determined. The remaining 10 mL of suspended cells were pelleted as before and the supernatant was removed. Cells were resuspended in an appropriate volume of PBS so that the final concentration of cells was 2×10^6 cells/mL. Subsequently, 1mL aliquots (~2×10^6 cells) were dispensed into 13 mL round-bottom polypropylene 100 × 16 mm tubes (Sarstedt). Cells were pelleted as above and the supernatant was removed. Cells were fixed and permeabilized with ice-cold 70% ethanol (Appendix A).

Cells were stored at 4°C for a minimum of overnight and a maximum of two weeks prior to immunofluorescent labeling and flow cytometric analysis.

2.5.2 *Indirect Immunofluorescent Staining*

Prior to immunofluorescent staining, the 1 mL aliquots of ethanol-fixed cells were pelleted by centrifugation at 1,500 RPM for 5 min and the supernatant removed. Cells were resuspended in 5 mL of PBS, pelleted at 1,500 RPM (5min) and the supernatant removed. Primary antibody dilutions were made so that each 75 µL antibody aliquot contained a 1:150 dilution of the methylation antibody or a 1:2000 dilution of the anti-γ-H2AX antibody. The diluted antibodies were then added to the pelleted cells as above, mixed and incubated at room temperature for 30 min. The cells were then pelleted and the supernatant was removed prior to a second 30 min incubation with a 75 µL aliquot of an appropriate secondary antibody (anti-rabbit AlexaFluor 488 and anti-mouse AlexaFluor 488 [Molecular Probes]). Secondary antibodies were diluted to 1:200 in PBS.

2.5.3 *Propidium Iodide Staining*

Following the incubation with the secondary antibody, the cells were pelleted as before. The supernatant was removed and a 1mL aliquot of freshly made 60 µM propidium iodide (PI – Appendix A) solution containing 25 µM RNase A (Appendix A) was added to the cells. Cells were incubated in the dark for 30 min at 37°C. Following the incubation, 4 mL of PBS were added and the cells were pelleted as before. The supernatant was removed and the cells were resuspended in a final volume of approximately 500 µL and transferred to 4 mL Facsort tubes (Falcon). Samples were maintained in the dark and flow cytometry was conducted immediately.

2.5.4 *Flow Cytometric Analysis*

All flow cytometry was performed on a FACSort (Becton Dickinson) using Cell Quest version 3.2.1f1 (Becton Dickinson). Briefly, instrument settings were optimized with specific controls prior to analyzing specific samples. The specific control employed include; 1) unstained cells with and without PI, 2) cells stained with the secondary antibody with and without PI, and, 3) cells stained with both primary and secondary antibodies but without PI. In all cases where mouse monoclonal antibodies were analyzed (e.g. PhosS10 and γ-H2AX) species-specific isotype controls (e.g. IgG1 or IgG2a) were also analyzed. In instances where rabbit polyclonal antibodies were analyzed (e.g. all anti-methylation antibodies), pre-bleed serum from an unrelated rabbit was used. Once the settings were optimized and the controls were analyzed, the immunofluorescently labeled samples were analyzed. A minimum of 1×10^4 events was collected for each antibody with each experiment being performed in triplicate. Once all data had been acquired, several key characteristics were determined and used in subsequent analyses. These include; 1) the total number of positively-staining cells, 2) the proportion of cells in G_0/G_1, S-phase or G_2/M, 3) the mean of both PI and the antibody fluorescent intensities of cells in G_0/G_1, S-phase or G_2/M, and, 4) the standard deviation of both PI and antibody fluorescent intensities of cells in G_0/G_1, S-phase or G_2/M.

2.6 IMMUNOBLOT ANALYSIS

Cells were grown on 15 cm tissue culture plates in parallel with those used for flow cytometric analysis. As a result, the proportion of cells calculated to be in G_0/G_1, S-phase or G_2/M by flow cytometry following mitotic-enrichment, could be extrapolated to the cells used in subsequent immunoblot analyses. In general, the signal intensities or abundance of specific posttranslational modifications were compared between protein preparations isolated from asynchronous cell populations (predominantly G_0/G_1) and mitotically-enriched populations (predominantly G_2/M). Unless otherwise indicated, all centrifugation steps were performed at 4°C.

2.6.1 *Nuclear Preparation*

Cells, either asynchronous or mitotically-enriched, were detached from 15 cm tissue culture dishes through treatment with 0.53 mM EDTA for 10 min at 37°C. Cells were resuspended in 10 mL PBS, transferred to a 15mL conical tubes and pelleted by centrifugation at 1,500 RPM for 5 min. Cells washed and pelleted two additional times as indicated above. The total number of cells were calculated using a particle count and size analyzer (Becton Dickinson) and were resuspended in PBS to a final concentration of 10×10^6 cells/mL. Approximately 1mL or 10×10^6 cells were transferred to a sterile 1.5 mL plastic tube. Cells were pelleted in a refrigerated centrifuge (Eppendorf – 5417 R) at 1,500RPM for 2min. Cells were lysed in cold Nuclei Buffer (Appendix A) containing phenylmethanesulfonyl fluoride (PMSF – Appendix A) for 1 min. Nuclei were harvested by centrifugation at 3,000×g for 1 min and the Nuclei Buffer was removed by micropipette.

2.6.2 *Acid-Extraction of Nuclear Proteins*

Approximately 570 µL of milli-Q water and 6.4 µL of concentrated sulfuric acid (H_2SO_4) were added to the 10×10^6 pelleted cells and samples were incubated on ice for 30 min. Nuclear debris was cleared from the acid-soluble nuclear proteins by centrifugation (Eppendorf – 5417 R) at 14,000 RPM for 10 min. The supernatant was transferred to a clean 1.5 mL tube containing 60 µL of Tris buffer, pH 8.0 (Appendix A). To this, 40 µL of 10 N sodium hydroxide (NaOH) was added and mixed. Finally, 210 µL of 3× Sample Loading Buffer (Appendix A) was added. Samples were mixed by vortexing and dispensed into 0.5 mL plastic tubes in 100 µL aliquots. Aliquots were stored at either -20°C for up to one month, or at -80°C for longer periods of time.

2.6.3 *Gel Preparation and Protein Resolution*

Polyacrylamide denaturing gels were prepared with a 15% separating gel (bottom) and a 5% stacking gel (top) as described in Appendix A. The 15% separating gel solution was mixed using a magnetic stir bar prior to the addition of 100 µL 10% ammonium persulfate (Sigma – A9164) followed immediately by 10 µL TEMED (Bio-Rad – 161-0801). The solution was mixed and poured between the two glass plates of the Mini Protean 3 electrophoresis module (Bio-Rad) system separated by 1.0 mm spacers. The gel was poured so that the gel front was approximately 1.5 to 2.0 cm from the top of the small plate. Isopropanol was added on top of the gel so that a clean, horizontal interface was generated. The gel was allowed to polymerize for 1 hr. Following polymerization, the isopropanol was removed, the wells were rinsed three times with milli-Q water and the interface was dried with a piece of 3MM Whatman paper. Next, a 5% stacking gel was prepared as described in Appendix A. The solution was mixed using a magnetic stir bar and 60 µL ammonium persulfate followed by 10 µL TEMED were added. The solution was mixed well by stirring. The gel was poured onto the 15% stacking gel and a 10-well plastic comb was inserted. The gel was permitted to polymerize for 15 min prior to removing the comb and rinsing each well with milli-Q water followed by Running Buffer (Appendix A). The gel running apparatus was assembled as described by the manufacturer and protein samples from 2×10^5 asynchronous or mitotically-enriched cells were loaded in parallel into alternating wells.

Prior to resolving individual proteins, acid solubilized proteins previously diluted with 3× Sample Loading Buffer were incubated in a thermal cycler (Eppendorf – Mastercycler Gradient) at 95°C for 3min. The protein equivalents from 2×10^5 cells were loaded per lane on duplicate gels, one to be transferred to a polyvinylidene difluoride (PVDF) membrane and one for Coomassie Blue staining. Denatured proteins were concentrated using a 5% stacking gel and resolved on a 15% separating gel by SDS-polyacrylamide gel electrophoresis (SDS-PAGE). Gels were electrophoresed in a Mini Protean 3 electrophoretic gel apparatus (Bio-Rad) containing Running Buffer (Appendix A) for 20 min at 85 V, 140 mA and 250 W immediately followed by 80 min at 158 V, 140 mA and 250 W in Running Buffer (Bio-Rad Power Pac 1000).

The proteins from one gel were transferred to a PVDF membrane for 1hr at 100 V, 140 mA and 300 W (Bio-Rad Power Pac 200) in Transfer Buffer (Appendix A), while the other gel was placed in Coomassie Blue (Appendix A) overnight to reveal protein loading. The following day, gels were placed in Coomassie Blue Destain (Appendix A) for 2hr. Gels were further destained in a weak solution of 5% methanol and 7.5% acetic acid and stored at 4°C. Coomassie-stained gels were imaged using the AlphaImager gel documentation system equipped with AlphaEase version 3.3.d software.

2.6.4 *Immunoblotting and Development*

Once the proteins had been transferred to PVDF membranes, the loading was confirmed by copper phthalocyanine 3,4',4'',4'''-tetrasulfonic acid tetrasodium salt (CPTS) staining as described by Bickar and Reid (Bickar and Reid, 1992) with slight modifications. Briefly, the PVDF membranes were incubated in 15 mL of CPTS (Appendix A) at room temperature for 5 min. The CPTS was replaced once followed by a 30 min incubation that permitted direct visualization of protein bands within the PVDF membrane. Non-specific CPTS staining, or 'background noise' was eliminated by incubating the membrane in 50% (v/v) methanol in milli-Q water for 5 min with gentle agitation. Images were collected with the AlphaImager gel documentation system. The PVDF membranes were destained in TBS (Appendix A) for 10 min with gentle agitation. Once the CPTS bands disappeared, membranes were blocked with 5% non-fat milk in TBST (Appendix A) for 1hr with gentle agitation. For each blot, 1 mL of the appropriate primary antibody dilution was placed in a plastic bag that was sealed on three sides. Individual blots were placed in the bags and all air bubbles were removed prior to sealing the final side. Blots were incubated overnight at 4°C on a shaker. The following day, blots were washed three times in TBST for 10 min each. Next, blots were incubated for 1 hr at room temperature with gentle agitation with an appropriate secondary antibody (anti-rabbit horseradish peroxidase [HRP] at 1:10,000 or anti-mouse HRP at 1:15,000) diluted in 5% skim milk in TBST. Blots were washed three times in TBST as above with excess TBST removed by dabbing the edge of the blot on a Kimwipe. Next, 500 μL of ECL plus (Amersham Biosciences) reagent was prepared as described by the manufacturer and was placed on Saran wrap. Blots were inverted (protein side down) onto the ECL plus reagent for 5 min at room temperature. Excess ECL plus reagent was removed by dabbing, and the blots were placed face down on a fresh piece of Saran wrap. Blots were wrapped in Saran wrap and exposed to FujiFilm Super RX medical X-Ray film in a film cassette for varying lengths of time (ranging from 30 sec to 1 hr) to optimize signal intensities. Films were developed in a Kodak X-OMAT 2000A film processor and scanned and saved as TIF files and montages were compiled in Photoshop.

2.7 PLASMID CONSTRUCTS AND TRANSIENT EXPRESSION

Plasmid constructs and their transient expression were only employed to determine the HAT specificity preferences of CBP and P300 in Chapter 5.

2.7.1 *Plasmid Constructs*

In Chapter 5, three distinct plasmid constructs were employed. Two of the plasmids contained coding sequences for two highly-related HATs – green fluorescent protein (GFP)-CBP (GFP-CBP) and hemagglutinin (HA)-P300 (HA-P300), while the third encoded the alternative splicing factor-GFP (ASF-GFP) control. The GFP-CBP plasmid was generated by Mr. F. M. Boisvert at the University of Calgary, Alberta (Dr. D. P. Bazett-Jones). It was constructed by fusing the full-length murine *CBP* cDNA in frame with the GFP coding sequence contained within the pEGFP-C1 vector (Clontech). The HA-P300 vector was purchased from Upstate (21-179) and was constructed by fusing full-length human *P300* cDNA (as a *NotI/Hind*III fragment) in frame with an HA coding sequence in a proprietary vector (Upstate). The final vector, ASF-GFP was a gift from Dr. A. I. Lamond (University of Dundee, Scotland) and serves as a nuclear localizing control that does not contain, nor recruit, HAT activity. It was constructed by fusing the full-length human *ASF* cDNA (as a *Bgl*II/*Xba*I) fragment into phGFP-S65T (Clontech). The constitutive expression of all three fusion proteins was driven by CMV promoters (pCMV IE for GFP-CBP and ASF-GFP, and pCMVβ for HA-P300).

All plasmid preparations were generated from pre-existing glycerol stocks. Briefly, 2 mL overnight cultures were grown at 37°C in the presence of a selectable drug (e.g. kanamycin or ampicillin). Plasmids were isolated and purified using a mini-prep plasmid purification kit (Qiagen) as specified by the manufacturer. Prior to analysis, endogenous expression patterns for the transiently expressed proteins was confirmed through comparisons with endogenous protein expression patterns as identified by antibody staining. Only cells expressing endogenous expression patterns were selected for further analyses. Furthermore, in an attempt to prevent the characterization of overexpression artifacts, only cells expressing minimal quantities of the transiently expressed proteins were selected for further analysis (see below).

2.7.2 *Lipid-based Transient Transfection*

Cells (HeLa, Cos-7, IM and 10T1/2) were plated onto ethanol-sterilized glass coverslips so that they were 50 to 80% confluent the following day. Cells were transiently transfected with the appropriate plasmid construct using Effectene (Qiagen Inc.) with slight modifications to the manufacturer's instructions. Briefly, 400 ng of mini-prep plasmid DNA and 4 μL of Effectene were used per coverslip. Cells were cultured for 12 to 18 hr post-transfection to allow for transient protein expression while minimizing the transcriptional coactivator functions of CBP and P300.

2.8 CELLULAR IMAGING

Two distinct types of cellular imaging were employed throughout this thesis. In general, DIM was restricted to the investigation of histone methylation and phosphorylation (Chapters 3 and 4), whereas confocal microscopy was restricted to the HAT assay (Chapter 5).

2.8.1 *Digital Imaging Microscopy*

DIM was performed exclusively on an Axioplan 2 (Zeiss) equipped with a 12-bit Coolsnap HQ cooled CCD camera (Photometrics) and a z-stage motor. The light source was a HBO 100 AttoArc lamp (Carl Zeiss, Inc.). Two distinct objectives were used during image acquisition and include a 40× oil-immersion fluar lens (numerical aperture [NA] = 1.3) and a 100× oil-immersion plan apochromat lens (NA = 1.4). The 40x objective was employed for both 2D field micrographs and the QIM experiments performed in Chapters 3 and 4. The 100× objective was used predominantly when high-resolution images were required, such as for image deconvolution or for the characterization of 3D spatial relationships. In general, the channel information was collected from three separate emission wavelengths including DAPI, GFP/AlexaFluor 488 and Cy3 and correspond to the 31000, 31001 and 31002 filter sets (Chroma Technology Corp.), respectively.

2.8.2 *Confocal Microscopy*

Confocal microscopy was performed on a laser scanning microscope LSM 510 (Carl Zeiss, Inc.), equipped with a 40× oil-immersion lens (NA = 1.3) and was used exclusively for the quantitative microscopy performed in Chapter 5 (HAT assay). Briefly, for each antibody trial the detector gain of the three channels (DAPI, GFP/ AlexaFluor 488 and Cy3) was first optimized and then maintained constant throughout the image acquisition stage. For each assay, a minimum of 50 transiently expressing cells was imaged. Individual channels were separated with Zeiss LSM 510 version 3.0 (Carl Zeiss, Inc.) and subjected to quantitative analysis as described below.

2.9 QUANTITATIVE IMAGING MICROSCOPY

Quantitative imaging microscopy (QIM) was utilized throughout these studies to investigate posttranslational histone modification dynamics and protein expression levels. It has several distinct advantages over conventional biochemical or flow cytometric approaches. First, QIM is performed at the single cell level. Therefore, cells exhibiting expression level related artifacts or those at specific cell cycle time points can easily be identified and eliminated or selected respectively. Second, the assay is performed *in situ*, rather than *in vitro*, and thereby utilized endogenous and physiologically relevant conditions. For example, HAT specificities (Chapter 5) were investigated using endogenous higher-order chromatin structure rather than physiologically irrelevant synthesized peptides, histones, or mononucleosomes. Finally, this methodology couples the spatial resolving power of fluorescence microscopy with robust statistical analyses to attain statistically significant quantification of the *in situ* posttranslational modification levels or enzymatic activities on a chromatinized substrate. For reference purposes Figure 2.1 presents the basic steps involved in QIM that are outlined below and detailed elsewhere (McManus and Hendzel, 2004).

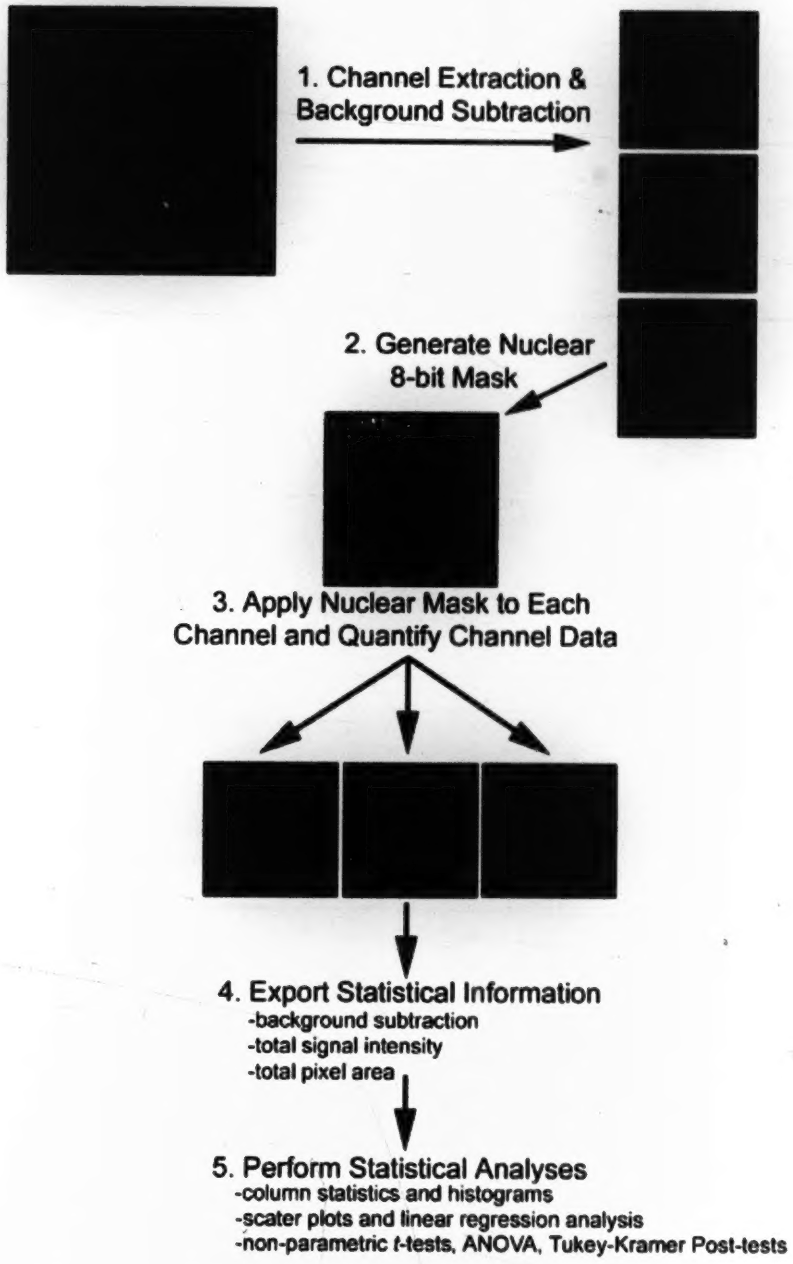
1. Channel Extraction &
Background Subtraction
2. Generate Nuclear
8-bit Mask
3. Apply Nuclear Mask to Each
Channel and Quantify Channel Data
4. Export Statistical Information
-background subtraction
-total signal intensity
-total pixel area
5. Perform Statistical Analyses
-column statistics and histograms
-scater plots and linear regression analysis
-non-parametric t-tests, ANOVA, Tukey-Kramer Post-tests

Figure 2.1. Schematic description of the principle steps involved in QIM
The protocol is performed for each image in each antibody treatment and for all enzymes and epitopes investigated. Images can be collected as either confocal or digital micrographs, however, the detector gain or exposure time of each individual channel (i.e. DAPI, GFP and Cy3) must be maintained constant throughout the entire acquisition stage.

Two-dimensional (2D) images were collected by either DIM or confocal microscopy as detailed. In either case, each individual channel was first optimized by randomly sampling various regions of a coverslip optimizing instrument settings (i.e. the exposure time [DIM] or detector gain [confocal]) to best represent the channel information. Once optimized, the settings were maintained constant throughout the entire image acquisition stage for any given antibody treatment. As a direct result, signal intensities for individual cells/nuclei can be characterized and both qualitative and quantitative comparisons can be made.

Prior to image quantification, background noise was subtracted from each acquired image in Metamorph. Briefly, a background region, devoid of any nuclear signal, was randomly selected and the average signal intensity within that region was determined. The average background signal intensity for each image was calculated and was subtracted from the total signal intensity for each image. Next, a binary mask defining the nuclear shape was generated by signal intensity thresholding of the DAPI channel. This nuclear mask was then applied to each channel (e.g. DAPI, AlexaFluor 488/GFP, and Cy3) and the pixel values within the binary mask were quantified. Various detailed data including total and average signal intensities and area for each nucleus in a given image were measured and the raw data was exported into Excel (Microsoft). In addition, an annotated image numbering each of the nuclei for a specific image was generated and was used to identify cells at specific stages of the cell cycle (Chapters 3 and 4) or those transiently expressing GFP-CBP or HA-P300 (Chapter 5). Data were compiled in Excel and exported into Prism version 3.03 (GraphPad) where all statistical analyses were performed (see Section 2.12).

2.9.1 *Normalizing Signal Intensity Data to Account for Histone Variability*

In order to permit the direct comparison of specific signal intensities between cells at various stages of the cell cycle it was first necessary to account for histone variability that occurs as cells progress through the cell cycle. To accomplish this, all channel information (i.e. total signal intensities [TSI]) were normalized to DNA content which increases accordingly as cells progress from G_1 to S-phase and into G_2 and mitosis. This was accomplished by calculating the ratio of methylation TSI:DAPI TSI in Chapter 3, γ-H2AX TSI:DAPI TSI in Chapter 4, and CBP/P300/ASF TSI:DAPI TSI in Chapter 5.

2.9.2 *Identification of Specific Cell Cycle Stages*

Because Chapters 3 and 4 specifically investigated the temporal dynamics of posttranslational histone modifications it was necessary to classify each cell according to its position within the cell cycle. In Chapter 3 (histone methylation), cells were staged based on two different but complementary approaches; 1) the various stages of mitosis (prophase to telophase) were easily discernable based on classical chromosomal morphological criteria, and 2) by co-immunofluorescently labeling of cells with anti-PhosS10 cells in early and late G_2 were easily identified. By combining these two criteria, nine distinct cell cycle stages were readily discernable and include; interphase (I), early G_2 (EG2), late G_2 (LG2), prophase (P), prometaphase (PM), metaphase (M), anaphase (A), telophase (T) and early G_1 (EG1). For the γ-H2AX study however, it was only necessary to classify cells as either being in interphase (I) or mitosis (M) therefore only the classical chromosomal morphological criteria were employed.

2.9.3 *Determining Protein Expression Levels by DIM*

To determine the fold overexpression of CBP and P300 in the HAT assay (Chapter 5), a quantitative microscopic approach similar to that described above, was employed. Briefly, cells transiently expressing GFP-CBP or HA-P300 were fixed and immunofluorescently labeled with antibodies recognizing CBP or P300, respectively. Because of the high degree of sequence identity between CBP and P300, preliminary experiments examining the cross reactivity of the antibodies were performed and established that each antibody was specific to the protein of interest. Images were then collected as detailed above and the DAPI channel was used to identify nuclear shape, while the GFP/AlexaFluor 488 channel identified transfected cells and the Cy3 channel identified total fluorescent signal intensities or protein expression levels. Once the background was removed from all images and all channels, a binary nuclear mask was generated by signal intensity thresholding the DAPI channel that was subsequently applied to each channel to extract quantitative information. The total signal intensities were logged and exported as raw data into Excel and imported into Prism for statistical analysis (see Section 2.12).

To determine whether there was an increase in HAT or HDAC expression in the presence of transient CBP and P300 expression, quantitative analyses were performed by QIM. Cells were transiently transfected with GFP-CBP or HA-P300 and immunofluorescently labeled with appropriate antibodies recognizing various HATs and HDACs (see Table 2.2). In turn, these anti-HAT and anti-HDAC antibodies were recognized by secondary antibodies conjugated with Cy3. As above, cells were imaged on an LSM 510 and QIM was performed as detailed above (Section 2.8). The total signal intensities were logged and exported as raw data into Excel and imported into Prism for statistical analysis (see Section 2.12) where quantitative comparisons were made.

2.9.4 *Three-Dimensional Colocalization Analysis*

High-resolution (100×) images were acquired and subjected to deconvolution as detailed below. Image colocalization between specific channels was performed in ImarisColoc (Bitplane, AG) where the AlexaFluor 488 and Cy3 channel information were manually thresholded. The DAPI channel was employed to define the region of interest (i.e. the nucleus) in which the colocalization between the AlexaFluor 488 and Cy3 channels were calculated. A colocalization channel was constructed and colocalization channel information was obtained and exported into Prism where mean channel correlations and standard deviation were calculated. Student *t*-tests assessing the differences between mean channel correlations were calculated for both HeLa and 10T1/2 cell lines.

2.10 IMAGE DECONVOLUTION

All images subjected to deconvolution were collected on an Axioplan 2 microscope (Zeiss) equipped with a 12-bit Coolsnap HQ cooled CCD camera (Photometrics) and a z-stage motor. A 100× oil-immersion plan apochromat lens (NA = 1.4) was used to collect three-dimensional (3D or z-series) images of individual nuclei. In general, three channels were collected and include DAPI, GFP/AlexaFluor 488 and Cy3, using the 31000, 31001 and 31002 filter sets (Chroma Technology Corp.), respectively. All images were acquired as 16-bit stack (*.STK) files in Metamorph (Universal Imaging Corp.) version 6.1r6 (Section 2.8.1), with each channel being individually optimized prior to acquisition for each separate image. Z-series extending above and below the individual nuclei were collected at 0.200 μm intervals.

Prior to actual software-driven image deconvolution, Metamorph stack (*.STK) files were converted to Delta Vision (*.DV) files using SoftWoRx (AppliedPrecision) on a Silicon Graphics Inc (SGI) workstation. Once converted, the DV files were processed by maximum-likelihood-expectation deconvolution using a constrained iterative algorithm and theoretical optical transfer files generated for emission wavelengths DAPI (460 nm), GFP/AlexaFluor 488 (505 nm) and Cy3 (565 nm). Deconvolved files were visualized in Imaris version 4.0.5 (Bitplane AG) where 3D spatial relationships were investigated.

2.11 IMAGE PREPARATION – IMARIS AND METAMORPH

Field micrographs or 3D images (original or deconvolved), were assembled in Imaris. Briefly, the DAPI channel was opened in Imaris and the additional channels were sequentially added (e.g. GFP/AlexaFluor 488 then Cy3). The voxel sizes of the images (x × y × z dimensions) were adjusted to reflect the correct voxel dimensions of the Coolsnap HQ camera; 0.0645 × 0.0645 × 0.200 μm for the 100× objective and 0.16125 × 0.16125 × 0.200 μm for the 40× objective. Individual channels were false coloured white and if necessary, gamma corrections were performed to increase the intensity of the lower range of the image data. Individual planes from each channel were exported as TIF files. In merged images, individual channels were pseudo-coloured to best represent the data. Merged images were exported as TIF files and montages were assembled in Photoshop version 6.0 (Adobe).

2.11.1 *3D Projections, Isosurface Renderings and Qualitative and Quantitative Measurements*

3D and isosurface renderings were generated in Imaris to facilitate the 3D spatial relationships between many of the histone posttranslational modifications and specific nuclear bodies, such as the centromere, heterochromatin, euchromatin, splicing factor compartments or various other nuclear bodies. They were generated as maximum intensity projections under 'Full 3D' and 'Surpass' as 3D projections and isosurface renderings, respectively. To generate an isosurface, a new volume was added for which an initial isosurface was generated. Both the 'resample dataset' and 'smooth dataset' options were deselected and the best threshold value was determined empirically. Once an appropriate isosurface was generated, statistical information could be obtained for each channel that included the number of unconnected surfaces (foci), the size of individual foci and the fluorescent intensities (minimum, maximum, median, mean standard deviation and sum) of the three different channels within those foci.

2.11.2 *Line Scanning in MetaMorph*

Line scans of DAPI, GFP/AlexaFluor 488, and Cy3 signal intensities were generated in MetaMorph. First the three independent image channels were opened in MetaMorph and assembled into a single colour combined image. A line with a scan width of three pixels was placed over the region of interest and the average gray value (signal intensity) versus pixel position was plotted.

2.12 STATISTICAL APPROACHES AND ANALYSES

Because of the multitude of experiments that employ various types statistical analysis (e.g. flow cytometry and QIM), a brief description of each method is included.

2.12.1 *Flow Cytometry Dot Plots and Cell Cycle Analyses*

Flow cytometry was performed as described in Section 2.5 using the Cell Quest software interface. Inherent in the Cell Quest software package, is the ability to produce dot plots comparing the fluorescent signal intensity for a given antibody treatment (e.g. histone methylation or phosphorylation) and the PI signal intensity within each cell. By placing three region markers that delineate the G_0/G_1, S-phase and G_2/M populations, statistical data including the number of cells, mean fluorescent intensity and standard deviation could be obtained for each cell cycle stage. Dot plots included in figures were copied into Graphic Converter version 3.9.1 (Lemkesoft), saved as TIF files and imported into Photoshop version 6.0 (Adobe) where montages were created.

2.12.2 *Analysis of Variance (ANOVA)*

For the histone methylation section only, analysis of variance (ANOVA) of unweighted means was performed in Prism. This analysis directly tests the null hypothesis (H_0) that all of the nine cell cycle stage group means are drawn from the same population. If the differences between group means is not statistically significant (*p*-value > 0.05), the H_0 is accepted. Conversely, if the H_0 is rejected (*p*-value < 0.05) and the alternative hypothesis (H_1) is accepted, it is assumed that at least one of the nine cell cycle stage means is drawn from a distinct group. In instances where the H_0 was rejected, multi-comparison pair-wise post-tests were performed (see Section 2.12.3). For reference purposes, *p*-values of <0.05 are considered statistically significant.

While calculating ANOVA, an F-ratio was also calculated. The F-ratio is equivalent to the ratio between the mean square between groups and the mean square within groups (MS_{BG}/MS_{WG}). Both MS_{BG} and MS_{WG} were calculated by determining the sum of squares/degrees of freedom (SS/df) either between groups (BG) or within groups (WG), respectively. For any given antibody treatment, the F-ratio provides information as to the variability within any one of those nine cell cycle stages and the variability between the nine cell cycle stages. The smaller the number, the greater the variability within any one of those cell cycle stages, while the larger the number, the greater the variability between those nine cell cycle stages.

2.12.3 *Tukey-Kramer Post-tests*

In instances where the H_0 calculated by ANOVA was rejected, Tukey-Kramer post-tests were performed (Prism). This test includes the extension by Kramer to account for unequal sample sizes. Using Tukey-Kramer post-tests, one can determine whether statistically significant differences occur between specific group means pairings. A *p*-value of <0.05 is considered to be statistically significant, while a *p*-value of <0.001 is considered highly statistically significant.

2.12.4 *Student t-tests*

For Chapter 5 (HAT assay), unpaired *t*-tests were calculated using Prism. Student *t*-tests investigate the possibility that significant differences exist between mean normalized acetylation (Norm-Ac) values calculated for untransfected and transfected populations for each antibody trial. Inherent in this test is the assumption that the Norm-Ac signal intensities within either of those groups (untransfected or transfected) follow a Gaussian distribution and that equal variance exists within each group. A *p*-value of <0.05 is considered to be statistically significant and is strongly suggestive of different means.

2.12.5 *Histogram Distributions*

For Chapter 5 (HAT assay), histograms were generated to assess global increases in Norm-Ac intensities in instances where a substrate specificity preference occurs. By comparing the Norm-Ac distributions for untransfected controls with those for GFP-CBP-, HA-P300-, or ASF-GFP-expressing cells, clues as to preferred substrates were gleaned. The first *y*-axis represent the number of untransfected cells while the second *y*-axis represents the number of transfected cells. The *x*-axis represents the distribution range for the Norm-Ac intensities for the acetylated epitope. Bin ranges, along the *x*-axis, were manually set every 0.25 units.

2.12.6 *Scatter Plots and Linear Regression Analysis*

Scatter plots were generated for Chapter 5 (HAT assay) in Prism to compare the GFP/AlexaFluor 488 total signal intensities of the transiently expressing cells to the Norm-Ac signal intensities for each antibody in Cos-7, HeLa and IM. Best-fit lines were applied to each scatter plot to identify potential trends for specific acetylation epitopes that are dependent on the expression level or nuclear abundance of GFP-CBP, HA-P300 or ASF-GFP.

Linear regression analysis was performed in Prism to investigate the relationship between signal intensity or expression level of GFP-CBP, HA-P300 or ASF-GFP and the signal intensity or abundance of specific acetylated epitopes. Linear regression analysis assumes that all data exhibit Gaussian distributions. Since we are only interested in analyzing the standard curve and the 'goodness-of-fit', only the R^2 value was determined. R^2 values range between 0.0 and +1.0 and provides information as to the dependence of one variable (e.g. acetylation signal intensity) on a second variable (e.g. GFP-CBP, P300-

HA and ASF-GFP). The larger the R^2 value, the closer the data are to the best-fit line. Conversely, the lower the R^2 the further the data are from the best-fit line. For example an R^2 value of 0 indicates that there is no relationship between the two variables.

2.12.7 *Calculating Relative Protein Expression Levels*

To determine the total amount of CBP or P300 expressed in cells transiently expressing GFP-CBP or HA-P300, respectively, a QIM approach was employed. Images were collected and total signal intensity information was extracted as detailed in Section 2.9.3. Once all raw data were imported into Excel, visual comparisons between the annotated image and the GFP/AlexaFluor 488 channel were used to identify only the cells transiently expressing GFP-CBP or HA-P300. The values corresponding to these nuclei were manually extracted from the original list and compiled into a separate list so that total signal intensities comparison between untransfected and transiently expressing cells could be made. Therefore, for each antibody trial, two distinct populations (untransfected and transfected) were generated and the data exported into Prism where simple statistical comparisons and student *t*-tests were performed. Box-and-whisker (or bootstrap) plots depicting and comparing their distributions were also generated. The box-and-whisker plots depict the total range of the total signal intensity within the untransfected and the transiently expressing populations (top and bottom whiskers), while the box identifies the 25th (bottom) and 75th (top) percentiles, with the middle line identifying the mean signal intensity for that population.

To investigate the expression level profiles of additional HATs and HDACs in GFP-CBP and HA-P300 expressing cells, a QIM approach similar to that described above was performed. As in the previous section, box-and-whisker plots were generated to graphically depict the range and various percentiles of those two populations.

2.13 REFERENCES

Bickar, D., and P.D. Reid. 1992. A high-affinity protein stain for western blots, tissue prints, and electrophoretic gels. *Anal Biochem*. 203:109-15.

Hendzel, M.J., Y. Wei, M.A. Mancini, A. Van Hooser, T. Ranalli, B.R. Brinkley, D.P. Bazett-Jones, and C.D. Allis. 1997. Mitosis-specific phosphorylation of histone H3 initiates primarily within pericentromeric heterochromatin during G2 and spreads in an ordered fashion coincident with mitotic chromosome condensation. *Chromosoma*. 106:348-60.

McManus, K.J., and M.J. Hendzel. 2004. Using quantitative imaging microscopy to define the target substrate specificities of histone posttranslational modifying enzymes. *Methods*. In Press

CHAPTER 3

Dynamic Changes in Histone Lysine Methylations: Identification of a Mitosis-specific Function for Dynamic Methylation in Chromosome Congression and Segregation[†]

Kirk J. McManus[1], Vincent L. Biron[2], D. Alan Underhill[2] and Michael J. Hendzel[1*]

[1] Department of Oncology, Cross Cancer Institute, 11560 University Avenue,
Edmonton, Alberta, Canada, T6G 1Z2

[2] Department of Medical Genetics, University of Alberta,
Edmonton, Alberta, Canada T6G 2H7

Running Title - Dynamic Changes in Histone Lysine Methylations

*Address for Correspondence
Dr. Michael J. Hendzel
Department of Oncology
Cross Cancer Institute
11560 University Avenue
Room 3332
Edmonton, Alberta
T6G 1Z2 CANADA
Tel # (780) 432-8493
Fax # (780) 432-8892
Email: michaelh@cancerboard.ab.ca

[†] A version of this chapter has been submitted for publication

Co-author Contributions
V. L. Biron/D. A. Underhill: mouse embryonic tissue collection and immunofluorescent labeling.

3.1 INTRODUCTION

The core histones (H2A, H2B, H3 and H4) are small basic proteins that form the fundamental building block of chromatin structure, the nucleosome. They function to compact over 2 metres of genomic DNA into a nucleus with a diameter of approximately 10 µm. Collectively, the core histones are the targets of at least five different types of posttranslational modifications. These include ADP-ribosylation, ubiquitination, phosphorylation, acetylation and methylation, and involve more than 40 amino acid residues (Zhang et al., 2003). The majority of these modifications occur within the amino- (N-) terminal tails of the core histones. Most modifications function in the regulation of gene expression by modulating chromatin structure and access of regulatory proteins (reviewed in Goll and Bestor, 2002; Sims et al., 2003). However, the function of some posttranslational modifications may also be explained by the existence of protein domains found in many key regulatory and transcription factors that specifically recognize and bind acetylated (bromodomain) or methylated (chromodomain) residues (reviewed in Brehm et al., 2004; Cavalli and Paro, 1998; Eissenberg, 2001; Zeng and Zhou, 2002).

Histone methylation was originally identified in the mid 1960's (Murray, 1964) and was shown to result from histone methyltransferases (HMTs) that catalyze the transfer of methyl groups from a S-adenosyl-L-methionine (SAM) onto the ε-amino group of lysine (K), or onto arginine and histidine residues (Paik and Kim, 1967). HMTs have been found to be specific for both the K or arginine (R) residue they modify (Lachner and Jenuwein, 2002) and the number of methyl groups (e.g. mono-, di- or tri-methylations) they attach to that specific residue (Paik and Kim, 1967) (see also

Bannister et al., 2002). Interestingly, although all core histones contain K and R residues, only histones H3 and H4 have been identified as *in vivo* HMT substrates. Histone H3 harbors six distinct K residues that can be methylated (K4, K9, K23, K27, K36 and K79), while histone H4 contains three target sites (K12, K20 and K59) (Goll and Bestor, 2002; Ng et al., 2002; van Leeuwen et al., 2002; Zhang et al., 2003).

Recent studies have revealed that histone methylation is an essential process required for developmental regulation of the metazoan genome (Bannister et al., 2002; Rice and Allis, 2001; Sims et al., 2003). For example, methylated K9 (H3) is required for proper heterochromatin protein 1 (HP1) binding and heterochromatin formation (Bannister et al., 2001; Fischle et al., 2003; Jacobs et al., 2001; Lachner et al., 2001; Nakayama et al., 2001). In contrast, methylated K4 (H3) is preferentially associated with transcriptionally active chromatin (Kiekhaefer et al., 2002; Litt et al., 2001; Noma et al., 2001) and is enriched in domains surrounding splicing factor compartments (McManus and Hendzel, in preparation). Unfortunately, many of these previous studies fail to distinguish between mono-, di-, or tri-methylated species. Nevertheless, in the few studies that have distinguished between various methylation levels, there does appear to be functional distinctions between them. For example, Santos-Rosa and colleagues (Santos-Rosa et al., 2002) demonstrated that dimethylated K4 (dMeK4) was enriched in active and inactive genes in yeast, while trimethylated K4 (tMeK4) was enriched only in active genes.

Methylation is known to be much more stable than other posttranslational histone modifications. Metabolic studies using radio-labeled isotopic tracers incorporated into the acetyl-, phospho-, or methyl-groups covalently attached to histones, revealed that acetylation and phosphorylation turnover is rapid and can occur within minutes, but that methylation appears much more stable. In fact, several research groups found that the methylation turnover rate was not resolved from the turnover of the histones themselves (Byvoet et al., 1972; Duerre and Lee, 1974; Waterborg, 1993). Due to its stability, histone methylation is an excellent candidate for an epigenetic mark that is faithfully transmitted from mother to daughter cells. However, a limitation of the radio-label studies is that they will not be sensitive to events that occur during short periods of the cell cycle or at specific methylated K residues. Furthermore, some radio-labeled tracer studies have provided evidence for methylation turnover (Annunziato et al., 1995; Borun et al., 1972). For example, Annunziato et al (Annunziato et al., 1995) demonstrated that radio-labeled methyl groups covalently attached to histone H3 in HeLa S3 cells occurred within a population of cells arrested at the G_1/S-boundary. Therefore, it is critical to define the temporal dynamics of the various methylation levels.

To characterize cell cycle-dependent changes in histone methylations we utilized a panel of eight antibodies that specifically recognize different methylated isoforms of K4 and K9 of histone H3 and K20 of histone H4. For all eight modifications analyzed, we document unique distributions within the nucleus as well as changes in methylation content during the cell cycle. These results are paralleled by observations in mid-gestation mouse embryos and non-immortalized mouse primary cultures. Remarkably, we find mitosis-specific methylation cycles for several methylation epitopes. This was most striking for tMeK9 where its levels rapidly increased as cells entered mitosis, attained maximal levels at metaphase and rapidly decreased throughout the remaining stages of mitosis to return to basal levels by cytokinesis. These results provide the first evidence of changes in histone methylation that preclude the faithful transmission of the methylated K residues present in metaphase chromosomes. Furthermore, analysis of mitotic events in cells lacking tMeK9 revealed overall increases in chromosome congression and segregation defects. This finding ascribes a mitosis-specific function for the dynamic increases and decreases of tMeK9.

3.2 RESULTS

3.2.1 *Histone Methylation in Asynchronous Cell Cultures*

To explore the possibility of cell cycle-dependent changes in histone H3 and H4 lysine methylation states, we examined asynchronous HeLa, Indian muntjac (IM) and mouse 10T1/2 cells by indirect immunofluorescence (IIF) using a panel of residue- and methylation level-specific antibodies. The antibodies were deemed to be highly specific for the specified epitope based on IIF peptide competition assays performed *in situ* (Figures 3.1 and 3.2). Asynchronous cells were typically employed as they present all stages of the cell cycle within a single sample and variations in the IIF signal intensities are indicative of potential cell cycle-dependent changes, some of which may be associated with morphologically identifiable cell cycle stages. This approach has been employed previously and identified dramatic and mitosis-specific changes in the abundance of phosphorylated serine 10 of histone H3 (PhosS10) (Hendzel et al., 1997). Figure 3.3 depicts the typical variation in methylation signal intensities amongst asynchronous HeLa populations immunofluorescently labeled with antibodies directed against mono-, di- and tri-methyl modifications at K4 (mMeK4, dMeK4 and tMeK4) and K9 (mMeK9, dMeK9 and tMeK9) of histone H3, and mono- and tri-methyl modification of K20 of histone H4 (mMeK20 and tMeK20). While it is difficult to discern cell cycle-dependent differences in abundance amongst cells labeled with anti-mMeK4, -dMeK4, -tMeK4 and -tMeK20 antibodies (Figure 3.3, A’, B’, C’ and H’), signal intensity variation is readily apparent in cells labeled with anti-mMeK9, -dMeK9, -tMeK9 and -mMeK20 antibodies (Figure 3.3, D’, E’ F’ and G’). In fact, several of the modifications exhibit maximal abundance during mitosis (mMeK9, dMeK9, tMeK9 and tMeK20).

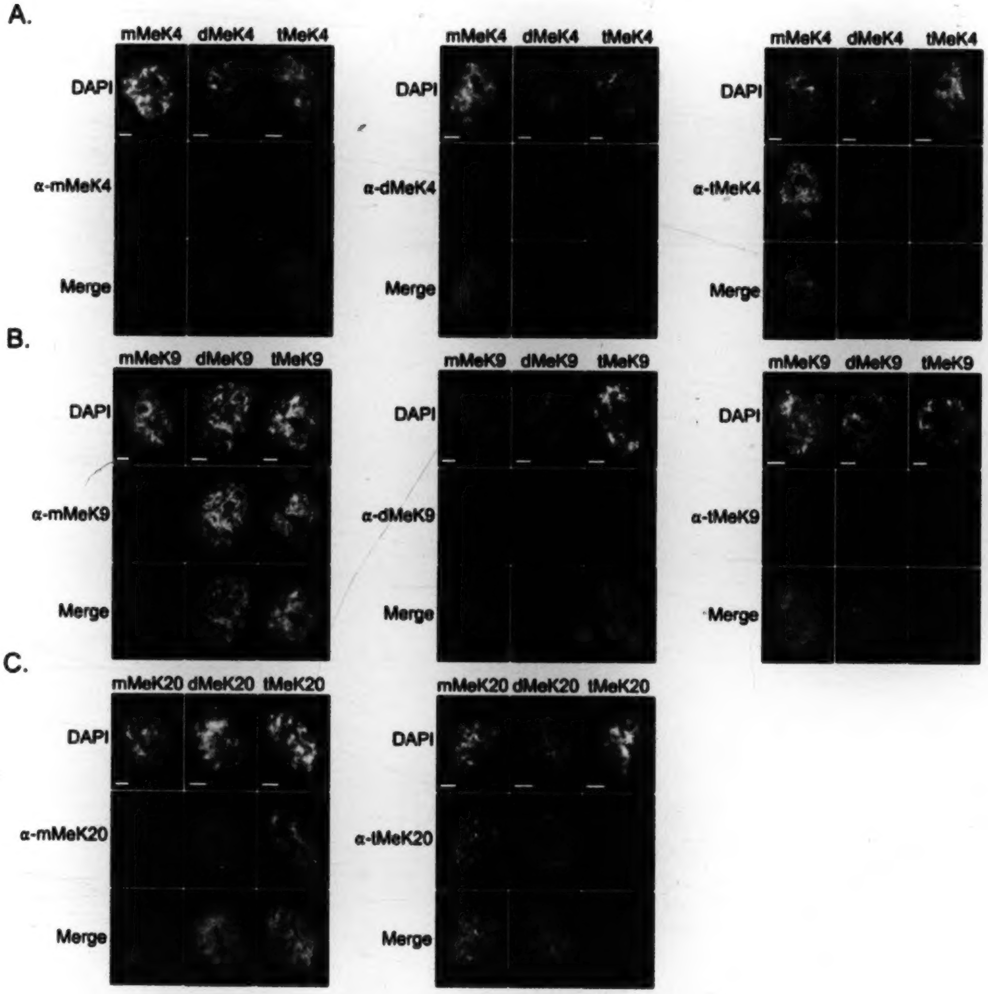
A.
mMeK4 dMeK4 tMeK4
DAPI
α-mMeK4
Merge
mMeK4 dMeK4 tMeK4
DAPI
α-dMeK4
Merge
mMeK4 dMeK4 tMeK4
DAPI
α-tMeK4
Merge
B.
mMeK9 dMeK9 tMeK9
DAPI
α-mMeK9
Merge
mMeK9 dMeK9 tMeK9
DAPI
α-dMeK9
Merge
mMeK9 dMeK9 tMeK9
DAPI
α-tMeK9
Merge
C.
mMeK20 dMeK20 tMeK20
DAPI
α-mMeK20
Merge
mMeK20 dMeK20 tMeK20
DAPI
α-tMeK20
Merge

Figure 3.1: Indirect immunofluorescent peptide competition assays.
Shown here are representative high resolution (100×) images of the peptide competition assays investigating the specificities of the mono-, di- and tri-methylated K4 (panel A) and K9 (panel B), and mono- and tri-methylated K20 (panel C). Indicated at the top of each group are the blocking peptides that were incubated with each antibody indicated in the second row of each group. Included in each group are the DAPI and antibody channels as well as a merged image where the DAPI and antibody channels are presented as red and green, respectively. Within each antibody treatment, identical exposure times for the methylation channel were utilized. Scale bars represent 3 μm.

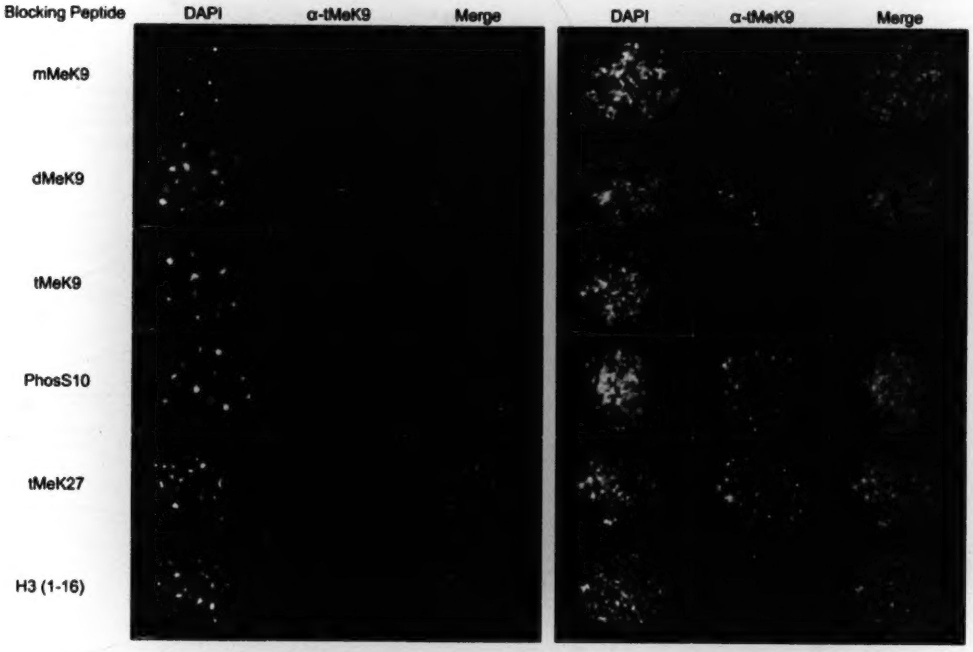
Blocking Peptide
DAPI
α-tMeK9
Merge
DAPI
α-tMeK9
Merge
mMeK9
dMeK9
tMeK9
PhosS10
tMeK27
H3 (1-16)

Figure 3.2: Indirect immunofluorescent peptide competition assays for anti-tMeK9. Depicted here are representative high resolution (100×) images of the peptide competition assays investigating the specificity of anti-tMeK9 in both interphase (left-side) and prophase (right-side) 10T1/2 mouse fibroblast cells. Cells were immunofluorescently labeled with anti-tMeK9 and counterstained with DAPI. The blocking peptides employed are indicated on the left. The merged images show the DAPI (red) and anti-tMeK9 (green). Identical exposure times for all three channels were employed throughout the entire acquisition stage but were independently optimized for the interphase and prophase groups. Scale bar represents 3μm.

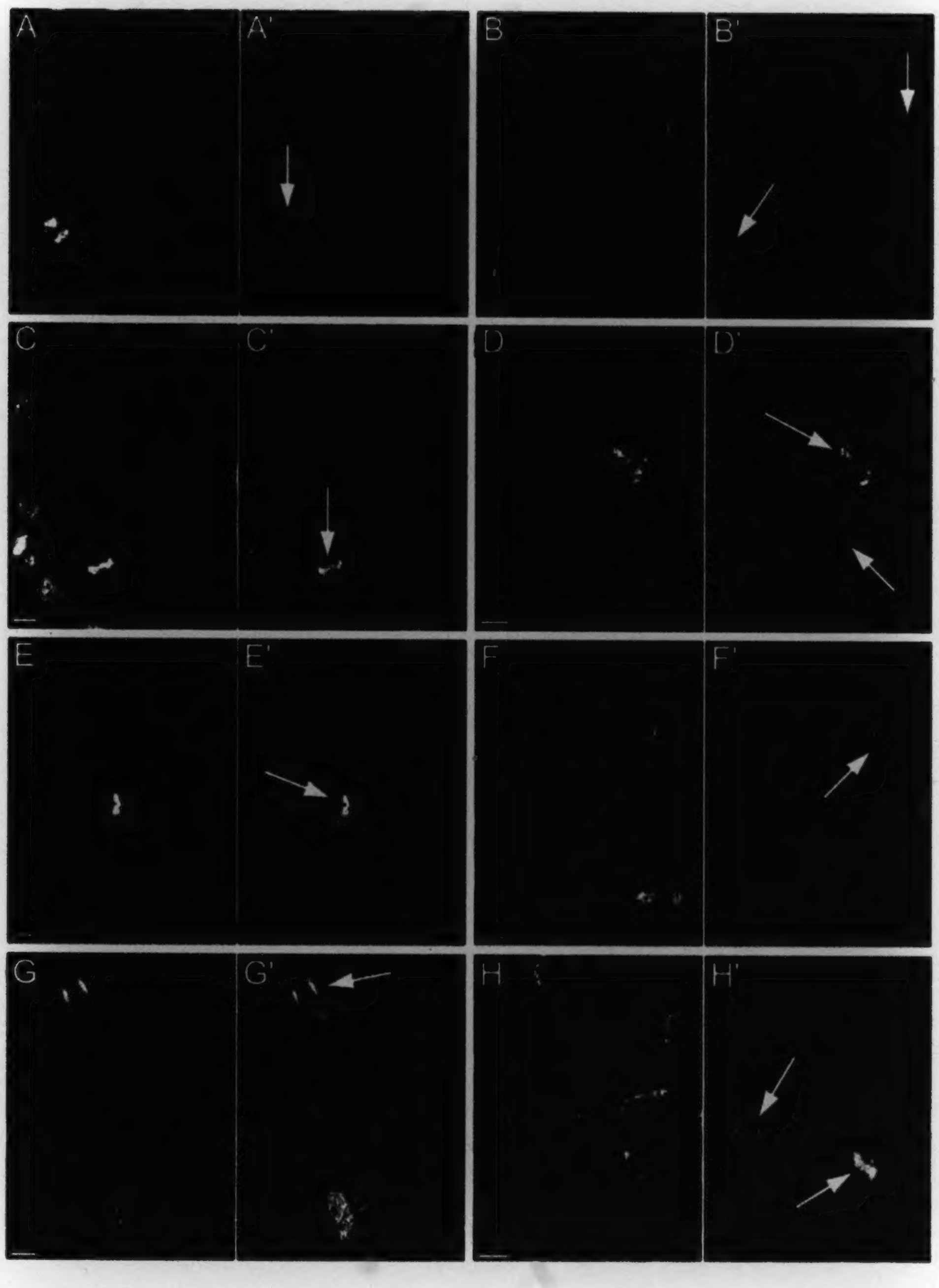

Figure 3.3: Spatial localization and signal intensities of various methylated lysine residues. Representative low-resolution (40×) digital images of HeLa cells immunofluorescently labeled with antibodies directed against mMeK4 (panels A and A'), dMeK4 (panels B and B'), tMeK4 (panels C and C'), mMeK9 (panels D and D'), dMeK9 (panels E and E'), tMeK9 (panels F and F'), mMeK20 (panels G and G') and tMeK20 (panels H and H'). For reference purposes the DAPI channel (A, B, C, D, E, F, G and H) has been included and mitotic cells are identified by white arrows. Scale bar indicates 7μm.

To further evaluate the changes in methylation that may coincide with mitosis, high-resolution (100×) images of 10T1/2 cells were collected at various stages of mitosis (prophase through telophase). For illustrative and comparative purposes only, each panel of Figure 3.4 contains one mitotic cell and at least one interphase cell for each of the methylation antibodies. The cells have been counterstained with DAPI to reveal DNA and facilitates a simple visual comparison of signal intensities between mitotic and interphase populations. The signal intensities of four modifications, mMeK9, dMeK9 tMeK9 and mMeK20, appear to be significantly greater in the mitotic cells than in the interphase cells (Figure 3.4). In the case of tMeK9, the increase was particularly striking as minimal signal intensities were observed in interphase cells (Figure 3.4). To more accurately depict the mitosis-specific increases associated with tMeK9, HeLa cells at various stages of cell cycle were qualitatively imaged (Figure 3.5). As cells progressed from late G_2 into prophase, there was a corresponding increase in overall tMeK9 signal intensities. Maximal tMeK9 signal intensities were reached at metaphase, where upon transition into anaphase, levels began to rapidly decrease until returning to basal levels by cytokinesis or early G_1. Similar results were also observed for 10T1/2 and IM cells (data not shown). Interestingly, in late G_2 or early prophase, tMeK9 (Figures 3.4 and 3.5) and tMeK20 (Figure 3.4) staining appeared in micro-punctate regions along the chromosome arms, but was particularly enriched within pericentromeric heterochromatin.

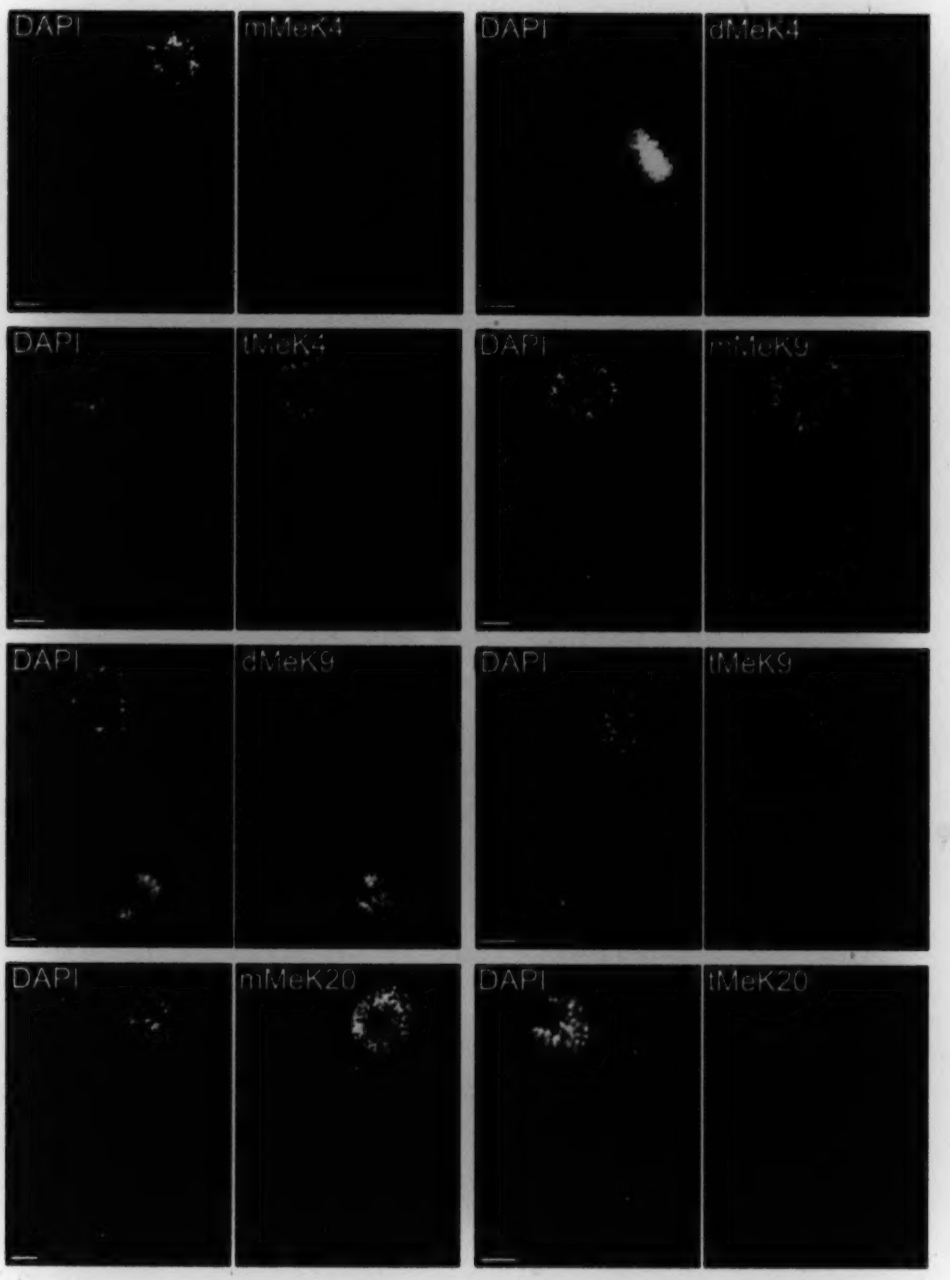
DAPI
mMeK4
DAPI
dMeK4
DAPI
tMeK4
DAPI
mMeK9
DAPI
dMeK9
DAPI
tMeK9
DAPI
mMeK20
DAPI
tMeK20

Figure 3.4: High-resolution images of various lysine methylation epitopes in mouse cells. Representative digital images of 10T1/2 cells immunofluorescently labeled with antibodies directed against mMeK4, dMeK4, tMeK4, mMeK9, dMeK9, tMeK9, mMeK20 and tMeK20. For reference purposes at least one mitotic cell (prophase to metaphase) has been included for signal intensity comparisons with the interphase cells. The DAPI channel has been included and pericentromeric heterochromatin is visible as DAPI intense staining regions. Scale bar represents 3μm.

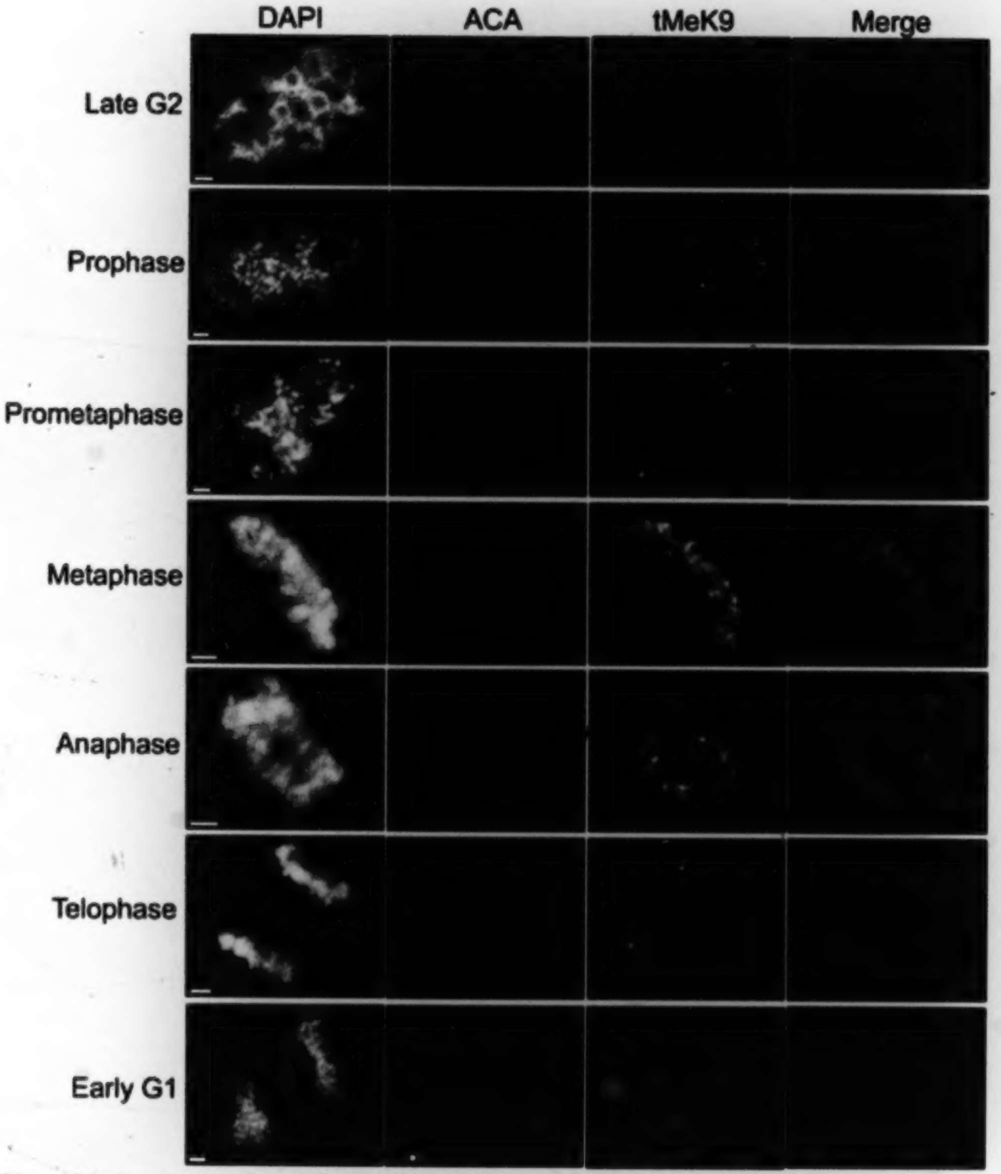
DAPI
ACA
tMeK9
Merge
Late G2
Prophase
Prometaphase
Metaphase
Anaphase
Telophase
Early G1

Figure 3.5: Temporal and spatial progression pattern of tMeK9 through mitosis.
Asynchronous HeLa cells were paraformaldehyde-fixed, immunofluorescently labeled with anti-tMeK9 and anti-ACA (anti-centromeric antigen) and counter-stained with DAPI. Images were collected as z-series and only a single representative plane is presented. The tMeK9 signal intensity differences are qualitative between all images as that channel information was collected with identical exposure times. Merge image presents ACA (green) and tMeK9 (red). Scale bar represents 3μm.

Surprisingly, the temporal progression pattern of tMeK9 closely resembles that of PhosS10, its neighboring residue. Because there is a possibility that the reactivity of the anti-tMeK9 antibody may be influenced by the presence or absence of PhosS10, we sought to establish whether the anti-tMeK9 antibody would still recognize its cognate epitope in the absence of PhosS10. Therefore, we developed a calf intestinal alkaline phosphatase (CIP) assay that is performed *in situ*. Live 10T1/2 cells were permeabilized and treated with or without CIP, paraformaldehyde fixed and immunofluorescently labeled with anti-tMeK9. Unfortunately, due to unfavorable combination of the natural occurrence of rounding up of mitotic cells and Saponin permeabilization, most mitotic cells (prometaphase to telophase) detached from the coverslips (data not shown). However, prophase cells remained adhered to the coverslips and exhibited robust anti-tMeK9 immuno-staining in both the presence and absence of PhosS10 (Figure 3.6). Furthermore, these prophase anti-tMeK9 signal intensities were visually more intense than those of interphase cells on the same coverslips (data not shown). These results establish that the phosphorylation status of S10 does not adversely influence the immunoreactivity of the anti-tMeK9 antibody. It further verifies that tMeK9 does exhibit temporal dynamics that are associated with mitosis.

DAPI
PhosS10
tMeK9
Control
DAPI
PhosS10
tMeK9
CIP

Figure 3.6: Phosphatase-treatment does not diminish anti-tMeK9 immunoreactivity. Depicted here are representative DIM images (100×) of 10T1/2 cells treated with Saponin with (CIP) or without (control) calf intestinal alkaline phosphatase (CIP) and immunofluorescently labeled with both anti-PhosS10 and anti-tMeK9. The prophase 10T1/2 fibroblast CIP-treated cell was specifically selected, as it should normally exhibit a dramatic increase in PhosS10 immuno-staining over interphase cells, particularly within pericentromeric heterochromatin. Identical exposure times were used in the top two rows for the DAPI and tMeK9 channels, while a 5-fold increase in exposure time was employed for the CIP-treated PhosS10 signal versus the PhosS10 control channel. Scale bars is 3μm.

The histone methyl derivatives were also evaluated for their distributions within chromatin and chromosomes. Remarkably, each methyl derivative was restricted to foci or elongated foci/fibers during interphase and exhibited discrete localizations within mitotic chromosomes. Furthermore, cells labeled with anti-tMeK4 and anti-tMeK9 exhibited distinct chromosome micro-banding patterns that were present from prometaphase through to anaphase. These banding patterns occurred along the entire length of the chromosome arms and were not restricted to the centromeres (Figure 3.7). The differential banding patterns for the various methylation epitopes serves to demonstrate fundamental differences in the activities and targeting of the upstream HMTs and indicates that they function specifically within defined regions of the chromatin.

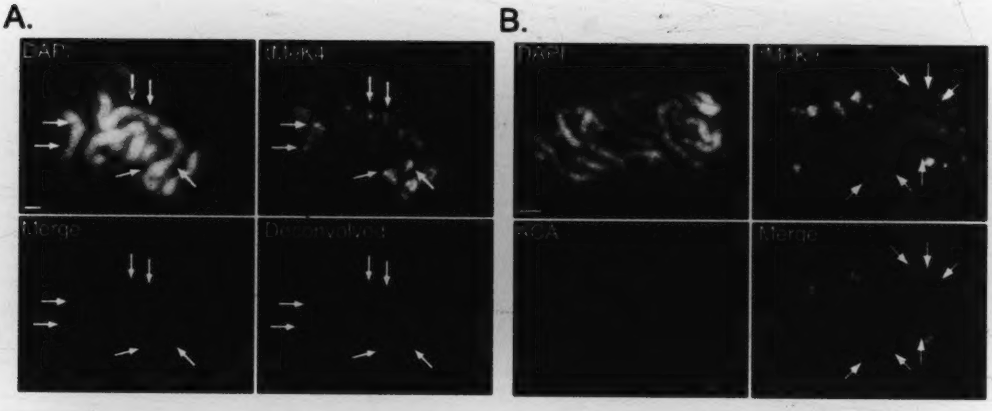

Figure 3.7: Chromosome banding patterns of tMeK4 and tMeK9.
Digital images depicting tMeK4 (A) and tMeK9 (B) chromosome banding patterns in Indian muntjac fibroblasts. Panel A depicts the banding pattern of tMeK4 and includes the DAPI channel for reference purposes. In the merged and deconvolved images, tMeK4 and DAPI are represented in red and blue, respectively. Panel B depicts the chromosome banding pattern of tMeK9. Anti-ACA (identifies pericentromeric heterochromatin) has been included to demonstrate that the banding pattern is both dependent and independent of pericentromeric heterochromatin. The merged image is a composite of the tMeK9 channel (red) and the ACA channel (green). In both panels, arrows identify specific bands present in the methylation channels that reside within regions of less intensity within the DAPI channel. Scale bar represents 2μm.

3.2.2 *Epitope Accessibility is Not Responsible for Qualitative Differences in Methylation Status*

Perhaps the most obvious explanation for the IIF results detailed above is the mitotic dissociation of proteins (e.g. HP1) which may bind to, and mask, a subset of the epitopes during interphase. This hypothesis can be easily examined by immunoblotting protein preparations isolated at specific stages of the cell cycle where any such proteins will be displaced during SDS PAGE. To establish that changes in epitope accessibility are not the principal determinant of the methylation dynamics observed, immunoblotting was carried out on acid-extracted proteins isolated from asynchronous and mitotically-enriched populations. In asynchronous HeLa cells, approximately 55.2 ± 0.8% of cells were in G_0/G_1, 16.9 ± 0.8% were in S-phase and 26.7 ± 1.2% were in G_2/M when assessed by flow cytometry. Following overnight treatment with nocodazole, a 3.4-fold increase in the proportion of cells in G_2/M was observed (91.1 ± 1.6%), while those in G_0/G_1 (3.6 ± 1.3%) and S-phase (5.4 ± 0.6%) were markedly decreased. Equivalent protein amounts from these populations were immunostained by immunoblotting to assess cell cycle-associated differences in the histone methylation derivatives. The results obtained are presented in Figure 3.8 and can be generally grouped into three distinct populations; a) those that exhibited increased signal intensities in the mitotically-enriched population relative to the asynchronous population (mMeK9, tMeK9 and mMeK20), b) those with equivalent signal intensities (tMeK4 and tMeK20) and, c) those with decreased signal intensities in the mitotic population compared with the asynchronous population (mMeK4, dMeK4 and dMeK9). Two additional methods for generating mitotically-enriched populations were employed, double thymidine block

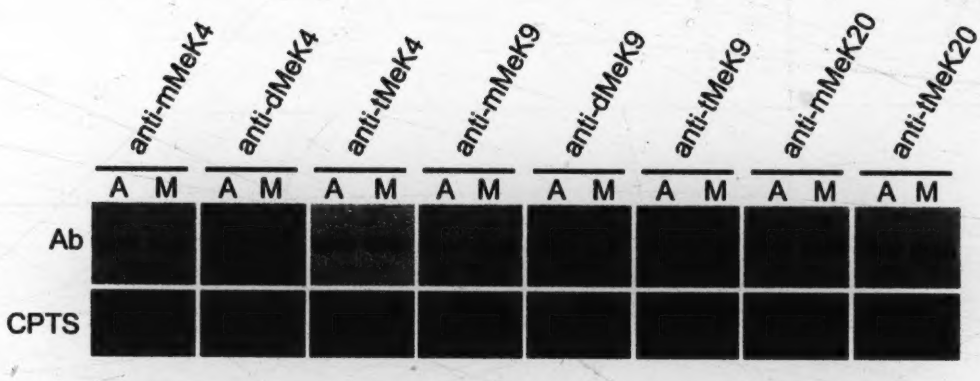
anti-mMeK4
anti-dMeK4
anti-tMeK4
anti-mMeK9
anti-dMeK9
anti-tMeK9
anti-mMeK20
anti-tMeK20
A M
A M
A M
A M
A M
A M
A M
A M
Ab
CPTS

Figure 3.8: Qualitative assessment of the abundance of various methylated lysine residues at different cell cycle stages.
Immunoblot analysis of nuclear proteins isolated from asynchronously-growing (A) or mitotically-arrested (M) cells were resolved on 15% SDS polyacrylamide gels and immunostained with the antibodies indicated (top). Shown here are representative results from one of three independent experiments. The upper panel (Ab) presents the antibody signal while the lower panel (CPTS) confirms equivalent protein loading as demonstrated by CPTS-staining of the PVDF membrane. Qualitative comparisons of methylation signal intensities can only be made within each given antibody treatment.

followed by either a 4 hr nocodazole or ALLN treatment, and yielded very similar results (data not shown). Remarkably, these immunoblotting results parallel changes in histone methylation status quantified *in situ* by IIF and establishes that both assays are detecting changes in total chromatin methylation. Furthermore, these data demonstrate that methylated lysine-binding proteins (e.g. HP1) and chromatin structure are not the basis of the observed changes in methylation content.

3.2.3 *Global Histone Methylation Dynamics Throughout the Cell Cycle*

The qualitative IIF and immunoblotting analyses detailed above identify the presence of a robust methylation process as cells enter mitosis. They further demonstrate that some methylations are lost as cells exit mitosis prior to cell division. To better understand the methylation dynamics observed in mitosis relative to the steady-state levels during interphase, we examined each of the eight methylation epitopes by flow cytometry (Figure 3.9). If methylation is indeed stable, we expect to only find evidence of a 2-fold increase in total chromatin methylation over the entire course of a cell cycle with the principal methylation intensity decrease corresponding with the 4N to 2N reduction of the genome during cytokinesis. Surprisingly, only one methyl modification, dMeK4, closely matched the expected distribution of a stable mark that is maintained in S-phase (Figure 3.9, B and K). These relationships are more apparent when we express mean intensities and standard deviation at different stages of the cell cycle (G_0/G_1, S-phase and G_2/M) after normalizing for DNA content (Supplementary Tables 1 and 2 [Appendix B]). When expressed this way, the mMeK9, tMeK9 and mMeK20 modifications produce peak intensities in G_2/M that are disproportionately higher than the 4N DNA content.

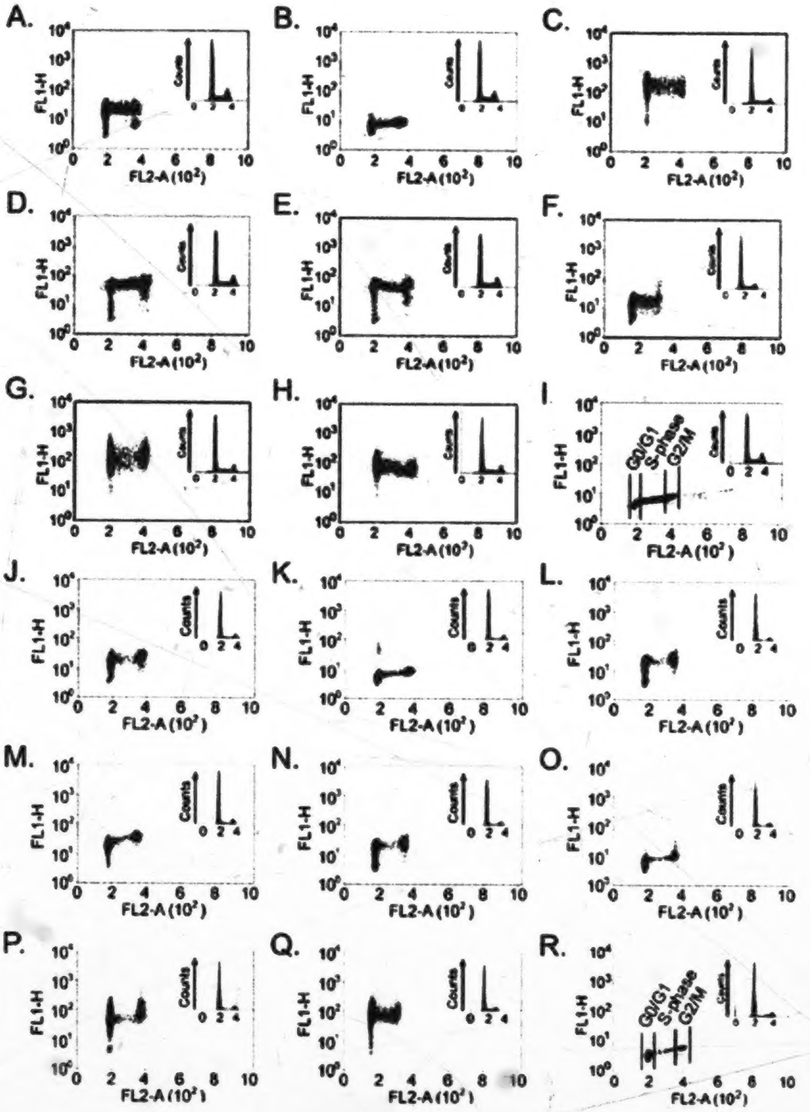

Figure 3.9: Cell cycle-dependent progression patterns of methylation epitopes as demonstrated by flow cytometry.

HeLa (panels A to I) and 10T1/2 (panels J to R) cells were ethanol-fixed, counterstained with PI to reveal cell cycle status and immunofluorescently labeled with each of the eight methylation antibodies; mMeK4 (panels A and J), dMeK4 (panels B and K), tMeK4 (panels C and L), mMeK9 (panels D and M), dMeK9 (panels E and N), tMeK9 (panels F and O), mMeK20 (panels G and P), and tMeK20 (panels H and Q). Panels I and R are PI-only controls. Shown here is one of three representative experiments. Each panel plots the fluorescent intensity of the methylation antibody (FL1-H) in arbitrary units against the PI or DNA fluorescent intensity (FL2-A) in arbitrary units. The inset in each panel has been included to demonstrate that the cells were actively cycling and provides relative cell counts at each cell cycle stage (G_0/G_1, S-phase and G_2/M). Panels I and R (controls) delineate the G0/G1, S-phase and G2/M populations that can be extrapolated to the corresponding graphs. See text for details.

Although the results depicted in Figure 3.9 and presented in Supplementary Tables 1 and 2 [Appendix B] are consistent with cell cycle-associated changes in methylated histone content, the variability within any given cell cycle population complicated a direct interpretation of these results. To better understand the relationship between the abundance of a specific modification and the cell cycle, statistical analyses were performed. Analysis of variance (ANOVA) of unweighted means was calculated for all methylation epitopes in 10T1/2 cells and is presented in Table 3.1. Similar results were obtained in HeLa cells (data not shown). In each case, the null hypothesis (H_0) that all cell cycle stages exhibit similar mean signal intensities was rejected. These results indicate that at least one cell cycle population mean for each epitope investigated differs significantly from the others. The large F-ratios calculated for mMeK9 (10340), mMeK20 (1286) and dMeK9 (1329) argues that the variability between cell cycle populations is greater than the variability within a specific cell cycle population. Conversely, the small F-ratio calculated for tMeK20 (10.34) indicates that the variability within any given cell cycle population is greater than the variability between them. To examine whether these differences were statistically significant, pair-wise Tukey-Kramer multi-comparison post-tests were performed for each methylation epitope. For all epitopes and between all groups (e.g. G_0/G_1:S-phase, G_0/G_1:G_2/M and S-phase:G_2/M), statistically significant differences ($p < 0.05$) were observed (Supplementary Table 3 [Appendix B]). This was most apparent for mMeK9 and dMeK9 where calculations for all pair-wise comparisons yielded highly significant *p*-values that were less than 0.001. These results validate the previous observations and clearly establish that unique cell cycle dynamics occur for many of the methylation epitopes.

Table 3.1: Analysis of variance of unweighted means for methylated histone epitopes in 10T1/2 cells as measured by flow cytometry.

Epitope	Group[a]	SS[b]	df[c]	MS[d]	F-Ratio[e]	*p*-value	Reject H_0[f]
mMeK4	BG	67890	2	33940	700.4	<0.0001	Yes
	WG	842700	17388	48.47			
dMeK4	BG	30180	2	15090	187.5	<0.0001	Yes
	WG	1416000	17595	80.46			
tMeK4	BG	4648000	2	2324000	618.5	<0.0001	Yes
	WG	63930000	17015	3757			
mMeK9	BG	818700	2	409400	10340	<0.0001	Yes
	WG	693100	17499	39.61			
dMeK9	BG	124000	2	62020	1329	<0.0001	Yes
	WG	793900	17008	46.68			
tMeK9	BG	65760	2	32880	758.9	<0.0001	Yes
	WG	735700	16979	43.33			
mMeK20	BG	5161000	2	2581000	1286	<0.0001	Yes
	WG	35220000	17548	2007			
tMeK20	BG	82660	2	41330	10.34	<0.0001	Yes
	WG	67060000	16771	3999			

[a] Defines whether or not the analysis is between groups (BG) or within the groups (WG)

[b] SS represents the sum of squares

[c] df represents degrees of freedom

[d] MS represents the mean square

[e] F-ratio is calculated by MS_{BG}/MS_{WG}

[f] The null hypothesis (H_0) is rejected if the *p*-value is <0.05

3.2.4 *Quantitative Imaging Microscopy Identifies Mitosis-Specific Methylation and Demethylation Cycles in Cycling Cells*

The previous sections demonstrate that the most striking changes in methylation occur as cells enter and exit mitosis. To precisely define the temporal progression throughout mitosis, quantitative imaging microscopy (QIM) was performed, which has several distinct advantages over conventional flow cytometry. For example, when comparing identical immunofluorescently labeled nuclear proteins, fluorescence microscopy has a much higher signal to noise ratio than flow cytometry. This is due to more robust staining and lower background from autofluorescence or non-specific fluorescent antibody binding. Perhaps the greatest advantage of QIM is that morphological criteria can be employed to subdivide the cell cycle into distinct stages (e.g. prophase, prometaphase, metaphase, etc.) without the requirement of drug-induced cell cycle arrest. Most importantly, QIM provides a temporal resolution capability during mitosis that is on the order of minutes, something that is not possible using conventional synchronization-dependent biochemical approaches. For any given antibody treatment, quantitative measurements of individual channels (e.g. DAPI, Alexa Fluor-488 or Cy3) are made and compared using statistical methods. QIM was performed in 10T1/2 cells for all eight methylation epitopes. However, the data were first normalized to account for histone variability that occur as cells progress through the cell cycle. This was accomplished by generating the ratio of the methylation epitope total signal intensity (TSI) to that of the DAPI total signal intensity (e.g. tMeK9 TSI:DAPI TSI) for all nuclei imaged (Figure 3.10).

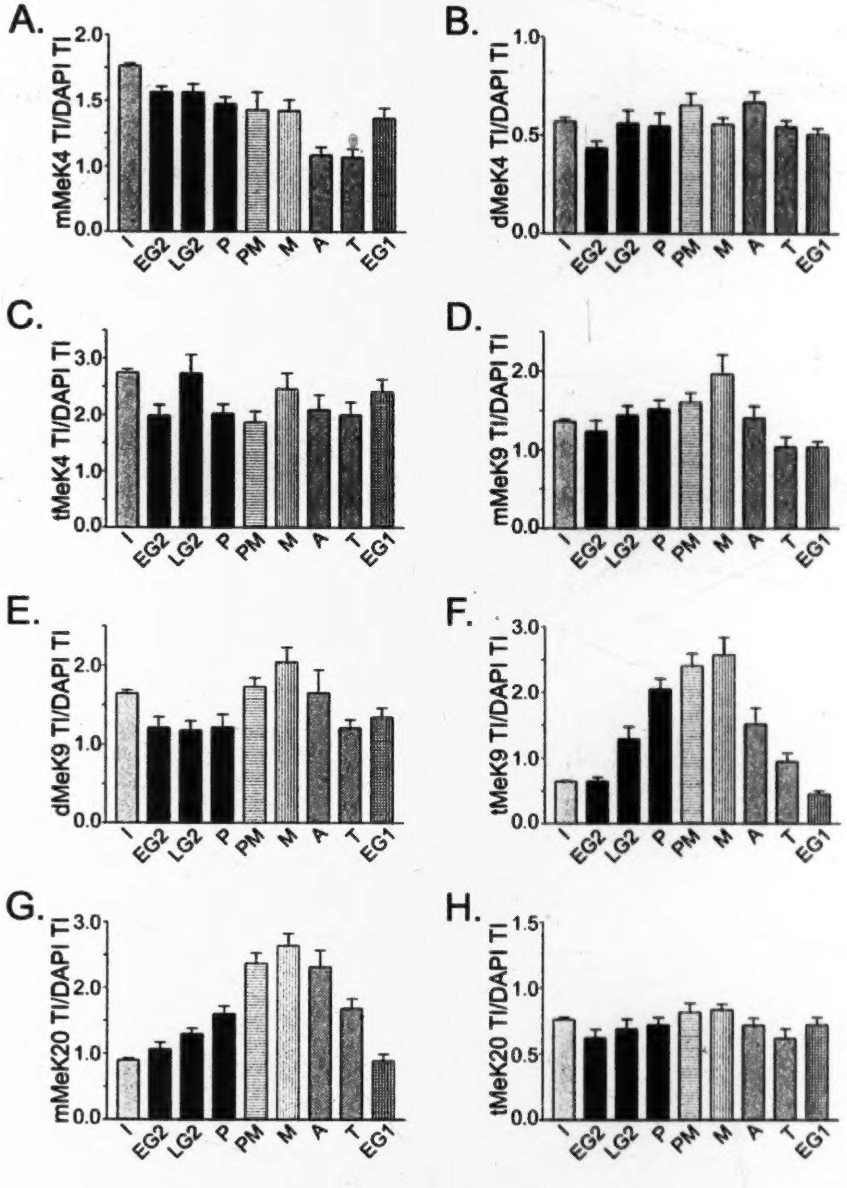

Figure 3.10: Quantitative comparisons of normalized methylation signal intensities at specific cell cycle stages.

QIM was performed on 10T1/2 cells immunofluorescently labeled with each methylation antibody; mMeK4 (panel A), dMeK4 (panel B), tMeK4 (panel C), mMeK9 (panel D), dMeK9 (panel E) tMeK9 (panel F), mMeK20 (panel G) and tMeK20 (panel H). For each antibody, cells were classified as belonging in one of nine distinct cell cycle stages: interphase (I), early G_2 (EG2), late G_2 (LG2), prophase (P), prometaphase (PM), metaphase (M), anaphase (A), telophase (T) and early G_1 (EG1). Depicted here are the mean normalized methylation signal intensities (represented as the mean methylation total intensity (TI)/mean DAPI TI) at each specific cell cycle stage ± the standard error of the mean (SEM).

From these analyses, three distinct classes of methylation temporal progression patterns emerged. The most prevalent class was one in which an increase in normalized-methylation (Norm-Me) signal intensities was observed that accompanied the entry of cells into mitosis (mMeK9, dMeK9, tMeK9 and mMeK20). In this group, Norm-Me signal intensities reached maximal abundance at metaphase and began to decrease as cells entered anaphase. The Norm-Me signal intensities continued to decrease throughout the later stages of mitosis, until basal steady-state levels were present by late telophase or early G_1. Within this group, the largest difference in Norm-Me signal intensities between interphase and metaphase occurred with tMeK9 where a 4.0-fold difference was observed (Supplementary Table 4 [Appendix B]). The smallest difference observed was for dMeK9 at 1.3-fold, while the differences for mMeK9 and mMeK20 were 1.4- and 2.9-fold, respectively. The second class of methylation patterns were those in which a steady decline in the Norm-Me signal intensity (mMeK4) accompanied progression through mitosis with minimal intensities occurring during anaphase and telophase. The largest difference in mean Norm-Me intensities was 2.2-fold and occurred between interphase and telophase populations. The final class of methylation patterns did not reveal any appreciable increase or decrease in Norm-Me signal intensities (dMeK4, tMeK4 and tMK20), although some heterogeneity did occur between cell cycle stages. Subsequent ANOVA analyses and Tukey-Kramer multi-comparison post-tests for each methylated epitope validated the relationships characterized above, and confirmed that significant changes in the abundance of mMeK20 and tMeK9 accompany the entry and the exit of cells from mitosis (Supplementary Tables 5 and 6 [Appendix B].

3.2.5 *Replication-Independent Nucleosome Assembly Does Not Account for the Dramatic Decrease in tMeK9 Abundance in the Late Stages of Mitosis*

Over two decades ago, it was recognized that histones can be deposited into chromatin outside of S-phase or DNA replication (Louters and Chalkley, 1984; Louters and Chalkley, 1985; Urban and Zweidler, 1983). Subsequent investigations have demonstrated that histone H3.3, a specialized histone H3 variant, can replace chromatinized H3 in an S-phase independent, but transcription-related, manner (Ahmad and Henikoff, 2002; Jackson, 1990; Waterborg, 1993). Because tMeK9 localizes predominantly within pericentromeric heterochromatin and the loss of methylation occurs during mitosis when the genome is transcriptionally silent, it appears extremely unlikely that H3.3 deposition accounts for the loss of tMeK9 during the later stages of mitosis. Nevertheless, since H3.3 is the major H3 variant available for replacement during this time, it remains possible that a novel exchange mechanism could exist that preferentially incorporates H3.3 into pericentromeric heterochromatin. To investigate this possibility, high-resolution DIM coupled with deconvolution was performed on HeLa cells co-immunofluorescently labeled with anti-H3.3 and pericentromeric heterochromatin as identified by anti-anticentromeric antigen (anti-ACA) staining. Cells in G_1 were specifically selected for this analysis, as they would potentially contain the greatest quantity of chromatinized H3.3. Not surprisingly, little if any colocalization was observed between ACA and H3.3 in either HeLa or 10T1/2 cells (data not shown).

Next, 3D colocalization analysis was performed using high-resolution (100×) deconvolved images acquired of HeLa and 10T1/2 G_1 nuclei immunofluorescently labeled with anti-ACA and anti-H3.3. Correlation coefficients were calculated to identify potential relationships, either positive [R = +1] or negative [R = -1]), between histone H3.3 and ACA/pericentromeric heterochromatin. As anticipated, no significant association between histone H3.3 and pericentromeric heterochromatin (anti-ACA) was apparent as the correlation coefficients approached 0 and were 0.0925 ± 0.1709 (N = 11) and 0.1195 ± 0.1655 (N = 12) for HeLa and 10T1/2, respectively. This is in stark contrast to the significant correlation coefficient calculated between tMeK9 and ACA (HeLa = 0.6045 ± 0.1221 [N = 12]; 10T1/2 = 0.7275 ± 0.02678 [N = 11]). Student *t*-tests yielded highly statistically significant differences (*p*-value <0.0001) between mean correlation coefficients from the respective pairings (i.e. ACA with histone H3.3 and ACA with tMeK9) for both HeLa and 10T1/2 cell lines. Therefore, replication-independent nucleosome assembly, or the incorporation of histone H3.3 outside of S-phase cannot account for the dramatic decrease in tMeK9 that occurs in late mitosis. Moreover, the general absence of colocalization between ACA and H3.3 at any stage of the cell cycle, including anaphase and telophase, further strengthens the argument that histone H3.3 replacement during the late stages of mitosis is not responsible for the dramatic decrease in tMeK9 that occurs between anaphase and early G_1.

3.2.6 *Dynamic Methylation of Lysine Residues in Developing Mouse Embryos and Primary Tissue Cultures*

To extend our tissue culture observations to an *in vivo* model system, the methylation status of cells from mid-gestation mouse embryos (E9.5) and non-immortalized primary tissue cultures was examined. In both cases, cell cycle-dependent changes in methyl modifications paralleled those observed in the tissue cultures (data not shown). However, these analyses also revealed unique developmental phenomena for several of the epitopes that are detailed elsewhere (see Biron et al., 2004). Perhaps the most striking observation was that the cell cycle-dependent changes observed for tMeK9 in the tissue cultures were exaggerated within the mouse embryo tissue sections. As detailed above, the most robust tMeK9 staining occurred between prophase and metaphase (Figure 3.11). Upon entry into anaphase the abundance of tMeK9 began to decline until basal levels were reached in interphase. Upon quantification, ratios of Norm-tMeK9 signal intensities between metaphase (0.1464) and either early G_1 (0.02502) or interphase (0.02044) were 5.85 and 7.16, respectively, which represents an approximately 15-fold increase in total tMeK9 when considered independent of DNA normalization. These results demonstrate the dynamic changes in tMeK9 observed in mitosis are not specific to tissue culture cells and that the differences appear to be exacerbated *in vivo* in mid gestation embryos.

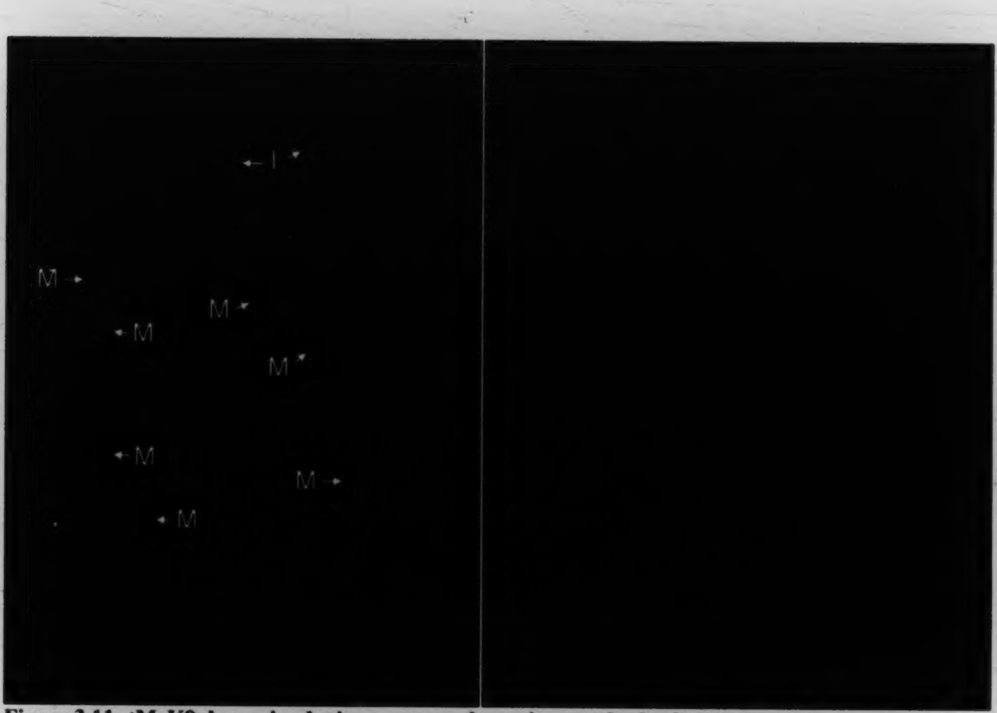

Figure 3.11: tMeK9 dynamics during mouse embryonic neural tube development.
A 3D image was collected of the neural tube of a day E9.5 mouse embryo stained with anti-tMeK9. The 3D image was subjected to deconvolution and is presented as a 2D projection. DNA is counterstained with DAPI (red), while tMeK9 labeling is in green. Shown here is the developing neural tube with the lumen localizing to the central black region devoid of cells. Note the dramatic increase in tMeK9 staining in mitotic cells compared with extremely weak staining in interphase cells. Due to the difficulty in assessing cell cycle stages from a 3D embryonic section projected in 2D, the following stages are identified by letters and arrows: I (interphase) and M (mitosis).

3.2.7 *Cells Lacking tMeK9 Exhibit a Wide Range of Abnormal Mitotic Phenotypes*

Previous investigations by Peters et al (2001) demonstrated that deletion of the HMTs responsible for tMeK9 in mice, namely Suv39h1 and Suv39h2, resulted in increased aneuploidy, or more specifically, increases in ploidy levels (e.g. 4N and 8N). The underlying defect manifesting in increased genomic instability was not examined in the Suv39h1/2 double null (dn) primary mouse embryonic fibroblasts (MEFs). However, Peters *et al* (2001) did observe a failure of the centromeres to segregate properly during mitosis resulting in a so-called "butterfly" chromosome morphology. To further address the functional role of tMeK9 in chromosome congression to, and chromosome segregation from, the metaphase plate, we examined mitoses in cells lacking tMeK9 within pericentromeric heterochromatin. We examined mitotic events in control (W8) and Suv39h1/2 dn (D5) immortalized MEFs (IMEFs). Cells lacking Suv39h1/2 have previously been shown to be devoid of tMeK9 staining in pericentromeric heterochromatin. We confirmed this observation with our anti-tMeK9 antibody (Figure 3.12) which further served to demonstrate the specificity of that antibody. We investigated the potential role of tMeK9 in chromosome dynamics during mitosis by investigating aberrant phenotypes associated with metaphase, anaphase, telophase and cytokinesis/early G_1 in mouse Suv39h1/2 dn immortalized MEFs (D5) and compared them with control IMEFs (W8). Aberrant mitotic phenotypes were observed during many mitotic stages and included misaligned chromosomes in metaphase, non-disjunction in anaphase, lagging chromosomes in telophase and the appearance of micronuclei at cytokinesis or early G_1 (Figure 3.13). Next, we manually scored the normal and aberrant phenotypes in both D5 (Suv39h1/2 dn IMEFs) and W8 cells and the

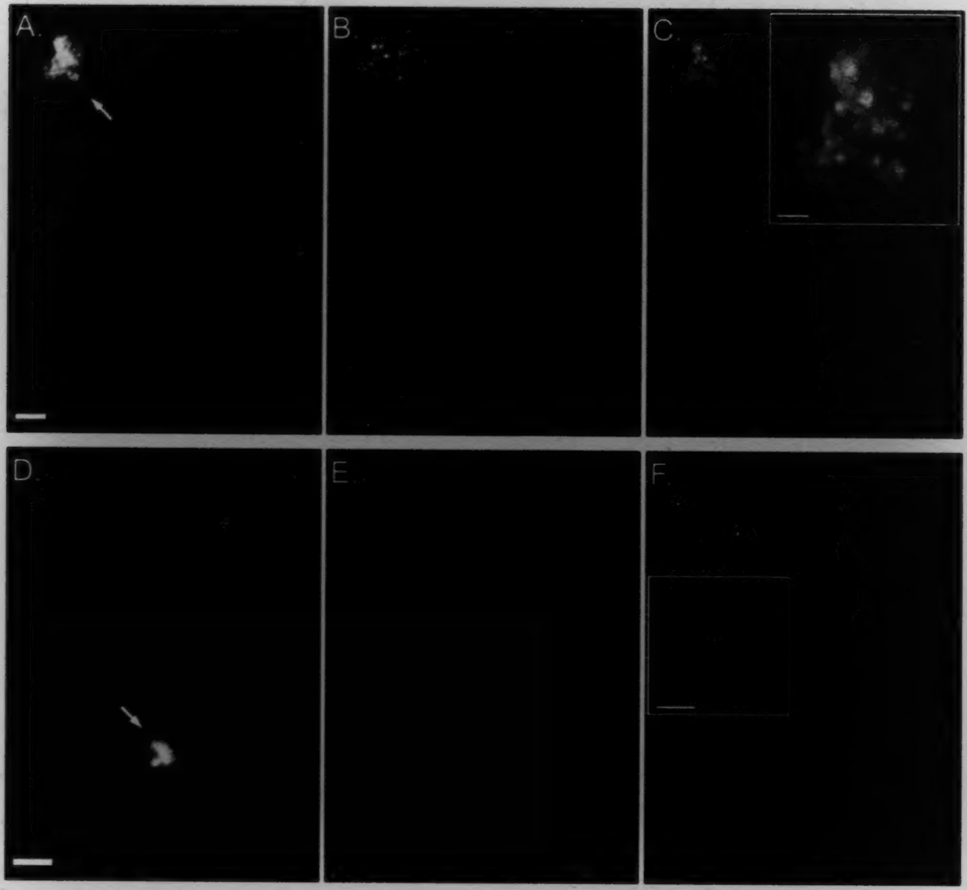

Figure 3.12: Suv39h1/2 dn IMEFs are devoid of tMeK9 in pericentromeric heterochromatin. Asynchronous control (W8 – panels A to C) and Suv39h1/2 (D5 – panels D to F) IMEF cells were immunofluorescently labeled with anti-tMeK9 (panels B and E) and the DNA was counterstained with DAPI (panels A and D). The merged images are shown in panels C and F with red and green representing DAPI and anti-tMeK9, respectively. High-resolution images of the mitotic cells are included in the insets of panels C and F. Identical exposure times were employed in all channels during acquisition and emphasize the dramatic loss of tMeK9 within the pericentromeric heterochromatin of D5 cells (panels E and F). Scale bars in panels A and D are 8μm while those in the insets of panels C and F are 2μm.

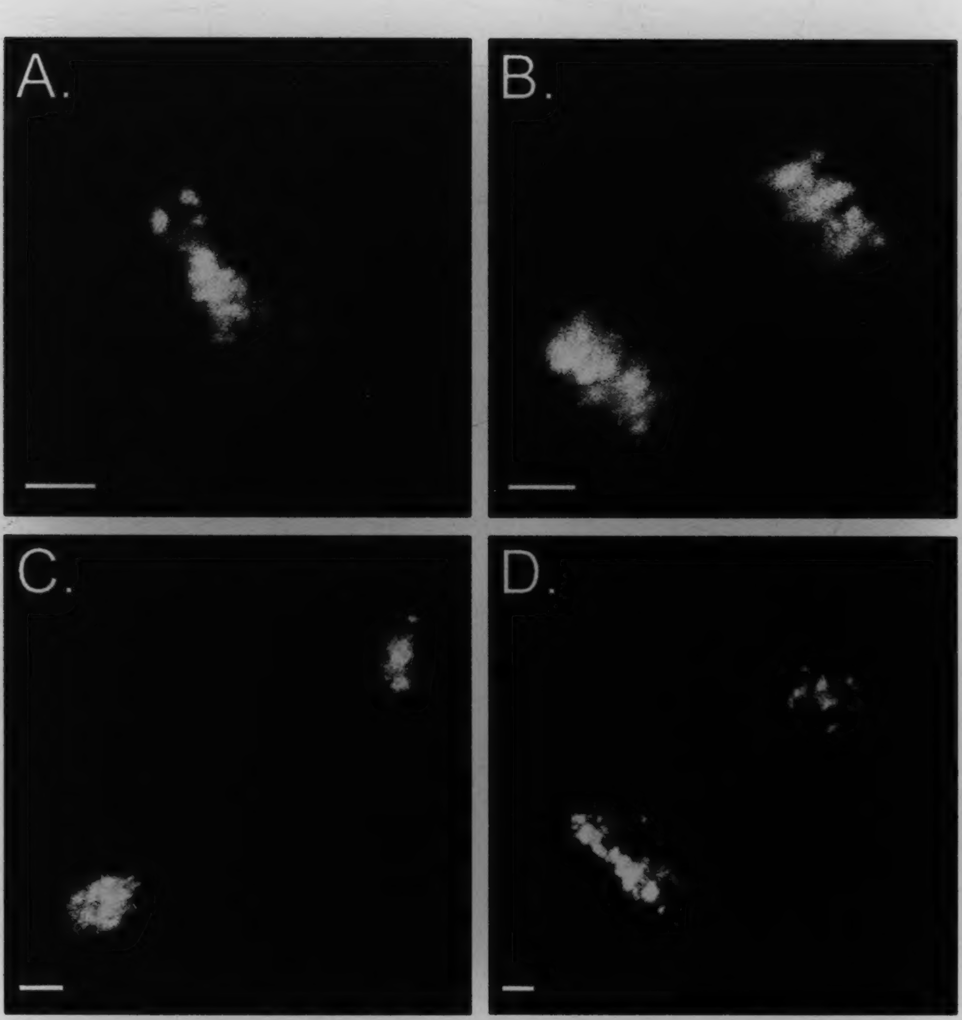

Figure 3.13: Typical abnormal mitotic phenotypes observed in the absence of tMeK9 (H3)
High-resolution (100×) digital image micrographs of representative abnormal mitotic phenotypes associated with the lack of tMeK9 in mouse IMEFS. Suv39h1/2 dn IMEFs were fixed and counterstained with DAPI to reveal mitotic abnormalities. Depicted here are 3D projections of misaligned chromosomes during metaphase (panel A), nondisjunction during anaphase (panel B), lagging chromosome during telophase (panel C) and lagging chromosomes and the appearance of micronuclei in cytokinesis or early G1 (panel D).

results are summarized in Table 3.2. In all cell cycle stages investigated, between 3.3- and 5.2-fold increases in aberrant phenotypes were observed in the D5 cells as compared with the W8 controls (Table 2). The greatest increase in aberrant phenotypes occurred in telophase (5.55-fold increase), where lagging chromosomes were most frequently observed, while the smallest increase in aberrant phenotypes was associated with anaphase (3.33-fold increase). Unlike Peters *et al* (2001), we did not observe any of the "butterfly" chromosomes occurring in the lymphocytes of the Suv39h-deficient mice, nor did we observe a large increase in ploidy (i.e. 4N or 8N). Rather, we noted significantly greater numbers of mis-aligned or lagging chromosomes, which would lead to greater levels of aneuploidy. These findings were further substantiated by comparative flow cytometry performed between D5 and W8 cell labeled with PI, which revealed an overall increase in aneuploidy occurring within the D5 cells (data not shown).

Table 3.2: Mitotic aberrations in Suv39h1/2 dn IMEFs.

Stage	Category[a]	IMEF Control (W8) Percentage	No.	Suv391/2$^{-/-}$ IMEF (D5) Percentage	No.	Fold Difference
Metaphase	N	96.14	523	84.36	151	
	A	3.86	21	15.30	28	4.05
Anaphase	N	95.83	161	85.51	62	
	A	4.17	7	14.49	10	3.33
Telophase	N	96.53	195	76.03	105	
	A	3.47	7	23.97	25	5.55
Cytokinesis/	N	95.88	489	84.89	389	
Early G_1	A	4.12	21	15.11	64	3.43

[a] N = Normal phenotype; A = Aberrant phenotype

3.3 DISCUSSION

Histone methylations are thought to be dominantly acting stable epigenetic marks whose overall pattern and density are transmitted to daughter cells during cell division. We examined this hypothesis by exploiting the advantages of QIM to precisely define the relationship between the cell cycle and the *in situ* genomic density and distribution of histone lysine methylations thought to imprint either transcriptional competency (e.g. K4) (Strahl et al., 1999) or repression (e.g. K9 and K20) (Bannister et al., 2001; Lachner et al., 2001). Using a combination of DIM, flow cytometry, immunoblotting and QIM, we detailed the abundance of H3 and H4 methylation over the course of the cell cycle. We document unexpected dynamics in global methylation as cell progress through the cell cycle in both mammalian tissue culture systems and mouse embryonic tissue sections. As expected, we identified several methylations that exhibit relatively stable concentrations as well as others that clearly exhibit dynamics. For example, mMeK9, mMeK20, dMeK9 and tMeK9 all exhibited increases during the initial stages (late G_2 to prometaphase), reached their maximal densities as chromosomes congress to the metaphase plate, and were rapidly lost as cells exited mitosis, returning to basal levels by early G_1. Furthermore, by extending our mammalian tissue culture results to mouse embryonic tissue sections, we find that these cell cycle-dependent changes are highly conserved or even enhanced *in vivo*.

To date, there have been very few studies examining the cell cycle regulation of histone methylation levels. Most of the current understanding of methylation dynamics was obtained during the late 1960's and early 1970's using radio-active tracers in methyl donors including SAM and methionine. The labeled methyl donors were added to living cells, incorporated into histone N-termini at K or R residues and the label turnover was monitored. By following the amount of radio-label incorporated into each histone and determining the rate at which it was lost, the turnovers of the radio-labeled modifications were calculated. Although the analysis of histone methylation was limited to the study of the individual histone subtypes (e.g. H3 and H4), and not the specific residue or level (e.g. mono-, di- or tri-methylation), these studies did reveal evidence for methylation turnover as well as a potential peak in HMT activity that corresponds with G_2 and M phase (Annunziato et al., 1995; Borun et al., 1972).

Recently, Rice and colleagues (Rice et al., 2002) established that PR-Set7, a K20-specific HMT, is activated during the onset of mitosis. They reported that K20 methylation initiates at prometaphase and rapidly accumulates in mitosis. The increases in methylated K20 correlates with the prophase loading of the PR-Set7 protein onto the chromosomes. However, the anti-methylated K20 antibody employed by Rice and colleagues (Rice et al., 2002) was prepared against a dimethylated polypeptide. Our results on the timing of mMeK20 differ subtly from the mitosis-specific increase they reported for dMeK20. By examining the stages of mitosis by QIM and employing criteria that allowed for higher temporal resolution throughout mitosis, we identify the initial increase in mMeK20 during G_2. By prophase, there is a substantial increase in the abundance of mMeK20 present on the chromosomes. Notably, we do not observe a concomitant or significant increase in the amount of tMeK20. These observations demonstrate that tMeK20 is not the product of the K20 HMT (PR-Set7) activity upregulated during mitosis. The discordance we observe between the cell cycle regulation of mMeK20 and tMeK20 is not surprising. It is now recognized that each of the three potential methylation states for each lysine is distinct in its location within the genome and its epigenetic consequences. This is further supported by the existence of at least 45 putative HMTs encoded in the human genome and the demonstrated differences in the number of methyl groups that the different HMTs can transfer to the same lysine residue.

Although some histone methylations undergo dynamics that were entirely unexpected, these mitosis-specific dynamics are not unprecedented for a posttranslational modification of a histone. For example, PhosS10 (Hendzel et al., 1997) and phosphorylated S28 of histone H3 exhibit very similar temporal dynamics (McManus and Hendzel, in preparation). Moreover, both phosphorylations are equally rapidly removed as cells enter anaphase and continue to decrease until basal levels are reached by early G_1 (Hendzel et al., 1997). Particularly pertinent is the finding that PhosS10 is intimately associated with the fidelity of numerous mitotic processes including chromosome condensation, congression and segregation (de la Barre et al., 2000; Wei et al., 1999). This modification serves as an established precedent for a rapid and mitosis-specific induction and removal of a posttranslational histone modification that exhibits functional consequences. Therefore, the identification of mitosis-specific dynamics associated with tMeK9 prompted us to re-investigate the roles of Suv39h1/2 and tMeK9 in the fidelity of the mitotic process. Suv39h1 is the principal trimethylating K9 HMT found in adult tissues, whereas Suv39h2 expression is normally restricted to testis (Peters et al., 2001). Although protein levels of Suv39h1 remain constant throughout the cell cycle, this HMT undergoes a mitosis-specific phosphorylation and coincident enrichment within pericentromeric heterochromatin (Aagaard et al., 2000). The reported timing of

Suv39h1 phosphorylation correlates well with the initial onset of tMeK9 that we observe (see also Biron et al., 2004). Therefore, we hypothesize that stimulation of Suv39h1 by a mitosis-specific phosphorylation event is consistent with this phosphorylation being directly involved in regulating its HMT activity *in vivo*.

Genetic modulation of Suv39h1 expression levels directly impacts the abundance of tMeK9 localizing within the pericentromeric heterochromatin and adversely affects the fidelity of mitosis itself. For example, Suv39h1 overexpression, accompanied by experimentally induced increases in tMeK9, is associated with defects in mitotic progression and chromosome segregation (Melcher et al., 2000). Conversely, mice lacking Suv39h1/2, which do not exhibit tMeK9 within pericentromeric heterochromatin, exhibit increased genomic instabilities and cancer predispositions that presumably arise from genomic instabilities brought about by increases in ploidy (e.g. 4N or 8N) (Cheutin et al., 2003; Peters et al., 2001). Although mitotic spreads of cells isolated from spontaneously arising lymphomas in Suv39h1/2-deficient mice were found to contain an abundance of "butterfly" chromosomes (Peters et al., 2001), neither the underlying mechanism(s) responsible for the mitotic defect nor the specific function(s) of this mitotic methylation have been characterized previously. When we analyzed the mitotic progression of Suv39h1/2 dn IMEFs, the absence of pericentromeric tMeK9 correlated with an increase in abnormal mitoses. For instance, chromosome misalignment, non-disjunction and lagging chromosomes were observed more frequently in Suv39h1/2 dn IMEFS (D5) than in control IMEFs (W8). The simplest interpretation of these results is that tMeK9 regulation is essential for some aspect of centromere/kinetochore function or the maintenance of chromosome cohesion during initial mitotic stages. These results are consistent with the established requirement for tMeK9 in the recruitment of cohesin subunits to centromeric repeats in fission yeast where abrogation of tMeK9 has been shown to lead to premature sister chromatid separation and chromosome mis-segregation (Partridge et al., 2002; Volpe et al., 2003).

A mitosis-specific function for tMeK9 is consistent with the unexpectedly rapid increase and decrease of tMeK9 upon entry into prophase and anaphase, respectively. To eliminate the possibility that the cell cycle-specific changes we observed for tMeK9 were altered by epitope accessibility issues or epitope masking by chromatin binding proteins (e.g. HP1) we employed both native (DIM, flow cytometry and QIM) and denaturing (immunoblot) assay conditions. Interestingly, the timing of tMeK9 loss coincides with the timing of the Suv39h1 dephosphorylation and dissociation from the pericentromeric heterochromatin (Aagaard et al., 2000) and strongly suggests that tMeK9 is tightly regulated by successfully inactivating and removing Suv39h1/2 from the chromatin target. In defining unique mitosis-specific methylation dynamics, our results seriously challenge the concept that the function of histone methylation is restricted to roles in regulating interphase gene expression. Furthermore, the current study provides the first clear evidence that a majority of the chromosomal methylation present at the time of chromosome formation, is not transmitted to the daughter cells, but rather is lost at a timepoint immediately preceding cellular division. The observation that similar cell cycle stage-specific dynamics also occur for other lysine methylations (mMeK9, dMeK9 and mMeK20) raises the possibility that there may be additional mitosis-specific functions for histone methylation during mitosis that have yet to be elucidated.

The loss of histone methylation as cells exit mitosis was particularly unexpected as these methylations are thought to be stable epigenetic imprints. We investigated the possibility that replication-independent nucleosome assembly or histone replacement could potentially account for the decrease in tMeK9 we observe as cells exit mitosis. Outside of S-phase or DNA replication, the unincorporated pool of histone H3 is predominated by the histone H3 sequence variant, H3.3 (Brush et al., 1985; Hendzel and Davie, 1990). In rapidly growing tissue culture cell lines and short-lived but terminally differentiated cells *in vivo*, histone H3.3 is known to accumulate in regions of chromatin that are transcriptionally active (Ahmad and Henikoff, 2002; Jackson, 1990; Waterborg, 1993). In longer lived post-replicative cells, such as neurons, histone H3.3 can become the predominant histone H3 incorporated into chromatin (Bosch and Suau, 1995). Therefore, replication-independent nucleosome assembly or histone replacement provides the only known mechanism of tMeK9 removal. Recently, Janicki et al (Janicki et al., 2004) demonstrated that H3.3 *in vivo*, could replace tMeK9-containing H3, however only upon transcriptional activation. Although the replacement of pre-existing chromatinized histone H3 with histone H3.3 is an event thought to be both transcription-dependent and restricted to interphase, we examined the possibility that a previously unknown replacement of chromatinized histone H3 with histone H3.3 within pericentromeric heterochromatin may occur during this brief period of mitosis. As expected, we found no evidence for the presence of histone H3.3 in pericentromeric heterochromatin, consistent with a previous report demonstrating that histone H3.2 is the major histone H3 species present in the pericentromeric heterochromatin of mice (Russanova et al., 1989).

Having now eliminated the possibility that H3.3 replacement mediates the decrease in tMeK9 in the later stages of mitosis, the most likely explanation for the decrease is an enzyme-mediated mechanism. Potentially this could occur via two independent mechanisms – either the subsequent modification of tMeK9, or the enzymatic removal of the three methyl groups by histone demethylases (HDMs). Given that no such subsequent covalent modifications have been identified that occur at K9 despite the increased use of mass spectrometry techniques (Zhang et al., 2003), the existence of a HDM appears most likely. Furthermore, the requisite removal of the supplemental covalent modification is essential if the same histone is to undergo similar methylation increases during the early stages of mitosis during the next cell cycle. Therefore, we believe that our observations are most easily explained by robust HDM activity that is activated at the metaphase to anaphase transition or when chromosomes are released from the metaphase plate. This would explain an early radio-labeling study in HeLa S3 cells where it was observed that mitotic histones have a greater proportion of methylated histones than cells examined outside of mitosis (Borun et al., 1972). Since we did not observe a concomitant increase in mMeK9 or dMeK9 in pericentromeric heterochromatin during the period of robust tMeK9 loss, there does not appear to be accumulation of intermediately methylated species during the putative demethylation event (Figures 3.9 and 3.10). This strongly suggests that the putative HDM reduces tMeK9 to an unmodified lysine species. Finally, the restriction of HDM activity to this brief window during mitosis may also explain the difficulties that have accompanied attempts to identify and purify this activity using conventional biochemical approaches. Our results indicate that cellular extracts obtained from synchronized cells simultaneously released from a mitotic block and lysed between anaphase and telophase could potentially be a rich source of the putative robust tMeK9 HDM activity. Finally, although the results detailed in the current study indicate that there is a rapid and specific decrease in tMeK9 occurring in the later stages of mitosis, it remains possible that a similar mechanism could exist during interphase for additional methylations not examined in the present study. If true, this would represent a novel mechanism, independent of histone H3.3 replacement, that would 'reset' the epigenetic imprint at specific genetic locus to potentially allow for activation of a previously silenced locus. This is highly speculative however, and remains to be explored experimentally.

3.4 ACKNOWLEDGMENTS

We thank Dr. T. Jenuwein and Dr. G. Chan for generously providing the D5/W8 IMEFs and ACA antibody, respectively, and Abcam for supplying the methylation antibodies. The authors thank Mr. D. McDonald for critical reading of this manuscript. This work was funded by grants from the Canadian Institutes of Health Research (CIHR) (MJH:DAU) and the Alberta Heritage Foundation for Medical Research (AHFMR) (DAU). KJM is the recipient of graduate studentships from CIHR and AHFMR and VLB was supported by a postgraduate scholarship from the National Sciences and Engineering Research Council. Both MJH and DAU are AHFMR Scholars, and MJH is also a CIHR New Investigator.

3.5 REFERENCES

Aagaard, L., M. Schmid, P. Warburton, and T. Jenuwein. 2000. Mitotic phosphorylation of SUV39H1, a novel component of active centromeres, coincides with transient accumulation at mammalian centromeres. *J Cell Sci.* 113 (Pt 5):817-29.

Ahmad, K., and S. Henikoff. 2002. The histone variant H3.3 marks active chromatin by replication-independent nucleosome assembly. *Mol Cell.* 9:1191-200.

Annunziato, A.T., M.B. Eason, and C.A. Perry. 1995. Relationship between methylation and acetylation of arginine-rich histones in cycling and arrested HeLa cells. *Biochemistry.* 34:2916-24.

Bannister, A.J., R. Schneider, and T. Kouzarides. 2002. Histone methylation: dynamic or static? *Cell.* 109:801-6.

Bannister, A.J., P. Zegerman, J.F. Partridge, E.A. Miska, J.O. Thomas, R.C. Allshire, and T. Kouzarides. 2001. Selective recognition of methylated lysine 9 on histone H3 by the HP1 chromo domain. *Nature.* 410:120-4.

Biron, V.L., K.J. McManus, M.J. Hendzel, and D.A. Underhill. 2004. Distinct dynamics and distribution of histone methyl-lysine derivatives in mouse development. Dev Biol. In Press.

Borun, T.W., D. Pearson, and W.K. Paik. 1972. Studies of histone methylation during the HeLa S-3 cell cycle. *J Biol Chem.* 247:4288-98.

Bosch, A., and P. Suau. 1995. Changes in core histone variant composition in differentiating neurons: the roles of differential turnover and synthesis rates. *Eur J Cell Biol.* 68:220-5.

Brehm, A., K.R. Tufteland, R. Aasland, and P.B. Becker. 2004. The many colours of chromodomains. *Bioessays.* 26:133-40.

Brush, D., J.B. Dodgson, O.R. Choi, P.W. Stevens, and J.D. Engel. 1985. Replacement variant histone genes contain intervening sequences. *Mol Cell Biol.* 5:1307-17.

Byvoet, P., G.R. Shepherd, J.M. Hardin, and B.J. Noland. 1972. The distribution and turnover of labeled methyl groups in histone fractions of cultured mammalian cells. *Arch Biochem Biophys.* 148:558-67.

Cavalli, G., and R. Paro. 1998. Chromo-domain proteins: linking chromatin structure to epigenetic regulation. *Curr Opin Cell Biol.* 10:354-60.

Cheutin, T., A.J. McNairn, T. Jenuwein, D.M. Gilbert, P.B. Singh, and T. Misteli. 2003. Maintenance of stable heterochromatin domains by dynamic HP1 binding. *Science*. 299:721-5.

de la Barre, A.E., V. Gerson, S. Gout, M. Creaven, C.D. Allis, and S. Dimitrov. 2000. Core histone N-termini play an essential role in mitotic chromosome condensation. *Embo J*. 19:379-91.

Duerre, J.A., and C.T. Lee. 1974. In vivo methylation and turnover of rat brain histones. *J Neurochem*. 23:541-7.

Eissenberg, J.C. 2001. Molecular biology of the chromo domain: an ancient chromatin module comes of age. *Gene*. 275:19-29.

Fischle, W., Y. Wang, S.A. Jacobs, Y. Kim, C.D. Allis, and S. Khorasanizadeh. 2003. Molecular basis for the discrimination of repressive methyl-lysine marks in histone H3 by Polycomb and HP1 chromodomains. *Genes Dev*. 17:1870-81.

Goll, M.G., and T.H. Bestor. 2002. Histone modification and replacement in chromatin activation. *Genes Dev*. 16:1739-42.

Hendzel, M.J., and J.R. Davie. 1990. Nucleosomal histones of transcriptionally active/competent chromatin preferentially exchange with newly synthesized histones in quiescent chicken erythrocytes. *Biochem J*. 271:67-73.

Hendzel, M.J., Y. Wei, M.A. Mancini, A. Van Hooser, T. Ranalli, B.R. Brinkley, D.P. Bazett-Jones, and C.D. Allis. 1997. Mitosis-specific phosphorylation of histone H3 initiates primarily within pericentromeric heterochromatin during G2 and spreads in an ordered fashion coincident with mitotic chromosome condensation. *Chromosoma*. 106:348-60.

Jackson, V. 1990. In vivo studies on the dynamics of histone-DNA interaction: evidence for nucleosome dissolution during replication and transcription and a low level of dissolution independent of both. *Biochemistry*. 29:719-31.

Jacobs, S.A., S.D. Taverna, Y. Zhang, S.D. Briggs, J. Li, J.C. Eissenberg, C.D. Allis, and S. Khorasanizadeh. 2001. Specificity of the HP1 chromo domain for the methylated N-terminus of histone H3. *Embo J*. 20:5232-41.

Janicki, S.M., T. Tsukamoto, S.E. Salghetti, W.P. Tansey, R. Sachidanandam, K.V. Prasanth, T. Ried, Y. Shav-Tal, E. Bertrand, R.H. Singer, and D.L. Spector. 2004. From silencing to gene expression: real-time analysis in single cells. *Cell*. 116:683-98.

Kiekhaefer, C.M., J.A. Grass, K.D. Johnson, M.E. Boyer, and E.H. Bresnick. 2002. Hematopoietic-specific activators establish an overlapping pattern of histone acetylation and methylation within a mammalian chromatin domain. *Proc Natl Acad Sci U S A*. 99:14309-14.

Lachner, M., and T. Jenuwein. 2002. The many faces of histone lysine methylation. *Curr Opin Cell Biol*. 14:286-98.

Lachner, M., D. O'Carroll, S. Rea, K. Mechtler, and T. Jenuwein. 2001. Methylation of histone H3 lysine 9 creates a binding site for HP1 proteins. *Nature*. 410:116-20.

Litt, M.D., M. Simpson, M. Gaszner, C.D. Allis, and G. Felsenfeld. 2001. Correlation between histone lysine methylation and developmental changes at the chicken beta-globin locus. *Science*. 293:2453-5.

Louters, L., and R. Chalkley. 1984. In vitro exchange of nucleosomal histones H2a and H2b. *Biochemistry*. 23:547-52.

Louters, L., and R. Chalkley. 1985. Exchange of histones H1, H2A, and H2B in vivo. *Biochemistry*. 24:3080-5.

Melcher, M., M. Schmid, L. Aagaard, P. Selenko, G. Laible, and T. Jenuwein. 2000. Structure-function analysis of SUV39H1 reveals a dominant role in heterochromatin organization, chromosome segregation, and mitotic progression. *Mol Cell Biol*. 20:3728-41.

Murray, K. 1964. The Occurrence of Epsilon-N-Methyl Lysine in Histones. *Biochemistry*. 127:10-5.

Nakayama, J., J.C. Rice, B.D. Strahl, C.D. Allis, and S.I. Grewal. 2001. Role of histone H3 lysine 9 methylation in epigenetic control of heterochromatin assembly. *Science*. 292:110-3.

Ng, H.H., Q. Feng, H. Wang, H. Erdjument-Bromage, P. Tempst, Y. Zhang, and K. Struhl. 2002. Lysine methylation within the globular domain of histone H3 by Dot1 is important for telomeric silencing and Sir protein association. *Genes Dev*. 16:1518-27.

Noma, K., C.D. Allis, and S.I. Grewal. 2001. Transitions in distinct histone H3 methylation patterns at the heterochromatin domain boundaries. *Science*. 293:1150-5.

Paik, W.K., and S. Kim. 1967. Enzymatic methylation of protein fractions from calf thymus nuclei. *Biochem Biophys Res Commun*. 29:14-20.

Partridge, J.F., K.S. Scott, A.J. Bannister, T. Kouzarides, and R.C. Allshire. 2002. cis-acting DNA from fission yeast centromeres mediates histone H3 methylation and recruitment of silencing factors and cohesin to an ectopic site. *Curr Biol.* 12:1652-60.

Peters, A.H., D. O'Carroll, H. Scherthan, K. Mechtler, S. Sauer, C. Schofer, K. Weipoltshammer, M. Pagani, M. Lachner, A. Kohlmaier, S. Opravil, M. Doyle, M. Sibilia, and T. Jenuwein. 2001. Loss of the Suv39h histone methyltransferases impairs mammalian heterochromatin and genome stability. *Cell.* 107:323-37.

Rice, J.C., and C.D. Allis. 2001. Histone methylation versus histone acetylation: new insights into epigenetic regulation. *Curr Opin Cell Biol.* 13:263-73.

Rice, J.C., K. Nishioka, K. Sarma, R. Steward, D. Reinberg, and C.D. Allis. 2002. Mitotic-specific methylation of histone H4 Lys 20 follows increased PR-Set7 expression and its localization to mitotic chromosomes. *Genes Dev.* 16:2225-30.

Russanova, V., E. Stephanova, I. Pashev, and R. Tsanev. 1989. Histone variants in mouse centromeric chromatin. *Mol Cell Biochem.* 90:1-7.

Santos-Rosa, H., R. Schneider, A.J. Bannister, J. Sherriff, B.E. Bernstein, N.C. Emre, S.L. Schreiber, J. Mellor, and T. Kouzarides. 2002. Active genes are tri-methylated at K4 of histone H3. *Nature.* 419:407-11.

Sims, R.J., 3rd, K. Nishioka, and D. Reinberg. 2003. Histone lysine methylation: a signature for chromatin function. *Trends Genet.* 19:629-39.

Strahl, B.D., R. Ohba, R.G. Cook, and C.D. Allis. 1999. Methylation of histone H3 at lysine 4 is highly conserved and correlates with transcriptionally active nuclei in Tetrahymena. *Proc Natl Acad Sci U S A.* 96:14967-72.

Urban, M.K., and A. Zweidler. 1983. Changes in nucleosomal core histone variants during chicken development and maturation. *Dev Biol.* 95:421-8.

van Leeuwen, F., P.R. Gafken, and D.E. Gottschling. 2002. Dot1p modulates silencing in yeast by methylation of the nucleosome core. *Cell.* 109:745-56.

Volpe, T., V. Schramke, G.L. Hamilton, S.A. White, G. Teng, R.A. Martienssen, and R.C. Allshire. 2003. RNA interference is required for normal centromere function in fission yeast. *Chromosome Res.* 11:137-46.

Waterborg, J.H. 1993. Dynamic methylation of alfalfa histone H3. *J Biol Chem.* 268:4918-21.

Wei, Y., L. Yu, J. Bowen, M.A. Gorovsky, and C.D. Allis. 1999. Phosphorylation of histone H3 is required for proper chromosome condensation and segregation. *Cell.* 97:99-109.

Zeng, L., and M.M. Zhou. 2002. Bromodomain: an acetyl-lysine binding domain. *FEBS Lett*. 513:124-8.

Zhang, L., E.E. Eugeni, M.R. Parthun, and M.A. Freitas. 2003. Identification of novel histone post-translational modifications by peptide mass fingerprinting. *Chromosoma*. 112:77-86.

CHAPTER 4

ATM-dependent Mitotic Phosphorylation of H2AX in Normally Growing Mammalian Cells[†]

Kirk J. McManus[1] and Michael J. Hendzel[1*]

[1]Department of Oncology, University of Alberta, Cross Cancer Institute,

11560 University Avenue, Edmonton, Alberta Canada T6G 1Z2

Running Title: Cell Cycle Dynamics of γ-H2AX

*Address for Correspondence
Dr. Michael J. Hendzel
Department of Oncology
Cross Cancer Institute
11560 University Avenue
Room 3332
Edmonton, Alberta
T6G 1Z2 CANADA
Tel # (780) 432-8493
Fax # (780) 432-8892
Email: michaelh@cancerboard.ab.ca

[†] A version of this chapter has been submitted for publication

4.1 INTRODUCTION

DNA double-strand breaks (DSBs) are one of the most detrimental lesions compromising genomic integrity (Jackson, 2002; Rothkamm and Lobrich, 2002). Not surprisingly, DSBs represent a heterogeneous class of lesions because the resulting broken ends depend on the origin of the break. DNA DSBs occur naturally during the cell cycle due to the activities of enzymes essential for genome duplication, chromosome segregation, meiotic recombination. In living systems, some naturally occurring DSBs are essential for viability and increased diversity. For example, homologous recombination (HR) during meiosis is essential for ensuring genetic diversity in future generations (Hunter et al., 2001; Mahadevaiah et al., 2001), while immunoglobulin V(D)J and class switch recombination increases the diversity required for efficient antigen recognition (Chen et al., 2000; Rogakou et al., 1998). DNA DSBs can also arise through exogenous sources of DNA-damaging agents. Regardless of the break origin, DNA DSBs must be efficiently repaired to ensure genomic integrity and maintain genetic stability for subsequent generations. DNA DSBs can be accurately repaired by HR with a sister chromatid (reviewed in Dudas and Chovanec, 2004; Helleday, 2003). In contrast, DSB repair by non-homologous end-joining (NHEJ) is more error-prone and can incorporate numerous mutagenic base changes and/or deletions (reviewed in Lees-Miller and Meek, 2003; Valerie and Povirk, 2003). In either case, inaccurate DNA DSB repair can incorporate detrimental genomic mutations manifesting as genetic instabilities that may underlie oncogenesis.

H2AX is a histone H2A variant that is highly conserved from *Giardia intestinalis* to humans (reviewed in Pilch et al., 2003). In humans, H2AX comprises approximately 2 to 25 percent of the total H2A population (Rogakou et al., 1998), while in yeast it is much more prevalent and represents approximately 95 percent of the total H2A population (Redon et al., 2002). H2AX is distinct from all other H2A variants in that it harbors a carboxy- (C-) terminal extension that includes an invariant serine/glutamine (SQ) motif located four amino acid residues from the C-terminus (Rogakou et al., 1998). There has been considerable research into the role(s) H2AX and its C-terminal phosphorylation have in regulating DNA DSB repair activities and targeting. For example, following ionizing radiation (IR) H2AX is rapidly phosphorylated at the γ-serine (the SQ motif) and it is this phosphorylated form that is more commonly referred to as γ-H2AX. Members of the phosphatidyl-inositol-3-kinase (PI3-K) protein kinase family, including ATM (ataxia telangiectasia mutated), DNA-PK_{CS} (DNA-protein kinase, catalytic subunit) and ATR (ATM and Rad3-related) are all thought to contribute to H2AX phosphorylation levels *in vivo* (Motoyama and Naka, 2004; Stiff et al., 2004). However, it is now generally accepted that ATM and ATR induce H2AX phosphorylation in response to DNA DSBs in mutually exclusive pathways that are dependent on the underlying insult. ATM induces H2AX phosphorylation in response to γ-irradiation, while ATR induces phosphorylation in response to ultra violet (UV) damage (reviewed in Nyberg et al., 2002; Zhou and Elledge, 2000). In either case, initial γ-H2AX increases following exogenous DNA DSB are extremely rapid and occur within minutes (Rogakou et al., 1999). H2AX phosphorylation continues to increase until maximal phosphorylation is achieved within 30 to 60 minutes (MacPhail et al., 2003a; Rogakou et al., 1998). Following artificial induction of DNA DSBs, the amount of H2AX phosphorylated is proportional to the number of DSBs incurred. It is estimated that there are approximately

2,000 H2AX molecules phosphorylated per DSB spanning approximately 2 megabase pairs of DNA (Rogakou et al., 1999). In haploinsufficient mice (*H2AX*$^{-/+}$) or mice lacking functional H2AX (*H2AX*$^{-/-}$ or *H2AX*$^{\Delta/\Delta}$), the efficacy of DNA DSB repair is dramatically impeded, the DNA damage-induced G_2/M checkpoint fails and numerous morphological abnormalities including chromosome- and mitotic-defects are observed (Bassing et al., 2002; Celeste et al., 2002; Fernandez-Capetillo et al., 2002). More recently, H2AX has been shown to function as a dosage-dependent suppressor of oncogenic translocations and tumors in mice (Bassing et al., 2003) while in humans, *H2AX* maps to a cytogenetic region frequently altered in human cancers. These observations are consistent with a role for altered or mutated H2AX expression in the onset and progression of at least some human tumors. Collectively, the above data demonstrate that H2AX performs a vital role in the identification and efficient repair of damaged genomes thereby circumventing genomic instabilities that could manifest as specific cancers.

In the absence of experimentally applied radiation, the steady-state levels of γ-H2AX is expected to reflect the sum of naturally occurring DNA DSBs, either biological or accidental, during the normal functions of the nucleus. Because natural exogenous DNA damage sources are generally cell cycle-independent, any global differences observed in the abundance of γ-H2AX is anticipated to reflect an underlying requirement for DNA DSB and/or repair at specific cell cycle stages. However, as with most posttranslational histone modifications with ascribed nuclear functions, it is possible that a subset of γ-H2AX may exist that is independent of DNA DSB repair. Recently, Olive and colleagues (MacPhail et al., 2003a) detailed the relationship between cell cycle and γ-

H2AX production in mammalian cells following exposure to DNA DSB-inducing agents. They concluded that γ-H2AX levels increase as cells progress from G_1 to S-phase and exhibit maximal signal intensities in S-phase. However, very little is known about the cell cycle-dependence of γ-H2AX that occurs naturally or in the absence of artificially induced DNA damage.

In this study we examine qualitative and quantitative differences in the abundance of γ-H2AX throughout the cell cycle. This type of analysis has been employed previously to successfully identify cell cycle-dependent changes in many additional posttranslational histone modifications that have later been determined to be of great functional importance. For example, phosphorylated serine 10 (PhosS10) of histone H3 exhibits mitosis-associated dynamics (Gurley et al., 1973; Hendzel et al., 1997) that were subsequently determined to be essential for chromosome compaction and segregation in a variety of organisms (Bui et al., 2004; Petersen et al., 2001; Wei et al., 1999). Therefore, it is imperative to characterize the cell cycle distribution and dynamics of γ-H2AX under normal physiological conditions. In this study, we employ indirect immunofluorescent *in situ* approaches including digital imaging microscopy (DIM), flow cytometry and quantitative imaging microscopy and denaturing conditions such as immunoblotting to characterize the distribution and dynamics of γ-H2AX in unirradiated mammalian cells. Here we provide the first description of a population of small γ-H2AX foci in unirradiated mammalian cells that are entirely independent of DNA DSB repair. We also demonstrate that γ-H2AX exhibits cell cycle-associated dynamics that are coupled to mitosis. Finally, we demonstrate that the mitosis-associated dynamics are dependent upon functional ATM expression and independent of functional DNA-PK_{CS} expression.

4.2 RESULTS

4.2.1 *Distinctive γ-H2AX Focal Populations in Unirradiated Nuclei*

Because exogenous DNA damaging reagents (e.g. γ-irradiation, α-irradiation, radio-mimetic drugs, etc.) result in the recruitment of specific factors to sites of DNA DSBs and chromatin reorganization, we reasoned that the γ-H2AX localization pattern may differ between unirradiated and γ-irradiated cells. Accordingly, we examined the three-dimensional (3D) localization pattern of γ-H2AX in both unirradiated and irradiated HeLa, SK-N-SH, COS-7, 10T1/2 and IM cells by indirect immunofluorescent (IIF) labeling. Using a highly specific (see below) mouse monoclonal antibody directed against γ-H2AX (JBW301 – Upstate) that has been employed extensively in numerous investigations from various research laboratories, we characterized specific differences occurring between unirradiated and irradiated mammalian cell lines. Although the main focus of this study is not to detail the specifics of γ-H2AX in irradiated cells, by comparing its γ-H2AX focal staining pattern with that of unirradiated cells, a greater appreciation of the fundamental differences between the two conditions is attained.

Upon initial investigation, three major differences were apparent between γ-H2AX foci in unirradiated and irradiated cells. First, γ-H2AX foci were observed in all unirradiated and irradiated nuclei of all cell lines investigated, and at all stages of the cell cycle (data not shown). In agreement with previous studies (MacPhail et al., 2003b), the γ-H2AX fluorescent signal intensities were markedly different between unirradiated and irradiated cells. The foci in unirradiated cells were considerably less intense (e.g. > 5-fold) than the large DNA damage-induced γ-H2AX foci in irradiated cells (data not shown). Second, differences in the γ-H2AX focal sizes in unirradiated and irradiated cells were readily apparent. In all unirradiated nuclei investigated, two distinct focal populations were present (Figure 4.1) – a predominant population of previously uncharacterized small foci, and a minor population of large amorphous foci that resemble the DNA repair foci induced by irradiation treatment. In unirradiated interphase (G_1 to G_2) nuclei there are typically between 250 to 350 small foci and between 1 to 15 large amorphous foci, while in mitotic cells (prophase) the average number of foci increased slightly and ranged between 300 and 400 (Table 4.1). Next, quantification of γ-H2AX focal volumes was performed in IM cells as they have large, relatively flat nuclei. They also exhibit highly distinct changes in chromatin structure associated with specific cell cycle stages that render them ideally suited for cytological investigations. The mean γ-H2AX focal volumes (± standard deviation [SD]) in unirradiated interphase (G_1/S) and mitotic (prophase) IM cells was 0.16 μm^3 ± 0.68 μm^3 and 0.18 μm^3 ± 1.9 μm^3 respectively (Table 4.1). The corresponding values in irradiated IM cells increased slightly to 0.57 μm^3 ± 2.5 μm^3 (G_1/S) and 0.76 μm^3 ± 3.6 μm^3 (mitosis) (Table 4.1). These differences correspond to 3.5- and 4.2-fold increases in the overall mean γ-H2AX volumes for G_1/S and mitosis respectively following irradiation and differs from previously published focal diameters (0.04 to 0.16 μm) of the large radiation induced foci (MacPhail et al., 2003a; MacPhail et al., 2003b). Similar results were observed in GM38 cells (data not shown). However, to accurately assess focal sizes, it is imperative to employ 3D analysis criteria due to the potential of introducing size artifacts by utilizing standard 2D analytical procedures to measure 3D phenomena that are presented as 2D projections. By subdividing the IM volumetric data into quartiles, we observe that the majority of the volumetric variation between all stages, independent of irradiation, is restricted to the

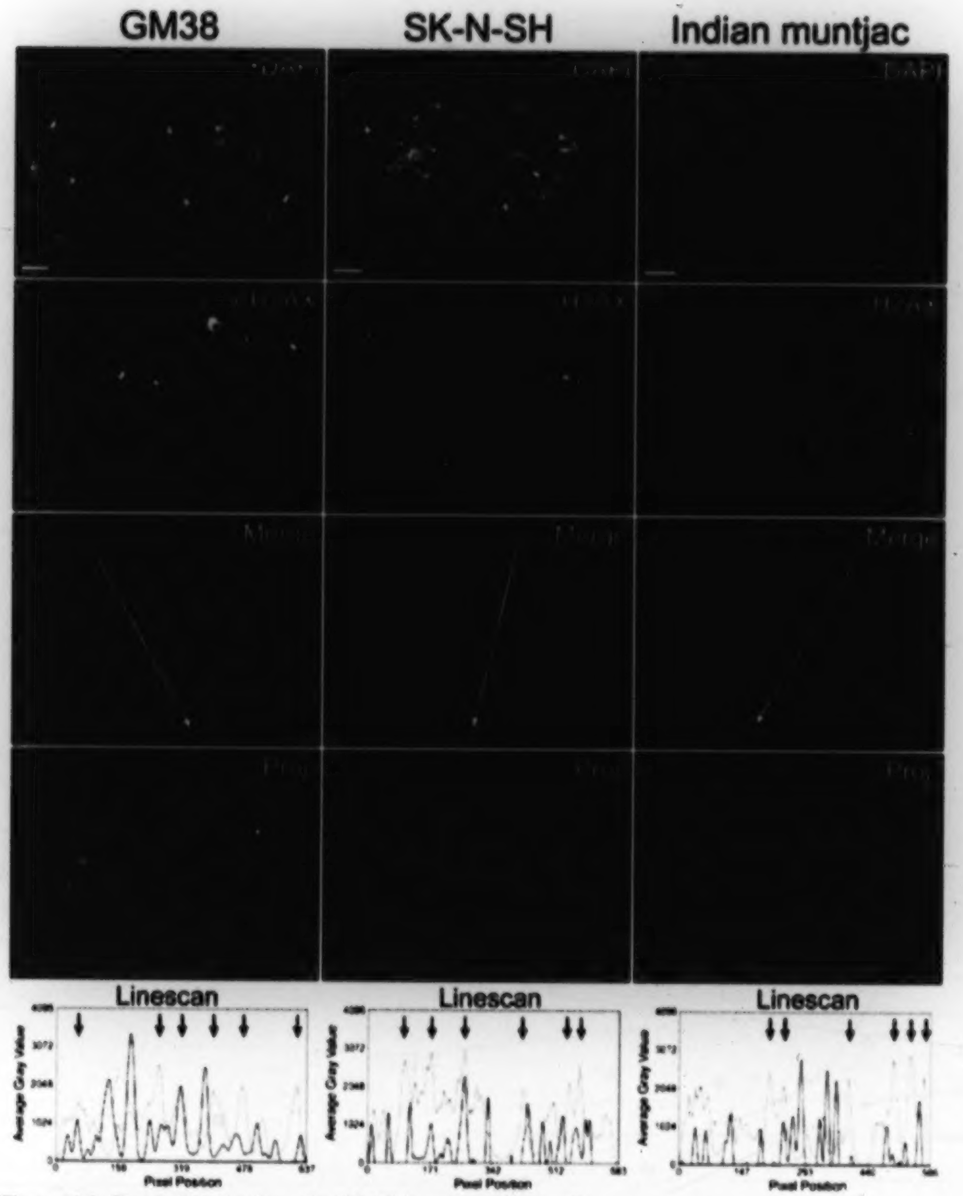
GM38
SK-N-SH
Indian muntjac
DAPI
γ-H2AX
Merge
Proj.
Linescan
Average Gray Value
Pixel Position
3072
2048
1024
0
159
319
478
637
171
342
512
683
147
293
440
586

Figure 4.1: Focal distribution of γ-H2AX in mammalian cells.
Depicted here are representative deconvolved, high-resolution (100×) DIM images of unirradiated GM38, SK-N-SH and IM cells immunofluorescently labeled with anti-γ-H2AX (green) and counterstained with DAPI (red) to reveal DNA. The merged image is a single plane from the 3D deconvolved series and is the plane used for the linescan analyses shown in the bottom panels. The entire 3D image is presented as a deconvolved projection in the fourth row (Proj.). Linescan analyses were performed with the arrows in the Merge panel indicating the regions and directions of the scans. A graph depicting the average grey level (*y*-axis) versus pixel position (*x*-axis) is shown in the fifth row with the DAPI channel information shown in red and the γ-H2AX channel information shown in green. Peak DAPI intensities identify heterochromatic regions and are identified by black arrows in the linescans, while euchromatic regions are identified by less intense DAPI staining. Scale bars represent 3μm.

Table 4.1: Volumetric distribution of γ-H2AX foci in unirradiated and irradiated IM fibroblasts.

				mVol ± SD[d]	Quartile – Mean Volume ± SD[a] ($\times 10^{-2}$ μm^3)			
Stage[b]	IR[c]	No. Cells	Foci/Cell	($\times 10^{-2}$ μm^3)	1	2	3	4
G_1/S	-	15	348.8 ± 67.3	16.20 ± 68.45	1.599 ± 0.3990	3.415 ± 0.6812	6.919 ± 1.535	52.90 ± 130.2
M	-	15	387.9 ± 87.4	17.98 ± 189.8	1.382 ± 0.2758	2.656 ± 0.4850	5.198 ± 1.146	62.74 ± 376.2
G_1/S	+	15	179.6 ± 68.9	56.51 ± 253.4	1.517 ± 0.3649	3.168 ± 0.6328	7.391 ± 2.545	212.7 ± 473.8
M	+	15	183.9 ± 58.2	75.73 ± 359.4	1.343 ± 0.2647	2.618 ± 0.5442	7.185 ± 3.024	292.2 ± 674.5

[a] SD = standard deviation

[b] cell cycle stage (G_1/S = G_1/S boundary; M = prophase)

[c] IR = γ-irradiation ('-' is unirradiated; '+' is irradiated with 2Gy and allowed to recover for 30min)

[d] mVol ± SD = mean focal volume ± SD

fourth quartile (Table 4.1). The mean focal volumes of the fourth quartile of the unirradiated (0.53 μm^3 ± 1.3 μm^3) G_1/S cells is approximately 4.0-fold smaller than those of the irradiated (2.1 μm^3 ± 4.7 μm^3) G_1/S cells, while those of the unirradiated (0.63 μm^3 ± 3.8 μm^3) mitotic cells are approximately 4.7-fold smaller than those of the irradiated (2.9 μm^3 ± 6.7 μm^3) mitotic cells (Table 4.1). Conversely, similar comparisons made within the first three quartiles failed to identify significant differences in mean γ-H2AX focal volumes between the respective G_1/S and prophase pairings. Finally, the average number of foci per nucleus was markedly different between unirradiated and irradiated cells irrespective of cell cycle stage (e.g. G_1/S or prophase) (Table 4.1). Quantification determined that there is approximately 2-fold **decrease** in the total number of foci in the irradiated populations and could be due to several different possibilities. These include the possible engulfment of several smaller foci into the large expanding γ-H2AX repair foci that eventually encompasses approximately 2 Mb of DNA, or the possibility that several smaller γ-H2AX foci may coalesce to form a larger focus as was recently demonstrated by Aten et al (2004) following α-irradiation.

4.2.2 *Anti-γ-H2AX Antibodies Specifically Recognize Phosphorylated H2AX*

It is well established that large γ-H2AX (repair) foci appear in response to DNA DSBs that occur through either endogenous or exogenous means. However, no information is currently available that describes the existence of γ-H2AX foci, specifically the small foci, within unirradiated (or irradiated) cells. Therefore it was of extreme importance to demonstrate that the qualitative characteristics detailed above using a mouse IgG_1 monoclonal antibody (JBW301 – Upstate) could be replicated with additional antibodies recognizing γ-H2AX. Consequently, two additional affinity purified (IgG) rabbit polyclonal anti-γ-H2AX antibodies were acquired (ab11174 and ab2893 – Abcam). When paraformaldehyde-fixed GM38, SK-N-SH, HeLa, 10T1/2 and IM cells were immunofluorescently labeled and examined by DIM, both JBW301 and ab2893 antibodies exhibited similar characteristics – they recognized both large and small γ-H2AX foci and in approximately similar quantities (Figure 4.2). However, based on the antibody dilutions and the channel exposure times, the *in situ* immunoreactivity of JBW301 was deemed to be superior to that of ab2893 and was therefore employed throughout the remaining experiments. Although SDS-PAGE and immunoblotting demonstrated that ab11174 recognized a single protein of the appropriate size that increased following IR-exposure, it did not appear to recognize γ-H2AX *in situ* as nuclei were completely devoid of γ-H2AX signal (Figure 4.2). This observation suggests that ab11174 recognizes a different (e.g. denatured) conformation of γ-H2AX, which is a common feature of many different polyclonal antibody preparations. Consequently, ab11174 was not employed in any subsequent investigations.

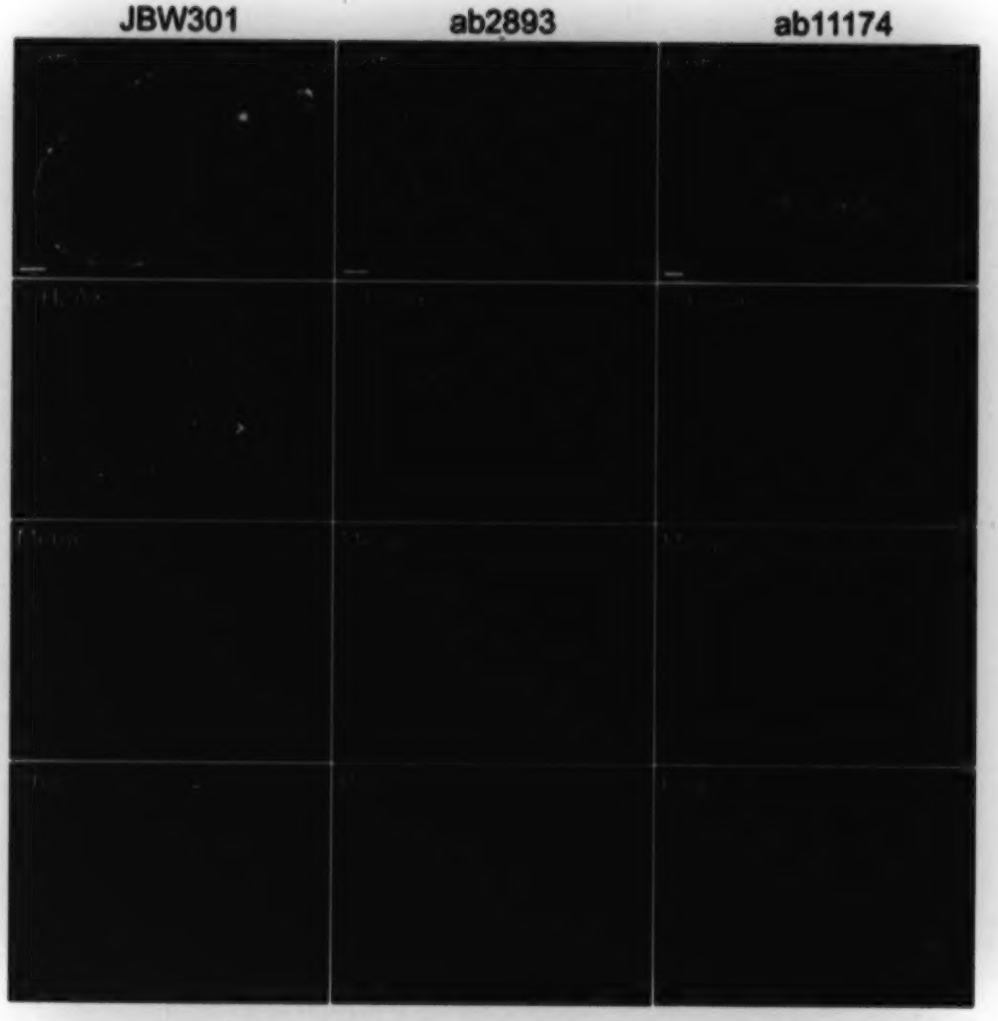

Figure 4.2: Localization of γ-H2AX foci using three different anti-γ-H2AX antibodies. Asynchronous HeLa cells were paraformaldehyde-fixed, permeabilized, immunofluorescently labeled with each of the three anti-γ-H2AX (indicated at top) and counterstained with DAPI. Depicted here are representative high-resolution (100×) DIM images. The merged DAPI, antibody and merged images are single planes from 3D image series, while the entire 3D image series in presented as a 2D projection (Proj.). Note that only JBW301 and ab2893 identify both large and small γ-H2AX foci and in approximately similar numbers, while ab11174 does not appear to recognize γ-H2AX *in situ*. Scale bar represents 2μm.

Having now established that JBW301 and ab2983 recognize similar epitopes and that the small γ-H2AX foci detailed above were not background artifacts, it was imperative to establish that both antibodies recognize the γ-H2AX epitope. As the predominant proportion of the subsequent experiments are performed *in situ*, an IIF calf intestinal alkaline phosphatase (CIP) assay was developed to determine if the antibodies recognized a phosphorylated epitope *in situ*. As shown in Figure 4.3, the recognition of the phosphorylated epitope by JBW301 was significantly diminished upon a 1 hr pretreatment of cells with CIP, but remained intact in the CIP-untreated controls (Figure 4.3). Similar results were obtained for ab2983 (data not shown). Moreover, the recognition of PhosS10, prominent positive histone phosphorylation control, was also depleted in the CIP-treated cells (Figure 4.3).

To further demonstrate the specificities of the anti-γ-H2AX antibodies, *in situ* IIF peptide competition assays were performed with a peptide, H2AXp, corresponding to amino acid residues 133 to 142 of H2AX and phosphorylated at the appropriate serine residue (139). As expected, H2AXp successfully out-competed the *in situ* binding of both antibodies to their respective targets (Figure 4.4). In addition, a peptide corresponding to residues 131 to 142, but not phosphorylated (H2AXnp), did not out-compete the *in situ* binding of either JBW301 or ab2893. The combined result from the CIP assay and the peptide competitions clearly demonstrate that JBW301 and ab2893 are highly specific for γ-H2AX. These results further serve to underscore that untreated interphase mammalian cells do exhibit two distinct γ-H2AX focal patterns – a predominant population of small foci and a minor population of larger foci that are reminiscent of the types of foci induced by DNA DSBs.

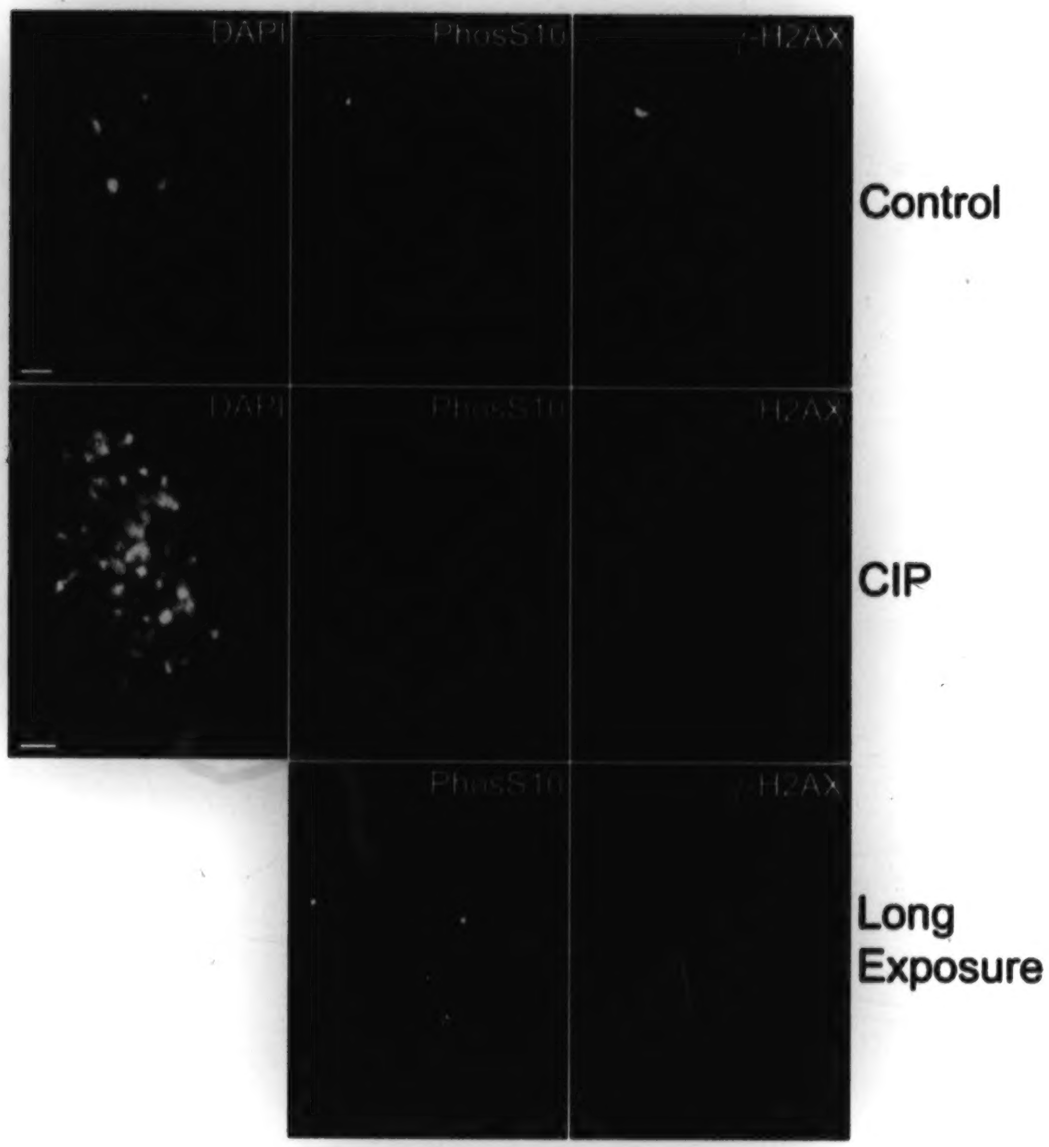

Figure 4.3: The anti-γ-H2AX antibody specifically recognizes a phospho-epitope *in situ*. Depicted here are representative DIM images (100×) of 10T1/2 cells treated with Saponin, with (CIP) or without (control) calf alkaline intestinal phosphatase (CIP), and immunofluorescently labeled with both anti-PhosS10 and anti-γ-H2AX (JBW301). The prophase 10T1/2 fibroblast CIP-treated cell was specifically selected, as it normally exhibits a dramatic increase in PhosS10 immuno-staining over interphase cells, particularly within pericentromeric heterochromatin. Identical exposure times were used in the top two rows for all three channels with a 5-fold increase in exposure time (long exposure) for the anti-PhosS10 and anti-γ-H2AX channels shown in the third row. Scale bar represents 2μm.

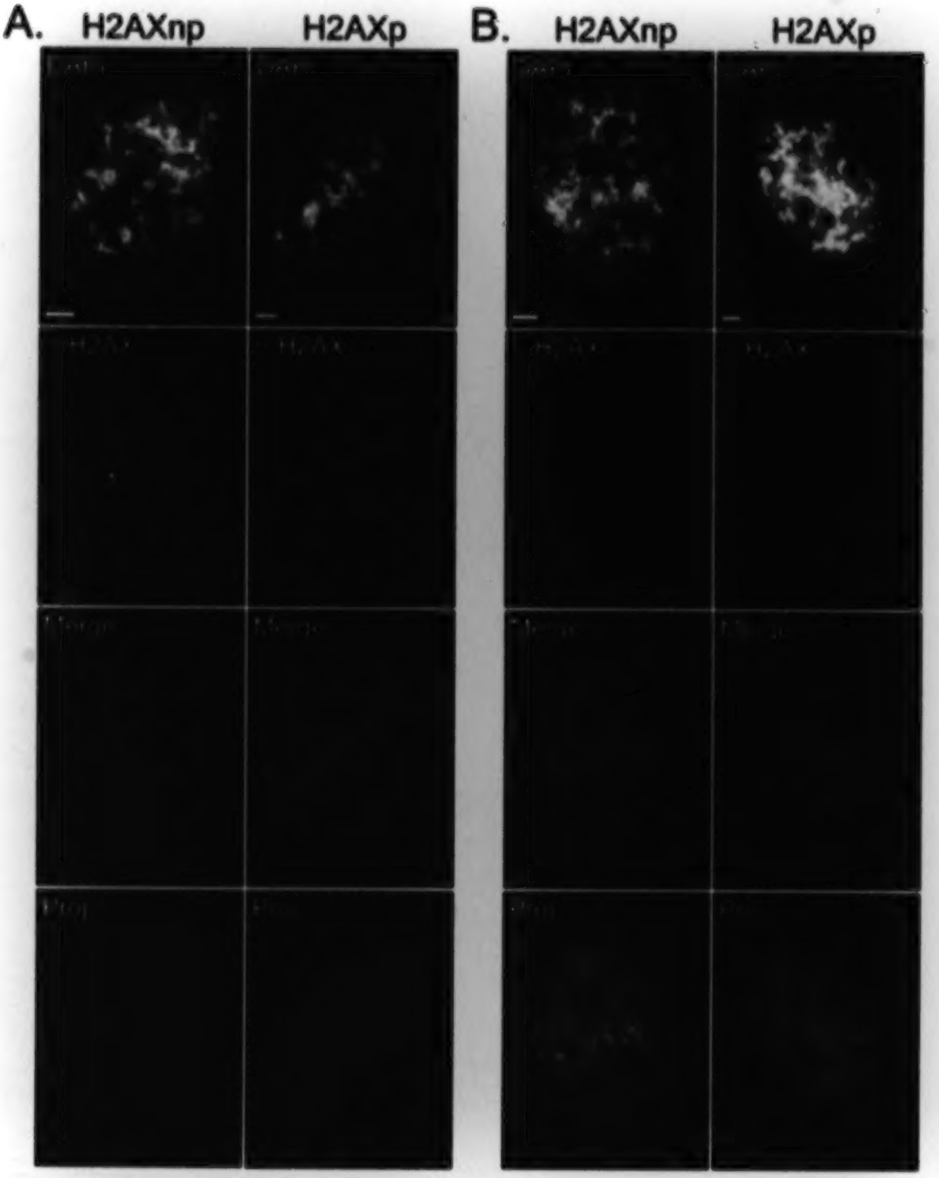

Figure 4.4: *In situ* indirect immunofluorescent peptide competition assay.
Asynchronous HeLa cells were immunofluorescently labeled with anti-γ-H2AX, JBW301 (A) and ab2893 (B), that were pre-incubated with either a competing H2AX peptide phosphorylated at the corresponding serine residue (H2AXp) or a similar non-phosphorylated H2AX peptide (H2AXnp). Depicted here are representative high-resolution (100×) DIM images. Increased (5-fold) exposure times were employed to image the γ-H2AX channel of the H2AXp experiments for both antibody treatments (i.e. JBW301 or ab2983). Note the absence of total γ-H2AX nuclear signal in the JBW301 H2AXp column (A) and the weak background staining pattern in the ab2893 H2AXp column (B) that is present in approximately equal amounts within both the cytoplasm and the nucleoplasm. For reference purposes a 3D projection (Proj) has been included as it presents 3D channel information of each nucleus. Scale bars represent 3μm.

4.2.3 *Small and Large γ-H2AX Foci Partition in Both Heterochromatin and Euchromatin*

It has previously been shown that changes in γ-H2AX signal intensities accompany changes in chromatin structure (Park et al., 2003; Reitsema et al., 2004; Schwartz et al., 1993). Therefore, we reasoned that γ-H2AX foci could preferentially partition within specific types of chromatin in a manner that reflects the different levels of higher-order chromatin compaction. Actively transcribing chromatin or euchromatin is easily discernable from transcriptionally silent or heterochromatin (highly folded chromatin) based on DAPI staining – euchromatin exhibits low DAPI signal intensity while heterochromatin exhibits high levels of DAPI signal intensity. Figure 4.1 presents representative deconvolved images of GM38, SK-N-SH and IM cells immunofluorescently labeled with anti-γ-H2AX and counterstained with DAPI. Surprisingly, no overwhelming distribution preference was observed as both small and large γ-H2AX foci partitioned within euchromatin and heterochromatin (Figure 4.1). However, the most intensely staining γ-H2AX foci (typically the large γ-H2AX foci) were frequently observed juxtaposed to, rather than superimposed over, highly compacted heterochromatin as identified by the sharp peaks in the DAPI channel (Figure 4.1). The highly abundant small γ-H2AX foci however, appeared to distribute equally between euchromatin and heterochromatin (Figure 4.1). These observations suggest that the alterations in the abundance of γ-H2AX that correlate with premature chromatin condensation (PCC) or relaxation of the chromatin structure accompanying hypertonic treatments, must differ significantly from the overall difference in folding associated with euchromatin and heterochromatin.

4.2.4 *Small γ-H2AX Foci are Distinguishable from Large γ-H2AX DNA Repair Foci*

Currently, there is a wealth of evidence demonstrating spatial relationships (i.e. colocalization) between the large γ-H2AX repair foci in DNA damaged cells (e.g. IR treated) and numerous DNA repair proteins such as Mre11, Nbs1 (MRN complex), Rad51, BRCA1 and 53BP1 (Fernandez-Capetillo et al., 2003; Paull et al., 2000; Rappold et al., 2001; Schultz et al., 2000) and a major upstream kinase, ATM (Andegeko et al., 2001). However, no information is currently available that describes these spatial relationships in unirradiated mammalian cells, particularly with respect to the small γ-H2AX foci we detailed above. To examine these spatial relationships, unirradiated interphase cells were immunofluorescently labeled with anti-γ-H2AX in combination with antibodies specifically recognizing each of the proteins listed above. Interphase cells harboring as few large γ-H2AX foci as possible were purposely selected to prevent the often overwhelming signal intensities of large foci (γ-H2AX and other proteins) from confounding the spatial characterization of the small, less intense γ-H2AX foci. Furthermore, by purposely excluding the larger, more intense foci, we effectively maximized the dynamic ranges of the small foci within each channel, which provided us with optimal images for 3D spatial comparisons. Figure 4.5 provides a representative deconvolved slice from each of the 3D spatial relationships investigated in unirradiated SK-N-SH cells with similar results occurring in HeLa and GM38 cells (data not shown). Due to the species specificities of many of the repair protein antibodies, we could not investigate the spatial relationships in 10T1/2, COS-7 or IM cells. In human cells however, very little, if any colocalization (as identified by yellow signal within the merged images) was detected between the small γ-H2AX foci and MRN complex

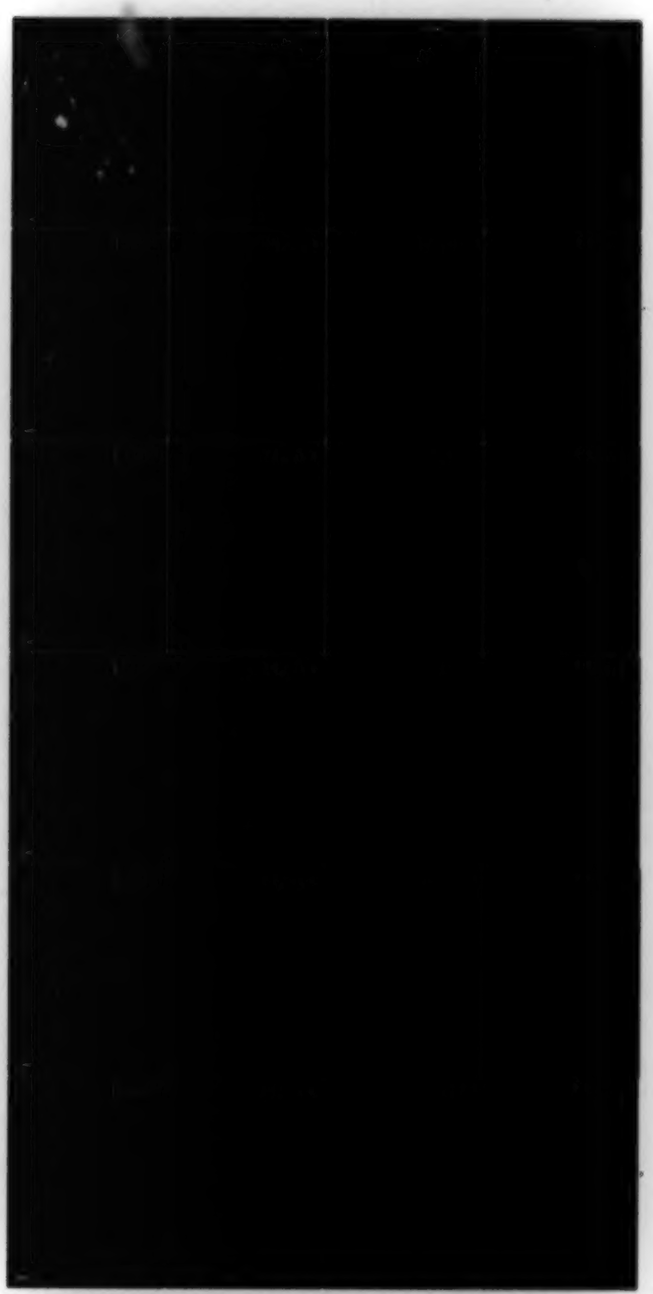

Figure 4.5: Spatial localization of the small γ-H2AX foci with DNA DSB repair proteins. Asynchronous and untreated SK-N-SH cells were immunofluorescently labeled with anti-γ-H2AX and individual components of the MRN complex (i.e. Mre11and Nbs1), Rad51, 53BP1, BRCA1 and ATM. The DNA was counterstained with DAPI. Depicted here are single planes from representative high-resolution (100×) 3D series that were subjected to software-driven deconvolution. Note the general lack of colocalization (absence of yellow signal) between the small γ-H2AX foci and all six proteins investigated. Scale bars represent 2μm.

members, BRCA1, 53BP1 or ATM (Figure 4.5), even though these proteins exhibit extensive colocalization with the large irradiation induced γ-H2AX repair foci (data not shown). When rare colocalization events were observed between these proteins and γ-H2AX foci, it predominantly involved only the large γ-H2AX foci. Consequently, these small foci are easily discernable from the large DNA DSB repair foci based solely on the colocalization of DNA repair proteins. Therefore, the small γ-H2AX foci represent unique foci that do not colocalize with DNA repair proteins or ATM. Furthermore, based on the differences in size and the lack of colocalization with DNA repair proteins, these small foci are extremely unlikely to be involved in DNA DSB repair.

4.2.5 *Dynamic Changes in the Abundance of γ-H2AX Accompany Cell Cycle Progression in Unirradiated Mammalian Cells*

Previous studies by Olive and colleagues (MacPhail et al., 2003a; MacPhail et al., 2003b) demonstrated that γ-H2AX foci in irradiated cells exhibit cell cycle-dependent increases. Therefore, we reasoned that in untreated mammalian cells, γ-H2AX foci might exhibit temporal kinetics reflecting the underlying functional requirement for either increases in γ-H2AX at specific cell cycle stages. To further explore these possibilities and better define the temporal progression of γ-H2AX, flow cytometry and DIM were performed. By coupling γ-H2AX IIF labeling with either PI (flow cytometry) or DAPI (DIM) staining of the DNA, we were able to easily discern distinct cell cycle stages.

In five unirradiated cell lines (HeLa, SK-N-SH, Cos-7, 10T1/2 and IM) examined by flow cytometry, a general increase in γ-H2AX signal intensity was observed as cell progressed through the cell cycle (Figure 4.6, A to E). There was an initial increase in γ-H2AX signal intensities as cells entered early S-phase that continued to increase as cells

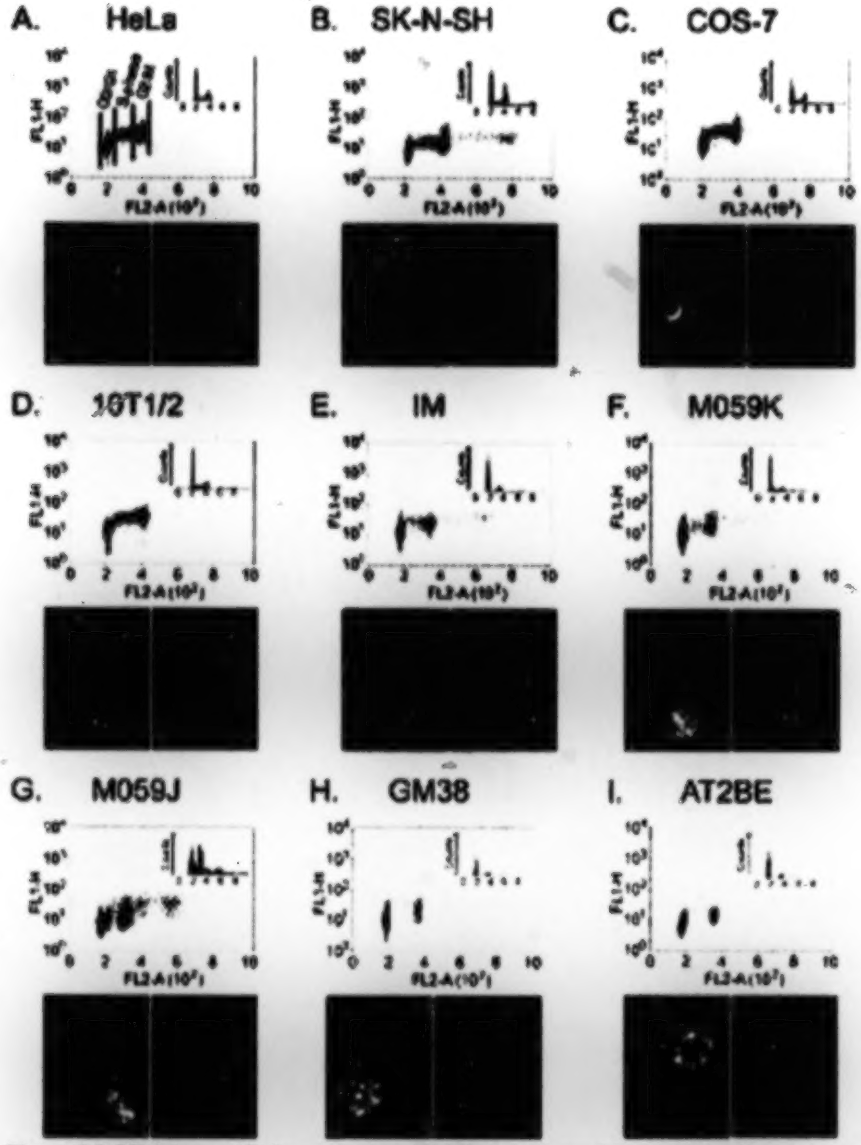

Figure 4.6: Mitotic-specific increases in γ-H2AX signal intensities in unirradiated mammalian cells. The temporal progression pattern of γ-H2AX in nine different unirradiated mammalian cell lines was investigated (panels A-I). Each panel contains a representative flow cytometric analysis dot plot depicting γ-H2AX (FL1-H, *y*-axis) signal intensity versus PI (FL2-A, *x*-axis) signal intensity of asynchronous populations. The G_0/G_1, S-phase and G_2/M populations have been denoted in HeLa (A) but can be extrapolated to all graphs. In addition, each panel contains a representative DIM image (40×) containing interphase and at least one mitotic cell (white arrow) to demonstrate the dramatic differences γ-H2AX signal intensities in those cells. In the left image, the DNA is counterstained with DAPI, while corresponding γ-H2AX-immunofluorescently labeled image is shown on the right. Note that the images were collected to best represent the signal intensities of the mitotic cells and were not acquired to best represent the small γ-H2AX foci in the interphase cells. Note the dramatic difference in signal intensities in all cell lines except the AT2BE cells. Scale bars represent 2μm.

progressed into mid- and late-S-phase. Surprisingly however, as cells entered G_2/M, γ-H2AX signal intensities continued to increase. In G_2/M, two populations became evident based on γ-H2AX signal intensities – a small subpopulation that exhibited increased γ-H2AX signal intensities over the predominant subpopulation that exhibited lower γ-H2AX signal intensities (Figure 4.6, A to E). The smaller, yet more intensely fluorescent population is reminiscent of a similar population observed in cells labeled with either PhosS10 or phosphorylated serine 28 (PhosS28) of histone H3 (McManus and Hendzel, 2004, submitted). PhosS10 and PhosS28 are known to exhibit dramatic increases during mitosis (Gernand et al., 2003; Hendzel et al., 1997; McManus and Hendzel, 2004 Submitted) and suggested that a similar mitosis-associated increase may occur within the γ-H2AX labeled cells (see below). Finally, upon cytokinesis and entry into G_1, γ-H2AX signal intensities rapidly returned to basal steady-state levels. In addition to these data demonstrating that the abundance of γ-H2AX increases in a cell cycle-dependent manner, they also demonstrate that maximal γ-H2AX levels occur during G_2/M.

To more precisely define the γ-H2AX temporal progression pattern specifically during mitosis, high-resolution DIM was performed on unirradiated HeLa, SK-N-SH, Cos-7, 10T1/2 and IM immunofluorescently labeled with anti-γ-H2AX. Visually appreciable differences in γ-H2AX signal intensities were observed between interphase and mitotic populations in all five cell lines examined (Figure 4.6, A to E). Upon closer inspection, a general temporal progression pattern was observed that parallels the results characterized by flow cytometry. As with flow cytometry, DIM identified some heterogeneity that occurred at each cell cycle stage (see Figure 4.7, A). Nevertheless, the most dramatic differences in γ-H2AX signal intensities occurred as cells entered or exited

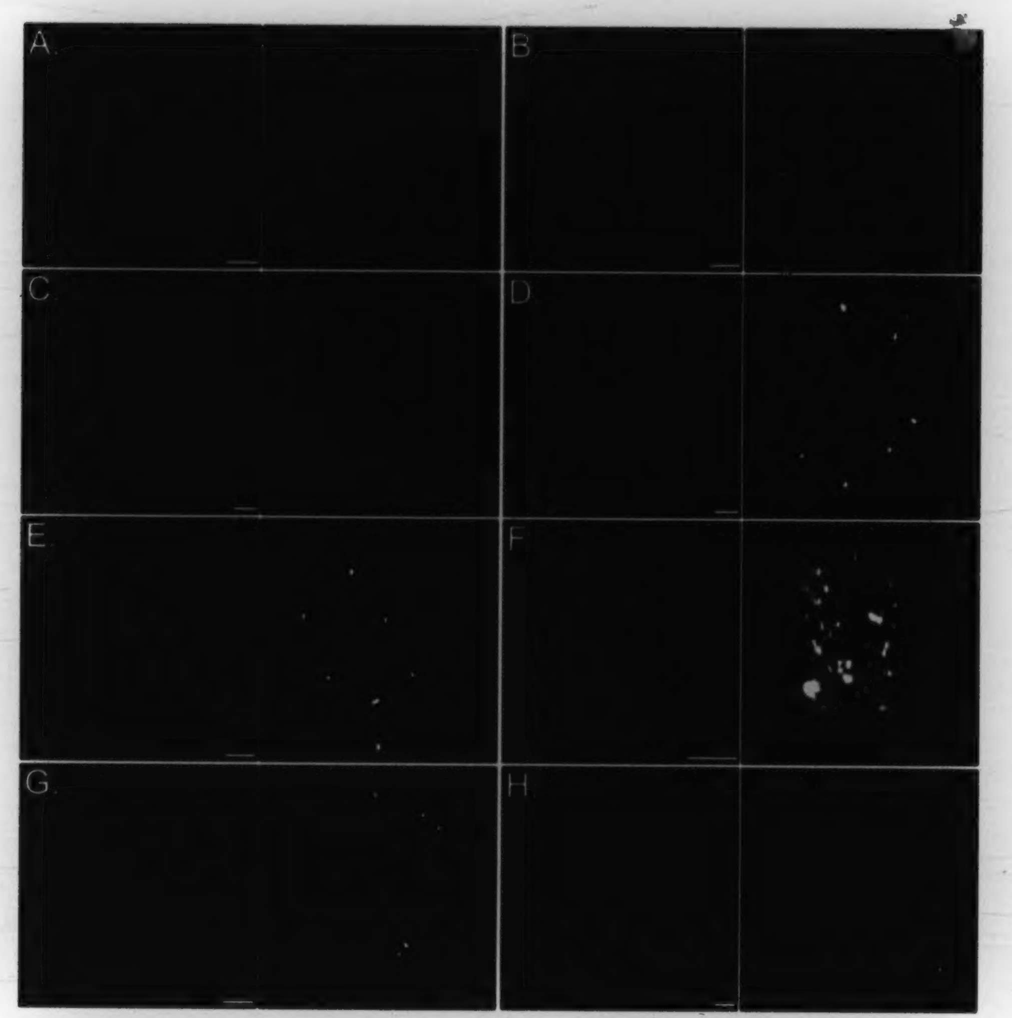

Figure 4.7: Typical γ-H2AX signal intensity variability observed throughout the cell cycle. Asynchronous and untreated mouse 10T1/2 fibroblasts were fixed and immunofluorescently labeled with anti-γ-H2AX (white) and counterstained with DAPI (green). 10T1/2 cells were specifically chosen to investigate the spatial localization of γ-H2AX foci relative to the DAPI-rich staining regions such as pericentromeric heterochromatin. Panel A is a 40× field micrograph depicting the γ-H2AX signal intensity variability routinely observed in interphase nuclei. Panels B through H are 3D projections of deconvolved high-resolution (100×) images at specific cell cycle stages: B) early G_2, C) late G_2, D) prophase, E) prometaphase, F) metaphase, G) telophase, and, H) early G_1. The exposure time of the γ-H2AX channel in panels B through H were maintained constant to permit the qualitative visual assessment of γ-H2AX signal intensity variability at specific cell cycle stages. Scale bars represent 20μm (A) and 3μm (B to H).

mitosis. As cells progressed through the initial stages of mitosis (prophase to prometaphase) γ-H2AX signal intensities continued to increase until maximal levels were reached at metaphase (Figure 4.7, B-H). Increases were evident throughout the chromosome arms and were not excluded from highly compacted pericentromeric heterochromatin as identified in 10T1/2 cells (Figure 4.7, B to H). As detailed in Table 4.1, the increases in γ-H2AX signal intensities that accompany entry into mitosis (compare G_1/S [-IR] with M [-IR]) were accounted for by slight increases in focal volumes (e.g. 0.16 μm^3 versus 0.18 μm^3) and numbers (e.g. 349 versus 388). Finally, as cells progressed from anaphase into telophase a corresponding decrease in γ-H2AX intensities was observed that reached basal steady-state levels immediately following cytokinesis. These results clearly indicate that maximal γ-H2AX signal intensities occur within mitosis, or more specifically between prometaphase and metaphase. Furthermore, they indicate that the small G_2/M populations identified by flow cytometry with elevated γ-H2AX intensities as determined by flow cytometry and detailed above, are most likely those in various stages of mitosis.

4.2.6 *Mitosis-specific Increases in γ-H2AX do not Reflect Changes in Epitope Accessibility*

When we examined the progression of γ-H2AX in asynchronously growing cell lines by DIM, we observed marked increases in γ-H2AX signal intensities in prometaphase and metaphase cells as compared to interphase cells (Figures 4.6 and 4.7). In order to eliminate the possibility that the observations detailed above were influenced by epitope accessibility issues that are dependent on changes in chromatin structure or interactions with additional proteins, immunoblot analyses were performed following sodium dodecyl-sulfate (SDS) polyacrylamide gel electrophoresis (PAGE). The abundance of γ-H2AX was compared between protein preparations isolated from asynchronous and mitotically-enriched HeLa, SK-N-SH, COS-7, 10T1/2 and IM cells. The relative percentages of asynchronous or nocodazole-treated cells at various stages of the cell cycle were determined by flow cytometry (Table 4.2). The majority of the asynchronous cells were in interphase (G_1 and S-phase), while the predominant proportions of nocodazole-treated cells were in G_2/M. Furthermore, the predominant proportion of nocodazole-treated cells were visually confirmed by DIM to be in prophase or prometaphase. Equivalent amounts of acid-solubilized proteins from each population (i.e. asynchronous or G_2/M-enriched) and cell line were resolved by SDS-PAGE and immunostained with anti-γ-H2AX. In agreement with the above results, significant increases in γ-H2AX were apparent in the mitotically-enriched populations as compared to the asynchronous, predominantly interphase, populations (Figure 4.8). For example, HeLa, SK-N-SH, Cos-7, and 10T1/2 cells exhibit dramatic differences in γ-H2AX signal intensities, while IM cells a less pronounced difference. The differences in γ-H2AX signal variation observed between cell lines is not likely to be significant as it correlates with the effectiveness of nocodazole to arrest cells at prometaphase (see Table 4.2). Similar qualitative differences between asynchronous and mitotically-enriched populations were observed using mitosis-enriched populations generated by double thymidine treatment followed by 4 hr treatment with ALLN or nocodazole (data not shown).

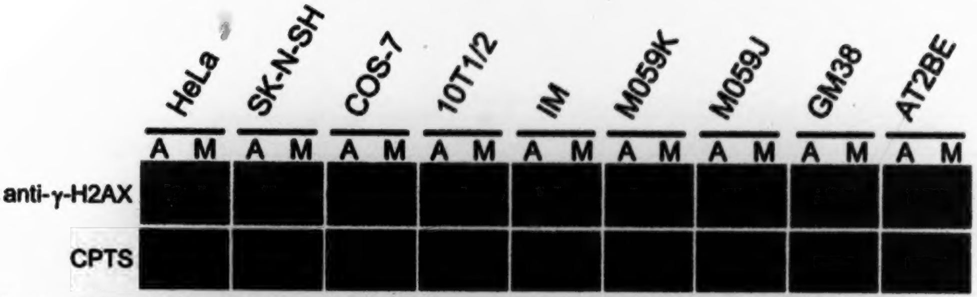

Figure 4.8: Qualitative increases in the abundance of γ-H2AX in mitotically-enriched cells. Acid-solubilized proteins were isolated from nuclear preparations of asynchronous (A) or mitotically-enriched (M) populations. Nine independent immunoblot assays were performed in triplicate and a single representative blot is shown for each cell line (indicated at top). The CPTS stained PVDF membrane has been included and serves as a loading control. Note that for the first eight cell lines (HeLa through to GM38) a marked difference in the abundance of γ-H2AX occurs, with the mitotically-enriched population exhibiting the greatest signal intensity. For the AT2BE cell line, nearly identical signal intensities of γ-H2AX occurs in the asynchronous and mitotically-enriched population, despite a 3.69-fold increase in the G2/M population (see Table 4.2).

Table 4.2: Relative percentage of cells in specific cell cycle stages[a].

		Percentage of Cells in			Fold Increase
Cell Line	Noc[b]	G_0/G_1	S-Phase	G_2/M[c]	in G2/M[d]
HeLa	-	56.39	16.94	26.67	
HeLa	+	3.46	6.04	90.50	3.39
SK-N-SH	-	51.06	20.49	28.45	
SK-N-SH	+	15.23	17.96	66.81	2.35
COS-7	-	51.63	21.89	26.48	
COS-7	+	3.22	14.96	81.82	3.09
10T1/2	-	60.41	18.57	21.02	
10T1/2	+	4.72	12.20	83.08	3.95
IM	-	76.58	6.79	16.63	
IM	+	70.81	4.74	24.45	1.47
M059K	-	82.34	7.69	9.97	
M059K	+	61.91	12.04	26.05	2.61
M059J	-	32.74	19.93	47.33	
M059J	+	18.99	19.19	61.82	1.31
GM38	-	90.30	2.51	7.46	
GM38	+	85.23	0.87	13.90	1.86
AT2BE	-	80.95	3.13	15.92	
AT2BE	+	38.30	2.98	58.72	3.69
AT5BI	-	66.21	13.87	19.92	
AT5BI	+	26.48	9.32	64.20	3.22

---

[a] Represents one of three individual flow cytometry trials examining the fold-increase in the percentage of G_2/M cells following nocodazole treatment.

[b] Nocodazole treatment (Noc); '-' is untreated, '+' is treated (15nM for 12 hr)

[c] The predominant proportion of nocodazole arrested cells were visually confirmed by DIM to be in prometaphase

[d] Similar results (i.e. fold-enrichment in proportion of cells in G_2/M) were observed in the two additional experiments.

4.2.7 *Functional ATM Expression Correlates with Mitosis-specific H2AX Phosphorylation*

Previous biochemical studies have demonstrated that PI3-K protein kinase family members regulate γ-H2AX kinetics in response to DNA DSBs (Burma et al., 2001; Park et al., 2003; Stiff et al., 2004; Ward and Chen, 2001) and independent roles for ATM and DNA-PK$_{CS}$ kinase activities in regulating H2AX phosphorylation have been established (Burma et al., 2001; Park et al., 2003; Stiff et al., 2004). Therefore, we hypothesized that either, or both, of these kinase activities may underlie the mitosis-associated increases in γ-H2AX detailed above. To investigate these possibilities we examined γ-H2AX during mitosis in cell lines deficient or defective for ATM and DNA-PK$_{CS}$. Using ATM-defective, AT2BE (Barfknecht and Little, 1982), and DNA-PK$_{CS}$ deficient, M059J (Lees-Miller et al., 1995), cell lines and the respective control lines, GM38 and M059K, we performed identical experiments to those detailed above, including DIM, flow cytometry and immunoblot analysis.

DIM investigations performed in AT2BE, GM38, M059J and M059K revealed similar γ-H2AX localization patterns to those detailed above. However, it was noted that the AT2BE cell line exhibited the lowest immunoreactivity with the anti-γ-H2AX antibody of all cell lines investigated and is not entirely unexpected as ATM is a major regulator of H2AX phosphorylation (Burma et al., 2001). Nevertheless, both large and small γ-H2AX foci were still readily apparent and visually distinguishable in AT2BE cells (Figure 4.9, A). GM38, M059J and M059K cells all exhibited a temporal progression pattern similar to that detailed above, where γ-H2AX signal intensities were minimal in interphase and maximal in mitosis (Figure 4.6, F to H). In contrast, AT2BE

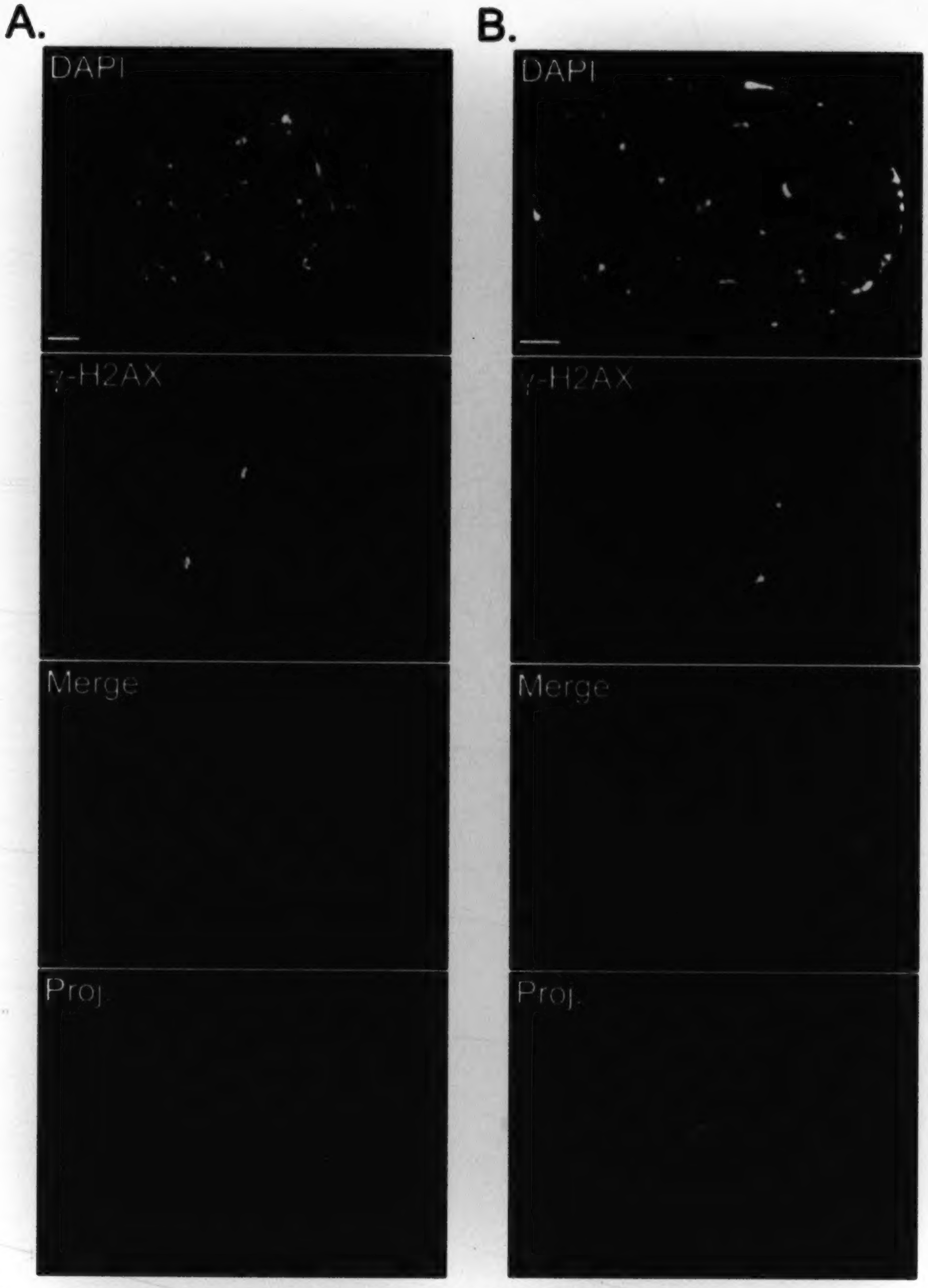

Figure 4.9: Localization of γ-H2AX in AT2BE and AT5BI fibroblasts.
Depicted here are representative deconvolved, high-resolution (100×) DIM images of unirradiated AT2BE (A) and AT5BI (B) cells immunofluorescently labeled with anti-γ-H2AX (green) and counterstained with DAPI (red) to reveal DNA. The merged image is a single plane from the 3D deconvolved series while the entire 3D image is presented as a deconvolved projection in the fourth row (Proj.). Scale bars represent 2μm.

cells lacked the mitosis-specific increase in γ-H2AX that all other cell lines exhibited (Figure 4.6, I).

To further investigate the potential roles ATM and DNA-PK$_{CS}$ may have in the mitosis-specific H2AX phosphorylation, flow cytometry was performed (Figure 4.6, F to I). γ-H2AX fluorescent signal intensities increased as M059J, M059K and GM38 cells progressed from G_0/G_1 to S-phase and continued to increase as cells entered G_2/M. The two G_2/M subpopulations observed previously in HeLa, SK-N-SH, COS-7, 10T1/2 and IM were also apparent in these three cell lines, but to a lesser extent. In addition, DNA content analysis demonstrated that the M059J cell line exhibits two distinct cell populations that differ with respect to their ploidy levels and was confirmed using ModFit LT software (Verity Software House, Inc) (data not shown). AT2BE cells exhibited a unique relationship between the abundance of γ-H2AX and the cell cycle. Initially, the γ-H2AX signal intensities from G_1 to mid-S-phase of AT2BE cells exhibited similar temporal kinetics to all other cell lines investigated. However, as AT2BE cells entered mid-S-phase, they began to exhibit differences that distinguished them from all other cell lines investigated – γ-H2AX signal intensities plateaued in mid-S-phase and began to decrease during late-S-phase. γ-H2AX signal intensities continued to decrease as cells entered G_2/M and unlike the other cell lines, a distinct subpopulation occurring within the G_2/M population was not readily apparent. These results suggest that the mitosis-specific increase in γ-H2AX that occurs in normal unirradiated mammalian cells requires functional ATM expression.

To eliminate the possibility of altered epitope accessibility or masking at specific points of the cell cycle immunoblot analyses were performed on histones isolated from

AT2BE, GM38, M059J and M059J cells. Qualitative differences were observed between asynchronous and mitotically-enriched M059K, M059J and GM38 populations (Figure 4.8). As noted above, the differences in γ-H2AX signal intensities between cell lines correlates with the ability of nocodazole to generate a mitotically-enriched population as determined by flow cytometry and confirmed visually by DIM (Table 4.2). Surprisingly, only comparatively small differences in signal intensities were observed for AT2BE cells despite the fact it exhibits the second largest G_2/M enrichment (3.69-fold increase) of all cell lines examined (Table 4.2). This observation corroborates those of DIM and flow cytometry data, and strongly implicates ATM in regulating the mitosis-specific H2AX phosphorylation.

4.2.8 *Quantitative Imaging Microscopy Reveals that Functional ATM is Required for Mitotic H2AX Phosphorylation*

QIM was performed to confirm the above findings and clearly demonstrate that the qualitative differences observed for the abundance of γ-H2AX between interphase and mitotic cells was based on the functional ATM expression. Five different cell lines, HeLa, M059K, M059J, GM38 and AT2BE were selected to evaluate the temporal progression of this modification *in situ*. Due to the manner in which images are acquired and analyzed for QIM, it has three major advantages over conventional flow cytometric or biochemical analyses; 1) the exposure times for each channel are maintained constant throughout image acquisition and permits both qualitative and quantitative comparisons between images from the same cell line, 2) cells at specific points of the cell cycle (e.g. interphase or mitosis) can be easily classified based on chromosome morphological criteria, and, 3) histone variability can be accounted for on a single cell basis by normalizing the γ-H2AX signal intensity to DAPI signal intensity (McManus and Hendzel, 2003; McManus and Hendzel, 2004). The combination of these three factors permitted us to define differences in the stoichiometry of γ-H2AX at specific cell cycle stages that are independent of histone concentration.

QIM was performed on asynchronous populations and Student *t*-tests were calculated comparing the mean normalized γ-H2AX fluorescent intensities (norm-γ-H2AX) of each cell within the interphase and mitotic populations. The results of five independent and cell line-specific experiments comparing the mean norm-γ-H2AX fluorescent intensities are graphically depicted in Figure 4.10. In four cell lines, HeLa, M059K, M059J and GM38, differences between interphase and mitotic mean norm-γ-H2AX fluorescent signal intensities were visually apparent and Student *t*-tests (Table 4.3) confirmed that these differences were all statistically significant (*p*-value <0.001). In contrast, visual comparisons between the mean norm-γ-H2AX fluorescent intensities from AT2BE cells did not reveal large qualitative differences (Figure 4.10), while the results of the Student *t*-tests demonstrated that the differences in mean values were not statistically significant (*p*-value = 0.528 [Table 4.3]). Rather, the *t*-tests indicated that the interphase and mitotic populations from AT2BE were most likely drawn from the same sample population. These data corroborate those of the previous sections and demonstrates that functional ATM expression correlates with mitosis-specific H2AX phosphorylation.

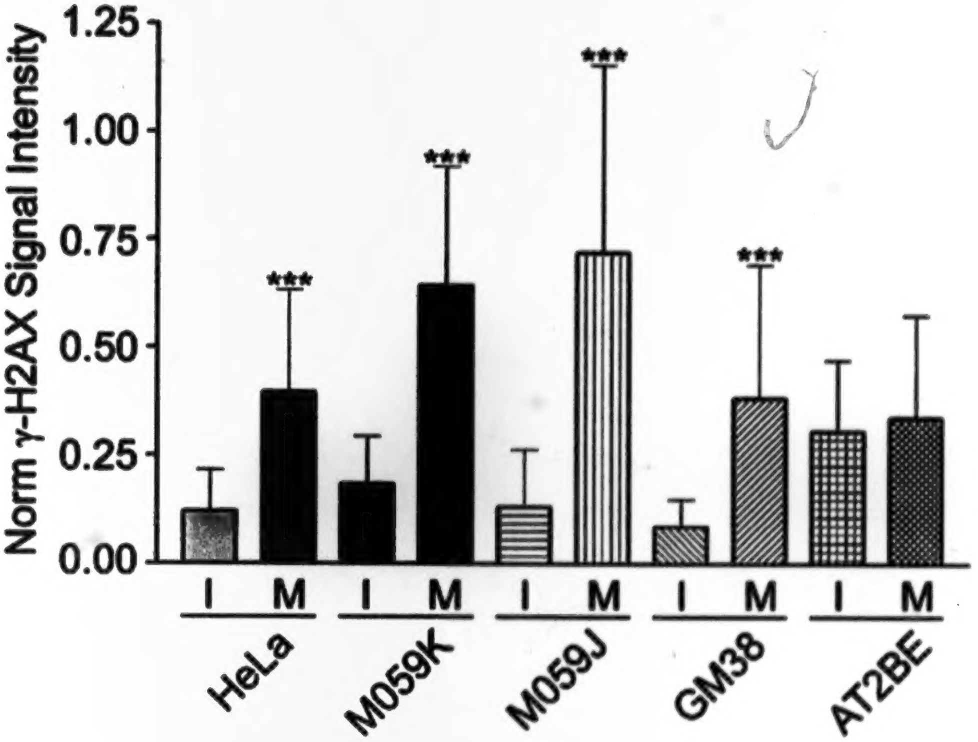

Figure 4.10: QIM reveals a mitotic-specific phosphorylation event that correlates with functional ATM expression.
Five distinct unirradiated mammalian cell lines (denoted on bottom of *x*-axis) were investigated by QIM. Depicted here are the mean norm-γ-H2AX signal intensities of interphase (I) and mitotically-enriched (M) populations (prophase through telophase). In four cases (HeLa, M059K, M059J and GM38), highly statistically significant differences (denoted by *** [*p*-value <0.001]) between I and M populations were calculated by student *t*-tests (see Table 4.3). The mean norm-γ-H2AX signal intensities of I and M populations in AT2BE cells appear to be similar visually and were not statistically different (*p*-value = 0.528).

Table 4.3: Quantitative analysis of normalized γ-H2AX signal intensity in mitotic and interphase cells.

Cell Line	Interphase Population Mean ± SEM[a]	N[b]	Mitotic Population Mean ± SEM	N	*p*-value[c]
HeLa	0.120 ± 0.006	226	0.397 ± 0.040	36	<0.001
M059K	0.185 ± 0.006	400	0.644 ± 0.053	27	<0.001
M059J	0.130 ± 0.006	483	0.721 ± 0.100	19	<0.001
GM38	0.085 ± 0.005	182	0.385 ± 0.069	20	<0.001
AT2BE	0.308 ± 0.050	141	0.340 ± 0.066	13	0.528

[a] Mean Norm- γ-H2AX Signal intensity ± standard error of the mean (SEM)

[b] N = number

[c] A *p*-value <0.05 is considered to be statistically significant

4.2.9 *Functional ATM Expression is Required for Mitosis-Associated Increases in γ-H2AX*

Although the results detailed in the above sections indicate that functional ATM expression correlates with mitosis-associated increases in γ-H2AX, they are only drawn from a single cell line, namely AT2BE. To further explore the role ATM may have in regulating γ-H2AX dynamics during mitosis we performed identical experiments to those outlined above using a second ATM-defective cell line (AT5BI) that is derived from an ataxia telangiectasia (AT) patient (Simons, 1979). Like AT2BE cells, DIM demonstrated that AT5BI exhibited lower immunoreactivity towards the anti-γ-H2AX antibody, but both large and small γ-H2AX foci were still readily apparent and clearly discernable (Figure 4.9, B). Next, DIM and flow cytometry were performed on AT5BI cells as above. These approaches revealed very similar results to those obtained for AT2BE (Figure 4.11, A and B) where the abundance of γ-H2AX did not increase in a mitosis-associated manner. In fact, following the initial increase in γ-H2AX as cells enter S-phase, γ-H2AX signal intensities plateaued (mid-S-phase) prior to decreasing in late-S-phase with continued decrease upon entry into G_2/M. Immunoblot analysis of acid solublized nuclear proteins resolved by SDS-PAGE confirmed these observations and revealed that γ-H2AX is found in approximately equivalent amounts in asynchronous (predominantly interphase) and mitotically-enriched populations (Figure 4.11, C and Table 4.2). Furthermore, the immunoblots also serve to demonstrate that the results obtained by IIF (i.e. flow cytometry, DIM and QIM) were not due to epitope masking as described above. Finally, QIM was performed on asynchronous AT5BI cells and Student *t*-tests evaluating the difference between mean norm-γ-H2AX signal intensities from

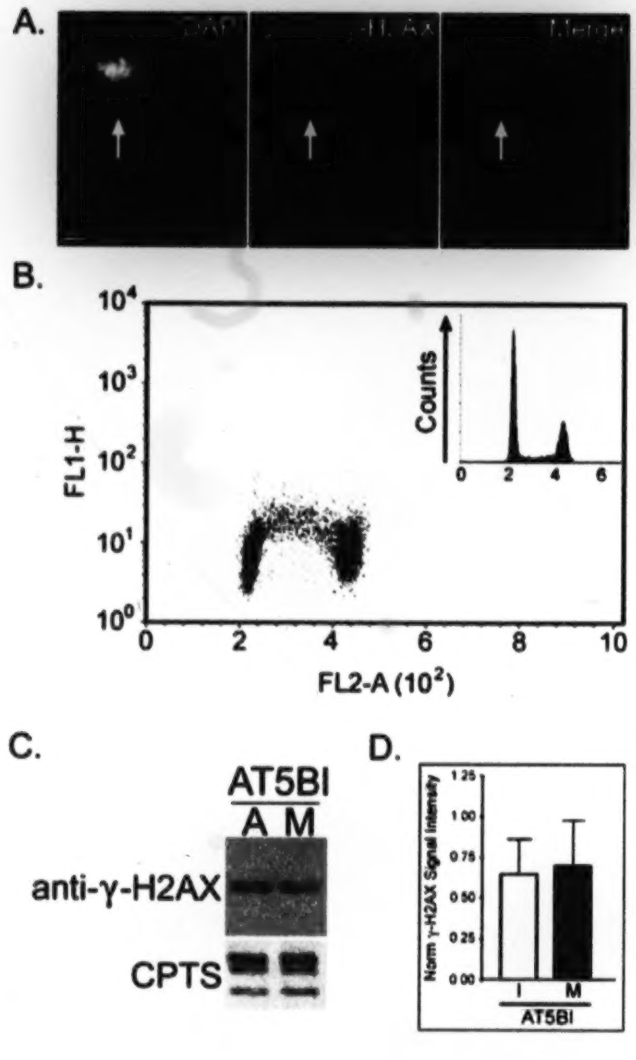

Figure 4.11: Normally growing AT5BI cells do not exhibit mitosis-associated increases in γ-H2AX. Panel A is a representative DIM image (100×) 3D projection that demonstrates the lack of a qualitative difference between mitotic (white arrow) and interphase cells immunofluorescently labeled with anti-γ-H2AX and counterstained with DAPI. The merged image presents the DAPI (red) and -γ-H2AX (green) channels. Scale bar represents 2μm. Panel B presents a single representative flow cytometric dot plot of an asynchronous AT5BI population immunofluorescently labeled with anti-γ-H2AX and counterstained with PI. The dot plot depicts γ-H2AX (FL1-H, *y*-axis) signal intensity versus PI (FL2-A, *x*-axis) signal intensity. The inset represents the PI-only pattern and demonstrates that the cells were cycling. Panel C is a representative immunoblot comparing the abundance of γ-H2AX in an asynchronous population (A) and a mitotically-enriched (M) population. Acid-solubilized, nuclear protein preparations from AT5BI cells were resolved on 15% SDS PAGE gels, and immunostained with anti-γ-H2AX. The CPTS stained PVDF membrane has been included and serves as a loading control. Panel D graphically depicts the results obtained by QIM. Note that the difference between the mean normalized γ-H2AX signal intensities from the interphase (I) and mitotic (M) populations is not statistically significant (*p*-value = 0.257).

interphase and mitotic populations were calculated. This statistical analysis revealed that the difference between population means was not statistically significant (*p*-value = 0.257) (Table 4.4). Therefore, these data combined with the data of the previous sections indicate that functional ATM expression is required for mitosis-associated increases in γ-H2AX.

Table 4.4: Quantitative analysis of mean normalized γ-H2AX signal intensity in interphase and mitotic AT5BI cells.

	Interphase Population		Mitotic Population		
Cell Line	Mean ± SEM[a]	N[b]	Mean ± SEM	N	*p*-value[c]
AT5BI	0.648 ± 0.012	305	0.698 ± 0.054	26	0.257

[a] Mean Norm- γ-H2AX Signal intensity ± standard error of the mean (SEM)
[b] N = number
[c] A *p*-value <0.05 is considered to be statistically significant

4.3 DISCUSSION

In this study, we demonstrate that in the absence of exogenous sources of DNA damage, γ-H2AX exists in normally growing cell lines from a diverse range of mammalian species. Within these cell lines, γ-H2AX exists as two highly discernable focal patterns. The predominant proportion of γ-H2AX foci are small and do not colocalize with numerous different DNA DSB repair proteins, including Mre11, NBS1, Rad51, 53BP1, BRCA1 and ATM. Moreover, these foci partition equally within both heterochromatin and euchromatin. The second minor population of γ-H2AX foci is considerably larger and is associated with DNA DSBs – these foci can be induced following γ-irradiation and colocalize with numerous DNA repair proteins. These foci preferentially distribute within euchromatin or are found within regions lying immediately adjacent to highly compacted heterochromatin and rarely superimposed over regions exhibiting intense DAPI staining (heterochromatin). This observation suggests that an underlying mechanism regulating chromatin structure following DNA DSBs may be required for DNA repair to occur.

We also demonstrate that γ-H2AX in unirradiated cells exhibits cell cycle associated dynamics that are tightly coupled with mitosis. Basal steady-state levels occur in early G_1 and as the cells progress through S-phase, there is a corresponding increase in the overall abundance of γ-H2AX. This initial increase in γ-H2AX correlates well with previously described DNA DSBs that occur during DNA replication as a result of stalled replication forks and the activities of Topoisomerases I and II (Furuta et al., 2003; Huang et al., 2004; Huang et al., 2003; Limoli et al., 2002). Unexpectedly however, as cells progress from S-phase through G_2 and into mitosis γ-H2AX levels continue to increase until maximal levels are attained at metaphase. Upon entry into anaphase, γ-H2AX levels begin to decrease and continue to decrease throughout the remaining stages of mitosis until basal steady-state levels are reached by late telophase or early G_1. Based on data gleaned from PI3-K-defective cell lines (AT2BE, AT5BI and M059J), this second γ-H2AX induction phase is dependent on functional ATM expression but is independent of functional DNA-PK_{CS} expression (Figures 4.6, 4.8, 4.10 and 4.11). These observations indicate that ATM kinase activity is temporally regulated in unirradiated mitotic cells where it normally phosphorylates H2AX during G_2 and mitosis. In keeping with this observation, the activated form of ATM (see Bakkenist and Kastan, 2003), as identified by anti-ATM phospho-serine 1981 (p-ATM) immunofluorescent staining, is readily apparent by DIM during G_2 and mitosis (Figure 4.12). However, the presence of p-ATM throughout all stages of the cell cycle suggests that additional mechanisms regulating its catalytic activity must exist. These could include subsequent posttranslational modifications or the dissociation of p-ATM from metaphase to telophase chromosomes (see Figure 4.12). Finally, the identification of a mitosis-specific γ-H2AX induction present in all unirradiated mammalian ($ATM^{+/+}$) cells examined suggests that there may be a conserved requirement for γ-H2AX.

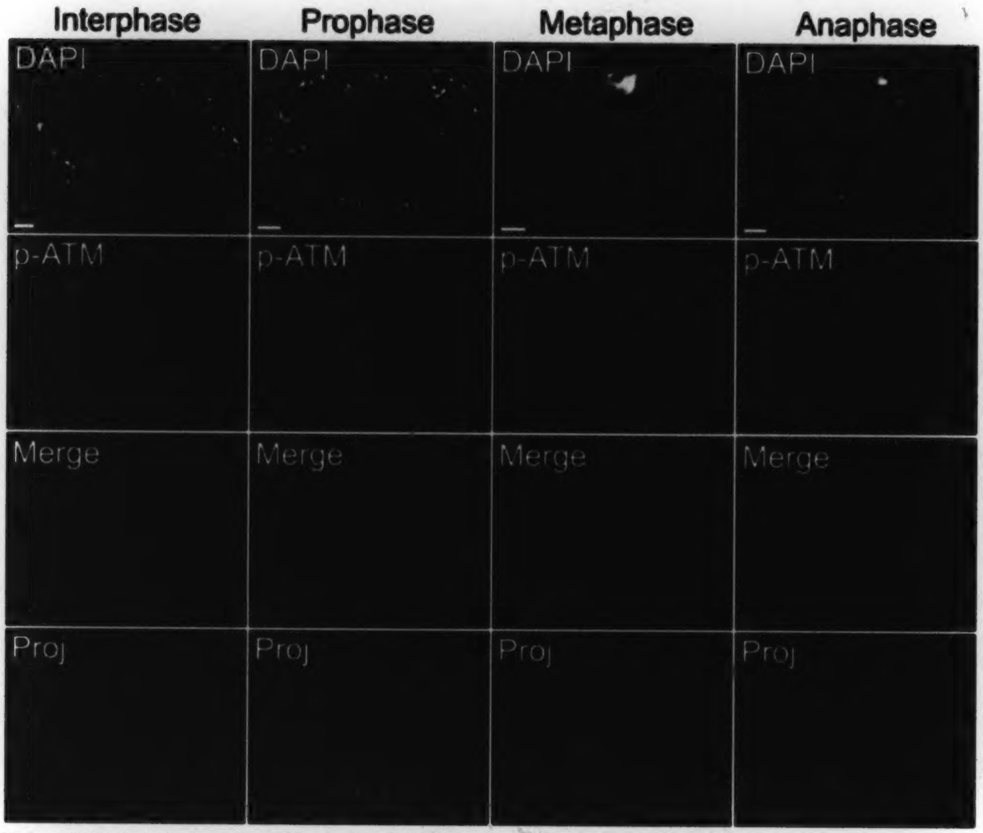
Interphase
Prophase
Metaphase
Anaphase
DAPI
DAPI
DAPI
DAPI
p-ATM
p-ATM
p-ATM
p-ATM
Merge
Merge
Merge
Merge
Proj
Proj
Proj
Proj

Figure 4.12: Spatial localization of phospho-ATM in IM fibroblasts.
Asynchronous IM Fibroblasts were paraformaldehyde-fixed, permeabilized, immunofluorescently labeled with anti-phospho-ATM (serine 1981 [p-ATM]) and counterstained with DAPI. Depicted here are high-resolution (100×) representative images at interphase, prophase, metaphase and anaphase that were subjected to image deconvolution. Single planes are presented for the DAPI (red), p-ATM (green) and Merge images, while the signals through each nucleus is presented as a 3D projection (Proj). Scale bars represent 3μm.

The spatial and temporal progression of γ-H2AX that we observe has functional implications on the enzymes regulating the covalent addition of the phosphate group and those that remove it. First, our data suggest that ATM activity is upregulated as cells progress from G_2 into mitosis or when chromosome compaction begins. Specifically, as cells enter prophase, there is a dramatic increase in γ-H2AX in most mammalian cells that does not occur in AT2BE or AT5BI. Furthermore, since increases in γ-H2AX occur in late G_1 and early to mid-S-phase in all cell lines examined, including AT2BE and AT5BI, it does not appear that ATM activity is regulating γ-H2AX levels at those particular stages of the cell cycle. These observations imply that ATM activity is upregulated during the initial onset of chromosome compaction. They also suggest that ATM activity towards H2AX is downregulated following transition into anaphase when chromosome segregation to opposite poles begins. This could occur through several mechanisms including the spatial partitioning of enzyme and substrate into distinct regions, inactivation of ATM through subsequent posttranslational modifications, or some unknown mechanism. Furthermore, our DIM results demonstrate that γ-H2AX decreases during the latter stages of mitosis (telophase to cytokinesis) and suggests that the responsible phosphatase and its activity towards γ-H2AX is also likely to be regulated in cell cycle dependent fashion. Recent *in vitro* biochemical studies have strongly implicated protein phosphatase 1α (PP1α) as the candidate phosphatase (Nazarov et al., 2003; Siino et al., 2002) although this has yet to be confirmed *in vivo*. As with ATM, PP1α phosphatase activity could be regulated through relocalization of PP1α and/or increased activity. These possibilities would necessarily accompany the increasing chromosome compaction that occurs as cells progress from metaphase to telophase and the segregation of chromosomes to opposite poles.

Although highly speculative, we propose three separate but plausible explanations for the observed mitosis-associated increases in γ-H2AX. First, the mitosis-associated increases in γ-H2AX could reflect the underlying changes in chromatin structure that accompany the assembly of metaphase chromosomes. The difference in chromatin compaction levels, or the 'packaging ratio', between interphase and mitotic chromosomes in mammalian cells is estimated to be approximately 40-fold (Turner, 2001) and is much greater than the difference between euchromatin and heterochromatin. An increase in γ-H2AX reflecting these gross changes in chromatin structure is not inconceivable as many researchers have observed changes in the abundance of γ-H2AX that correlate with experimentally-induced changes in chromatin structure (Park et al., 2003; Reitsema et al., 2004; Schwartz et al., 1993). A second possibility is that increased γ-H2AX levels may be required to preserve the fidelity of the mitotic process. Previous observations involving other posttranslational histone modifications such as PhosS10 or trimethylated lysine 9 (H3) have demonstrated that they are essential for genomic integrity specifically with respect to chromosome compaction and dynamics during mitosis (Bui et al., 2004; Hendzel et al., 1997; McManus et al., 2004 submitted; Peters et al., 2001; Petersen et al., 2001; Wei et al., 1999). This prospect is further substantiated by observations that haploinsufficient H2AX mice ($H2AX^{-/+}$) or mice lacking H2AX ($H2AX^{-/-}$ or $H2AX^{\Delta/\Delta}$) exhibit increases in genomic instability (Bassing et al., 2002; Celeste et al., 2003; Celeste et al., 2002). Celeste and colleagues (Celeste et al., 2002) demonstrated that H2AX is not essential for viability but that aspects reminiscent of proliferation- and mitosis-defects, such as low mitotic indices and elevated chromosomal aberrations, were readily apparent in cells lacking H2AX. Although many of the aberrant phenotypes associated with the absence of H2AX and γ-H2AX can be ascribed to activation of specific cell cycle checkpoints, they can also be explained by the inability of cells to progress to, and through, mitosis. This possibility may reflect a currently undefined, yet essential underlying functional requirement for mitosis-associated changes in γ-H2AX. Finally, the small γ-H2AX foci may serve to prime and protect the genome against detrimental lesions manifesting as DNA DSB by detecting changes in chromatin structure associated with DNA DSBs. As such, the mitosis-associated increase in γ-H2AX occurs when DNA repair and the resection of broken ends is most critical. Having the ability to respond quickly following DNA DSB is essential to the maintenance of genomic integrity prior to chromosome segregation and daughter cell formation. In any case, it is clear that the mitosis-associated changes in γ-H2AX abundance that we observe by IIF (e.g. DIM and flow cytometry) are not artifacts reflecting altered chromatin compaction states that affect the accessibility of the γ-H2AX epitope at various stages of the cell cycle as SDS-PAGE and immunoblot analyses confirmed the IIF *in situ* findings.

4.4 ACKNOWLEDGEMENTS

The authors thank Drs. J. Allalunis-Turner (University of Alberta) and R. Mirzayans (University of Alberta) for generously providing the M059J/K and AT2BE/AT5BI/GM38 cell lines respectively, and for helpful discussions, Dr. X. Sun of the Cell Imaging Facility for microscopy assistance and helpful discussions and Ms. J. Wizniak for technical assistance with flow cytometry. We thank Abcam for generously providing the rabbit polyclonal anti-γ-H2AX (ab11174 and ab2983), anti-Brca1, anti-53BP1 antibodies and H2AX peptides and are extremely grateful to Drs. J. Y. Masson (l'Université Laval) and G. K. Chan (University of Alberta) for generously providing the Mre11, Rad51 and Nbs1, and ATM antibodies, respectively.

The authors thank the Canadian Institutes of Health Research (CIHR) and the Alberta Heritage Foundation for Medical Research (AHFMR) for operational funding support. During the course of this study KJM was supported by studentships CIHR and AHFMR. MJH is supported by scholarships from the CIHR and AHFMR.

4.5 REFERENCES

Andegeko, Y., L. Moyal, L. Mittelman, I. Tsarfaty, Y. Shiloh, and G. Rotman. 2001. Nuclear retention of ATM at sites of DNA double strand breaks. *J Biol Chem*. 276:38224-30.

Aten, J.A., J. Stap, P.M. Krawczyk, C.H. van Oven, R.A. Hoebe, J. Essers, and R. Kanaar. 2004. Dynamics of DNA double-strand breaks revealed by clustering of damaged chromosome domains. *Science*. 303:92-5.

Bakkenist, C.J., and M.B. Kastan. 2003. DNA damage activates ATM through intermolecular autophosphorylation and dimer dissociation. *Nature*. 421:499-506.

Barfknecht, T.R., and J.B. Little. 1982. Hypersensitivity of ataxia telangiectasia skin fibroblasts to DNA alkylating agents. *Mutat Res*. 94:369-82.

Bassing, C.H., K.F. Chua, J. Sekiguchi, H. Suh, S.R. Whitlow, J.C. Fleming, B.C. Monroe, D.N. Ciccone, C. Yan, K. Vlasakova, D.M. Livingston, D.O. Ferguson, R. Scully, and F.W. Alt. 2002. Increased ionizing radiation sensitivity and genomic instability in the absence of histone H2AX. *Proc Natl Acad Sci U S A*. 99:8173-8.

Bassing, C.H., H. Suh, D.O. Ferguson, K.F. Chua, J. Manis, M. Eckersdorff, M. Gleason, R. Bronson, C. Lee, and F.W. Alt. 2003. Histone H2AX: a dosage-dependent suppressor of oncogenic translocations and tumors. *Cell*. 114:359-70.

Bui, H.T., E. Yamaoka, and T. Miyano. 2004. Involvement of histone H3 (Ser10) phosphorylation in chromosome condensation without CDC2 kinase and mitogen-activated protein kinase activation in pig oocytes. *Biol Reprod*. 70:1843-51.

Burma, S., B.P. Chen, M. Murphy, A. Kurimasa, and D.J. Chen. 2001. ATM phosphorylates histone H2AX in response to DNA double-strand breaks. *J Biol Chem*. 276:42462-7.

Celeste, A., S. Difilippantonio, M.J. Difilippantonio, O. Fernandez-Capetillo, D.R. Pilch, O.A. Sedelnikova, M. Eckhaus, T. Ried, W.M. Bonner, and A. Nussenzweig. 2003. H2AX haploinsufficiency modifies genomic stability and tumor susceptibility. *Cell*. 114:371-83.

Celeste, A., S. Petersen, P.J. Romanienko, O. Fernandez-Capetillo, H.T. Chen, O.A. Sedelnikova, B. Reina-San-Martin, V. Coppola, E. Meffre, M.J. Difilippantonio, C. Redon, D.R. Pilch, A. Olaru, M. Eckhaus, R.D. Camerini-Otero, L. Tessarollo, F. Livak, K. Manova, W.M. Bonner, M.C. Nussenzweig, and A. Nussenzweig. 2002. Genomic instability in mice lacking histone H2AX. *Science*. 296:922-7.

Chen, H.T., A. Bhandoola, M.J. Difilippantonio, J. Zhu, M.J. Brown, X. Tai, E.P. Rogakou, T.M. Brotz, W.M. Bonner, T. Ried, and A. Nussenzweig. 2000. Response to RAG-mediated VDJ cleavage by NBS1 and gamma-H2AX. *Science*. 290:1962-5.

Dudas, A., and M. Chovanec. 2004. DNA double-strand break repair by homologous recombination. *Mutat Res*. 566:131-67.

Fernandez-Capetillo, O., A. Celeste, and A. Nussenzweig. 2003. Focusing on foci: H2AX and the recruitment of DNA-damage response factors. *Cell Cycle*. 2:426-7.

Fernandez-Capetillo, O., H.T. Chen, A. Celeste, I. Ward, P.J. Romanienko, J.C. Morales, K. Naka, Z. Xia, R.D. Camerini-Otero, N. Motoyama, P.B. Carpenter, W.M. Bonner, J. Chen, and A. Nussenzweig. 2002. DNA damage-induced G2-M checkpoint activation by histone H2AX and 53BP1. *Nat Cell Biol*. 4:993-7.

Furuta, T., H. Takemura, Z.Y. Liao, G.J. Aune, C. Redon, O.A. Sedelnikova, D.R. Pilch, E.P. Rogakou, A. Celeste, H.T. Chen, A. Nussenzweig, M.I. Aladjem, W.M. Bonner, and Y. Pommier. 2003. Phosphorylation of histone H2AX and activation of Mre11, Rad50, and Nbs1 in response to replication-dependent DNA double-strand breaks induced by mammalian DNA topoisomerase I cleavage complexes. *J Biol Chem*. 278:20303-12.

Gernand, D., D. Demidov, and A. Houben. 2003. The temporal and spatial pattern of histone H3 phosphorylation at serine 28 and serine 10 is similar in plants but differs between mono- and polycentric chromosomes. *Cytogenet Genome Res*. 101:172-6.

Gurley, L.R., R.A. Walters, and R.A. Tobey. 1973. Histone phosphorylation in late interphase and mitosis. *Biochem Biophys Res Commun*. 50:744-50.

Helleday, T. 2003. Pathways for mitotic homologous recombination in mammalian cells. *Mutat Res*. 532:103-15.

Hendzel, M.J., Y. Wei, M.A. Mancini, A. Van Hooser, T. Ranalli, B.R. Brinkley, D.P. Bazett-Jones, and C.D. Allis. 1997. Mitosis-specific phosphorylation of histone H3 initiates primarily within pericentromeric heterochromatin during G2 and spreads in an ordered fashion coincident with mitotic chromosome condensation. *Chromosoma*. 106:348-60.

Huang, X., M. Okafuji, F. Traganos, E. Luther, E. Holden, and Z. Darzynkiewicz. 2004. Assessment of histone H2AX phosphorylation induced by DNA topoisomerase I and II inhibitors topotecan and mitoxantrone and by the DNA cross-linking agent cisplatin. *Cytometry*. 58A:99-110.

Huang, X., F. Traganos, and Z. Darzynkiewicz. 2003. DNA damage induced by DNA topoisomerase I- and topoisomerase II-inhibitors detected by histone H2AX phosphorylation in relation to the cell cycle phase and apoptosis. *Cell Cycle*. 2:614-9.

Hunter, N., G.V. Borner, M. Lichten, and N. Kleckner. 2001. Gamma-H2AX illuminates meiosis. *Nat Genet*. 27:236-8.

Jackson, S.P. 2002. Sensing and repairing DNA double-strand breaks. *Carcinogenesis*. 23:687-96.

Lees-Miller, S.P., R. Godbout, D.W. Chan, M. Weinfeld, R.S. Day, 3rd, G.M. Barron, and J. Allalunis-Turner. 1995. Absence of p350 subunit of DNA-activated protein kinase from a radiosensitive human cell line. *Science*. 267:1183-5.

Lees-Miller, S.P., and K. Meek. 2003. Repair of DNA double strand breaks by non-homologous end joining. *Biochimie*. 85:1161-73.

Limoli, C.L., E. Giedzinski, W.M. Bonner, and J.E. Cleaver. 2002. UV-induced replication arrest in the xeroderma pigmentosum variant leads to DNA double-strand breaks, gamma -H2AX formation, and Mre11 relocalization. *Proc Natl Acad Sci U S A*. 99:233-8.

MacPhail, S.H., J.P. Banath, T.Y. Yu, E.H. Chu, H. Lambur, and P.L. Olive. 2003a. Expression of phosphorylated histone H2AX in cultured cell lines following exposure to X-rays. *Int J Radiat Biol*. 79:351-8.

MacPhail, S.H., J.P. Banath, Y. Yu, E. Chu, and P.L. Olive. 2003b. Cell cycle-dependent expression of phosphorylated histone H2AX: reduced expression in unirradiated but not X-irradiated G1-phase cells. *Radiat Res*. 159:759-67.

Mahadevaiah, S.K., J.M. Turner, F. Baudat, E.P. Rogakou, P. de Boer, J. Blanco-Rodriguez, M. Jasin, S. Keeney, W.M. Bonner, and P.S. Burgoyne. 2001. Recombinational DNA double-strand breaks in mice precede synapsis. *Nat Genet*. 27:271-6.

McManus, K.J., V.L. Biron, D.A. Underhill, and M.J. Hendzel. 2004 Submitted. Dynamic Changes in Histone Lysine Methylations: Identification of a Mitosis-specific Function for Dynamic Methylation in Chromosome Congression and Segregation.

McManus, K.J., and M.J. Hendzel. 2003. Quantitative analysis of CBP- and P300-induced histone acetylations in vivo using native chromatin. *Mol Cell Biol*. 23:7611-27.

McManus, K.J., and M.J. Hendzel. 2004. Using Quantitative Imaging Microscopy to Define the Target Substrate Specificities of Histone Post-translational Modifying Enzymes. *Methods*.

McManus, K.J., and M.J. Hendzel. 2004 Submitted. The Relationship between Histone H3 Phosphorylation and Acetylation throughout the Mammalian Cell Cycle.

Motoyama, N., and K. Naka. 2004. DNA damage tumor suppressor genes and genomic instability. *Curr Opin Genet Dev*. 14:11-6.

Nazarov, I.B., A.N. Smirnova, R.I. Krutilina, M.P. Svetlova, L.V. Solovjeva, A.A. Nikiforov, S.L. Oei, I.A. Zalenskaya, P.M. Yau, E.M. Bradbury, and N.V. Tomilin. 2003. Dephosphorylation of histone gamma-H2AX during repair of DNA double-strand breaks in mammalian cells and its inhibition by calyculin A. *Radiat Res*. 160:309-17.

Nyberg, K.A., R.J. Michelson, C.W. Putnam, and T.A. Weinert. 2002. Toward maintaining the genome: DNA damage and replication checkpoints. *Annu Rev Genet*. 36:617-56.

Park, E.J., D.W. Chan, J.H. Park, M.A. Oettinger, and J. Kwon. 2003. DNA-PK is activated by nucleosomes and phosphorylates H2AX within the nucleosomes in an acetylation-dependent manner. *Nucleic Acids Res*. 31:6819-27.

Paull, T.T., E.P. Rogakou, V. Yamazaki, C.U. Kirchgessner, M. Gellert, and W.M. Bonner. 2000. A critical role for histone H2AX in recruitment of repair factors to nuclear foci after DNA damage. *Curr Biol*. 10:886-95.

Peters, A.H., D. O'Carroll, H. Scherthan, K. Mechtler, S. Sauer, C. Schofer, K. Weipoltshammer, M. Pagani, M. Lachner, A. Kohlmaier, S. Opravil, M. Doyle, M. Sibilia, and T. Jenuwein. 2001. Loss of the Suv39h histone methyltransferases impairs mammalian heterochromatin and genome stability. *Cell*. 107:323-37.

Petersen, J., J. Paris, M. Willer, M. Philippe, and I.M. Hagan. 2001. The S. pombe aurora-related kinase Ark1 associates with mitotic structures in a stage dependent manner and is required for chromosome segregation. *J Cell Sci*. 114:4371-84.

Pilch, D.R., O.A. Sedelnikova, C. Redon, A. Celeste, A. Nussenzweig, and W.M. Bonner. 2003. Characteristics of gamma-H2AX foci at DNA double-strand breaks sites. *Biochem Cell Biol*. 81:123-9.

Rappold, I., K. Iwabuchi, T. Date, and J. Chen. 2001. Tumor suppressor p53 binding protein 1 (53BP1) is involved in DNA damage-signaling pathways. *J Cell Biol*. 153:613-20.

Redon, C., D. Pilch, E. Rogakou, O. Sedelnikova, K. Newrock, and W. Bonner. 2002. Histone H2A variants H2AX and H2AZ. *Curr Opin Genet Dev*. 12:162-9.

Reitsema, T.J., J.P. Banath, S.H. MacPhail, and P.L. Olive. 2004. Hypertonic saline enhances expression of phosphorylated histone H2AX after irradiation. *Radiat Res*. 161:402-8.

Rogakou, E.P., C. Boon, C. Redon, and W.M. Bonner. 1999. Megabase chromatin domains involved in DNA double-strand breaks in vivo. *J Cell Biol*. 146:905-16.

Rogakou, E.P., D.R. Pilch, A.H. Orr, V.S. Ivanova, and W.M. Bonner. 1998. DNA double-stranded breaks induce histone H2AX phosphorylation on serine 139. *J Biol Chem*. 273:5858-68.

Rothkamm, K., and M. Lobrich. 2002. Misrepair of radiation-induced DNA double-strand breaks and its relevance for tumorigenesis and cancer treatment (review). *Int J Oncol*. 21:433-40.

Schultz, L.B., N.H. Chehab, A. Malikzay, and T.D. Halazonetis. 2000. p53 binding protein 1 (53BP1) is an early participant in the cellular response to DNA double-strand breaks. *J Cell Biol*. 151:1381-90.

Schwartz, J.L., J.M. Cowen, E. Moan, B.A. Sedita, J. Stephens, and A.T. Vaughan. 1993. Metaphase chromosome and nucleoid differences between CHO-K1 and its radiosensitive derivative xrs-5. *Mutagenesis*. 8:105-8.

Siino, J.S., I.B. Nazarov, M.P. Svetlova, L.V. Solovjeva, R.H. Adamson, I.A. Zalenskaya, P.M. Yau, E.M. Bradbury, and N.V. Tomilin. 2002. Photobleaching of GFP-labeled H2AX in chromatin: H2AX has low diffusional mobility in the nucleus. *Biochem Biophys Res Commun*. 297:1318-23.

Simons, J.W. 1979. Development of a liquid-holding technique for the study of DNA-repair in human diploid fibroblasts. *Mutat Res*. 59:273-83.

Stiff, T., M. O'Driscoll, N. Rief, K. Iwabuchi, M. Lobrich, and P.A. Jeggo. 2004. ATM and DNA-PK function redundantly to phosphorylate H2AX after exposure to ionizing radiation. *Cancer Res*. 64:2390-6.

Tidwell, T., V.G. Allfrey, and A.E. Mirsky. 1968. The methylation of histones during regeneration of the liver. *J Biol Chem*. 243:707-15.

Turner, B.M. 2001. Chromatin and gene regulation: mechanisms in epigenetics. Blackwell Science Ltd., London. 284 pp.

Valerie, K., and L.F. Povirk. 2003. Regulation and mechanisms of mammalian double-strand break repair. *Oncogene*. 22:5792-812.

Ward, I.M., and J. Chen. 2001. Histone H2AX is phosphorylated in an ATR-dependent manner in response to replicational stress. *J Biol Chem*. 276:47759-62.

Wei, Y., L. Yu, J. Bowen, M.A. Gorovsky, and C.D. Allis. 1999. Phosphorylation of histone H3 is required for proper chromosome condensation and segregation. *Cell*. 97:99-109.

Zhou, B.B., and S.J. Elledge. 2000. The DNA damage response: putting checkpoints in perspective. *Nature*. 408:433-9.

CHAPTER 5

Quantitative Analysis of CBP- and P300-Induced Histone Acetylations *In Situ* Using a Native Chromatin Template[†]

Kirk J. McManus[1] and Michael J. Hendzel[1*]

[1] Department of Oncology, Cross Cancer Institute, 11560 University Avenue,
Edmonton, Alberta, Canada, T6G 1Z2

Running Title – CBP and P300 HAT specificity profiles

*Address for Correspondence:
Dr. Michael J. Hendzel
Department of Oncology
Cross Cancer Institute
11560 University Avenue
Room 3332
Edmonton, Alberta
T6G 1Z2 CANADA
Tel. # 780-432-8493
Fax. # 780-432-8892
email: michaelh@cancerboard.ab.ca

[†] A version of this chapter has been published. McManus, K. J. and Hendzel, M. J. (2001). Quantitative analysis of CBP- and P300-Induced Histone Acetylations In Vivo Using Native Chromatin. *Mol Cell Biol.* **23**:7611-7627

5.1 INTRODUCTION

Since the initial identification of specific enzymes with nuclear histone acetyltransferase (HAT) activity in 1996 (Brownell et al., 1996; Yang et al., 1996), an enormous research effort has centred upon defining the nuclear functions that these enzymes participate in. Two members of the nucleoplasmic HAT A family, CBP and its close homologue P300, are of particular interest because of their involvement in important cellular processes, including differentiation, development and apoptosis. CBP and P300 exhibit a high degree of sequence similarity and have similar domain and motif structures (Chan and La Thangue, 2001; Ogryzko et al., 1996). Both have a nuclear receptor binding domain, three zinc fingers, a bromodomain and a large internal HAT domain (Giles et al., 1998). Over 40 different proteins have been shown to interact with CBP and/or P300 *in vitro*, and fall roughly into four different categories; nuclear receptors, transcription factors, signaling molecules and viral proteins (Blobel, 2000; Chan and La Thangue, 2001; Giles et al., 1998; Goodman and Smolik, 2000; McManus and Hendzel, 2001). CBP and P300 were first identified as transcriptional co-activators proposed to function by bridging the basal transcription machinery to upstream regulatory sequences (Bannister and Kouzarides, 1996; Chrivia et al., 1993; Ogryzko et al., 1996). They have since been shown to positively and negatively regulate a number of gene activation pathways and be integral players in a variety of developmental processes including apoptosis, cell proliferation and embryogenesis (reviewed in Blobel, 2000; Giles et al., 1998; Goodman and Smolik, 2000; McManus and Hendzel, 2001).

Central to the functions ascribed to CBP and P300 is their ability to alter chromatin structure through histone acetylation. The nucleosome is the fundamental repeating unit of chromatin. It is comprised of an octomeric core particle consisting of two molecules each of histones H2A, H2B, H3 and H4, around which 146 base pairs of DNA is wrapped. The amino (N)-terminal 'unstructured' domains found on each of the four core histones undergo several types of post-translational modifications (e.g. acetylation, phosphorylation, methylation) that are believed to influence histone function potentially through chromatin alterations (Berger, 2002; Zhang and Reinberg, 2001).

Histone acetylation in particular has been strongly correlated with the chromatin remodeling that is associated with transcriptional activation and characterized by DNase I sensitivity. The individual nucleosomes are connected by short intervening DNA sequences (termed linker DNA) forming the 10 nm chromatin fiber or 'beads-on-a-string'. Although the 10 nm fiber conformation has been well characterized *in vitro* by electron microscopy, nucleosomal arrays do not adopt this fully extended conformation unless very low ionic strength buffers are utilized (Georgel, 2002; Hansen, 2002; Horn and Peterson, 2001; Widom, 1989). Hence, the chromatin substrate is rarely, if ever, presented to the nuclear HATs as 10 nm extended nucleosomal fibers. Rather, emerging evidence indicates that euchromatin and heterochromatin are found in structures that are folded beyond the 30 nm level to fibers of 80-200 nm in diameter (Hansen, 2002; Hayes and Hansen, 2001). In this environment, the tails are essential and engaged in contacts within and between chromatin fibers. Therefore, the presentation of the histone N-termini is not reconstituted *in vitro* using current reconstitution approaches.

In vitro biophysical studies performed on isolated nucleosomes and model nucleosomal arrays have clearly demonstrated that the histone N-termini function in a variety of interactions including nucleosome-DNA, nucleosome-nucleosome, and higher-order fiber-fiber interactions (Annunziato and Hansen, 2000; Ausio et al., 2001; Hansen, 2002; Hayes and Hansen, 2001; Wang et al., 2001; Wang et al., 2000). One conclusion of these studies is that the interactions that engage the N-termini *in vitro* are highly dependent upon the model system employed and the ionic composition of buffers. Consequently, the presentation of core histone tails *in vitro* (i.e. as histones, purified nucleosomes or short nucleosomal arrays) as HAT substrates, may differ significantly from their presentation *in vivo* within native chromatin. The most obvious difference is the presence of higher-order chromatin compaction states (i.e. those beyond the 30 nm fiber) that are highly dependent on the histone tails which regulate the fiber-fiber interactions (Hayes and Hansen, 2001). The addition of a broad spectrum of chromatin associated proteins is also anticipated to add to the complexity of the system and impact histone tail presentation. For example, histone H1 has been shown to modulate histone acetylation activity *in vivo* and contribute to the conformation of the endogenous chromatin substrate (Gunjan et al., 2001). Consequently, the current *in vitro* assays, which do not account for any structure beyond the nucleosome, may not accurately reflect the accessibility to the substrate and/or the specificity of the nuclear HAT *in situ*.

Histone acetylation is not a binary process whereby chromatin is either acetylated or not. Rather, there are basal steady-state acetylation levels for all acetylated histone lysine residues present throughout euchromatic and heterochromatic regions of the nucleus. These steady-state levels arise through the balance of continually acting HATs and histone deacetylases (HDACs) with the specific site utilization reflecting the net result of this balance. In 1990, Thorne *et al.* (1990) demonstrated that basal histone acetylation levels in unsynchronized HeLa cells were relatively low. For example, only one of four (histone H4) or five (histone H3) possible acetylation sites was typically utilized/occupied, with the most frequently acetylated sites being K14 (H3) and K16 (H4). The existence of di-, tri-, tetra- and penta- acetylated histones at steady-state have been demonstrated, however they are much less abundant, particularly tetra- and penta-acetylated forms (Thorne et al., 1990). More recent determinations by Schiltz *et al.* (1999) suggest that approximately 60% of K16 sites are acetylated in mononucleosomes isolated from HeLa cells while other sites, such as K5 of histone H4, are found on a very small subset of the nucleosomes at steady-state. These observations collectively argue that all potential acetylation sites will be significantly represented in chromatin. Therefore we can assess differences in global acetylation at specific histone residues that are contingent upon minimal increases in CBP and P300 expression.

In this study, we examined CBP/P300 HAT specificities *in vivo* using native chromatin structure as a substrate. We demonstrate that both HATs induce increased acetylation on specific lysine residues in endogenous chromatin. By developing a single cell quantitative HAT assay, we were able to investigate HAT specificities under conditions where the chromatin is compact and the histone tails are engaged in their native molecular interactions. Our studies demonstrate that CBP and P300 are able to acetylate histones in a concentration-dependent manner *in vivo* and that these proteins are capable of acting on large regions of the genome rather than being confined to a small number of promoter/enhancer sequences.

5.2 RESULTS

5.2.1 *Development of an in vivo HAT Assay*

We have previously characterized through microscopy, differences in global steady-state acetylation in cells treated with HDAC inhibitors (Hendzel et al., 1998; Kruhlak et al., 2001). As a result, we reasoned it should be possible to use fluorescence microscopy to detect and quantify differences in specific acetylation levels in cells transfected with constructs encoding HATs and comparing them with untransfected controls. Initial experiments were conducted to determine whether or not transiently expressing GFP-CBP or HA-P300 would alter the steady-state acetylation level of lysine 5 (K5) of histone H4. Figure 5.1 shows fluorescence images of K5 acetylation in cells transfected with GFP-CBP (Fig. 5.1A) or HA-P300 (Fig. 5.1B). Figure 5.1C shows a control transfection of a nuclear protein that does not contain endogenous HAT activity (alternative splicing factor, ASF, fused to GFP). Although increases in acetylation were observed in cells expressing the HAT constructs, a direct relationship between HAT expression and specific increases in acetylation could not be concluded until several key control experiments and selection criteria were performed (and are detailed below).

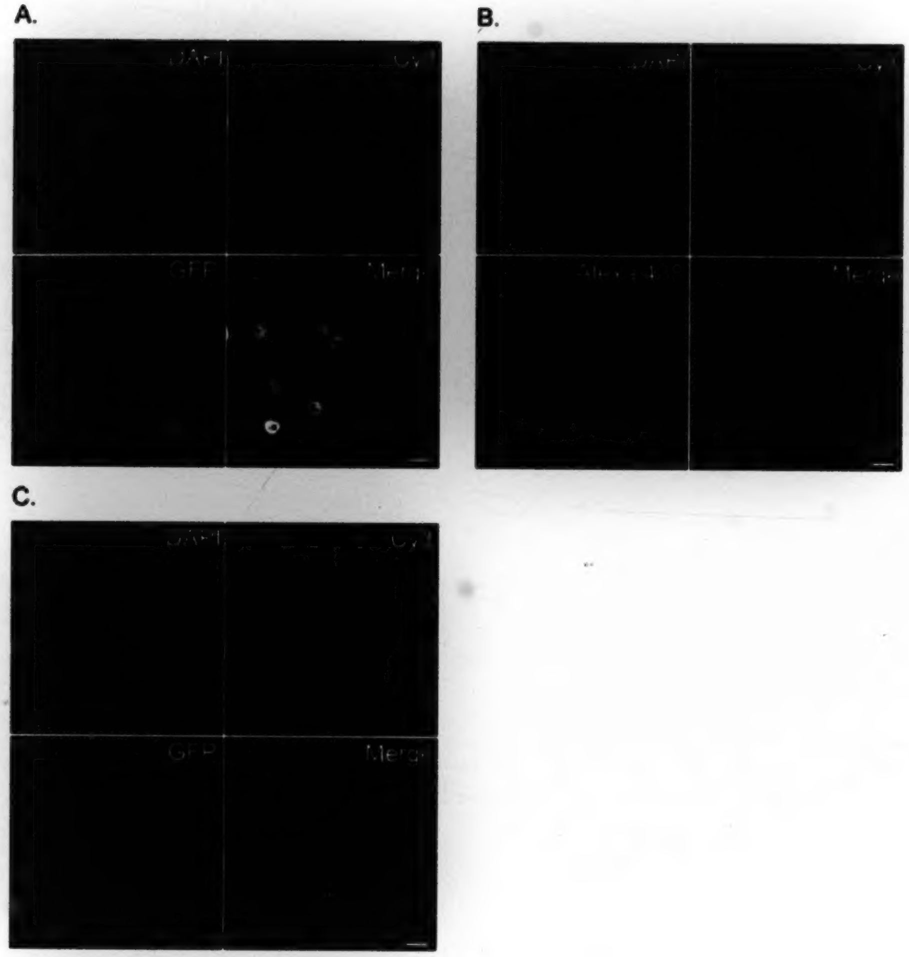
A.
DAPI
Cy3
GFP
Merge
B.
DAPI
Cy3
Alexa 488
Merge
C.
DAPI
Cy3
GFP
Merge

Figure 5.1: GFP-CBP and HA-P300 expression correlate with increased lysine 5 acetylation. Confocal micrographs depicting the K5 (histone H4) acetylation status in COS-7 cells transiently expressing GFP-CBP (panel A), HA-P300 (panel B) and ASF-GFP (panel C). DNA is stained with DAPI (blue), acetylated K5 is identified by a secondary antibody conjugated to Cy3 that recognizes the acetylated K5 antibody (red), and GFP-CBP, HA-P300 and ASF-GFP expression are identified in green. The merge image is an overlay of the three channels. Scale bar represents 25μm.

5.2.2 *GFP-CBP and HA-P300 Recapitulate Endogenous Expression Patterns*

When cells were transfected with the HAT fusion proteins, there was a significant range of protein expression observed at the time of fixation (18-20 hours post-transfection). When cells were examined 48-72 hours post-transfection, a significant amount of cell death had occurred and most viable cells expressed high levels of the transfected protein. By employing several key selection criteria, our image-based approach to determine *in vivo* HAT specificities has several distinct advantages over conventional biochemical approaches. For example, we are able to select only those cells which recapitulate the expression patterns of the endogenous proteins (Figure 5.2, A and B) and eliminate those cells which are apoptotic, express high levels of the protein, or exhibit atypical subcellular protein distributions (Figure 5.2C).

In order to validate that the majority of transfected cells were suitable for analysis, we determined whether or not transfected cells organized CBP or P300 into the several hundred sub-nuclear foci that are characteristic of this class of nuclear protein (Hendzel et al., 2001). In addition, we confirmed that both the endogenous and transiently expressed HATs had similar subcellular distributions relative to acetylated chromatin. The endogenous staining pattern of CBP and P300 were investigated in para-formaldehyde-fixed COS-7, HeLa, Indian Muntjac (IM) and 10T1/2 cells, using anti-CBP (Ac238) or anti-P300 (Rockland). In agreement with previous descriptions (Hendzel et al., 1998; McManus and Hendzel, 2001), CBP, P300 and specific histone acetylations localize to between 200 and 500 discrete foci scattered non-randomly throughout the nucleoplasm (Figure 5.2). These foci are massive on a molecular scale with an estimated diameter of 100nm each. If we assume the acetylation foci and the

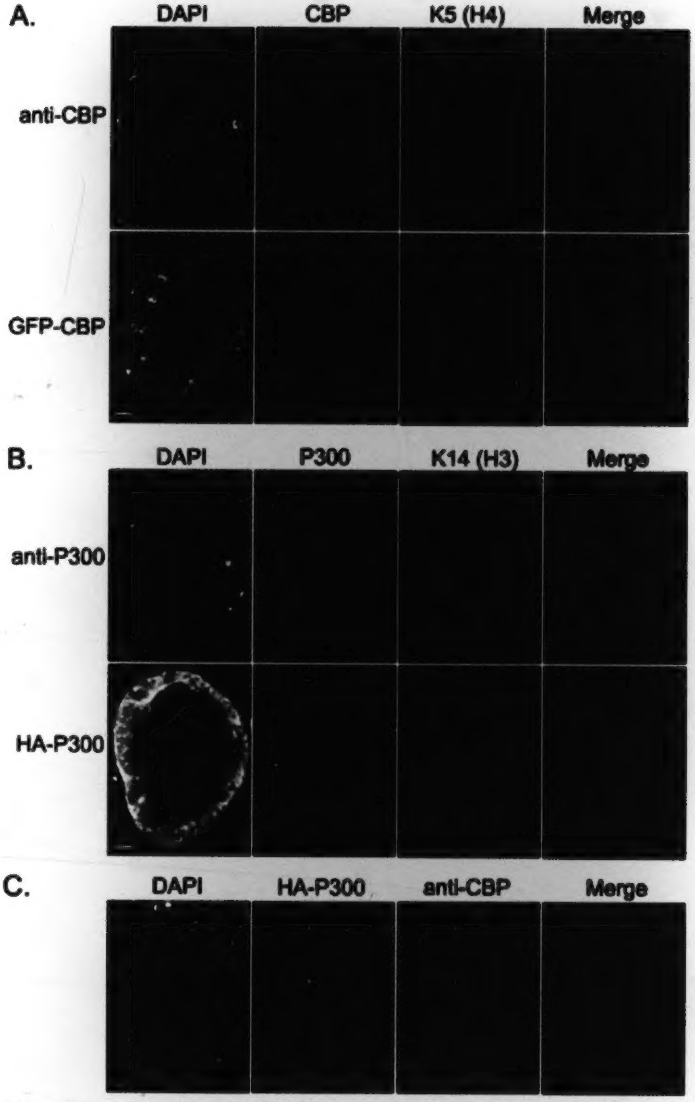

Figure 5.2: Sub-nuclear distribution of transiently expressed GFP-CBP/HA-P300 and endogenous CBP/P300 in relation to acetylation and chromatin.

Representative images are shown to highlight the ability of transiently expressed GFP-CBP (panel A) or HA-P300 (panel B) to recapitulate the expression patterns of their endogenous counterparts. Cells were para-formaldehyde fixed, co-stained with either anti-K5 (H4) or anti-acetylated K14 (H3) for panels A and B, respectively, and counterstained with DAPI to visualize bulk chromatin. Text on left identifies cells stained for endogenous CBP or P300 (anti-CBP or anti-P300, respectively) or transiently expressing either GFP-CBP or HA-P300. Merged images depict the 3D inter-relationship between CBP/GFP-CBP/P300/HA-P300 (green), acetylated K5/K14 (red) or chromatin (blue) in a single plane isolated from deconvolved z-series collected using digital imaging microscopy. Panel C is an example of the type of cell excluded from subsequent analysis bases on morphological abnormalities (i.e. large HA-P300 aggregates concomitant with the re-organization of CBP into similar regions). HA-P300 and endogenous CBP are identified in the merged image as green and red respectively, with DAPI staining indicated in blue. Bars represent 2μm.

nucleosomes are spherical with radii of 50 nm and 5.5 nm respectively, we can estimate the total number of nucleosomes per foci to be approximately 750 $(\frac{3}{4}\pi r^{3}_{\text{foci}}/\frac{3}{4}\pi r^{3}_{\text{nucleosome}})$. CBP, P300 and acetylation foci are noticeably absent in nucleoli and are depleted in chromatin-dense regions (identified by highly intense DAPI staining).

Transient expression of GFP-CBP or HA-P300 in COS-7, HeLa, IM and 10T1/2 cells yielded two distinct localization patterns – a predominant pattern indistinguishable from the endogenous counterpart (Figure 5.2, A and B) and a much less abundant pattern that formed larger aggregates typically numbering between 50-75 per nuclei (Figure 5.2C). Cells with the latter pattern (i.e. large aggregates) exhibited striking increases in overall GFP-CBP or HA-P300 fluorescence when compared to the predominant focal pattern. Since structures of this size were never observed with the endogenous proteins, these cells were excluded from all subsequent analyses.

To investigate the spatial relationship between transient GFP-CBP/HA-P300 expression and acetylation (K14 and K5 of histones H3 and H4, respectively), three dimensional (3D) digital imaging microscope (DIM) images were collected and compared to those obtained for endogenous CBP/P300 and acetylation. Endogenous CBP/P300, GFP-CBP/HA-P300 and acetylation (K14 and K5) were non-randomly distributed throughout the nucleoplasm, absent in nucleoli, and significantly depleted in dense regions of chromatin. Although a focal staining pattern was observed in all cases, a general lack of co-localization was apparent between CBP/P300 and GFP-CBP/HA-P300 with acetylated K14 or K5. Figure 5.2 shows representative images depicting the spatial relationship between endogenous CBP/P300 or transiently expressed GFP-CBP/HA-P300 and acetylation. Despite the general lack of co-localization, a striking complementarity between the HAT (endogenous CBP/P300 and GFP-CBP/HA-P300) distribution and the acetylated chromatin (K14 and K5) was observed and has been previously described (Hendzel et al., 1998; Hendzel et al., 2001; Kruhlak et al., 2001). Briefly, the acetylated chromatin often localizes to the intervening spaces between the chromatin-dense regions (DAPI-intense regions) and the HAT foci.

5.2.3 *Transient HAT Expression Results in Minimal Increases in Total Protein Expression*

To address the possibility that high overexpression could artificially impact our results we elected to quantify total CBP and P300 expression levels in transfected cells and compare them with the respective levels in untransfected controls. Total protein levels were determined using a single cell approach, similar to that of the HAT assay, which couples confocal microscopy, quantitative image analysis and statistical analyses. Because the detector gain is maintained constant throughout the image acquisition process, the fluorescent signal intensities in nuclei of one image can be compared to those in another. In other words, total CBP or P300 signal intensities can be used to quantify their respective protein expression levels. This allows quantitative comparisons between untransfected and GFP-CBP or HA-P300 expressing cells, respectively.

Total CBP and P300 expression levels were calculated in three separate experiments for both GFP-CBP and HA-P300 expressing cells, respectively. As shown in Figure 5.3, both transfected and untransfected cells showed significant variability in CBP expression levels (panels A and B) that was also observed for P300 in untransfected and transfected cells (panels C and D). A general increase in total signal intensity was observable for cells transiently expressing either GFP-CBP or HA-P300 over

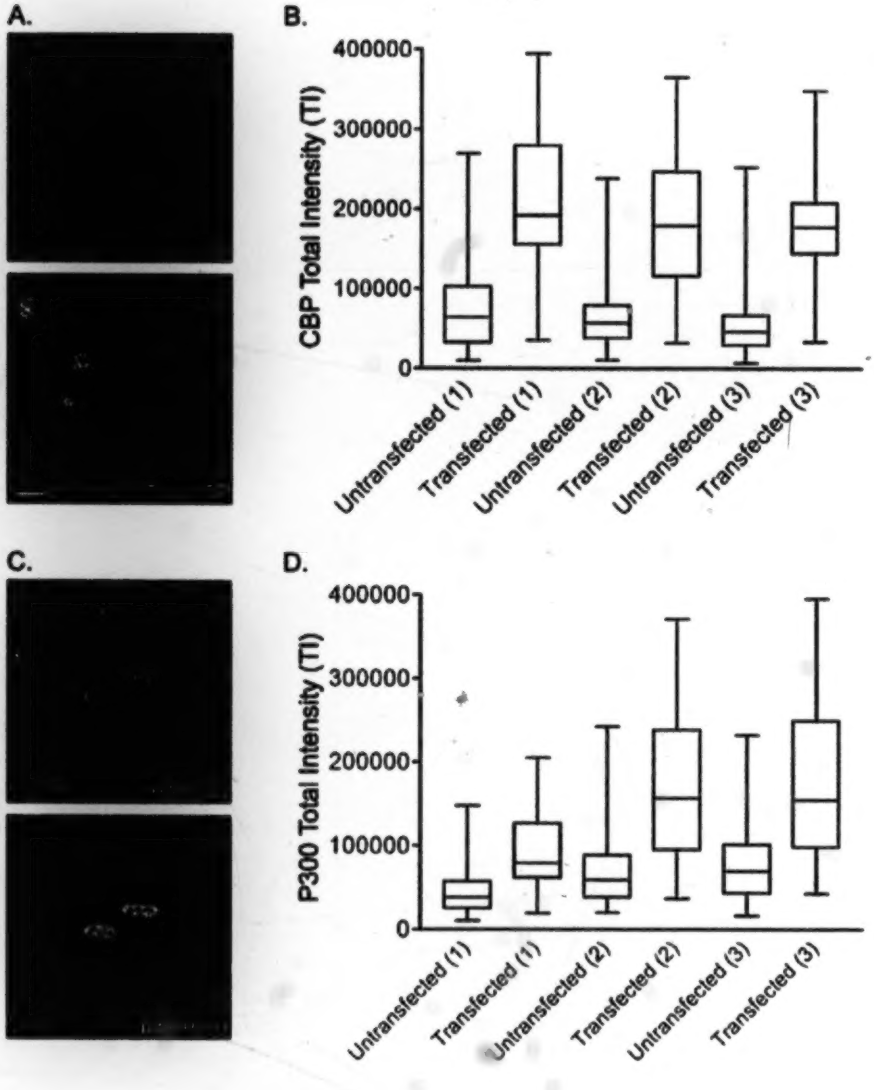

Figure 5.3: Determination of total HAT expression in GFP-CBP and HA-P300 expressing cells. Total CBP and P300 expression levels in GFP-CBP expressing HeLa and HA-P300 expressing 10T1/2 cells, respectively. Representative images used in the calculation are shown in panels A (GFP-CBP) and C (HA-P300). Box-and-whisker plots, panels B and D, depict the distribution ranges for three separate experiments examining the total intensity (TI) distributions of both untransfected and transfected populations for GFP-CBP and HA-P300 expressing cells, respectively. Experimental pairs of untransfected and transfected populations are identified by 1, 2 or 3. The entire TI distribution is depicted by the whiskers, while the lower and upper horizontal lines of the box identify the 25th and 75th percentiles, respectively. The middle horizontal line identifies the mean value calculated for each population. Bars represent 15μm.

untransfected controls. Upon further inspection of the box-and-whisker plots two additional trends were noted. First, the CBP/P300 total intensity (TI) distributions for the transfected populations are super-shifted compared to their respective untransfected counterpart populations. Second, although all CBP/P300 TI distributions are super-shifted in the transfected populations, a predominant proportion (approximately 75 percent) of this distribution still remains within the normal CBP/P300 TI distribution range calculated for their untransfected population.

To determine the mean fold increase in CBP/P300 expression in GFP-CBP/HA-P300 expressing cells it was first necessary to discern if the differences in mean TI between untransfected and transfected populations were statistically significant. Unpaired t-tests were performed to evaluate the differences between mean TI values for the untransfected and transfected populations (both CBP and P300) for each triplicate experiment (Table 5.1). In all cases, *p*-values were of less than 0.05 were calculated and therefore identify statistically significant differences between mean TI for untransfected and transfected populations for both CBP and P300. Since total fluorescent signal intensities are proportional to protein expression levels, mean TI ratios for untransfected and transfected populations were calculated to quantify the mean-fold overexpression. Cells transiently expressing GFP-CBP exhibited between 2.89 and 3.50 mean fold-increase in total CBP, while in HA-P300 expressing cells, the mean fold-increase in P300 expression varied between 2.34 and 2.84 (Table 5.1). Although statistically significant increases in mean TI were calculated, the **majority** of cells transiently expressing GFP-CBP or HA-P300 (approximately 75 percent) still exhibit total CBP and P300 expression levels within the normal distribution ranges of untransfected cells.

TABLE 5.1: Total CBP and P300 expression levels in cells transiently expressing GFP-CBP and HA-P300.

Protein	Population[a]	Number of Cells	Mean TI[b] (10^4)	SEM[c] (10^3)	*p*-value[d]	Ratio[e]
CBP – Trial 1	Untransfected	291	7.37	2.95	<0.001	2.89
	Transfected	78	21.3	10.0		
CBP – Trial 2	Untransfected	457	6.14	1.50	<0.001	3.00
	Transfected	118	18.4	7.20		
CBP – Trial 3	Untransfected	331	5.18	1.87	<0.001	3.50
	Transfected	97	18.1	5.86		
P300 – Trial 1	Untransfected	299	4.37	1.49	<0.001	2.34
	Transfected	47	10.2	7.78		
P300 – Trial 2	Untransfected	328	7.01	2.33	<0.001	2.84
	Transfected	42	19.9	15.0		
P300 – Trial 3	Untransfected	431	7.82	2.21	<0.001	2.44
	Transfected	55	19.0	13.5		

[a] Population refers to cells either untransfected control cells or cells transfected with GFP-CBP

[b] The mean total intensity (TI) is calculated by averaging the total signal intensity for each nuclei in that population

[c] SD = standard deviation

[d4] Unpaired t-tests (two-tailed) were performed to identify statistical differences between the mean TI for the transfected versus untransfected populations. A p-value of <0.05 is considered statistically significant.

[e] The ratio between Mean TI (transfected) versus Mean TI (untransfected) describes the mean fold overexpression in transfected cells

Based on these findings, all subsequent analyses were restricted to cells exhibiting normal physiologic behaviour. Cells exhibiting atypical protein distributions, abnormal cellular morphologies, or high levels of transiently expressed protein (GFP-CBP, HA-P300 or ASF-GFP) were manually eliminated from all subsequent analyses.

5.2.4 *Transient HAT Expression Does Not Alter HDAC or other HAT Expression Levels*

From the initial experiments, we were able to determine that minimal increases in CBP or P300 expression resulted in detectable increases in K5 acetylation. However, prior to examining subsequent acetylated epitopes it was necessary to demonstrate that additional HAT and HDAC genes were not induced. Moreover, both P300 and CBP have been found in protein complexes that can include additional HATs such as PCAF. Conceivably, if p300 and/or CBP are required to form complexes with other nuclear proteins in order to function as HATs, we would anticipate that those proteins would be up-regulated in order to generate the increased cellular HAT activity we observed. Furthermore, CBP and p300 are also transcriptional co-activators that could indirectly alter steady-state acetylation levels by inducing endogenous HAT and/or HDAC expression. As a result, efforts were first made to minimize/optimize the time between transfection and fixation so as to minimize CBP/P300 co-activator potential while still maintaining appropriate protein expression levels to perform the HAT assay. Accordingly, we investigated the expression levels of several critical nuclear HATs and HDACs in cells transiently expressing GFP-CBP or HA-P300 and compared them to untransfected controls.

Using the same procedure that we applied to quantify increases in total HAT expression, we employed a panel of antibodies to quantify the expression levels of HDACs 1, 2, 3 and 4 and of HATs namely, CBP, P300, PCAF, $TAF_{II}250$, TIP60 and the MYST family of HATs including ESA1, TIP60, MOZ, MOF, SAS2 and SAS3/YBF. Figure 5.4 displays a representative image for each HDAC (panels A to D) or HAT investigated in GFP-CBP expressing cells (panels E to I) and a box-and-whisker-plot describing the TI distributions for the respective HDAC or HAT for both untransfected and transfected populations. Particularly notable amongst all experiments is the expression level variability that is normally observed in all interphase nuclei. All HDACs and HATs investigated exhibited considerable heterogeneity in the amounts of total protein expressed. Importantly, the ranges characterized for GFP-CBP and HA-P300 expressing cells generally fall within the larger range of the untransfected populations. Unpaired t-tests were performed to identify potential differences in mean TI values between the transfected and untransfected populations. The results for GFP-CBP and HA-P300 expressing cells are shown in Tables 5.2 and 5.3, respectively. No statistically significant differences (i.e. p-value <0.05) in mean TI values between the untransfected and transfected populations were observed in cells expressing either GFP-CBP or HA-P300. Since the cross-reactivity of anti-CBP and anti-P300 antibodies is often a concern, it was necessary to demonstrate the neither cross-reacts with the opposite HAT. The specificity of each antibody is demonstrated by the fact that no statistically significant increases in expression levels were evident when GFP-CBP expressing cells were stained with anti-P300 ($p = 0.12$ [Table 5.2]) or HA-P300 expressing cells were stained with anti-CBP ($p = 0.21$ [Table 5.3]).

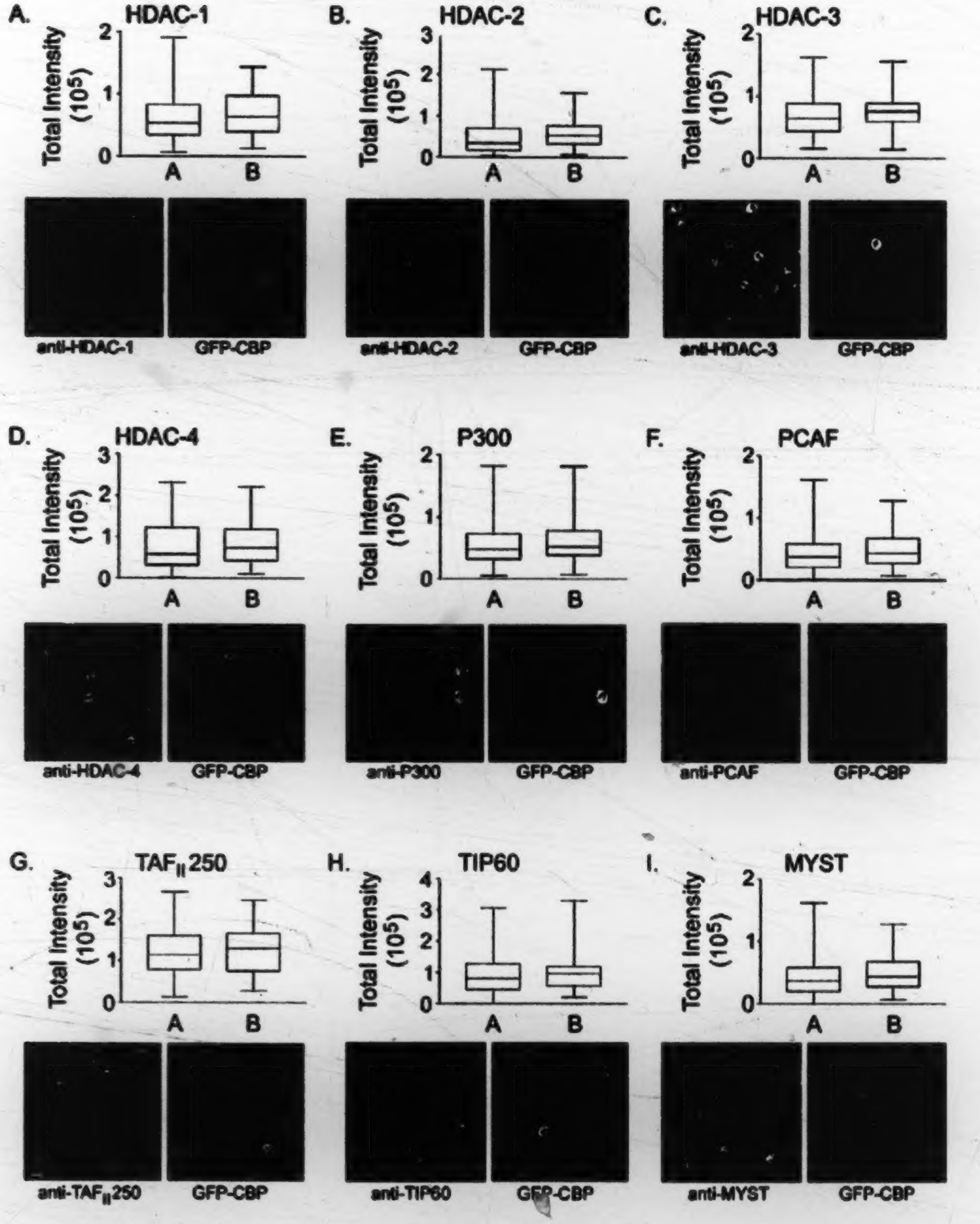

Figure 5.4: Determination of HDAC and HAT expression levels in GFP-CBP expressing cells. The distribution ranges for cells transiently expressing GFP-CBP were determined for HDACs and HATs with the label at the top of each panel identifying the specific HDAC or HAT investigated. Each panel includes a box and whisker plot defining the total intensity (TI) distribution range (whiskers), the 25th and 75th percentiles (bottom and top lines of the box, respectively), and the mean TI (middle horizontal bar) for the untransfected (A) and transfected (B) populations. Representative images are included for reference purposes with bars representing 15μm. Note that in panel F (PCAF), 10T1/2 cells were substituted for COS-7 cells owing to the species specificity of the anti-PCAF antibody.

TABLE 5.2: Calculation of total HDAC and HAT expression levels in GFP-CBP expressing COS-7 cells.

Protein	Population[a]	No.[b]	Mean TI[c] (10^4)	SEM[d] (10^3)	*p*-value[e]
HDAC-1	Untransfected	320	6.34	2.30	0.25
	Transfected	42	7.10	5.69	
HDAC-2	Untransfected	320	4.87	2.31	0.13
	Transfected	42	5.88	5.49	
HDAC-3	Untransfected	184	6.98	2.44	0.25
	Transfected	48	7.59	4.46	
HDAC-4	Untransfected	180	7.61	4.20	0.32
	Transfected	42	8.55	7.79	
P300	Untransfected	167	5.31	2.43	0.12
	Transfected	55	6.05	4.03	
PCAF[f]	Untransfected	204	4.31	2.01	0.19
	Transfected	42	4.96	4.47	
$\text{TAF}_{II}250$	Untransfected	100	5.94	2.68	0.30
	Transfected	54	6.42	3.66	
MYST[g]	Untransfected	207	4.25	2.01	0.15
	Transfected	42	4.96	4.47	
TIP60	Untransfected	124	9.00	5.26	0.29
	Transfected	38	10.2	9.86	

[a] Population refers to cells either untransfected control cells or cells transfected with GFP-CBP

[b] No. = number of cells

[c] The mean total intensity (TI) is calculated by averaging the total signal intensity for each nuclei in that population

[d] SD = standard deviation

[e] Unpaired t-tests (two-tailed) were performed to identify statistical differences between the mean TI for the transfected versus untransfected populations. A p-value of <0.05 is considered statistically significant.

[f] 10T1/2 cells were substituted for COS-7 cells due to the specificity of the anti-PCAF antibody for murine CBP

[g] MYST antibody collectively recognizes six members of the MYST HAT family including ESA1, TIP60, MOZ, MOF, SAS2 and SAS3/YBF

TABLE 5.3: Calculation of total HDAC and HAT expression levels in HA-P300 expressing HeLa cells.

Protein	Population[a]	No.[b]	Mean TI[c] (10^6)	SEM[d] (10^4)	*p*-value[e]
HDAC-1	Untransfected	255	2.50	9.13	0.15
	Transfected	63	2.79	14.4	
HDAC-2	Untransfected	232	1.92	6.93	0.15
	Transfected	40	2.18	15.8	
HDAC-3	Untransfected	202	2.43	8.44	0.18
	Transfected	45	2.68	15.1	
HDAC-4	Untransfected	234	3.21	10.7	0.15
	Transfected	64	3.53	18.4	
CBP	Untransfected	180	2.20	13.8	0.21
	Transfected	47	2.57	23.2	
PCAF	Untransfected	328	2.03	6.35	0.15
	Transfected	47	2.28	17.6	
$TAF_{II}250$	Untransfected	239	2.11	7.97	0.44
	Transfected	68	2.23	14.5	
MYST[f]	Untransfected	338	2.17	6.94	0.13
	Transfected	52	2.46	14.8	

[a] Population refers to cells either untransfected control cells or cells transfected with HA-P300

[b] No. = Number of cells

[c] The mean total intensity (TI) is calculated by averaging the total signal intensity for each nuclei in that population

[d] SD = standard deviation

[e] Unpaired t-tests (two-tailed) were performed to identify statistical differences between the mean TI for the transfected versus untransfected populations. A p-value of <0.05 is considered statistically significant.

[f] MYST antibody collectively recognizes six members of the MYST HAT family including ESA1, TIP60, MOZ, MOF, SAS2 and SAS3/YBF

5.2.5 *Transient and Minimal Increases in HAT Expression Correlate with Acetylation Increases*

By employing criteria that allow the exclusion of the cells significantly overexpressing the transfected protein and/or cells that have altered cellular or nuclear distributions of the transfected protein, we were able to accurately assay for CBP and P300 HAT activity. To determine the *in vivo* substrate specificity preferences of CBP and P300, cells were transiently transfected with GFP-CBP, HA-P300 or alternative-splicing factor-GFP (ASF-GFP), and immunofluorescently stained for specific acetylated histone epitopes. Images were collected and fluorescent intensity values were extracted for the transfected protein and each specific acetylated epitope. A panel comprised of nine different sequence-specific anti-acetylated antibodies was used and is listed in Table 5.4. ASF-GFP serves as a negative control as it localizes to the nucleus (Kruhlak et al., 2000). ASF-GFP does not have, nor does it recruit, HAT activity.

Table 5.4: Anti-acetylation antibody panel

Acetylated Epitope[a]	Histone	Antibody Dilution	Company
K5 (K5)	H4	1:200	Upstate
K8 (K8)	H4	1:8,000	Upstate
K5,8,12,16 (AcH4)	H4	1:15,000	Upstate
K9 (K9)	H3	1:400	Upstate
K14 (K14)	H3	1:200	Upstate
K12 (K12)	H4	1:2,000	Serotec
K16 (K16)	H4	1:100	Serotec
K9,14 (Ac3)	H3	1:500	Serotec
K5,12,15,20 (H2B)	H2B	1:800	Serotec

[a] each number represents the acetylated lysine (K) residue contained within the N-terminal tail of the indicated histone that is recognized by the respective antibody. Antibody labels contained in brackets indicate the nomenclature used in the text to describe the acetylated epitope.

Eighteen to twenty hours post-transfection approximately 5-60% of COS-7, HeLa, IM, or 10T1/2 cells expressed the protein of interest (data not shown). Figure 5.1 is a representative image used for the analysis and specifically depicts the relationship between GFP-CBP, HA-P300 and ASF-GFP expression and acetylation at K5 of histone H4. Note that the images for this data set are prepared to illustrate the range of staining for each trial (i.e. GFP-CBP, HA-P300 or ASF-GFP). The apparently higher steady-state acetylation in the ASF-GFP panels is actually equal in intensity to the weakly staining non-transfected cells of the GFP-CBP and HA-P300 panels. Figure 5.1 shows that increases in K5 acetylation are observed for cells expressing GFP-CBP or HA-P300, but not ASF-GFP, relative to untransfected controls. For all cell lines investigated, increases in acetylation signal intensities were most obvious for K14 and K5; smaller apparent increases were observed for H2B, Ac3 and AcH4 (data not shown). Not surprisingly, no acetylation increases for any epitope were observed in ASF-GFP expressing cells.

5.2.6 *GFP-CBP and HA-P300 Alter the Steady-state Levels of Specific Acetylated Species of Histones*

Histograms comparing normalized acetylation (N-Ac) levels for three separate cell lines were generated to quantify the differences observed in transfected and untransfected cells. The results obtained from the COS-7 cells are shown in Figure 5.5 and are consistent with those obtained in the other cell lines (data not shown). Distribution increases for the transfected versus the untransfected population were only expected to occur if the acetylation levels are dependent upon GFP-CBP or HA-P300 expression and HAT activity. Histone acetylation was increased on several lysines when GFP-CBP or HA-P300 transfected cells were compared to their untransfected

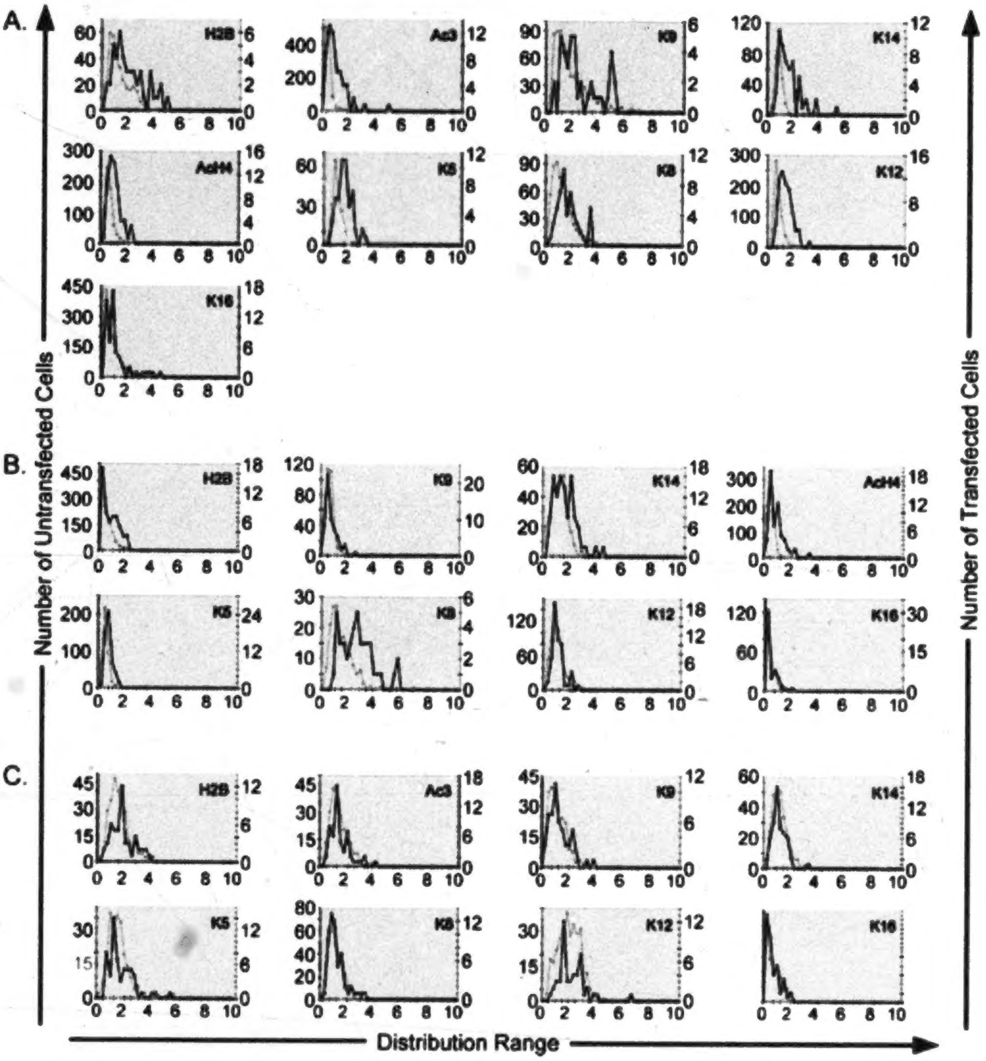

Figure 5.5: Distribution of normalized acetylation intensities.
Histograms comparing the normalized acetylation distributions for COS-7 cells transfected with GFP-CBP (panel A), HA-P300 (panel B) or ASF-GFP (panel C) and untransfected cells are shown. The generated histograms are representative of the results obtained for IM and HeLa cell lines. The first y-axis represents the number of untransfected cells (indicated in pink), the second y-axis represents the number of transfected cells (indicated in blue) and the x-axis represents the distribution range for the N-Ac intensities for the acetylated epitope indicated in the top right corner of each graph.

counterparts (Figure 5.5, A and B). In contrast, no significant relationship was observed between ASF-GFP expression and specific histone acetylations (Figure 5.5C). In cells transfected with GFP-CBP, increases in N-Ac distributions were found for H2B, Ac3 (H3), K14 (H3), AcH4 (H4), K5 (H4), K12 (H4) but not K9 (H3), K8 (H4) or K16 (H4) (panel A). In HA-P300 expressing cells, N-Ac distribution increases were found for H2B, K14, AcH4, K5 and K8 but not K9, K12 or K16 (panel B). These results indicate that both CBP and P300 expression may induce specific changes in global nuclear histone acetylation levels.

5.2.7 *Transient HAT Expression Correlates with Increased Histone Acetylation*

The results from the preceding sections demonstrate that CBP and P300 can induce specific acetylation increases that are independent of the upregulation of additional HATs or downregulation of common HDACs. However, it is not apparent whether or not the observed result is direct or indirect. To further examine the relationship between CBP or P300 expression and the amount of histone acetylation, scatter plots were generated comparing GFP-CBP or HA-P300 fluorescence with acetylated histone fluorescence (Figures 5.6 and 5.7, respectively).

As expected, no significant relationship between ASF-GFP expression and N-Ac levels was observed (Figure 5.8). In contrast, positive linear relationships between GFP-CBP/HA-P300 expression and N-Ac levels were observed for several specific lysine residues. Figures 5.6, 5.7 and 5.8 graphically depict the results obtained from COS-7 cells. Similar results were obtained in HeLa and IM cell lines (data not shown). Strong positive correlations were observed for H2B, Ac3, K9, K14, AcH4, K5 and K12 in GFP-CBP expressing cells, while in HA-P300 expressing cells, strong positive correlations were observed for H2B, K9, K14, AcH4, K5, and K8. In HeLa and IM cell lines Ac3 was also noted to exhibit a strong positive relationship in cells expressing HA-P300 (data not shown). Therefore, under the conditions of our single cell-based assay, the observed increases in global acetylation levels are dependent on the amount of CBP or P300 expressed.

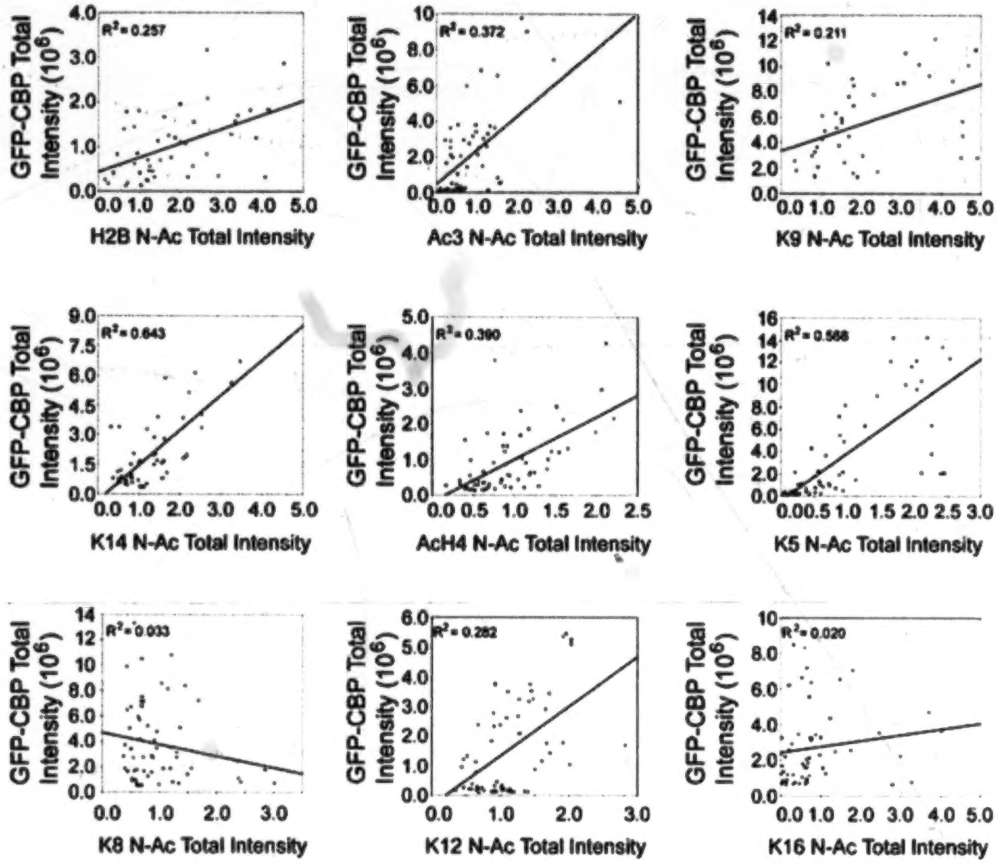

Figure 5.6: Relationship between GFP-CBP expression and acetylation.
Scatter plots were generated for cells expressing GFP-CBP to identify potential relationships between protein expression and N-Ac intensities. Linear regression analysis was performed and R^2 values were calculated and are indicated for each epitope investigated. Larger R^2 values identify instances where N-Ac intensities is dependent on protein expression levels.

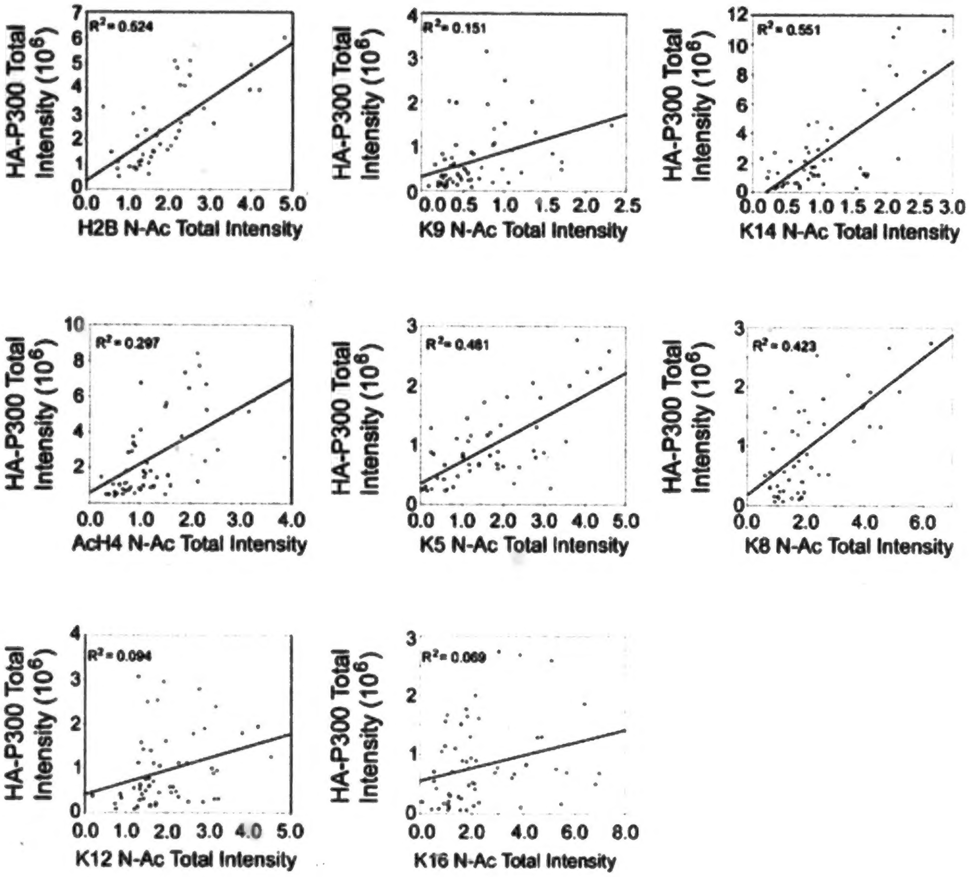

Figure 5.7: Relationship between HA-P300 expression and acetylation
Scatter plots were generated for cells expressing HA-P300 to identify potential relationships between protein expression and N-Ac intensities. Linear regression analysis was performed and R^2 values were calculated and are indicated for each epitope investigated. Larger R^2 values identify instances where N-Ac intensities is dependent on protein expression levels.

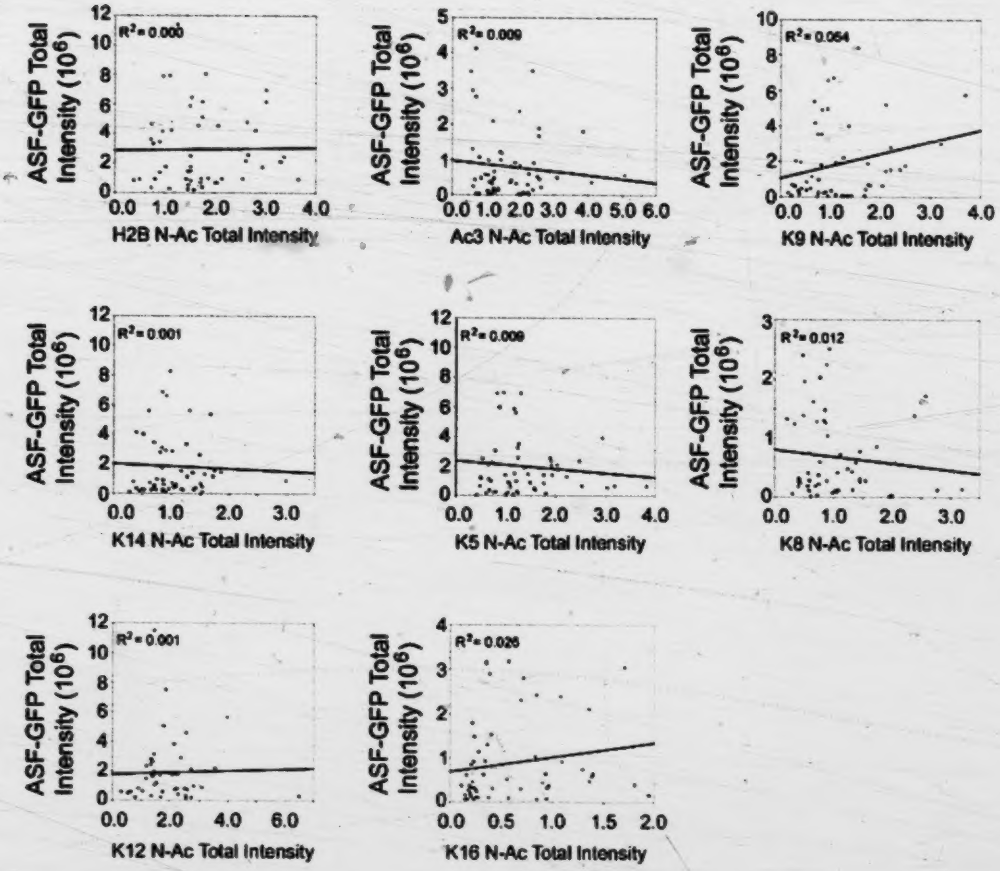

Figure 5.8: Relationship between ASF-GFP expression and acetylation
Scatter plots were generated for cells expressing ASF-GFP to identify potential relationships between protein expression and N-Ac intensities. Linear regression analysis was performed and R^2 values were calculated and are indicated for each epitope investigated. Larger R^2 values identify instances where N-Ac intensities is dependent on protein expression levels.

Because there was an apparent correlation between CBP/P300 expression level and N-Ac values for several acetylated epitopes, linear regression analysis was performed to describe the correlation. An R-value of 0 signifies no correlation between HAT expression and N-Ac values, whereas values of +1 or –1 identify perfect positive and negative correlations. By squaring the R-value (R^2), a greater appreciation of a correlation is achieved. Linear regression analysis was performed in COS-7, HeLa and IM cell and the calculated R^2 values for COS-7 cells are presented in the top left panel of each graph of Figures 5.6, 5.7 and 5.8. Figure 5.9 graphically depicts the R^2 values calculated for the each acetylated epitope of histone H3 and H4. While both proteins are closely correlated with K14 acetylation of histone H3 and K5 acetylation of histone H4, CBP expression was closely correlated with K12 acetylation but not K8, whereas P300 exhibits the opposite relationship. Variability in R^2 values was observed and can be roughly grouped into three distinct populations; a) less than 0.100 ($R^2 < 0.100$), b) between 0.100 and 0.250 ($0.100 \leq R^2 \leq 0.250$) and, c) greater than 0.250 ($R^2 > 0.250$). For GFP-CBP, the R^2 value for only two epitopes, K8 and K16 fall below 0.100, while for the remaining epitopes, all but K9 (0.211), have R^2 values greater than 0.250. For HA-P300 expressing cells, only the R^2 values for K12 and K16 are less than 0.100, while those of H2B, K14, AcH4, K5 and K8 are greater than 0.250 and for K9, R^2 equals 0.151.

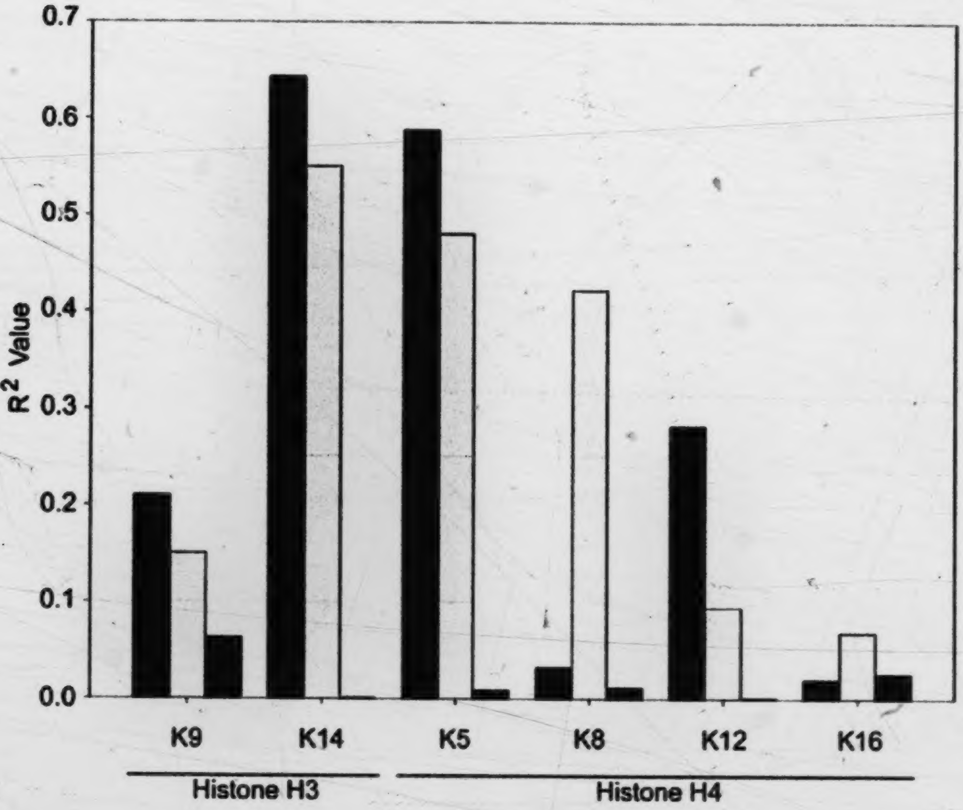

Figure 5.9: Relationships between HAT expression and acetylation of specific lysine residues. Graphical representation of the R^2 values calculated for the correlation between GFP-CBP (■), HA-P300 (▨) or ASF-GFP (■),and specific acetylated lysine residues (indicated on the *x*-axis) contained in histones H3 and H4. Horizontal lines have been included at $R^2 = 0.100$ and $R^2 = 0.250$ for reference purposes [see text for details]).

5.2.8 *Transient HAT Expression Induces Acetylation at Specific Histone Residues*

Since it was anticipated that increases in bulk acetylation would occur in cells where a specificity preference was demonstrated, unpaired t-tests (two-tailed) were used to compare mean N-Ac values between transfected and untransfected populations. Table 5.5 summarizes the results calculated for COS-7 cells transiently expressing GFP-CBP, HA-P300 or ASF-GFP. Additional experiments were conducted in HeLa and IM cell lines with very similar results (data not shown). Recall that only cells minimally expressing the protein of interest were included in the analysis. GFP-CBP expressing COS-7 cells exhibited statistical significance for a number of acetylated epitopes including H2B, Ac3, K14, AcH4, K5, and K12 but not for K9, K8 or K16. HA-P300 expressing cells exhibited statistical significance for H2B, K14, AcH4, K5, and K8, but did not exhibit significance for K9, K12 or K16. The statistical significance value calculated for the K9 epitope in the COS-7 HA-P300 trial fell just outside the cut-off value ($p < 0.05$) at 0.06. Subsequent t-tests performed for HeLa and IM cells revealed similar results to those outlined above (data not shown) – no statistical significance was calculated for K9, K8 or K16 in GFP-CBP expressing cells or, K9, K12 or K16 in HA-P300 expressing cells. These results strongly corroborate those detailed in the previous two sections. By comparing the results generated from histograms, regression analysis and t-tests for all three cell lines, we ordered the acetylation site specificity changes induced by GFP-CBP (K14>K5>K12>H2B) and HA-P300 (K14>H2B>K5>K8). Interestingly, although the GFP-CBP and HA-P300 induce different changes in steady-state histone acetylation, three of the top four acetylated species (K14, K5 and H2B) are altered by both proteins, with the final substrate residues, K12 or K8, representing unique targets for GFP-CBP and HA-P300, respectively.

5.3 DISCUSSION

The HAT assay detailed here is conceptually similar in design to standard reporter gene assays. Transfection of cells with a construct encoding an enzymatic activity, such as luciferase, results in the cellular production of an enzymatic activity that can be quantitatively correlated with a separate activity, such as DNA binding or transcription. An important distinction and improvement over traditional transfection assays is that the HAT assay employs additional selection criteria to maximize the representation of normal physiologic behavior. The major advantages of our approach is that 1) each cell used in the final measurement contributes equally and 2) criteria can be employed to specifically eliminate the higher overexpressors from the analysis. In conventional biochemical approaches, large numbers of cells are pooled to to make a single measurement. As a result, the contribution of a single cell within the total population is not equal to, but rather is directly proportional to, its relative expression level. By specifically eliminating the highest expressing cells and those most likely to generate expression-related artifacts, this assay is likely to be a more reliable measure of physiologically relevant activities.

The histone tails are presented in a much different manner *in vivo* than they are *in vitro*. *In vivo*, histone N-termini associate with DNA and adjacent nucleosomes contained within the same fiber or an adjacent fiber to facilitate further chromatin compaction states (Hansen, 2002; Hayes, 2002; Hayes and Hansen, 2001). The relative absence of 10nm and 30nm chromatin fibers *in vivo* (Georgel, 2002; Horn and Peterson, 2001; Widom, 1989) implies that the substrates typically utilized *in vitro*, namely histone tails, purified histones or reconstituted mononucleosomes, do not accurately recapitulate the endogenous counterparts that they are meant to recapitulate. In fact, the prevalence of higher-order chromatin (i.e. beyond the 30 nm fiber) implies that the HAT substrates may be much less accessible *in vivo* than *in vitro*. Consistent with the hypothesis that certain types of higher-order chromatin structure (i.e. at or beyond the 200 nm chromonema fiber level) may limit the accessibility of the histone N-termini to HATs, nucleoplasmic regions exhibiting intense DAPI staining fail to incorporate any of the acetylations associated with transient CBP or P300 expression. The *in vivo* HAT assay, therefore, presents the substrate in a natural conformation and relies upon statistical analyses to determine if there is a relationship between a specific HAT (i.e. CBP or P300) and a specific acetylated lysine residue contained within the histone N-termini. Because we observe significant increases in global acetylation for several histone residues, we can conclude that either, a) CBP/P300 do not require additional activities (i.e. co-factors) to acetylated the endogenous chromatin or, b) that such co-factors are not limiting relative to the endogenous levels of CBP and P300.

In this study, we have developed a novel imaging approach to characterize CBP- and P300-dependent histone acetylation. Most importantly, the assay is performed under physiologically relevant conditions and uses native chromatin structure as the substrate. The complexity of the physiological *in vivo* environment inherent in our quantitative HAT assay does not allow us to conclusively state that GFP-CBP and HA-P300 HAT activities directly regulate the global acetylation levels of specific subsets of histone lysine residues. For example, although we demonstrated that GFP-CBP and HA-P300 expression did not alter the expression levels of many additional HATs and HDACs, we cannot exclude the possibility that their expression may alter the enzymatic activity of other HATs or HDACs. While this remains possible, the striking similarity between the utilization of specific lysines by P300 *in vitro* (Ogryzko et al., 1996) and the changes in acetylation induced when P300 is transiently expressed *in vivo* and its distinction from other *in vitro* HAT activities (Mizzen et al., 1996; Smith et al., 1998; Tse et al., 1998) are more consistent with the HAT activity inherent to the transfected enzymes being responsible for the histone acetylations we observe. Furthermore, the short post-transfection period prior to fixation and analysis limits the potential of translation-dependent events from CBP or P300-regulated genes to impact on the observed acetylation pattern. Finally, by employing viability, morphological and expression criteria, we confine our analysis to cells that are expressing very close to physiological levels, further minimizing the limitations of conventional transfection-based assays. Therefore, although we cannot conclude with certainty that the HAT activity inherent in the expressed GFP-CBP or HA-P300 is directly responsible for the changes in histone acetylation we observe, we can conclude that the changes in acetylation that we observe upon transfection are directly dependent on CBP and P300 expression levels. Hence, CBP or P300 are directly responsible for these acetylations or they are responsible indirectly by regulating the activity of HATs or HDACs without the requirement for increasing or decreasing their protein levels.

In the past, CBP and P300 have largely been considered functionally redundant proteins. The overlapping changes in histone acetylation, specifically at K5 and K14, may account for the observed functional redundancies. More recently however, functional differences between CBP and P300 have been described (Kawasaki et al., 1998; Kung et al., 2000; Lipinski et al., 1999; Ugai et al., 1999; Yuan et al., 1999). For example, genetic studies involving *CBP* or *P300* hemizygous or knockout mice clearly demonstrate that one HAT cannot simply substitute for the other (Kung et al., 2000; Oike et al., 1999a; Oike et al., 1999b; Tanaka et al., 2000; Tanaka et al., 1997; Yamauchi et al., 2002; Yao et al., 1998). The observation of distinct phenotypes associated with *P300* and *CBP* knockout mice in embryogenesis and development, further underscores the disparate roles for each. Studies involving antisense oligodeoxynucleotides and hammerhead ribozymes specific to either CBP or P300 messenger RNAs have also identified distinct roles for CBP and P300 in retinoic-acid induced differentiation, cell-cycle exit and apoptosis of embryonal carcinoma F9 cells (Kawasaki et al., 1998; Ugai et al., 1999). Although it is clear that CBP and P300 have some overlapping and redundant functions, it is now equally apparent they have distinct and separable functions. Currently, little to no evidence is available to adequately account for the underlying functional differences observed between them. Our characterization of novel differences in the acetylation induced by GFP-CBP (K12) and HA-P300 (K8) represents the first differences demonstrated between these two HATs which may account for the observed functional differences.

In conclusion, we have developed a novel *in vivo* HAT assay and used it to characterize the HAT specificity preferences of CBP and P300. This approach couples the spatial resolving power of a laser scanning confocal microscope and the quantitative analytical power of basic statistical approaches. This approach overcomes conventional biochemical limitations by enabling cells to be analyzed either on an individual or population basis. Because it is performed under normal physiologic conditions and on endogenous substrates, the conformational differences of histone tails that exist between different substrates *in vitro* (i.e. purified histone tails, mononucleosomes or as short polynucleosome arrays) are avoided. We feel this methodology harbors many advantages over conventional biochemical approaches and should be generally amenable to the determination of any substrate specificity with minimal modifications.

5.4 ACKNOWLEDGEMENTS

We thank Darin McDonald and Dr. Roseline Godbout for critical reading of the manuscript. We also thank Dr. Eric Verdin (University of California, San Francisco) and Dr. X. Yang (McGill University) for the generous gifts of anti-HDACs 3 and 4 and anti-PCAF, respectively.

We thank the Canadian Institute of Health Research (CIHR) and the Alberta Heritage Foundation for Medical Research (AHFMR) for operational funding support. During the course of this study K. J. M. was supported by studentships from the Natural Sciences and Engineering Research Council of Canada, CIHR, AHFMR and the Department of Oncology Endowed PhD Studentship. M. J. H. is supported by scholarships from CIHR and AHFMR.

5.5 REFERENCES

Annunziato, A.T., and J.C. Hansen. 2000. Role of histone acetylation in the assembly and modulation of chromatin structures. *Gene Expr*. 9:37-61.

Ausio, J., D.W. Abbott, X. Wang, and S.C. Moore. 2001. Histone variants and histone modifications: a structural perspective. *Biochem Cell Biol*. 79:693-708.

Bannister, A.J., and T. Kouzarides. 1996. The CBP co-activator is a histone acetyltransferase. *Nature*. 384:641-3.

Berger, S.L. 2002. Histone modifications in transcriptional regulation. *Curr Opin Genet Dev*. 12:142-8.

Blobel, G.A. 2000. CREB-binding protein and p300: molecular integrators of hematopoietic transcription. *Blood*. 95:745-55.

Brownell, J.E., J. Zhou, T. Ranalli, R. Kobayashi, D.G. Edmondson, S.Y. Roth, and C.D. Allis. 1996. Tetrahymena histone acetyltransferase A: a homolog to yeast Gcn5p linking histone acetylation to gene activation. *Cell*. 84:843-51.

Chan, H.M., and N.B. La Thangue. 2001. p300/CBP proteins: HATs for transcriptional bridges and scaffolds. *J Cell Sci*. 114:2363-73.

Chrivia, J.C., R.P. Kwok, N. Lamb, M. Hagiwara, M.R. Montminy, and R.H. Goodman. 1993. Phosphorylated CREB binds specifically to the nuclear protein CBP. *Nature*. 365:855-9.

Georgel, P.T. 2002. Chromatin structure of eukaryotic promoters: a changing perspective. *Biochem Cell Biol*. 80:295-300.

Giles, R.H., D.J. Peters, and M.H. Breuning. 1998. Conjunction dysfunction: CBP/p300 in human disease. *Trends Genet*. 14:178-83.

Goodman, R.H., and S. Smolik. 2000. CBP/p300 in cell growth, transformation, and development. *Genes Dev*. 14:1553-77.

Gunjan, A., D.B. Sittman, and D.T. Brown. 2001. Core histone acetylation is regulated by linker histone stoichiometry in vivo. *J Biol Chem*. 276:3635-40.

Hansen, J.C. 2002. Conformational dynamics of the chromatin fiber in solution: determinants, mechanisms, and functions. *Annu Rev Biophys Biomol Struct*. 31:361-92.

Hayes, J.J. 2002. Changing chromatin from the inside. *Nat Struct Biol*. 9:161-3.

Hayes, J.J., and J.C. Hansen. 2001. Nucleosomes and the chromatin fiber. *Curr Opin Genet Dev*. 11:124-9.

Hendzel, M.J., M.J. Kruhlak, and D.P. Bazett-Jones. 1998. Organization of highly acetylated chromatin around sites of heterogeneous nuclear RNA accumulation. *Mol Biol Cell*. 9:2491-507.

Hendzel, M.J., M.J. Kruhlak, N.A. MacLean, F. Boisvert, M.A. Lever, and D.P. Bazett-Jones. 2001. Compartmentalization of regulatory proteins in the cell nucleus. *J Steroid Biochem Mol Biol*. 76:9-21.

Horn, P.J., and C.L. Peterson. 2001. The bromodomain: a regulator of ATP-dependent chromatin remodeling? *Front Biosci*. 6:D1019-23.

Kawasaki, H., R. Eckner, T.P. Yao, K. Taira, R. Chiu, D.M. Livingston, and K.K. Yokoyama. 1998. Distinct roles of the co-activators p300 and CBP in retinoic-acid-induced F9-cell differentiation. *Nature*. 393:284-9.

Kruhlak, M.J., M.J. Hendzel, W. Fischle, N.R. Bertos, S. Hameed, X.J. Yang, E. Verdin, and D.P. Bazett-Jones. 2001. Regulation of global acetylation in mitosis through loss of histone acetyltransferases and deacetylases from chromatin. *J Biol Chem*. 276:38307-19.

Kruhlak, M.J., M.A. Lever, W. Fischle, E. Verdin, D.P. Bazett-Jones, and M.J. Hendzel. 2000. Reduced mobility of the alternate splicing factor (ASF) through the nucleoplasm and steady state speckle compartments. *J Cell Biol*. 150:41-51.

Kung, A.L., V.I. Rebel, R.T. Bronson, L.E. Ch'ng, C.A. Sieff, D.M. Livingston, and T.P. Yao. 2000. Gene dose-dependent control of hematopoiesis and hematologic tumor suppression by CBP. *Genes Dev*. 14:272-7.

Lipinski, K.S., P. Fax, B. Wilker, H. Hennemann, D. Brockmann, and H. Esche. 1999. Differences in the interactions of oncogenic adenovirus 12 early region 1A and nononcogenic adenovirus 2 early region 1A with the cellular coactivators p300 and CBP. *Virology*. 255:94-105.

McManus, K.J., and M.J. Hendzel. 2001. CBP, a transcriptional coactivator and acetyltransferase. *Biochem Cell Biol*. 79:253-66.

Mizzen, C.A., X.J. Yang, T. Kokubo, J.E. Brownell, A.J. Bannister, T. Owen-Hughes, J. Workman, L. Wang, S.L. Berger, T. Kouzarides, Y. Nakatani, and C.D. Allis. 1996. The TAF(II)250 subunit of TFIID has histone acetyltransferase activity. *Cell*. 87:1261-70.

Ogryzko, V.V., R.L. Schiltz, V. Russanova, B.H. Howard, and Y. Nakatani. 1996. The transcriptional coactivators p300 and CBP are histone acetyltransferases. *Cell.* 87:953-9.

Oike, Y., A. Hata, T. Mamiya, T. Kaname, Y. Noda, M. Suzuki, H. Yasue, T. Nabeshima, K. Araki, and K. Yamamura. 1999a. Truncated CBP protein leads to classical Rubinstein-Taybi syndrome phenotypes in mice: implications for a dominant-negative mechanism. *Hum Mol Genet.* 8:387-96.

Oike, Y., N. Takakura, A. Hata, T. Kaname, M. Akizuki, Y. Yamaguchi, H. Yasue, K. Araki, K. Yamamura, and T. Suda. 1999b. Mice homozygous for a truncated form of CREB-binding protein exhibit defects in hematopoiesis and vasculo-angiogenesis. *Blood.* 93:2771-9.

Schiltz, R.L., C.A. Mizzen, A. Vassilev, R.G. Cook, C.D. Allis, and Y. Nakatani. 1999. Overlapping but distinct patterns of histone acetylation by the human coactivators p300 and PCAF within nucleosomal substrates. *J Biol Chem.* 274:1189-92.

Smith, E.R., A. Eisen, W. Gu, M. Sattah, A. Pannuti, J. Zhou, R.G. Cook, J.C. Lucchesi, and C.D. Allis. 1998. ESA1 is a histone acetyltransferase that is essential for growth in yeast. *Proc Natl Acad Sci U S A.* 95:3561-5.

Tanaka, Y., I. Naruse, T. Hongo, M. Xu, T. Nakahata, T. Maekawa, and S. Ishii. 2000. Extensive brain hemorrhage and embryonic lethality in a mouse null mutant of CREB-binding protein. *Mech Dev.* 95:133-45.

Tanaka, Y., I. Naruse, T. Maekawa, H. Masuya, T. Shiroishi, and S. Ishii. 1997. Abnormal skeletal patterning in embryos lacking a single Cbp allele: a partial similarity with Rubinstein-Taybi syndrome. *Proc Natl Acad Sci U S A.* 94:10215-20.

Thorne, A.W., D. Kmiciek, K. Mitchelson, P. Sautiere, and C. Crane-Robinson. 1990. Patterns of histone acetylation. *Eur J Biochem.* 193:701-13.

Tse, C., E.I. Georgieva, A.B. Ruiz-Garcia, R. Sendra, and J.C. Hansen. 1998. Gcn5p, a transcription-related histone acetyltransferase, acetylates nucleosomes and folded nucleosomal arrays in the absence of other protein subunits. *J Biol Chem.* 273:32388-92.

Ugai, H., K. Uchida, H. Kawasaki, and K.K. Yokoyama. 1999. The coactivators p300 and CBP have different functions during the differentiation of F9 cells. *J Mol Med.* 77:481-94.

Wang, X., C. He, S.C. Moore, and J. Ausio. 2001. Effects of histone acetylation on the solubility and folding of the chromatin fiber. *J Biol Chem.* 276:12764-8.

Wang, X., S.C. Moore, M. Laszckzak, and J. Ausio. 2000. Acetylation increases the alpha-helical content of the histone tails of the nucleosome. *J Biol Chem.* 275:35013-20.

Widom, J. 1989. Toward a unified model of chromatin folding. *Annu Rev Biophys Biophys Chem.* 18:365-95.

Yamauchi, T., Y. Oike, J. Kamon, H. Waki, K. Komeda, A. Tsuchida, Y. Date, M.X. Li, H. Miki, Y. Akanuma, R. Nagai, S. Kimura, T. Saheki, M. Nakazato, T. Naitoh, K. Yamamura, and T. Kadowaki. 2002. Increased insulin sensitivity despite lipodystrophy in Crebbp heterozygous mice. *Nat Genet.* 30:221-6.

Yang, X.J., V.V. Ogryzko, J. Nishikawa, B.H. Howard, and Y. Nakatani. 1996. A p300/CBP-associated factor that competes with the adenoviral oncoprotein E1A. *Nature.* 382:319-24.

Yao, T.P., S.P. Oh, M. Fuchs, N.D. Zhou, L.E. Ch'ng, D. Newsome, R.T. Bronson, E. Li, D.M. Livingston, and R. Eckner. 1998. Gene dosage-dependent embryonic development and proliferation defects in mice lacking the transcriptional integrator p300. *Cell.* 93:361-72.

Yuan, Z.M., Y. Huang, T. Ishiko, S. Nakada, T. Utsugisawa, H. Shioya, Y. Utsugisawa, Y. Shi, R. Weichselbaum, and D. Kufe. 1999. Function for p300 and not CBP in the apoptotic response to DNA damage. *Oncogene.* 18:5714-7.

Zhang, Y., and D. Reinberg. 2001. Transcription regulation by histone methylation: interplay between different covalent modifications of the core histone tails. *Genes Dev.* 15:2343-60.

CHAPTER 6

Discussion

6.0 DISCUSSION

The results detailed in the preceding chapters focus primarily on the characterization of histone methylation (Chapter 3) and phosphorylation (Chapter 4) dynamics and detail the substrate specificity preferences of two highly related HATs, CBP and P300 (Chapter 5). Chapter 3 details the cell cycle associated dynamics of individual methylation states observe in aa residues located within the NTDs of histones H3 and H4. This chapter documents previously unknown dynamics for several specific methylation states (e.g. tMeK9, mMeK9 and mMeK20) as cells enter and exit mitosis. Furthermore, we establish that tMeK9 is lost from chromatin independent of proteolytic processing of H3 amino-termini or RINA. Additional experiments demonstrate that the mitosis-associated trimethylation of K9 is critical in the maintenance of genomic stability. Chapter 4 documents the temporal dynamics of γ-H2AX in unirradiated mammalian cell lines. Here I present the first description of γ-H2AX foci that do not colocalize with six proteins common to DNA DSB repair. Although the exact function(s) of these small γ-H2AX foci remains to be elucidated, it is plausible that they 'survey' the genome looking for DNA DSBs. Furthermore, we demonstrate that the mitosis-associated increase in γ-H2AX is dependent on functional ATM expression and is independent of functional DNA-PK$_{CS}$ expression. Finally, Chapter 5 documents the *in situ* substrate specificity preferences of CBP and P300, two highly related HATs that are frequently considered to be functionally redundant. We identify subtle but measurable differences in acetylation of histone induced in vivo through the transient overexpression of CBP and P300. These differences may account for, or contribute to, the functional disparity observed between CBP and P300.

In addition to the novel findings documented in Chapters 3, 4 and 5, a major focus of this work has been to develop novel approaches to investigate posttranslational histone modifications *in situ*. This is particularly true of the enzymatic assay developed for quantifying changes in histone acetylations, where the presentation of histone NTDs to modifying enzymes only occurs within the context of higher-order chromatin structure *in vivo*. As detailed in Chapter 5, HATs can exhibit differences in substrate specificity preferences depending upon the context in which the substrate is presented (i.e. as synthesized peptides, recombinant histones, mononucleosomes, or short polynucleosomal arrays). Accordingly, to measure the *bone fide* substrate preferences for HATs, we developed a quantitative imaging approach that measures *in situ* changes through fluorescence microscopy. QIM couples the spatial resolving power of confocal or digital microscopy with robust statistical analyses to quantify changes at the level of a single cell. We utilized this novel approach to investigate the dynamics of histone modifications (Chapters 3 and 4) and determine the HAT specificity preferences of CBP and P300 *in situ* using endogenous chromatin structure as a substrate (Chapter 5). This methodology is a significant advance for several reasons. First, the structure of chromatin is highly dependent upon the environmental (buffer) conditions, where small changes in ionic strength or pH can lead to large changes in structure. Thus, it is unclear what the 'correct' conditions are for *in vitro* measurements of enzymatic activities on chromatin substrates. Our experiments are performed *in situ* where we can be certain that the chromatin is present in its native conformation. Second, QIM inherently includes complexities that are overlooked when biochemical reactions are performed that utilize reconstituted components. For example, the inclusion of non-histone but chromatin-associated proteins (e.g. HMG proteins or condensins) has a direct effect on the formation and/or the stability of higher-order chromatin structure. Third, the use of asynchronous populations, relying upon morphological and other indications to stage each cell within the cell cycle, alleviates the potential of indirect side effects. Many studies have demonstrated that drug-induced synchrony does not and cannot generate a perfectly synchronized population. As a direct result, these synchronized populations are comprised of a mixture of cells at different cell cycle stages and are only enriched for a particular cell cycle stage. This significantly limits the sensitivity of traditional biochemical approaches. Fourth, specific cell cycle stages can easily be identified through classical chromosome morphological criteria (mitosis) or by coimmunofluorescently labeling cells with additional stage specific markers (e.g. anti-PhosS10, BrdU, etc.). By selecting only those cells exhibiting the predefined criteria, not only does QIM provide a temporal resolution that far surpasses those of conventional biochemical approaches but it provides a much more homogeneous population for each measurement. This property permits QIM to accurately and completely resolve the five major stages of mitosis – a feature that cannot currently be accomplished by biochemical or flow cytometric means. Fifth, by normalizing the posttranslational histone modification total signal intensities to the DAPI total signal intensities for each and every cell nucleus, one can control for histone variability that occurs as cells progress through the cell cycle. By controlling for histone variabilities, QIM can accurately compare modification signal intensities on a cell-by-cell basis – in essence resolving the specific biological question down to the single cell level. Finally, QIM provides a robust means of statistically evaluating the temporal progression of various posttranslational modifications (Chapters 3 and 4) or substrate specificities preferences of the histone modifying enzymes (Chapter 5).

6.1 HISTONE CODE HYPOTHESIS – DOES A HISTONE CODE EXIST?

A major criticism of the Histone Code Hypothesis is the lack of evolutionary conservation across species. Implicit in the Histone Code Hypothesis is that functions will be conserved between organisms. The system should be robust because to effect an evolutionary change, both the targeted aa and the protein that binds to it must simultaneously evolve/mutate. A single change will result in an inactivation of the system. Although many modifications and functional outcomes appear to be highly conserved across eukaryotic species, subtle differences exist and are important to highlight in the context of a code. As described in Chapter 1, the non-random site utilization observed for global acetylation is significantly different between cuttlefish and mammals (Couppez et al., 1987; Thorne et al., 1990). Although heterochromatization in most eukaryotes involves tMeK9 and the silencing effect imparted by HP1, no such methylation or Suv39h1 ortholog exists in *S. cerevisiae*. Furthermore, this observation suggests that in *S. cerevisiae*, additional or redundant mechanisms must exist to regulate heterochromatization that are entirely independent of those involving HP1.

The results detailed in Chapters 3, 4 and 5, question the current elaboration of the Histone Code Hypothesis, which suggests that modified histone residues are predominantly bound by cognate proteins containing bromo- or chromo-domains. The most obvious paradox is that methylated (Chapter 3), phosphorylated (Chapter 4) and acetylated (Chapter 5) epitopes can be easily identified using modification-specific antibodies *in situ*. Hence, the availability of these epitopes in cells fixed using methods essentially identical to those utilized in chromatin immunoprecipitation (ChIP) experiments, is difficult to reconcile with proteins that stably bind these modifications. Furthermore, the observation that the results obtained by IIF approaches (e.g. DIM, flow cytometry and QIM) for histone methylation (Chapter 3), phosphorylation (Chapter 4 and McManus, Submitted) and acetylation (McManus, Submitted), quantitatively parallel those obtained from immunoblots of denatured histones, argues that neither higher-order chromatin structure nor the presence of bromo- and chromo-domain containing proteins, significantly alters the presentation of the histone modification epitopes *in vivo*. Therefore, the observations presented in this thesis coupled with the wealth of data indicating that both bromo- and chromo-domain containing proteins are highly dynamic challenge the current embodiment of the Histone Code Hypothesis and the concept of Binary Switches.

As described in Chapter 1, one of the primary requirements of the Histone Code Hypothesis is that proteins must be able to recognize and interpret a code to evoke specific functional outcomes. The code posits that this is accomplished through protein docking modules contained within specific nuclear proteins (e.g. HATs, transcription factors, transcription co-activators or -repressors etc.) that bind the residue specific modifications. Indeed crystallographic data have been presented characterizing the *in vitro* interaction of acetylated and methylated histone NTD peptides with their respective cognate proteins (see (Dhalluin et al., 1999; Hudson et al., 2000; Jacobs and Khorasanizadeh, 2002; Jacobson et al., 2000; Min et al., 2003; Nielsen et al., 2002; Owen et al., 2000)). Additionally, numerous ChIP analyses have demonstrated that many nuclear factors, including HATs and HMTs, interact specifically with posttranslationally modified histones. ChIP is a versatile immunological-based assay commonly performed to investigate protein:DNA or protein:histone interactions in a native chromatin context (see (Braunstein et al., 1993; Dedon et al., 1991; Ebralidse et al., 1993)). ChIP assays have been employed extensively to investigate and identify numerous interactions between a specific posttranslational histone modification and a cognate chromatin-interacting protein within various genetic loci. However, the initial chemical cross-linking step (e.g. formaldehyde treatment) frequently ranges between 10 min to 12 hr. This lengthy cross-linking treatment is unfortunately orders of magnitude longer than many of the transient interactions known to occur between nuclear factors and modifications (see below), and is significantly longer than the half lives of many modifications – global acetylation exhibits a half life as short as 3 min (Covault and Chalkley, 1980). Furthermore, it has been shown in several different cell types it is precisely this rapid turnover of acetylation that best distinguishes transcribed sequences from the remainder of the genome (Boffa et al., 1990; Davie and Hendzel, 1994; Ip et al., 1988; Zhang and Nelson, 1988). This lengthy step can therefore serve to artificially enrich the associations of various modifications with proteins that may only ever transiently interact with the modification at specific loci.

The Histone Code Hypothesis also neglects to account for several additional, yet basic characteristics of the protein:modification interactions. First, the affinities between specific modifications and their cognate proteins are relatively weak. Dissociation constants (Kd) between acetylated or methylated histone residues and their respective bromo- and chromo-domains generally range between 10^{-4} to 10^{-6} M (Fischle et al., 2003). Second, many of the interactions between proteins and cognate peptides are known to be transient rather than stable. In practice, most nuclear factors including transcription factors, DNA repair enzymes and histone modifying enzymes (e.g. HATs, HMTs, etc.), are bound for seconds to minutes in duration rather than stably associated with chromatin. Fluorescence recovery after photobleaching (FRAP) experiments have been conducted on transcription factors (e.g. STAT1), co-activators (e.g. CBP) and silencers (e.g. HP1) containing bromo- or chromo-domains and clearly demonstrate that these factors are highly mobile. For instance, fluorescently tagged versions of STAT1, CBP and HP1 exhibit recovery times that are only slightly slower (t_{50} = <1s) than those of empty GFP itself (t_{50} = ~ 0.2s), which is presumed to be freely mobile (Cheutin et al., 2003; Lillemeier et al., 2001) (McManus, unpublished observations). In fact, complete recovery of almost any nuclear factors studied to date occurs within 30 to 45 sec (Phair et al., 2004), and is significantly faster than the recovery times of the histones themselves (t_{50} > 2 hr) (Kimura and Cook, 2001). Most importantly, the conclusions drawn from FRAP analyses indicate that only an extremely minute percentage (i.e. <1%) of any nuclear protein investigated is stably bound to chromatin (reviewed in (Phair et al., 2004; Phair and Misteli, 2000)). In other words, the vast majority of nuclear factors such as transcription factors, DNA repair proteins or histone modifying enzymes are highly mobile and are not stably associated with chromatin as suggested by the Histone Code Hypothesis. These observations coupled with the knowledge that most posttranslational modifications are reversible and can have half lives as short as 3 min make it highly unlikely that the mechanism controlling transcriptional regulation occurs as implied by the Histone Code Hypothesis.

6.2 BINARY SWITCHES – DO THEY REGULATE PROTEIN (HP1) DYNAMICS?

The Allis research group has recently suggested that binary 'on/off' switches exist that regulate the on/off rates of specific protein:modification interactions in order to ablate the functional outcomes the interaction regulates (Fischle et al., 2003; Wang et al., 2004a). In particular, they propose that the interaction of HP1 with tMeK9 that results in heterochromatization or gene silencing, is 'turned off' by subsequent phosphorylation of S10. Consistent with this hypothesis, HP1 is reported to dissociate from chromatin as cells enter mitosis and then reassociate with chromatin as cells exit mitosis (Kellum et al., 1995; Mateescu et al., 2004; Minc et al., 1999). However, if the Binary Switch model functions as proposed, one would predict that the methyl (K9)/phos (S10) switch would be most active during mitosis or meiosis, when increases in PhosS10 levels are rapidly induced and reach maximal values. The underlying requirement for gene derepression imparted by the dissociation of HP1 at that specific point of the cell cycle is certainly unclear, as transcription rates are extremely low. However, it is possible that derepression may occur during entry into mitosis so that as both daughter cells enter G_1, they do so with a 'blank' epigenetic canvas onto which they can build transcriptional regulatory modifications. Perhaps too conveniently this model agrees with some of the cytological observations detailing HP1 dynamics during mitosis (Kellum et al., 1995; Mateescu et al., 2004; Minc et al., 1999). In fact, the dissociation of HP1 from chromatin during mitosis is a contentious issue that remains to be resolved (see below). Moreover, alternative explanations exist that could equally account for the mitotic dissociation of HP1 from chromosomes. First, chromatin compaction reaches maximal levels during mitosis and in mammals is approximately 40-fold greater in mitosis than in interphase. It is reasonable to suggest that in addition to the transient and dynamic interaction that HP1 normally exhibits with chromatin (Cheutin et al., 2003), increases in chromatin folding may sterically prevent HP1 from interacting with tMeK9. Second, as alluded to above, the mitotic dissociation of HP1 from chromosomes does not appear to be universally conserved. More data are currently available confirming a spatial overlap between HP1 and mitotic chromosomes than confirming its mitotic dissociation. For example, Gilbert *et al* (2003) provided cytological evidence that endogenous HP1 in DT40 (chicken) cells, localizes with chromosomes during early prophase. Furthermore, two independent Japanese groups have demonstrated that YFP-HP1 (Hayakawa et al., 2003) and RFP-HP1 (Sugimoto et al., 2001) are clearly associated with pericentromeric regions during metaphase in a variety of mammalian cells including HeLa, 10T1/2 and IM. These observations are particularly difficult to reconcile in the context of the 'Binary Switch' hypothesis as the mitosis-associated increases in PhosS10 initially occur within pericentromeric heterochromatin. Interestingly, upon closer inspection of microscopy data from articles that are frequently cited as demonstrating the mitotic dissociation of HP1, a significant amount of signal overlap is clearly evident between metaphase chromosomes (labeled with DAPI) and endogenous HP1, which is especially pronounced within centromeric regions (Kellum et al., 1995). Finally, HP1 has also been shown to associate with meiotic chromosomes. For example, in male meioses, the entire XY body is decorated with endogenous HP1 specifically during early and late pachytene (Metzler-

Guillemain et al., 2003). Evidence has now been presented that disputes the ability of PhosS10 to prevent the HP1:tMeK9 interaction. Surprisingly, Mateescu *et al* (2004) demonstrated that in BY-2 cells or transgenic tobacco plants expressing human HP1, in late G_2 and early prophase the presence of PhosS10 actually increases the affinity of HP1 for tMeK9. Furthermore, they demonstrated that HP1 dissociation was only readily detectable when an additional acetylation event, occurring at K14 (H3), was present (Mateescu et al., 2004). Together these observations question the working model postulated by the 'Binary Switch' hypothesis. In light of all this information, it appears highly unlikely that PhosS10 acts as a binary off switch to prevent the heterochromatic state imparted by HP1 binding to tMeK9.

6.3 FUTURE DIRECTIONS

In the coming of a new epigenomic era, the regulation of the posttranslational modifications and the enzymes responsible for adding or subtracting these modifications are poised to take center stage. They are emerging themes in the study of the mechanisms underlying the regulation of gene expression and understanding the molecular etiology of human diseases such as cancer. The identification of altered histone modification activities in a range of human cancers supports the involvement of epigenetic mechanisms during oncogenesis (Kondo et al., 2003). In order to fully appreciate the mechanisms underlying the manifestation of various diseases and cancers and devise novel therapeutic strategies, it is of extreme importance that the regulation, dynamics and functions of posttranslational histone modifications be characterized.

From a basic science perspective, understanding the fundamental regulatory pathways, dynamics and functions associated with the posttranslational modifications are of utmost importance. This knowledge would provide critical insights into the mechanisms and processes involving chromatin that include the regulation of higher-order chromatin structure, transcription, DNA repair, apoptosis, differentiation, and tumorigensis. From a clinical perspective, this basic knowledge would ultimately provide crucial information required to develop a wide array of novel therapeutic agents that target the mechanisms regulating key posttranslational histone modifications as well as tests that predict patient responses to standard therapies.

6.3.1 *Identification of All Posttranslational Histone Modifications*

At least seven different types of posttranslational modifications have been identified that are covalently attached directly to the core histones. Many of these modifications however, only occur on a small fraction of the total number of possible residues and only on a subset of those. For example, phosphorylation of cellular proteins occurs on six different aa residues, namely serine, threonine, tyrosine, lysine, histidine and arginine. To date, histone phosphorylation has only been identified on serine and threonine residues and only on a small subfraction of the total number of available residues. Despite the fact that lysine residues within the four core histones frequently serve as major targets for posttranslational histone modifications (e.g. acetylation, methylation, ubiquitination, sumoylation, and biotinylation), they currently do not appear to be a substrate for phosphorylation. However, based on new mass spectrometry approaches investigating posttranslational histone modifications (see below), novel sites and modifications are now being routinely identified (Bonaldi et al., 2004a; Bonaldi et al., 2004b; Freitas et al., 2004; Person etal., 2003; Pesavento et al., 2004; Smith et al., 2003; Zhang et al., 2003). Therefore, it is not unreasonable to suggest that lysine or any of the three additional residues (tyrosine, histidine or arginine) located within histones, particularly within their NTDs, may yet be identified as substrates of phosphorylation *in vivo*.

It was recently shown that posttranslational histone modifications can undergo subsequent reactions to yield entirely new modifications. Wang *et al* (2004b) demonstrated that PAD4 targets several methylated arginine residues located in histones H3 and H4 NTDs and converts them to citrulline thereby releasing methylamine. They demonstrate that in MCF-7 cells, citrullination or PAD4 activity, is associated with increased transcription of estrogen responsive genes. This seminal paper established for the first time, that specific posttranslational histone modifications can undergo subsequent modifications. At the very least, this observation suggests that other methylated arginine residues are good candidates for similar types of subsequent modifications. Moreover, if extrapolated to include additional modifications such as lysine methylation, it suggests that similar secondary reactions could yield additional modifications that have yet to be identified.

Although the histones and many posttranslational modifications are evolutionarily conserved, differences do exist. These differences are particularly evident between lower (e.g. yeast) and higher (e.g. mammals) eukaryotes. For instance, *S. cerevisiae*, unlike all other eukaryotes investigated, does not contain a Suv39h1 ortholog nor is it ever methylated at K9 (H3) (Briggs et al., 2001). Fundamental differences also exist within the epigenetic status or transcriptional states of lower and higher eukaryotes. Lower eukaryotes generally maintain an epigentically active or transcriptionally permissive state, while higher eukaryotes generally maintain an epigenetically repressed or transcriptionally silent state (Hake et al., 2004). For example, *Tetrahymena* and yeast are predominantly methylated at K4 (H3) (i.e. 'on') but not at K9 (H3) (i.e. 'off'), while in humans and chickens, the opposite holds true (Briggs et al., 2001). These examples alone serve to indicate that in order to identify all posttranslational histone modifications, studies will necessarily have to include countless numbers of diverse organisms and different developmental stages (Ramaswamy et al., 2003).

Differences in posttranslational histone modifications are not restricted to variability between various organisms; differences also occur within the same species. Chapter 3 details fundamental differences between minimal and maximal tMeK9 TSI occurring in mouse cells grown in 2D cultures and those from mid-gestation embryos and established that they are approximately 4- and 15-fold, respectively. Although variation in tMeK9 abundance could simply reflect differences in tissue origin or differentiation status or reflect an adaptation of the mouse cells grown in 2D cultures, it indicates that the epigenetic status is highly complex and likely differs between various cell-, tissue- and organ-types even within the same species. Therefore, it is critical that the modifications be investigated in the context of normal tissue and developmental backgrounds. This task alone will be extremely difficult and very laborious. These observations plus those detailed above indicate that to identify all posttranslational histone modifications and characterize their dynamics a diverse array of conditions will be required. Especially important in this venture would be the inclusion of various organisms and cell and tissue types as well as various culture conditions.

The observations detailed in this thesis and elsewhere strongly indicate that most modifications exhibit variable dynamics (Borun et al., 1972; Gurley et al., 1973; Gurley et al., 1974; Hendzel et al., 1997; Paulson and Taylor, 1982) (McManus and Hendzel, submitted). Many of these dynamic modifications exhibit critical functional roles in regulating numerous cellular and nuclear processes including chromosome compaction and segregation during mitosis (Bui et al., 2004; Petersen et al., 2001; Wei et al., 1999). The demonstration that some modifications exhibit cell cycle-dependent dynamics (e.g. tMeK9 [Chapter 3] and γ-H2AX [Chapter 4]) while others (e.g. PhosS10) can be induced under specific conditions (e.g.. mitogen- or stess-stimulation [reviewed in (Davie, 2003)]) illustrates how the identification of all posttranslational modifications will require a diverse array of experimental systems and conditions. Perhaps the most obvious place to begin is with protein preparations isolated from cells enriched at various stages of the cell cycle. Ideally, stage-specific cellular populations would be generated through mechanical means (e.g. mitotic shake-off or centrifugal elutriation) rather than through drug-induced synchrony. However, these approaches have limited uses as they predominantly produce mitotically-enriched populations. Alternatively, live cells could be labeled and sorted by fluorescence activated cell sorting (FACS). The DNA from cells could be fluorescently labeled with Hoechst 33342, and cells could be sorted based on DNA content (e.g. 2N or 4N). A third approach is to use the diverse array of agents (i.e. drugs) currently available that arrest/enrich cells at various stages of the cell cycle. Work detailed in this thesis suggests that double thymidine-, nocodazole- and ALLN-treatments are particularly successful at generating cellular populations enriched at the G_1/S boundary, prometaphase and metaphase, respectively. However, as shown in Chapter 4, the abilities of these agents to enrich for stage-specific populations, does exhibit some cell line variability. In any case, protein preparations derived from any of these approaches generally yields sufficient quantities for mass spectrometry to be performed (McManus and Hendzel, unpublished observations).

Recent technological advancements coupled with increased research efforts within the past two years have yielded an explosion in the number of novel sites being identified that harbor various posttranslational modifications. Most approaches utilize mass spectrometry and protein peptide mass fingerprinting (Bonaldi et al., 2004a; Bonaldi et al., 2004b; Freitas et al., 2004; Person et al., 2003; Pesavento et al., 2004; Smith et al., 2003; Zhang et al., 2003) and can now easily distinguish between acetylation and tri-methylation occurring at the same lysine residues (Zhang et al., 2004). Unfortunately these experiments routinely employ asynchronous populations and have not attempted to address cell cycle-specific dynamics. Perhaps only once the majority of modifications have been identified will the temporal dynamics be investigated.

6.3.2 *Characterization of the Temporal Dynamics of Posttranslational Histone Modifications*

The QIM approaches developed and utilized throughout this thesis are ideally suited to the characterization of the cell cycle-specific dynamics of posttranslational histone modifications. Inherent in these approaches is the requirement for quality immunological reagents (i.e. antibodies) that are highly specific towards each unique posttranslational modification. Currently, there is a major effort for research laboratories and commercial companies to design, develop and test antibodies directed against all posttranslational histone targets. Experiments similar to those conducted in Chapters 3 and 4 could easily identify the temporal progression patterns of any posttranslational modification provided that an appropriate and specific antibody is available.

6.3.3 *Evaluating and Identifying Potential Functions Regulated by Posttranslational Histone Modifications*

Once the temporal progression patterns have been identified, experiments can be conducted to investigate whether the presence or absence of specific modifications is causally linked with certain cellular processes. Intuitively, the dynamics of a particular modification must temporally coincide with the cellular process that it may regulate. To evaluate the functional consequences of a particular modification, various different depletion experiments could be performed. For example, many mouse models have been generated that lack a specific modifying enzyme such as a HAT or HMT. In addition, RNA interference (RNAi) or small inhibitory RNA (siRNA) experiments could be designed to remove specific enzymes regulating specific modifications throughout the entire cell cycle or at specific stages of the cell cycle. Using these approaches one could quickly ascertain whether a particular modification underlies a specific cellular event. Additionally, site-directed mutagenesis of the histone could be performed where the modified residue is replaced by a residue that cannot be modified. However, this particular methodology will likely have far reaching effects on the structure of histone NTDs and higher-order chromatin structure that could adversely influence numerous different processes. In addition, several modifications can occur on the identical residue, so any observed phenotype associated with the substitution could have numerous underlying causes. Finally, gain-in-function studies could also be performed that may identify potential functions. For instance, ectopic expression of the controlling enzyme (e.g. HAT, HMT, HDAC etc.) through the introduction of an expression vector has been employed previously. These studies have identified aberrant phenotypes that result from the increased abundance of that particular modification and/or the lack of its strict temporal regulation. In any case, a combination of the experimental approaches outlined above is highly likely to identify specific functions associated with the various posttranslational histone modifications.

6.3.4 *Identification of Histone Modifying Enzyme Specificity Preferences In Vivo*

The quantitative approaches detailed in Chapter 5 are ideally suited to the identification of preferred enzyme targets provided that highly-specific antibodies that recognize all relevant epitopes are readily available. QIM has the added benefit of investigating enzyme specificities under physiologically relevant conditions and is performed on endogenous chromatin structures that contain all relevant non-histone proteins. As demonstrated in Chapter 5, this analysis is extremely sensitive and allowed us to identify subtle differences in the preferred HAT substrate specificity preferences of CBP and P300 – two HATs that are commonly reported to be functionally redundant. One caveat of this approach is that minimal overexpression does exist within cells for up to 12-16 hr. As overexpression of histone modifying enzymes (e.g. HATs, HMTs, etc.) has been associated with regulating the transcriptional status of specific genes, this slight overexpression has the potential to introduce nonspecific side-effects. However, these side-effects can be minimized by only analyzing cells that minimally over-express the protein of interest and including appropriate controls. Moreover the widespread use RNAi or siRNA could also be incorporated into these assays to investigate whether global decreases of a particular modification, accompanies the loss of a specific enzymatic activity. These experiments however, have the added complexity of compensatory or redundant mechanisms that could potentially mask the differences rendering them undetectable by QIM. In addition to examining the specificity preferences of enzymes catalyzing the addition of modifications, this type of analysis could also be adapted to examine the preferences of enzymes that remove specific modifications (e.g. HDACs, phosphatases, etc.). Importantly, the combination of these investigations would provide significant insights into the regulation of posttranslational modifications and the functions of the enzymes that regulate them. They would also identify the principle and minor enzymes regulating specific modifications *in situ*. Moreover, these studies would contribute to the overall understanding of the mechanisms regulating posttranslational histone modifications and provide fundamental information about the regulation of such processes as regulation of higher-order chromatin structure, transcriptional regulation, DNA repair, apoptosis, differentiation, and tumorigenesis. Overall QIM is ideally suited to the *in situ* characterization of enzyme target specificities.

6.3.5 *Epigenetic Regulation as Novel Therapeutic Targets*

By identifying all posttranslational histone modifications and understanding the basic dynamics, regulation and function(s) associated with each of them, a greater understanding of the fundamental biology of epigenetic inheritance will be attained. This knowledge can then be used to investigate physiological differences between normal cells and those associated with specific diseases such as cancer. The ultimate goals of these studies would be the identification of novel candidate therapeutic targets. Perhaps the most successful therapeutic approaches would target modifications that affect genomic stability, such as those that regulate cell cycle progression or ensure the fidelity of the mitotic process (e.g. PhosS10 or tMeK9). However, posttranslational modifications that regulate transcription also serve as excellent targets. For example, HDAC inhibitors (e.g.

phenylbutyric acid, SAHA, depsipeptide and valproic acid) are currently being utilized in numerous clinical trials evaluating their efficacy in down-regulating tumor progression. In a broad spectrum of transformed cells and in animal tumor models, HDAC inhibitors have been shown to induce differentiation, growth arrest and/or apoptosis. In fact, HDAC inhibitors in clinical trials have shown a great deal of promise, particularly in the treatment of hematological and solid tumors (Marks et al., 2003). Although the exact mechanism of HDAC inhibition has yet to be established, it is proposed to result in the accumulation of acetylated histones. In turn, this leads to the induction of genes whose expression causes inhibition of tumor growth (e.g. tumor suppressor genes) (Agalioti et al., 2002; Jenuwein and Allis, 2001; Zhang and Reinberg, 2001). However, because most HATs exhibit acetyltransferase activity towards numerous non-histone proteins (e.g. transcription factors, co-activators, etc.), there is also the likelihood that alternative mechanisms regulating transcription may also function in addition to histone acetylation. Accordingly, expression profiling of cultured cells incubated with HDAC inhibitor supports this model as the expression of a small percentage of genes (2-5%) is generally altered (Butler et al., 2002; Della Ragione et al., 2001; Suzuki et al., 2002; Van Lint et al., 1996). Surprisingly, although increases in histone acetylation are most frequently associated with increased transcription, these profiling experiments determined that decreases in expression occurred within a small subset of genes (some of which are oncogenes). Correspondingly, the factor acetyltransferase activity inherent in many HATs, such as CBP, has been shown to down-regulate the expression of specific genes through acetylation of non-histone proteins. For example, CBP acetylation of HMG I(Y) is required for the post-induction turnoff of *IFNβ* expression (Agalioti et al., 2000).

Acetylation of HMG I(Y), specifically at K65, destabilizes its association with the NF-κB transcription factor leading to the disassembly of the enhanceosome required for *IFNβ* transcription (Munshi et al., 1998). Nevertheless, the exact mechanisms regulating gene activation or repression following treatment with HDAC inhibitors are not well characterized and may result from either direct or indirect effects of histone or factor acetylation. The development of supplemental agents that alter the epigenetic imprint is likely to be effective by altering gene expression profiles. Perhaps once the fundamental dynamics, regulation and function associated with every posttranslational modification are known, specific targets will be identified for subsequent drug development.

6.4 REFERENCES

Agalioti, T., G. Chen, and D. Thanos. 2002. Deciphering the transcriptional histone acetylation code for a human gene. *Cell*. 111:381-92.

Agalioti, T., S. Lomvardas, B. Parekh, J. Yie, T. Maniatis, and D. Thanos. 2000. Ordered recruitment of chromatin modifying and general transcription factors to the IFN-beta promoter. *Cell*. 103:667-78.

Boffa, L.C., J. Walker, T.A. Chen, R. Sterner, M.R. Mariani, and V.G. Allfrey. 1990. Factors affecting nucleosome structure in transcriptionally active chromatin. Histone acetylation, nascent RNA and inhibitors of RNA synthesis. *Eur J Biochem*. 194:811-23.

Bonaldi, T., A. Imhof, and J.T. Regula. 2004a. A combination of different mass spectroscopic techniques for the analysis of dynamic changes of histone modifications. *Proteomics*. 4:1382-96.

Bonaldi, T., J.T. Regula, and A. Imhof. 2004b. The use of mass spectrometry for the analysis of histone modifications. *Methods Enzymol*. 377:111-30.

Borun, T.W., D. Pearson, and W.K. Paik. 1972. Studies of histone methylation during the HeLa S-3 cell cycle. *J Biol Chem*. 247:4288-98.

Braunstein, M., A.B. Rose, S.G. Holmes, C.D. Allis, and J.R. Broach. 1993. Transcriptional silencing in yeast is associated with reduced nucleosome acetylation. *Genes Dev*. 7:592-604.

Briggs, S.D., M. Bryk, B.D. Strahl, W.L. Cheung, J.K. Davie, S.Y. Dent, F. Winston, and C.D. Allis. 2001. Histone H3 lysine 4 methylation is mediated by Set1 and required for cell growth and rDNA silencing in Saccharomyces cerevisiae. *Genes Dev*. 15:3286-95.

Bui, H.T., E. Yamaoka, and T. Miyano. 2004. Involvement of histone H3 (Ser10) phosphorylation in chromosome condensation without CDC2 kinase and mitogen-activated protein kinase activation in pig oocytes. *Biol Reprod*. 70:1843-51.

Butler, L.M., X. Zhou, W.S. Xu, H.I. Scher, R.A. Rifkind, P.A. Marks, and V.M. Richon. 2002. The histone deacetylase inhibitor SAHA arrests cancer cell growth, up-regulates thioredoxin-binding protein-2, and down-regulates thioredoxin. *Proc Natl Acad Sci U S A*. 99:11700-5.

Cheutin, T., A.J. McNairn, T. Jenuwein, D.M. Gilbert, P.B. Singh, and T. Misteli. 2003. Maintenance of stable heterochromatin domains by dynamic HP1 binding. *Science*. 299:721-5.

Couppez, M., A. Martin-Ponthieu, and P. Sautiere. 1987. Histone H4 from cuttlefish testis is sequentially acetylated. Comparison with acetylation of calf thymus histone H4. *J Biol Chem*. 262:2854-60.

Covault, J., and R. Chalkley. 1980. The identification of distinct populations of acetylated histone. *J Biol Chem*. 255:9110-6.

Davie, J.R. 2003. MSK1 and MSK2 mediate mitogen- and stress-induced phosphorylation of histone H3: a controversy resolved. *Sci STKE*. 2003:PE33.

Davie, J.R., and M.J. Hendzel. 1994. Multiple functions of dynamic histone acetylation. *J Cell Biochem*. 55:98-105.

Dedon, P.C., J.A. Soults, C.D. Allis, and M.A. Gorovsky. 1991. A simplified formaldehyde fixation and immunoprecipitation technique for studying protein-DNA interactions. *Anal Biochem*. 197:83-90.

Della Ragione, F., V. Criniti, V. Della Pietra, A. Borriello, A. Oliva, S. Indaco, T. Yamamoto, and V. Zappia. 2001. Genes modulated by histone acetylation as new effectors of butyrate activity. *FEBS Lett*. 499:199-204.

Dhalluin, C., J.E. Carlson, L. Zeng, C. He, A.K. Aggarwal, and M.M. Zhou. 1999. Structure and ligand of a histone acetyltransferase bromodomain. *Nature*. 399:491-6.

Ebralidse, K.K., T.R. Hebbes, A.L. Clayton, A.W. Thorne, and C. Crane-Robinson. 1993. Nucleosomal structure at hyperacetylated loci probed in nuclei by DNA-histone crosslinking. *Nucleic Acids Res*. 21:4734-8.

Fischle, W., Y. Wang, and C.D. Allis. 2003. Binary switches and modification cassettes in histone biology and beyond. *Nature*. 425:475-9.

Freitas, M.A., A.R. Sklenar, and M.R. Parthun. 2004. Application of mass spectrometry to the identification and quantification of histone post-translational modifications. *J Cell Biochem*. 92:691-700.

Gilbert, N., S. Boyle, H. Sutherland, J. de Las Heras, J. Allan, T. Jenuwein, and W.A. Bickmore. 2003. Formation of facultative heterochromatin in the absence of HP1. *Embo J*. 22:5540-50.

Gurley, L.R., R.A. Walters, and R.A. Tobey. 1973. Histone phosphorylation in late interphase and mitosis. *Biochem Biophys Res Commun*. 50:744-50.

Gurley, L.R., R.A. Walters, and R.A. Tobey. 1974. Cell cycle-specific changes in histone phosphorylation associated with cell proliferation and chromosome condensation. *J Cell Biol*. 60:356-64.

Hake, S.B., A. Xiao, and C.D. Allis. 2004. Linking the epigenetic 'language' of covalent histone modifications to cancer. *Br J Cancer*. 90:761-9.

Hayakawa, T., T. Haraguchi, H. Masumoto, and Y. Hiraoka. 2003. Cell cycle behavior of human HP1 subtypes: distinct molecular domains of HP1 are required for their centromeric localization during interphase and metaphase. *J Cell Sci*. 116:3327-38.

Hendzel, M.J., Y. Wei, M.A. Mancini, A. Van Hooser, T. Ranalli, B.R. Brinkley, D.P. Bazett-Jones, and C.D. Allis. 1997. Mitosis-specific phosphorylation of histone H3 initiates primarily within pericentromeric heterochromatin during G2 and spreads in an ordered fashion coincident with mitotic chromosome condensation. *Chromosoma*. 106:348-60.

Hudson, B.P., M.A. Martinez-Yamout, H.J. Dyson, and P.E. Wright. 2000. Solution structure and acetyl-lysine binding activity of the GCN5 bromodomain. *J Mol Biol*. 304:355-70.

Ip, Y.T., V. Jackson, J. Meier, and R. Chalkley. 1988. The separation of transcriptionally engaged genes. *J Biol Chem*. 263:14044-52.

Jacobs, S.A., and S. Khorasanizadeh. 2002. Structure of HP1 chromodomain bound to a lysine 9-methylated histone H3 tail. *Science*. 295:2080-3.

Jacobson, R.H., A.G. Ladurner, D.S. King, and R. Tjian. 2000. Structure and function of a human TAFII250 double bromodomain module. *Science*. 288:1422-5.

Jenuwein, T., and C.D. Allis. 2001. Translating the histone code. *Science*. 293:1074-80.

Kellum, R., J.W. Raff, and B.M. Alberts. 1995. Heterochromatin protein 1 distribution during development and during the cell cycle in Drosophila embryos. *J Cell Sci*. 108 (Pt 4):1407-18.

Kimura, H., and P.R. Cook. 2001. Kinetics of core histones in living human cells: little exchange of H3 and H4 and some rapid exchange of H2B. *J Cell Biol*. 153:1341-53.

Kondo, Y., L. Shen, and J.P. Issa. 2003. Critical role of histone methylation in tumor suppressor gene silencing in colorectal cancer. *Mol Cell Biol*. 23:206-15.

Lillemeier, B.F., M. Koster, and I.M. Kerr. 2001. STAT1 from the cell membrane to the DNA. *Embo J*. 20:2508-17.

Marks, P.A., T. Miller, and V.M. Richon. 2003. Histone deacetylases. *Curr Opin Pharmacol*. 3:344-51.

Mateescu, B., P. England, F. Halgand, M. Yaniv, and C. Muchardt. 2004. Tethering of HP1 proteins to chromatin is relieved by phosphoacetylation of histone H3. *EMBO Rep*. 5:490-6.

Metzler-Guillemain, C., J. Luciani, D. Depetris, M.R. Guichaoua, and M.G. Mattei. 2003. HP1beta and HP1gamma, but not HP1alpha, decorate the entire XY body during human male meiosis. *Chromosome Res*. 11:73-81.

Min, J., Y. Zhang, and R.M. Xu. 2003. Structural basis for specific binding of Polycomb chromodomain to histone H3 methylated at Lys 27. *Genes Dev*. 17:1823-8.

Minc, E., Y. Allory, H.J. Worman, J.C. Courvalin, and B. Buendia. 1999. Localization and phosphorylation of HP1 proteins during the cell cycle in mammalian cells. *Chromosoma*. 108:220-34.

Munshi, N., M. Merika, J. Yie, K. Senger, G. Chen, and D. Thanos. 1998. Acetylation of HMG I(Y) by CBP turns off IFN beta expression by disrupting the enhanceosome. *Mol Cell*. 2:457-67.

Nielsen, P.R., D. Nietlispach, H.R. Mott, J. Callaghan, A. Bannister, T. Kouzarides, A.G. Murzin, N.V. Murzina, and E.D. Laue. 2002. Structure of the HP1 chromodomain bound to histone H3 methylated at lysine 9. *Nature*. 416:103-7.

Owen, D.J., P. Ornaghi, J.C. Yang, N. Lowe, P.R. Evans, P. Ballario, D. Neuhaus, P. Filetici, and A.A. Travers. 2000. The structural basis for the recognition of acetylated histone H4 by the bromodomain of histone acetyltransferase gcn5p. *Embo J*. 19:6141-9.

Paulson, J.R., and S.S. Taylor. 1982. Phosphorylation of histones 1 and 3 and nonhistone high mobility group 14 by an endogenous kinase in HeLa metaphase chromosomes. *J Biol Chem*. 257:6064-72.

Person, M.D., T.J. Monks, and S.S. Lau. 2003. An integrated approach to identifying chemically induced posttranslational modifications using comparative MALDI-MS and targeted HPLC-ESI-MS/MS. *Chem Res Toxicol*. 16:598-608.

Pesavento, J.J., Y.B. Kim, G.K. Taylor, and N.L. Kelleher. 2004. Shotgun annotation of histone modifications: a new approach for streamlined characterization of proteins by top down mass spectrometry. *J Am Chem Soc*. 126:3386-7.

Petersen, J., J. Paris, M. Willer, M. Philippe, and I.M. Hagan. 2001. The S. pombe aurora-related kinase Ark1 associates with mitotic structures in a stage dependent manner and is required for chromosome segregation. *J Cell Sci*. 114:4371-84.

Phair, R.D., S.A. Gorski, and T. Misteli. 2004. Measurement of dynamic protein binding to chromatin in vivo, using photobleaching microscopy. *Methods Enzymol*. 375:393-414.

Phair, R.D., and T. Misteli. 2000. High mobility of proteins in the mammalian cell nucleus. *Nature*. 404:604-9.

Ramaswamy, V., J.S. Williams, K.M. Robinson, R.L. Sopko, and M.C. Schultz. 2003. Global control of histone modification by the anaphase-promoting complex. *Mol Cell Biol*. 23:9136-49.

Smith, C.M., P.R. Gafken, Z. Zhang, D.E. Gottschling, J.B. Smith, and D.L. Smith. 2003. Mass spectrometric quantification of acetylation at specific lysines within the amino-terminal tail of histone H4. *Anal Biochem*. 316:23-33.

Sugimoto, K., H. Tasaka, and M. Dotsu. 2001. Molecular behavior in living mitotic cells of human centromere heterochromatin protein HPLalpha ectopically expressed as a fusion to red fluorescent protein. *Cell Struct Funct*. 26:705-18.

Suzuki, H., E. Gabrielson, W. Chen, R. Anbazhagan, M. van Engeland, M.P. Weijenberg, J.G. Herman, and S.B. Baylin. 2002. A genomic screen for genes upregulated by demethylation and histone deacetylase inhibition in human colorectal cancer. *Nat Genet*. 31:141-9.

Thorne, A.W., D. Kmiciek, K. Mitchelson, P. Sautiere, and C. Crane-Robinson. 1990. Patterns of histone acetylation. *Eur J Biochem*. 193:701-13.

Van Lint, C., S. Emiliani, and E. Verdin. 1996. The expression of a small fraction of cellular genes is changed in response to histone hyperacetylation. *Gene Expr*. 5:245-53.

Wang, Y., W. Fischle, W. Cheung, S. Jacobs, S. Khorasanizadeh, and C.D. Allis. 2004a. Beyond the double helix: writing and reading the histone code. *Novartis Found Symp*. 259:3-17; discussion 17-21, 163-9.

Wang, Y., J. Wysocka, J. Sayegh, Y.H. Lee, J.R. Perlin, L. Leonelli, L.S. Sonbuchner, C.H. McDonald, R.G. Cook, Y. Dou, R.G. Roeder, S. Clarke, M.R. Stallcup, C.D. Allis, and S.A. Coonrod. 2004b. Human PAD4 regulates histone arginine methylation levels via demethylimination. *Science*. 306:279-83.

Wei, Y., L. Yu, J. Bowen, M.A. Gorovsky, and C.D. Allis. 1999. Phosphorylation of histone H3 is required for proper chromosome condensation and segregation. *Cell*. 97:99-109.

Zhang, D.E., and D.A. Nelson. 1988. Histone acetylation in chicken erythrocytes. Rates of acetylation and evidence that histones in both active and potentially active chromatin are rapidly modified. *Biochem J*. 250:233-40.

Zhang, K., P.M. Yau, B. Chandrasekhar, R. New, R. Kondrat, B.S. Imai, and M.E. Bradbury. 2004. Differentiation between peptides containing acetylated or tri-methylated lysines by mass spectrometry: an application for determining lysine 9 acetylation and methylation of histone H3. *Proteomics*. 4:1-10.

Zhang, L., E.E. Eugeni, M.R. Parthun, and M.A. Freitas. 2003. Identification of novel histone post-translational modifications by peptide mass fingerprinting. *Chromosoma*. 112:77-86.

Zhang, Y., and D. Reinberg. 2001. Transcription regulation by histone methylation: interplay between different covalent modifications of the core histone tails. *Genes Dev*. 15:2343-60.

APPENDIX A

Solutions and Recipes

General Solutions

Tris HCl (1 M)

Name	Amount
Tris-HCl	15.8 g
Milli-Q water	up to 100 mL total volume
Total Volume	100 mL

-titrate to pH 8.3 with 4 M NaOH

NaOH (4 M)

Name	Amount
NaOH	40.0 g
Milli-Q water	up to 1.0 L total volume
Total Volume	1.0 L

KCl (1 M)

Name	Amount
KCl	7.5 g
Milli-Q water	up to 100 mL total volume
Total Volume	100.0 mL

$MgCl_2$ (1 M)

Name	Amount
$MgCl_2$	20.3 g
Milli-Q water	up to 100 mL total volume
Total Volume	100.0 mL

Ethylenediaminetetraacetic acid (EDTA) (0.5 M) pH 8.0

Name	Amount
EDTA (Sigma – E9884)	186.2 g
NaOH	20.0 g
Milli-Q water	up to 1.0 L total volume
Total Volume	1.0 L

-titrate to pH 8.0 with 10N NaOH

70% Ethanol

Name	Amount
95% Ethanol	737.0 mL
Milli-Q water	263.0 mL
Total Volume	1.0 L

10× Phosphate Buffered Saline (PBS)

Name	Amount
NaCl	80.0 g
KCl	2.0 g
Na_2PO_4	14.4 g
KH_2PO_4	2.4 g
Milli-Q water	800 mL
Total Volume	1.0 L

-titrate pH to 7.4 with HCl

1× PBS

Name	Amount
10× PBS	100.0 mL
Milli-Q water	900.0 mL
Total Volume	1.0 L

10× Tris Boric Acid EDTA (TBE) Buffer (stock solution)

Name	Amount
Tris	157.5 g
Boric Acid	27.8 g
Na_2EDTA	9.3 g
Milli-Q water	up to 1.0 L total volume
Total Volume	1.0 L

1× TBE Buffer (working solution)

Name	Amount
10× TBE	100.0 mL
Milli-Q water	900.0 mL
Total Volume	1.0 L

10× Tris Acetic Acid EDTA (TAE) Buffer pH 8.1 (stock solution)

Name	Amount
Tris	193.6 g
Acetic Acid	45.7 mL
Na_2EDTA	29.8 g
Total Volume	4.0 L

-titrate to pH 8.1 with glacial acetic acid

1× TAE Buffer (working solution)

Name	Amount
10× TAE Buffer	100.0 mL
Milli-Q water	900.0 mL
Total Volume	1.0 L

Tris EDTA (TE) Buffer (low)

Name	Amount
1 M Tris pH 8.0	1.0 mL
0.5 M EDTA pH 8.0	0.2 mL
Milli-Q water	98.8 mL
Total Volume	100.0 mL

N-(2-Hydroxyethyl)piperazine-N'-(2-ethanesulfonic acid), 4-(2-Hydroxyethyl)piperazine-1-ethanesulfonic acid (HEPES Buffer) (0.2 M)

Name	Amount
HEPES (Sigma – H3375)	47.66 g
Milli-Q water	up to 1.0 L total volume
Total Volume	1.0 L

-titrate pH to 7.5 with glacial acetic acid

Ethylene glycol-bis(2-aminoethylether)-N,N,N',N'-tetraacetic acid (EGTA) (0.5 M)

Name	Amount
EGTA (Sigma – E4378)	190.18 g
Milli-Q water	up to 1.0 L total volume
Total Volume	1.0 L

-titrate to pH 8.0 with 10N NaOH

Microscopy Reagents

4% Paraformaldehyde (w/v)

Name	Amount
Paraformaldehyde (BDH – 294474L)	0.4 g
1× PBS	up to 10.0 mL total volume
Total Volume	1.0 L

-bring to slight boil with mixing
-allow to cool prior to use

PBS 0.5% Triton X-100 (v/v)

Name	Amount
Triton X-100	5.0 mL
1× PBS	995.0 mL
Total Volume	1.0 L

PBS 0.1% Triton X-100 (v/v)

Name	Amount
Triton X-100	1.0 mL
1× PBS	999.0 mL
Total Volume	1.0 L

p-paraphenylenediamine solution (*p*PDA)

Name	Amount
*p*PDA	0.005 g
10× PBS	0.5 mL
Glycerol	4.5 mL
Total Volume	5.0 mL

-mix overnight until pPDA is dissolved and protect from light
-store at -20°C

100× 4',6-Diamidino-2-phenylindole (DAPI)

Name	Amount
DAPI	50 µg
Milli-Q water	1.0 mL
Total Volume	1.0 mL

-store at 4°C

Mounting Media

Name	Amount
*p*PDA solution	1.0 mL
100× DAPI	10 µL
Total Volume	1.0 mL

5-Fluorouridine (FU) Stock Solution (134 mM)

Name	Amount
FU (Sigma – F5130)	35.13 mg
Milli-Q water	1.0 mL
Total Volume	1.0 mL

5-bromo-2'-deoxyuridine (BrdU) Stock Solution (163 mM)

Name	Amount
BrdU (Sigma – B5002)	50.0 mg
DMSO	1.0 mL
Total Volume	1.0 mL
-store at -20°C	

Saponin Buffer

Name	Amount
200mM Hepes	100.0 mL
KCl	10.28 g
1 M $MgCl_2$	4.0 mL
0.5 M EGTA	6.0 mL
Milli-Q water	up to 1.0 L total volume
Total Volume	1.0 L
-titrate to pH 7.5 with glacial acetic acid	

Immunoblotting Reagents

EDTA (0.53 mM)

Name	Amount
0.5 M EDTA	1.06 mL
Milli-Q water	998.94 mL
Total Volume	1.0 L

Nuclei Buffer

Name	Amount
Sucrose	8.6 g
NaCl	1.16 g
1 M Tris-HCl pH 8.0	1.0 mL
1 M $MgCl_2$	0.2 mL
1 M $CaCl_2$	0.1 mL
25% (v/v) Triton X-100	4.0 mL
Milli-Q water	up to 100 mL total volume
Total Volume	100.0 mL

Phenylmethanesulfonyl fluoride (PMSF) (100 mM)

Name	Amount
PMSF (Sigma – P7626)	17.4 mg
Ethanol	1.0 mL
Total Volume	1.0 mL
-store at -20°C	

3× Sample Buffer (Immunoblot)

Name	Amount
Glycerol	30.0 mL
B-mercaptoethanol	3.0 mL
SDS	6.0 g
Tris	2.28 g
Bromophenol Blue	1.5 mg
Milli-Q water	up to 100.0 mL total volume
Total Volume	100.0 mL
-titrate pH to 6.8 with HCl	

30% Acrylamide:Bis-Acrylamide (29:1)

Name	Amount
Acrylamide	30.0 g
Bis-acrylamide	0.8 g
Milli-Q water	up to 100.0 mL total volume
Total Volume	100.0 mL

-protect from light and place at 4°C

4x Stacking Buffer

Name	Amount
Tris	6.05 g
SDS	0.4 g
Milli-Q water	up to 100 mL total volume
Total Volume	100.0 mL

-titrate pH to 6.8 with HCl

4x Separating Buffer

Name	Amount
Tris	91.0 g
SDS	2.0 g
Milli-Q water	up to 500 mL total volume
Total Volume	500 mL

-titrate pH to 8.7 with HCl

10% Ammonium Persulfate

Name	Amount
Ammonium Persulfate	0.1 g
Milli-Q water	1.0 mL
Total Volume	1.0 mL

10× Running Buffer

Name	Amount
Tris Base	30.0 g
Glycine	144.0 g
SDS	10.0 g
Milli-Q water	up to 1.0 L
Total Volume	1.0 L

1× Running Buffer

Name	Amount
10× Running Buffer	100.0 mL
Milli-Q water	900.0 mL
Total Volume	1.0 L

Transfer Buffer

Name	Amount
10× Running Buffer	100.0 mL
Methanol	200.0 mL
Milli-Q water	700.0 mL
Total Volume	1.0 L

10× Tris Buffered Saline (TBS)

Name	Amount
NaCl	80.0 g
KCl	2.0 g
1 M Tris pH 7.5	250.0 mL
Milli-Q water	up to 1.0 L total volume
Total Volume	1.0 L

TBS-Tween20 (TBST)

Name	Amount
10× TBS	100.0 mL
Tween-20	1.0 mL
Milli-Q water	899.0 mL
Total Volume	1.0 L

5% Non-fat Milk (w/v)

Name	Amount
Non-fat milk	5.0 g
1× TBS	100.0 mL
Total Volume	100.0 mL

Copper phthalocyanine 3,4',4'',4'''-tetrasulfonic acid tetrasodium salt (CPTS)

Name	Amount
CPTS	50.0 mg
HCl (concentrated)	1.0 mL
Milli-Q water	1.0 L
Total Volume	1.0 L

Coomassie Blue Stain

Name	Amount
Coomassie Blue R-250	0.25 g
Ethanol	100.0 mL
Milli-Q water	100.0 mL
Acetic Acid	25.0 mL
Milli-Q water	up to a total volume of 250.0 mL
Total Volume	250.0 mL

-store at room temperature

Coomassie Blue Destain

Name	Amount
Ethanol	400.0 mL
Acetic Acid	100.0 mL
Milli-Q water	up to a total volume of 1.0 L
Total Volume	1.0 L

-store at room temperature

Cell Cycle Inhibitors

Nocodazole Stock Solution (~15 mM)

Name	Amount
Nocodazole (Sigma - M1404)	5.0 mg
Dimethyl Sulfoxide (DMSO)	1.0 mL
Total Volume	1.0 mL

-store at -20°C

Thymidine Stock Solution (100 mM)

Name	Amount
Thymidine (Sigma – T9250)	24.2 mg
Milli-Q water	1.0 mL
Total Volume	1.0 mL

-store at -20°C

ALLN Stock Solution

Name	Amount
ALLN (Calbiochem - 208719)	25.0 mg
DMSO	1.0 mL
Total Volume	1.0 mL

-store at -20°C

Flow Cytometry Reagents

Propidium Iodide Stock Solution

Name	Amount
Propidium Iodide (Sigma – P4170)	1.0 mg
Milli-Q water	1.0 mL
Total Volume	1.0 mL

-store at 4°C away from light

RNase A Stock Solution

Name	Amount
RNase A (Sigma – R5500)	1.0 mg
Milli-Q water	1.0 mL
Total Volume	1.0 mL

-store at -20°C

APPENDIX B

Supplemental Statistical Analyses from Chapter 3

Supplementary Table 1: Flow cytometric analysis of specific methylation epitopes in HeLa cells at defined stages of the cell cycle.

Epitope	Stage	Mean[a]	SD[b]	N[c]
mMeK4	G_0/G_1	17.860	6.150	6532
	S-phase	22.180	6.960	1813
	G_2/M	24.090	8.050	2978
dMeK4	G_0/G_1	6.750	2.270	6602
	S-phase	7.810	1.990	1328
	G_2/M	8.600	2.290	2423
tMeK4	G_0/G_1	184.240	90.950	6665
	S-phase	186.390	97.130	1596
	G_2/M	183.300	108.380	1558
mMeK9	G_0/G_1	37.310	13.760	6370
	S-phase	53.930	20.780	2140
	G_2/M	73.960	25.210	2783
dMeK9	G_0/G_1	59.470	19.530	6540
	S-phase	55.150	19.360	1632
	G_2/M	59.900	26.350	2097
tMeK9	G_0/G_1	15.720	7.140	6077
	S-phase	21.300	14.527	1765
	G_2/M	45.640	48.750	2072
mMeK20	G0/G1	227.650	175.430	6054
	S-phase	262.670	242.450	1829
	G_2/M	327.280	250.840	1992
tMeK20	G_0/G_1	106.750	52.340	5689
	S-phase	97.020	47.550	3003
	G_2/M	95.290	50.130	3766

[a] only the results from one representative trial of the three replicates is shown

[b] SD = standard deviation

[c] N = number of cells

Supplementary Table 2: Flow cytometric analysis of specific methylation epitopes in 10T1/2 cells at defined stages of the cell cycle.

Epitope	Stage	Mean[a]	SD[b]	N[c]
mMeK4	G_0/G_1	16.940	6.780	12286
	S-phase	18.620	6.310	1990
	G_2/M	22.140	7.990	3115
dMeK4	G_0/G_1	6.220	7.080	12276
	S-phase	7.610	5.850	2155
	G_2/M	9.630	15.150	3167
tMeK4	G_0/G_1	100.550	54.380	12974
	S-phase	119.840	66.620	1547
	G_2/M	136.650	86.570	2497
mMeK9	G_0/G_1	19.060	4.630	12450
	S-phase	26.470	7.130	2105
	G_2/M	37.270	10.410	2947
dMeK9	G_0/G_1	15.470	6.080	12890
	S-phase	19.320	7.870	1710
	G_2/M	22.930	9.370	2411
tMeK9	G_0/G_1	6.020	5.590	12767
	S-phase	7.550	4.780	1632
	G_2/M	11.530	10.770	2583
mMeK20	G_0/G_1	56.610	36.420	12325
	S-phase	49.350	20.700	2167
	G_2/M	100.300	76.600	3059
tMeK20	G_0/G_1	90.130	60.740	13005
	S-phase	96.770	87.090	1410
	G_2/M	94.400	59.690	2359

[a] only the results from one representative trial of the three replicates is shown

[b] SD = standard deviation

[c] N = number of cells

Supplementary Table 3: Tukey-Kramer multi-comparison post-tests for differences between mean norm-Me signal intensities at various cell cycle stages.

Epitope	Statistical Significance (*p*-value)[a]		
	Group	G_0/G_1	S-phase
mMeK4	S-Phase	++	
	G_2/M	+++	++
dMeK4	S-Phase	++	
	G_2/M	++	++
tMeK4	S-Phase	++	
	G_2/M	+++	++
mMeK9	S-Phase	+++	
	G_2/M	+++	+++
dMeK9	S-Phase	+++	
	G_2/M	+++	++
tMeK9	S-Phase	++	
	G_2/M	+++	++
mMeK20	S-Phase	++	
	G_2/M	+++	+++
tMeK20	S-Phase	++	
	G_2/M	++	++

[a] the following notations are used to define varying degrees of statistical significance; extremely statistically significant (p <0.001 [+++]), highly statistically significant (p < 0.01 [++]), statistically significant (p < 0.05 [+]), and not statistically significant (p > 0.05 [NS])

Supplementary Table 4: Channel statistics for the methylated epitopes in 10T1/2 cells as determined by quantitative imaging microscopy.

Epitope	Cell Cycle Stage	Mean[a]	SEM[b]	N[c]
mMeK4	Interphase	1.262	0.01845	443
	Early G_2	1.063	0.04294	39
	Late G_2	1.061	0.06305	15
	Prophase	0.9726	0.05206	25
	Prometaphase	0.9264	0.1362	12
	Metaphase	0.9223	0.08262	14
	Anaphase	0.5867	0.05962	13
	Telophase	0.5705	0.06216	15
	Early G_1	0.8681	0.07439	30
dMeK4	Interphase	0.5718	0.01908	264
	Early G_2	0.4346	0.03590	26
	Late G_2	0.5629	0.06369	12
	Prophase	0.5480	0.06538	12
	Prometaphase	0.6519	0.06173	13
	Metaphase	0.5573	0.03322	13
	Anaphase	0.6693	0.05173	22
	Telophase	0.5459	0.03178	20
	Early G_1	0.5057	0.03080	40
tMeK4	Interphase	2.754	0.05742	371
	Early G_2	1.988	0.1923	21
	Late G_2	2.739	0.3275	17
	Prophase	2.025	0.1645	30
	Prometaphase	1.869	0.1982	16
	Metaphase	2.463	0.2827	12
	Anaphase	2.094	0.2585	12
	Telophase	2.001	0.2229	14
	Early G_1	2.408	0.2266	26
mMeK9	Interphase	1.361	0.02719	297
	Early G_2	1.237	0.1357	19
	Late G_2	1.442	0.1167	15
	Prophase	1.521	0.1103	21
	Prometaphase	1.602	0.1216	17
	Metaphase	1.963	0.2455	14
	Anaphase	1.406	0.1507	13
	Telophase	1.036	0.1281	12
	Early G_1	1.035	0.07030	19
dMeK9	Interphase	1.634	0.04136	283
	Early G_2	1.208	0.1392	16
	Late G_2	1.175	0.1211	13
	Prophase	1.210	0.1685	13
	Prometaphase	1.727	0.1132	12

	Metaphase	2.047	0.1812	15
	Anaphase	1.649	0.2935	16
	Telophase	1.205	0.1075	12
	Early G_1	1.343	0.1189	32
tMeK9	Interphase	0.3183	0.008297	441
	Early G_2	0.3219	0.02992	13
	Late G_2	0.6424	0.09482	19
	Prophase	1.024	0.08012	27
	Prometaphase	1.204	0.09106	12
	Metaphase	1.284	0.1347	12
	Anaphase	0.7582	0.1252	12
	Telophase	0.4742	0.06574	12
	Early G_1	0.2278	0.02444	19
mMeK20	Interphase	0.4496	0.01334	286
	Early G_2	0.5320	0.05391	14
	Late G_2	0.6452	0.04461	15
	Prophase	0.7986	0.06217	15
	Prometaphase	1.184	0.08023	12
	Metaphase	1.318	0.09115	13
	Anaphase	1.158	0.1235	14
	Telophase	0.8416	0.07357	11
	Early G_1	0.4441	0.05192	15
tMeK20	Interphase	0.7602	0.01563	537
	Early G_2	0.6227	0.06174	45
	Late G_2	0.6882	0.07428	17
	Prophase	0.7189	0.05807	23
	Prometaphase	0.8158	0.06922	17
	Metaphase	0.8361	0.04222	13
	Anaphase	0.7179	0.05377	12
	Telophase	0.6206	0.07014	16
	Early G_1	0.7213	0.05644	32

[a] Mean normalized signal intensity as determined by mean methylation signal intensity/mean DAPI signal intensity

[b] SEM = standard error of the mean

[c] N = number of cells

Supplementary Table 5: Analysis of variance (ANOVA) tests for the normalized methylation intensities as measured by quantitative imaging microscopy.

Epitope	Group[a]	SS[b]	df[c]	MS[d]	F-Ratio[e]	*p*-value	Reject H_0[f]
mMeK4	BG	19.44	8	2.430	7.74	<0.0001	Yes
	WG	81.75	597	0.1369			
dMeK4	BG	0.9400	8	0.1175	1.562	0.1343	No
	WG	31.07	413	0.07524			
tMeK4	BG	44.76	8	5.594	4.819	<0.0001	Yes
	WG	592.1	510	1.161			
mMeK9	BG	10.24	8	1.280	5.263	<0.0001	Yes
	WG	101.6	418	0.2432			
dMeK9	BG	14.33	8	1.791	3.746	0.0003	Yes
	WG	192.7	403	0.4782			
tMeK9	BG	33.90	8	4.237	86.26	<0.0001	Yes
	WG	27.41	558	0.04912			
mMeK20	BG	22.69	8	2.836	48.99	<0.0001	Yes
	WG	22.34	386	0.05788			
tMeK20	BG	1.334	8	0.1668	1.342	0.2194	No
	WG	87.39	703	0.1243			

[a] Defines whether or not the analysis is between groups (BG) or within the groups (WG)
[b] SS represents the sum of squares
[c] df represents degrees of freedom
[d] MS represents the mean square
[e] F-ratio is calculated by MS_{BG}/MS_{WG}
[f] The null hypothesis (H_0) is rejected if the *p*-value is <0.05

Supplementary Table 6: Tukey-Kramer multi-comparison post-tests for differences between normalized methylation means at defined cell cycle stages as measured by quantitative imaging microscopy.

Epitope Group[a]		Statistical Significance (p-value)[b]							
		I	EG2	LG2	P	PM	M	A	T
mMeK4	EG2	+							
	LG2	NS	NS						
	P	++	NS	NS					
	PM	NS	NS	NS	NS				
	M	+	NS	NS	NS	NS			
	A	+++	++	+	NS	NS	NS		
	T	+++	+++	+	+	NS	NS	NS	
	EG1	+++	NS	NS	NS	NS	NS	NS	NS
tMeK4	EG2	+							
	LG2	NS	NS						
	P	+	NS	NS					
	PM	+	NS	NS	NS				
	M	NS	NS	NS	NS	NS			
	A	NS	NS	NS	NS	NS	NS		
	T	NS	NS	NS	NS	NS	NS	NS	
	EG1	NS	NS	NS	NS	NS	NS	NS	NS
mMeK9	EG2	NS							
	LG2	NS	NS						
	P	NS	NS	NS					
	PM	NS	NS	NS	NS				
	M	+++	++	NS	NS	NS			
	A	NS	NS	NS	NS	NS	NS		
	T	NS	NS	NS	NS	NS	+++	NS	
	EG1	NS	NS	NS	NS	+	+++	NS	NS
dMeK9	EG2	NS							
	LG2	NS	NS						
	P	NS	NS	NS					
	PM	NS	NS	NS	NS				
	M	NS	+	+	+	NS			
	A	NS	NS	NS	NS	NS	NS		
	T	NS	NS	NS	NS	NS	NS	NS	
	EG1	NS	NS	NS	NS	NS	+	NS	NS

tMeK9	EG2	NS							
	LG2	+++	++						
	P	+++	+++	+++					
	PM	+++	+++	+++	NS				
	M	+++	+++	+++	+	NS			
	A	+++	+++	NS	+	+++	+++		
	T	NS	NS	NS	+++	+++	+++	NS	
	EG1	NS	NS	+++	+++	+++	+++	+++	NS
mMeK20	EG2	NS							
	LG2	NS	NS						
	P	+++	NS	NS					
	PM	+++	+++	+++	++				
	M	+++	+++	+++	+++	NS			
	A	+++	+++	+++	++	NS	NS		
	T	+++	+	NS	NS	+	+++	+	
	EG1	NS	NS	NS	++	+++	+++	+++	++

[a] Group refers to the cell cycle stage; Interphase (I), early G_2 (EG2), late G_2 (LG2), prophase (P), prometaphase (PM), metaphase (M), anaphase (A), telophase (T) and early G_1 (EG1)

[b] the following notations are used to define varying degrees of statistical significance; extremely statistically significant (p <0.001 [+++]), highly statistically significant (p < 0.01 [++]), statistically significant (p < 0.05 [+]), and not statistically significant (p > 0.05 [NS])